



HAL
open science

Mécanismes de fragilisation de l'acier inoxydable super-martensitique X4CrNi16-4 Virgo™38 : Effets couplés des traitements thermiques et des milieux corrosifs contenant Na₂S ou H₂S

Clément Gayton

► **To cite this version:**

Clément Gayton. Mécanismes de fragilisation de l'acier inoxydable super-martensitique X4CrNi16-4 Virgo™38 : Effets couplés des traitements thermiques et des milieux corrosifs contenant Na₂S ou H₂S. Autre. Université de Lyon, 2018. Français. NNT : 2018LYSEM004 . tel-01844249

HAL Id: tel-01844249

<https://theses.hal.science/tel-01844249>

Submitted on 19 Jul 2018

HAL is a multi-disciplinary open access archive for the deposit and dissemination of scientific research documents, whether they are published or not. The documents may come from teaching and research institutions in France or abroad, or from public or private research centers.

L'archive ouverte pluridisciplinaire **HAL**, est destinée au dépôt et à la diffusion de documents scientifiques de niveau recherche, publiés ou non, émanant des établissements d'enseignement et de recherche français ou étrangers, des laboratoires publics ou privés.



N°d'ordre NNT : 2018LYSEM004

THESE de DOCTORAT DE L'UNIVERSITE DE LYON
opérée au sein de
l'Ecole des Mines de Saint-Etienne

Ecole Doctorale N° 488
Sciences, Ingénierie, Santé

Spécialité de doctorat : Sciences et Génie des Matériaux

Soutenue publiquement le 29/01/2018, par :
Clément GAYTON

**Mécanismes de fragilisation de l'acier
inoxydable super-martensitique
X4CrNi16-4 Virgo™38 :
Effets couplés des traitements
thermiques et des milieux corrosifs
contenant Na₂S ou H₂S**

Devant le jury composé de :

Crépin, Jérôme	Directeur de recherche	Mines Paristech	Président
Deschamps, Alexis	Professeur	Grenoble INP	Rapporteur
Mantel, Marc	Professeur	Grenoble INP	Rapporteur
Crépin, Jérôme	Directeur de recherche	Mines Paristech	Examinateur
Duret-Thual, Claude	Professeur associé	INSA Lyon	Examinatrice
Stolarz, Jacques	Chargé de recherche	EMSE	Directeur de thèse
Wolski, Krzysztof	Directeur de recherche	EMSE	Co-directeur de thèse
Bosch, Cédric	Chargé de recherche	EMSE	Encadrant
Rozinoer, Alexia	Docteur	Thermodyn SAS	Encadrante

Spécialités doctorales	Responsables :	Spécialités doctorales	Responsables
SCIENCES ET GENIE DES MATERIAUX MECANIQUE ET INGENIERIE GENIE DES PROCEDES SCIENCES DE LA TERRE SCIENCES ET GENIE DE L'ENVIRONNEMENT	K. Wolski Directeur de recherche S. Drapier, professeur F. Gruy, Maître de recherche B. Guy, Directeur de recherche D. Graillot, Directeur de recherche	MATHEMATIQUES APPLIQUEES INFORMATIQUE SCIENCES DES IMAGES ET DES FORMES GENIE INDUSTRIEL MICROELECTRONIQUE	O. Roustant, Maître-assistant O. Boissier, Professeur JC. Pinoli, Professeur X. Delorme, Maître assistant Ph. Lalevée, Professeur

EMSE : Enseignants-chercheurs et chercheurs autorisés à diriger des thèses de doctorat (titulaires d'un doctorat d'État ou d'une HDR)

ABSI	Nabil	CR	Génie industriel	CMP
AUGUSTO	Vincent	CR	Image, Vision, Signal	CIS
AVRIL	Stéphane	PR2	Mécanique et ingénierie	CIS
BADEL	Pierre	MA(MDC)	Mécanique et ingénierie	CIS
BALBO	Flavien	PR2	Informatique	FAYOL
BASSEREAU	Jean-François	PR	Sciences et génie des matériaux	SMS
BATTON-HUBERT	Mireille	PR2	Sciences et génie de l'environnement	FAYOL
BEIGBEDER	Michel	MA(MDC)	Informatique	FAYOL
BLAYAC	Sylvain	MA(MDC)	Microélectronique	CMP
BOISSIER	Olivier	PR1	Informatique	FAYOL
BONNEFOY	Olivier	MA(MDC)	Génie des Procédés	SPIN
BORBELY	Andras	MR(DR2)	Sciences et génie des matériaux	SMS
BOUCHER	Xavier	PR2	Génie Industriel	FAYOL
BRODHAG	Christian	DR	Sciences et génie de l'environnement	FAYOL
BRUCHON	Julien	MA(MDC)	Mécanique et ingénierie	SMS
CAMEIRAO	Ana	MA(MDC)	Génie des Procédés	SPIN
CHRISTIEN	Frédéric	PR	Science et génie des matériaux	SMS
DAUZERE-PERES	Stéphane	PR1	Génie Industriel	CMP
DEBAYLE	Johan	MR	Sciences des Images et des Formes	SPIN
DEGEORGE	Jean-Michel	MA(MDC)	Génie industriel	Fayol
DELAFOSSE	David	PR0	Sciences et génie des matériaux	SMS
DELORME	Xavier	MA(MDC)	Génie industriel	FAYOL
DESRAYAUD	Christophe	PR1	Mécanique et ingénierie	SMS
DJENIZIAN	Thierry	PR	Science et génie des matériaux	CMP
DOUCE	Sandrine	PR2	Sciences de gestion	FAYOL
DRAPIER	Sylvain	PR1	Mécanique et ingénierie	SMS
FAUCHEU	Jenny	MA(MDC)	Sciences et génie des matériaux	SMS
FAVERGEON	Loïc	CR	Génie des Procédés	SPIN
FEILLET	Dominique	PR1	Génie Industriel	CMP
FOREST	Valérie	MA(MDC)	Génie des Procédés	CIS
FRACZKIEWICZ	Anna	DR	Sciences et génie des matériaux	SMS
GARCIA	Daniel	MR(DR2)	Sciences de la Terre	SPIN
GAVET	Yann	MA(MDC)	Sciences des Images et des Formes	SPIN
GERINGER	Jean	MA(MDC)	Sciences et génie des matériaux	CIS
GOEURIOT	Dominique	DR	Sciences et génie des matériaux	SMS
GONDRAN	Natacha	MA(MDC)	Sciences et génie de l'environnement	FAYOL
GONZALEZ FELIU	Jesus	MA(MDC)	Sciences économiques	FAYOL
GRAILLOT	Didier	DR	Sciences et génie de l'environnement	SPIN
GROSSEAU	Philippe	DR	Génie des Procédés	SPIN
GRUY	Frédéric	PR1	Génie des Procédés	SPIN
GUY	Bernard	DR	Sciences de la Terre	SPIN
HAN	Woo-Suck	MR	Mécanique et ingénierie	SMS
HERRI	Jean Michel	PR1	Génie des Procédés	SPIN
KERMOUCHE	Guillaume	PR2	Mécanique et Ingénierie	SMS
KLOCKER	Helmut	DR	Sciences et génie des matériaux	SMS
LAFORREST	Valérie	MR(DR2)	Sciences et génie de l'environnement	FAYOL
LERICHE	Rodolphe	CR	Mécanique et ingénierie	FAYOL
MALLIARAS	Georges	PR1	Microélectronique	CMP
MOLIMARD	Jérôme	PR2	Mécanique et ingénierie	CIS
MOUTTE	Jacques	CR	Génie des Procédés	SPIN
NEUBERT	Gilles			FAYOL
NIKOLOVSKI	Jean-Pierre	Ingénieur de recherche	Mécanique et ingénierie	CMP
NORTIER	Patrice	PR1	Génie des Procédés	SPIN
O CONNOR	Rodney Philip	MA(MDC)	Microélectronique	CMP
OWENS	Rosin	MA(MDC)	Microélectronique	CMP
PERES	Véronique	MR	Génie des Procédés	SPIN
PICARD	Gauthier	MA(MDC)	Informatique	FAYOL
PIJOLAT	Christophe	PR0	Génie des Procédés	SPIN
PINOLI	Jean Charles	PR0	Sciences des Images et des Formes	SPIN
POURCHEZ	Jérémy	MR	Génie des Procédés	CIS
ROUSSY	Agnès	MA(MDC)	Microélectronique	CMP
ROUSTANT	Olivier	MA(MDC)	Mathématiques appliquées	FAYOL
SANAUR	Sébastien	MA(MDC)	Microélectronique	CMP
STOLARZ	Jacques	CR	Sciences et génie des matériaux	SMS
TRIA	Assia	Ingénieur de recherche	Microélectronique	CMP
VALDIVIESO	François	PR2	Sciences et génie des matériaux	SMS
VIRICELLE	Jean Paul	DR	Génie des Procédés	SPIN
WOLSKI	Krzystof	DR	Sciences et génie des matériaux	SMS
XIE	Xiaolan	PR1	Génie industriel	CIS
YUGMA	Gallian	CR	Génie industriel	CMP



N°d'ordre NNT : 2018LYSEM004

THESE de DOCTORAT DE L'UNIVERSITE DE LYON
opérée au sein de
l'Ecole des Mines de Saint-Etienne

Ecole Doctorale N° 488
Sciences, Ingénierie, Santé

Speciality: Materials Science and Engineering

Soutenue publiquement le 29/01/2018, par :
Clément GAYTON

**Embrittlement mechanisms of the
X4CrNi16-4 super-martensitic stainless
steel Virgo™38:
Effects of heat treatments and corrosive
environments containing Na₂S or H₂S**

Devant le jury composé de :

Crépin, Jérôme	Directeur de recherche	Mines Paristech	Président
Deschamps, Alexis	Professeur	Grenoble INP	Rapporteur
Mantel, Marc	Professeur	Grenoble INP	Rapporteur
Crépin, Jérôme	Directeur de recherche	Mines Paristech	Examineur
Duret-Thual, Claude	Professeur associé	INSA Lyon	Examinatrice
Stolarz, Jacques	Chargé de recherche	EMSE	Directeur de thèse
Wolski, Krzysztof	Directeur de recherche	EMSE	Co-directeur de thèse
Bosch, Cédric	Chargé de recherche	EMSE	Encadrant
Rozinoer, Alexia	Docteur	Thermodyn SAS	Encadrante

Remerciements

Je tiens à adresser mon respect à l'ensemble des membres du jury ayant fait le déplacement et qui m'ont fait l'honneur d'évaluer mes travaux. Je les remercie pour l'intérêt qu'ils ont porté à cette étude et pour leur discussion lors de la (longue et très redoutée) séance de discussion. Ainsi, je tiens à remercier Monsieur Jérôme Crépin pour avoir accepté de présider ce jury. Je remercie tout particulièrement Madame Claude Duret-Thual, non seulement pour sa présence dans le jury mais surtout pour la chance qu'elle m'a donnée de pouvoir réaliser des essais de traction en présence d'H₂S au sein de son entreprise. Je remercie également Monsieur Alexis Deschamps pour ses échanges très instructifs sur la métallurgie physique de ces alliages complexes et pour avoir accepté notre point de vue sur l'austénite de réversion. Je remercie aussi Monsieur Marc Mantel pour sa vision générale du sujet et pour toutes les discussions que nous avons eu au cours de ces trois années grâce à la proximité de ce sujet de thèse et de celui qu'il encadrait en parallèle.

Cette thèse n'aurait jamais pu être ce qu'elle a été sans la participation très active de toute l'équipe encadrante. Alexia, je vous remercie pour votre accompagnement au cours de ses trois années (et quelques) et surtout pour votre gentillesse et pour la confiance que vous nous avez accordé. Cédric, merci d'avoir apporté cet aspect de corrosionniste et surtout l'idée de l'emploi de la solution poisonnée contenant Na₂S qui a donné des ruptures fantastiques pour l'étude. Krzysztof, merci à toi d'avoir toujours été présent au cours de cette thèse malgré tes nombreuses autres occupations. Je suis conscient que si cette thèse s'est tenue dans des délais raisonnables c'est essentiellement grâce à toi ! Tu m'as toujours poussé à aller plus loin tout en gardant un œil sur la montre car, comme tu me l'as dit au début, une thèse ce n'est QUE 36 mois. Ta grande expérience, ta vision d'ensemble et ta capacité à tout comprendre plus vite que tout le monde auront été des atouts majeurs dans ce travail et plus généralement dans ma formation de chercheur. Jacques, merci de ton soutien technique, surtout sur la partie métallurgique où tu as su débusquer des résultats que je ne soupçonnais même pas. Merci pour ces discussions sur la physique de la métallurgie et sur la remise en question de bons nombres d'écrits. Tu m'as permis une ouverture d'esprit et un sens critique indispensable à un travail de recherche. Merci également pour toutes tes capacités rédactionnelles et pour ta maîtrise de la langue de Shakespeare, et de ces subtilités.

Je n'oublie bien évidemment pas le personnel de Thermodyn qui m'a toujours réservé un très bon accueil. Notamment Pierre qui m'a expliqué les différents enjeux de ce domaine et surtout François qui a su me confier la responsabilité de torturer son Virgo™38, et qui m'a fait comprendre le pourquoi de sa passion pour cet alliage.

Merci aux personnes en charge de l'accueil et de l'assistance à l'école des mines: Olivier et Thierry pour votre expertise informatique, les assistantes du centre pour votre aide administrative : Sophie, Christel, Céline, Géraldine, Julie et Gaëlle et Christophe pour le service reprographie.

Ma thèse, essentiellement expérimentale, s'est appuyée sur bons nombres d'essais qui n'auraient pas pu être réalisés et approfondis sans le soutien et l'accompagnement de tout le personnel de l'école. C'est pourquoi, je souhaite remercier particulièrement les boute-en-train de l'atelier, Marc, Gilles et Bernard, qui hormis leurs blagues ont également toujours répondu présent lorsqu'il fallait usiner des éprouvettes en grandes séries (Marc) ou réaliser des montages sortant de mon imaginaire et plus douteux les uns que les autres (Bernard et Gilles). Merci à Gilles Blanc pour la

Remerciements

tenue impeccable de son laboratoire, pour son expertise en métallographie et également pour les discussions que nous avons les matins lorsque nous étions seuls dans l'école. Je remercie le service microscopie pour la formation et l'aide qu'ils m'ont apporté : Sergio et Marilynne vous m'avez permis de dompter l'EBSD récalcitrant et avez toujours accepté de me montrer les à-côtés des manips afin de satisfaire ma (grande) curiosité. Merci à Vincent et Yoann pour leur accompagnement sur les ruptures in-situ Auger, sur les mesures XPS et sur l'AFM. Yoann, merci également pour le soutien lors du dessin des plans de prélèvement des éprouvettes et pour les matinées passées à recharger en azote liquide devant l'Auger. Merci à Huguette et Nathalie pour l'ensemble des mesures de DRX, et tout particulièrement Nathalie pour m'avoir laissé quartier libre pour « jouer » une semaine complète en autonomie sur le diffracto afin de faire mes mesures de déformation in-situ. Merci également à Delphine d'avoir réalisé toutes les solutions chimiques de ma thèse même les plus tenaces et merci de ton ouverture d'esprit sur la sécurité au travail. Ces solutions qui étaient en partie utilisées dans la fameuse manip' de perméation, que je ne peux citer sans son plus fidèle admirateur (ou détracteur ?) : Max. Merci à toi d'avoir accepté (non sans ronchonner, ou « boudier » diraient certains) de m'accompagner sur cette usine à gaz... pleine de fuites... Tu auras compris tout l'intérêt de la CAF (!!!) ce qui fait de toi l'... (je te laisse compléter avec les lettres : e x p e r t) de cette cellule. Pour finir cette partie, un immense merci à Claire pour la formation sur l'ensemble des machines mécaniques et particulièrement sur les tests de traction lente. Ta gentillesse (même lorsque je cassais tout) m'a permis de relativiser lorsque les essais ne fonctionnaient pas.

Résumer une thèse à trois années de labeurs et de déconvenues serait malhonnête! En effet, c'est aussi parfois surtout trois années de blagues en tout genre, de rire et de soutien au K4 (et J3)! Alors que je m'apprête à mettre un point final à cette thèse d'autre commence à rédiger la leur : je pense bien évidemment à toi Elia qui ne sera peut-être pas le prochain doctorant de MPI à soutenir (hein Quentin... ☺) mais qui restera mon acolyte non seulement dans les manips foireuses, mais surtout dans les blagues (tout aussi foireuses d'ailleurs...). En parlant de blagues foireuses, je ne peux pas omettre le roi en la matière Régnière (baaaaaa) qui, par sa roublardise et son aplomb sans faille, arriverait à vous faire avaler n'importe quoi ! Merci d'avoir été là (même si tu as refusé de m'attendre pour soutenir...), j'espère que cette amitié continuera au-delà des montagnes russes hongroises suisses. Un Mat(t)hieu en cache souvent un autre et en parlant de ne pas attendre pour soutenir sa thèse celui-ci fera également bien la paire : Dutto. Merci aussi à tous les gens ayant partagé ces années : Michal, Joris, Antonis, Hao... Bon courage à tous les nouveaux qui auront le bonheur de découvrir ce magnifique endroit qu'est le K4 (et son annexe J3). Je n'oublie bien évidemment pas les 'anciens' qui ont su donner les notes de noblesse à ce couloir : JG, Robin, Guillaume, Jerem, Ernesto, David... Je finirai ce paragraphe par une note féminine et maternelle nécessaire à l'encadrement de tous ces jeunes délinquants. Merci tout d'abord à toi Lisa de m'avoir accueilli dans ton bureau, de m'avoir écouté (beaucoup) parler, (un peu) râler, mais surtout de m'avoir beaucoup conseillé. Merci aussi Julia d'avoir recadré le 'dégueulasse' Matthieu et de nous avoir supporté. Merci aussi d'avoir saboté l'ensemble des manips de l'école afin que nous restions un peu plus longtemps.

Enfin, ce dernier paragraphe pour remercier l'ensemble de ma famille (au sens large) pour leur soutien et pour tous les week-ends que nous avons passés et qui permettent de décompresser après des semaines rudes. Merci particulièrement à ma femme qui aura su me supporter durant tout ce temps et qui le fera pendant longtemps encore je l'espère. C'est à toi que je dédie les 'quelques' pages suivantes.

Contents

General introduction	9
Chapter I: Bibliographic review	17
1. Description of (super)-martensitic stainless steels	21
1.1. Introduction.....	21
1.2. Composition	21
1.2.1. Major elements: Fe-C-Ni-Cr.....	21
1.2.2. Secondary elements: Mn-Mo-Ti.....	25
1.2.3. Relations of equivalence	25
1.3. Microstructure of supermartensitic stainless steels	27
1.3.1. α' martensite	27
1.3.2. γ austenite	27
1.3.3. Martensitic transformations	28
1.3.4. Austenite/martensite interface.....	31
1.3.5. Carbide precipitation.....	31
1.4. Heat treatment applied to SMSS for oil & gas applications	32
1.4.1. Standard profile imposed by NACE MR0175.....	32
1.4.2. Austenite stability as a function of tempering temperature and composition	34
2. Cracking of (super)-martensitic stainless steels.....	35
2.1. Introduction.....	35
2.2. Crack initiation.....	36
2.2.1. Initiation by pitting	36
2.2.2. Initiation by chemical depassivation	37
2.2.3. Initiation by mechanical defects.....	38
2.2.4. Initiation in presence of H ₂ S	38
2.3. Adsorption, absorption and desorption of hydrogen	39
2.3.1. Hydrogen formation	39
2.3.2. Hydrogen adsorption.....	40
2.3.3. Hydrogen absorption or recombination.....	40
2.3.4. Hydrogen desorption.....	40
2.3.5. Influence of H ₂ S	41
2.4. Interactions between hydrogen and metal.....	42
2.4.1. Diffusible hydrogen	42
2.4.1.1. Diffusion in concentration gradient	42

Contents

2.4.1.2.	Short circuit diffusion along grain boundaries	43
2.4.1.3.	Hydrogen transport by dislocations	43
2.4.2.	Trapped hydrogen	43
2.4.3.	Equilibrium between diffusible and trapped hydrogen	45
2.4.4.	Hydrogen diffusion and trapping measured by electrochemical permeation	45
2.5.	Crack propagation	46
2.5.1.	Various forms of cracking	46
2.5.1.1.	Stress Corrosion Cracking (SCC).....	46
2.5.1.2.	Hydrogen Sulfide Cracking (HSC) and Sulfide Stress Cracking (SSC)	46
2.5.1.3.	Hydrogen Induced Cracking (HIC).....	48
2.5.1.4.	Stress Oriented Hydrogen Induced Cracking (SOHIC)	48
2.5.1.5.	Cracking assisted by dissolution	48
2.5.2.	Various mechanisms of Hydrogen Embrittlement (HE) and crack propagation	48
2.5.2.1.	Adsorption Induced Dislocation Emission (AIDE)	48
2.5.2.2.	Hydrogen Enhanced Localized Plasticity (HELP).....	49
2.5.2.3.	Hydrogen Enhanced DEcohesion (HEDE)	49
2.5.2.4.	Selective dissolution	50
2.6.	Use of Stress Corrosion Cracking tests to reproduce cracking susceptibility.....	50
2.6.1.	Different type of tests	50
2.6.2.	Different types of environments	50
2.7.	Parameters influencing the resistance to hydrogen embrittlement	50
2.7.1.	Metallurgical parameters	50
2.7.2.	Other parameters.....	53
2.7.2.1.	Temperature.....	53
2.7.2.2.	Humidity	53
2.7.2.3.	Stress concentration.....	53
2.7.2.4.	Aggressiveness of the environment : Influence of pH, pH ₂ S, CO ₂ and chlorides ..	54
3.	Summary and objectives	56
Chapter II: Metallurgy and mechanical behavior of Virgo™38		57
1.	Metallurgy of Virgo™38.....	61
1.1.	Composition and metallurgy of the industrial alloy.....	61
1.2.	Influence of heat treatments on the microstructure	67
1.2.1.	Microstructure of re-austenitized samples and influence of the sub-zero treatment after oil-quenching	67

1.2.2.	Influence of tempering on the retained austenite content	70
1.2.2.1.	Influence of the tempering temperature	70
1.2.2.2.	Influence of the tempering holding time at 620°C.....	75
1.2.2.3.	Influence of the second tempering treatment.....	75
1.2.3.	Influence of tempering on carbide precipitation	77
2.	Mechanical behavior of Virgo™38.....	81
2.1.	Influence of the direction of sampling in industrially forged material	81
2.2.	Mechanical behavior as a function of heat treatment applied.....	82
2.2.1.	Tensile properties of Virgo™38 in different microstructural states.....	82
2.2.2.	Impact toughness of Virgo™38 in different microstructural states	84
2.2.3.	Relationships between microstructure and the 0.01% yield stress in Virgo™38.....	85
2.3.	Mechanical stability of retained austenite after industrial heat treatment	91
2.4.	Summary.....	97
Chapter III: Hydrogen Embrittlement and Stress Corrosion Cracking of Virgo™38 in acid environments		99
1.	Depassivation of Virgo™38 studied by an electrochemical approach	103
1.1.	Experimental procedure.....	103
1.2.	Depassivation study of Virgo™38 without loading.....	104
1.3.	Depassivation study of Virgo™38 under constant load.....	107
1.4.	Parameters influencing depassivation of Virgo™38.....	108
1.4.1.	Influence of composition heterogeneities	108
1.4.1.1.	Influence of Cr content.....	108
1.4.1.2.	Influence of Ni content.....	109
1.4.2.	Influence of applied load.....	110
1.5.	Interpretations of the depassivation of Virgo™38	111
2.	Experimental methods	118
3.	Hydrogen embrittlement of industrial Virgo™38 during SSRT tests	122
3.1.	Conditions of the tests	122
3.2.	Study of industrial Virgo™38 under cathodic charging in different acid environments	123
3.3.	Conclusions on HE under cathodic charging in acid environments	131
4.	Stress Corrosion Cracking of industrial Virgo™38 during SSRT tests	133
4.1.	Conditions of the tests	133
4.2.	SCC behavior of Virgo™38 under applied potential	134
4.2.1.	SSRT tests at a potential in the active dissolution domain of martensite.....	134

4.2.2.	SSRT tests at a potential in the active dissolution domain of retained austenite	136
4.3.	Conclusions on SCC tests under applied potential in acid environment.....	139
5.	Conclusions.....	140
Chapter IV: Hydrogen embrittlement of Virgo™38 in different metallurgical states under cathodic charging in an environment containing Na ₂ S.....		
1.	Definition of an environment with elevated hydrogen activity to reproduce hydrogen embrittlement observed in service	145
1.1.	Composition of the environment containing Na ₂ S and conditions.....	145
1.2.	Influence of the poison on the HE behavior of industrial Virgo™38	146
1.2.1.	Reference tests in basic environment without poison.....	146
1.2.2.	Influence of the addition of Na ₂ S on the hydrogen activity	147
1.3.	Conclusions.....	153
2.	Effect of the microstructure on the resistance to HE of Virgo™38	154
2.1.	Reference metallurgical state: Virgo™38 impeller industrially heat treated	154
2.2.	Influence of the amount of retained austenite on the resistance to HE of Virgo™38.....	158
2.2.1.	Influence of the heat treatment.....	158
2.2.2.	Influence of the pre-straining.....	167
2.3.	An industrial case study: the Cover	169
2.3.1.	Description of the material: composition, metallurgy and industrial failure.....	169
2.3.2.	Behavior of the Cover during SSRT test under cathodic charging.....	170
3.	Discussion	173
3.1.	Summary of the results	173
3.2.	Interpretation on the optimal amount of retained austenite in terms of its quantity and stability	174
3.3.	Interpretation of the fracture mode	176
3.4.	Proposed mechanisms of Hydrogen Embrittlement.....	178
3.4.1.	Intergranular fractures	178
3.4.2.	Transgranular fractures	180
3.5.	Interpretation of the cracking of the Cover	180
3.5.1.	Interpretation based on the retained austenite content and the fracture mode	180
3.5.2.	Explanations based on the precipitation state on the Cover	182
3.5.3.	Phosphorous Grain Boundary Segregation (PGBS) in the Cover	182
4.	Conclusions.....	187
Chapter V: Sulfide Stress Cracking and Stress Corrosion Cracking assisted by H ₂ S of Virgo™38		
1.	Compositions of environments used and test conditions.....	193

2. Influence of the pH on the cracking resistance: a synthetic view	195
3. Detailed analysis of crack initiation and propagation in presence of H ₂ S and proposed mechanisms.....	200
3.1. Crack initiation.....	200
3.1.1. Experimental illustration of three different crack initiation mechanisms	200
3.1.1.1. ‘Very low’ pH domain	200
3.1.1.2. ‘Low’ pH domain.....	200
3.1.1.3. ‘High’ pH domain.....	201
3.1.1.4. Conclusions on the crack initiation mechanisms	201
3.1.2. Proposition of two crack initiation mechanisms	202
3.1.2.1. Crack initiation by chemical depassivation	202
3.1.2.2. Crack initiation by pitting corrosion	202
3.2. Crack propagation	204
3.2.1. ‘Low’ pH domain.....	204
3.2.2. ‘High’ pH domain.....	207
3.2.3. Proposition of two crack propagation mechanisms.....	209
3.2.3.1. Crack propagation assisted by dissolution	209
3.2.3.2. Crack propagation assisted by hydrogen: influence of experimental parameters and mechanism proposed.....	210
4. Conclusions.....	218
General conclusions	221
Bibliography.....	227
Chapter VI: Appendixes.....	237
1. Sample preparation for EBSD and XRD	iii
2. Safety report for the use of Na ₂ S containing environments	iv
2.1. Présentation du banc d’essai	iv
2.2. Analyse du risque	iv
2.3. Documents utilisés pour prévenir le personnel	vi
2.4. Vérifications et précautions avant et en cours de manipulation	vi
2.5. Procédure d’urgence mise en place	vii
2.6. Check-list avant lancement de l’expérience.....	vii
2.7. Fin d’expérience	vii
2.8. Détails du calcul Na ₂ S → H ₂ S.....	vii
3. Influence of different parameters on cracking resistance of Virgo™38 in presence of H ₂ S	viii
3.1. Influence of strain rate	viii

Contents

3.2. Influence of H ₂ S partial pressure	ix
3.3. Influence of chloride content	ix
3.4. Influence of stress localization	x
3.5. Influence of the grain boundary composition (study on the Cover)	xi
3.6. Influence of δ -ferrite on the crack propagation.....	xii
4. Dead weight tests at H ₂ S a partial pressure of 2 bar.....	xiii
4.1. Conditions.....	xiii
4.2. Results obtained.....	xiii
5. SSC study of F6NM supermartensitic stainless steel.....	xiii
5.1. Composition of the alloy and conditions of the tests	xiii
5.2. Results	xiii
6. Summaries in French	xv
6.1. Table des matières	xv
6.2. Introduction.....	xviii
6.3. Chapitre I	xxi
6.4. Chapitre II	xxii
6.5. Chapitre III	xxiv
6.6. Chapitre IV.....	xxv
6.7. Chapitre V.....	xxvi
6.8. Conclusions et perspectives	xxvii

General introduction

The present work is devoted to the study of cracking mechanisms in highly corrosive environments of a particular supermartensitic stainless steel used for Oil & Gas applications. It was performed in the SMS Materials and mechanical engineering R&D center (associated with CNRS as a mixed research unit - LGF laboratory) of Mines Saint-Etienne (France) in collaboration CIFRE with Thermodyn SAS in Le Creusot (France) which is part of Baker Hughes, a GE company (NYSE: BHGE) group.

This work was initially motivated by a case of environmentally assisted damage of centrifugal compressor impellers working in sour environments containing CO_2 and H_2S . Centrifugal compressors are turbomachineries with one or several compression stages in one machine. The number of stages is adapted to the targeted compression ratio. The domain of application of these compressors is very large: they are used to compress any gas with a flux between 200 and 200 000 m^3/h and the exit pressure can reach 700 bars (100 000 m^3/h and 250 bars maximum for compressor produced in Le Creusot). Centrifugal compressor impellers' are in series in a rotating shaft, and an impeller is feed by the exit of the previous impeller as shown on the cross section presented in Figure 1.

The gas to be compressed enters in the centrifugal compressor impeller (Figure 2) by the "eye" of the impeller to flow within the passages created by the blades. As the impeller rotates at high velocity, the gas gains momentum during its flow across the blades, and at the exit of the impeller, the gas passes into a stationary diffuser, where it decelerates, its dynamic pressure being converted into static pressure.

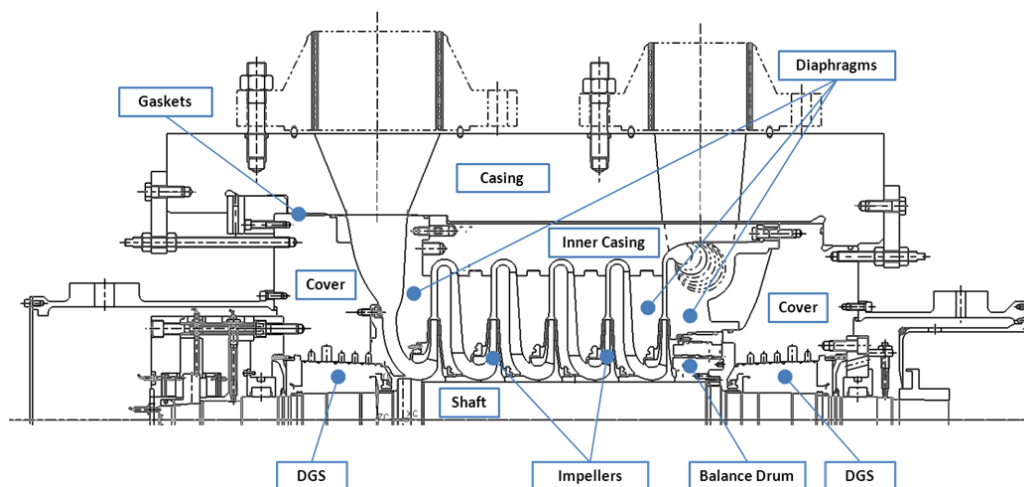


Figure 1 - Cross section of a centrifugal compressor used for oil and gas applications



Figure 2 - Centrifugal compressor impeller

General introduction

In stationary regime, centrifugal compressors are steady flow machines, which enable reducing the amount of vibrations they are submitted to. Nevertheless, local stresses in the rotating elements can exceed 500 MPa. The heavy mechanical solicitations occurring at elevated temperature over long periods of time increase the risk of damage through fatigue and creep. However, the major risk to material's integrity arises from possible synergetic interactions of mechanical factors with the corrosive environment.

In our approach, we focus on the harshest environments containing wet H₂S, CO₂ and chlorides, all with low pH. Examples of natural gas composition that can be encountered before refining are given in Table 1 and Table 2.

Table 1 - Typical makeup of mid-stream natural gas (from naturalgas.org)

Gas Types	Chemical Formulation	Percentage
<i>Methane</i>	<i>CH₄</i>	<i>70-90%</i>
<i>Ethane</i>	<i>C₂H₆</i>	<i>0-20%</i>
<i>Propane</i>	<i>C₃H₈</i>	
<i>Butane</i>	<i>C₄H₁₀</i>	
<i>Carbon Dioxide</i>	<i>CO₂</i>	<i>0-8%</i>
<i>Oxygen</i>	<i>O₂</i>	<i>0-0.2%</i>
<i>Nitrogen</i>	<i>N₂</i>	<i>0-5%</i>
<i>Hydrogen Sulphide</i>	<i>H₂S</i>	<i>0-5%</i>
<i>Rare gases</i>	<i>Ar, He, Ne, Xe</i>	<i>Traces</i>

Table 2 - Typical gas composition encountered in exploration before refining (from GE)

Gas Types	Percentage
<i>Water</i>	<i>0.8%</i>
<i>Carbon Dioxide</i>	<i>4%</i>
<i>Hydrogen Sulphide</i>	<i>36.5%</i>
<i>Methane</i>	<i>23.5%</i>
<i>Ethane</i>	<i>5%</i>
<i>Propane</i>	<i>6.5%</i>
<i>Butane</i>	<i>12%</i>
<i>Pentane</i>	<i>6%</i>
<i>Hexane</i>	<i>3%</i>
<i>Hydrogen</i>	<i>2.4%</i>
<i>Sulfur contaminant</i>	<i>0.3%</i>

H₂S is a corrosive and poisonous gas increasingly present in newly exploited oil and gas fields around the world and its partial pressure can reach several tenths of bars. It has been identified to favor hydrogen entry in metals and lead to failure through stress corrosion cracking or sulfide stress cracking.

H₂S is not only harmful for metals and alloys but it is also an inflammable and extremely toxic gas (Table 3). Consequently, its use for research purpose is only possible in a restricted number of accredited laboratories. At Ecole des Mines de Saint-Étienne, experiments using H₂S are not allowed but collaborations with specialized companies, like the French Corrosion Institute based in Fraisses (France), give access to this kind of experiments.

Table 3 - H₂S toxicity according to ANSI standard N° Z37.2, - 1972

Amount	Effect according to ANSI Standard N° Z37.2, - 1972
0.13 ppm	Minimal perceptible odor
4.60 ppm	Easily detectable, moderate odor
10 ppm	Threshold for eye irritation
100 ppm	Strong, unpleasant odor, but not intolerable
200 – 300 ppm	Marked conjunctivitis (eye inflammation) and respiratory tract irritation after one hour of exposure
500 – 700 ppm	Loss of consciousness and possibly death in 30 minutes to 1 hour
700 – 1000 ppm	Rapid unconsciousness, cessation (stopping or pausing) of respiration, and death
1000 – 2000 ppm	Unconsciousness at once, with early cessation of respiration and death in few minutes. Death may occur even if an individual is removed to fresh air at once

The material selection for impellers is mainly driven by the equivalent pH estimated for the corresponding gas field on the basis of data provided by the customers. Empirical formulas are used to calculate the equivalent pH as a function of H₂S and CO₂ partial pressures.

$$pH = a * \ln(P_{CO_2} + P_{H_2S}) + b$$

The chloride content also influences the material selection, the objective being to avoid pitting corrosion.

Supermartensitic stainless steels (SMSS) are frequently used in Oil&Gas applications due to their good corrosion resistance in aggressive environments and a satisfactory combination of high mechanical strength and fracture toughness [1]. They also offer an interesting economical solution compared to superduplex stainless steels (SDSS) and Ni-based alloys [2]. However, to be safely used in oil and gas applications, SMSS must satisfy strict conditions in terms of heat treatments and resulting fracture toughness, consequently their application range is limited. These requirements are published in the NACE standard MR0175 [3].

Virgo™38 (Creusot Loire trademark), a 16Cr-4Ni low-carbon supermartensitic steel, is a nominally precipitation-free SMSS belonging to the GE Oil&Gas portfolio. More than 200 compressors equipped with impellers made of Virgo™38 are in operation for BHGE all around the world.

Initially, Virgo™38 was developed for seawater applications in 1960. Its first application in compression of sour gas was in 1970 for Lacq Field in France. This field is known to be one of the most aggressive onshore fields due to its high and unexpected chloride content and led to the first failures of martensitic stainless steels in 2004 after a stop of one compressor made of Virgo™38 [4]. Nowadays, around 30% of the machines installed by Thermodyn contain impellers made of Virgo™38, which became a GE Oil & Gas material in 2002.

As mentioned previously, this alloy is massively used because it presents strategic advantages such as high mechanical properties, high NACE threshold application stress and low production costs compared to 17-4PH or superalloys from Inconel family [2] [5]. Furthermore, contrary to its competitors, Virgo™38 has the capability to be brazed [6], which avoids the use of welding processes known to be damageable for the resistance in aggressive environments [7].

However, present NACE specifications limit the use of SMSS to a hardness level of 23HRC because of some unexplained failures that occurred in service, even if others NACE testing conditions were satisfied. As Virgo™38 cannot satisfy this condition (HRC=28), it is not considered as a NACE SMSS even if it successfully works in such environments.

NACE standardized tests have been performed on Virgo™38 to explain such failures but no physical mechanisms have been identified up to now. That is why, nowadays, for some applications, GE Oil & Gas specifications based on NACE standards require the use of Ni-base alloys.

Recently, centrifugal compressors made of Virgo™38 have exhibited new isolated cases of radial intergranular failures in service as visible in Figure 3. Static component can also exhibit intergranular cracks.

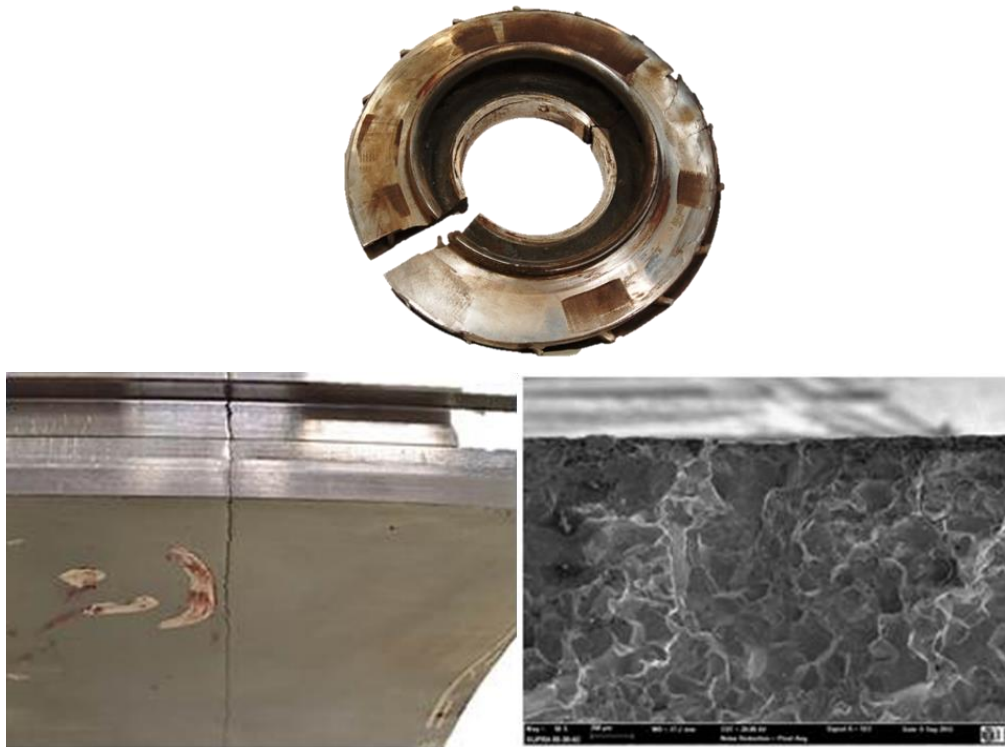


Figure 3 - Radial intergranular failure observed on Virgo™38 impeller and intergranular crack on a static component made of Virgo™38 used for oil and gas applications

These cases motivated the present study, aiming to identify the mechanisms involved in these failures in the objective to better define the limit of use of Virgo™38. Furthermore, the knowledge of damage mechanisms could also enable extending the application domain of SMSS in oil and gas applications leading to costs reduction through the replacement of Ni-based alloys in some cases.

Hence, the main objective of this PhD work is to understand the mechanisms involved in cases of Virgo™38 failures. The environmentally assisted damages of SMSS have to be correlated with the complex metallurgy of such steels. The first objective is thus to understand and to control the microstructure and resulting mechanical properties of Virgo™38.

The second objective is to check whether Virgo™38 is capable to resist to stress corrosion cracking in sweet environments and hopefully, by applying Slow Strain Rate Tensile tests as described in standards, to demonstrate that this is the case.

Then, it was necessary to reproduce intergranular failures observed in service by using SSRT tests in very aggressive environments. Most of the experiments were performed in a severe environment containing Na_2S poison, developed during this PhD, the objective being to find a sufficiently hydrogenating environment to reproduce in service failures and to determine the main cracking mechanism.

Finally, several tests in presence of H_2S were performed in conditions far from the usual application range of SMSS in order to validate cracking mechanisms identified in presence of Na_2S and in prevision of a potential enlargement of the application domain of Virgo™38. As previously mentioned, these tests were performed in collaboration with an industrial laboratory accredited for the use of H_2S (French Corrosion Institute).

The thesis will be divided in five chapters, the first one being the literature review.

The microstructure understanding and control being a key point for SMSS, chapter II will be dedicated to the study of the microstructure and mechanical properties of Virgo™38 in different metallurgical states.

The third chapter is dedicated to the study of the behavior of Virgo™38 in acid environments and under applied potential. Tests in environments with gradually increasing severity will be presented showing the progressive reduction of alloy's ductility. Two mechanisms are highlighted in this chapter: Hydrogen Embrittlement and Stress Corrosion Cracking assisted by dissolution.

Chapter four will be focused on the development and subsequent tests in a very hydrogenating environment containing Na_2S . Hydrogen Embrittlement resistance of Virgo™38 under cathodic charging will be investigated in this chapter. Furthermore, as the embrittlement is particularly related to the microstructure, this chapter will also be devoted to the study of the influence of the microstructure on the Hydrogen Embrittlement resistance of Virgo™38. A particular attention will be focused on the role of retained austenite and on the chemical composition of former austenitic grain boundaries (where failure occurred in service). We consider that the environmental conditions proposed in this chapter are well representative of the application conditions in presence of low partial pressure of H_2S .

Finally, the fifth chapter will be devoted to the study of the behavior of Virgo™38 in presence of H_2S . It is important to note that, in this chapter, most of the conditions will be out of the actual application range of SMSS in Oil&Gas industry and that the presented mechanisms will not correspond to the ones presently encountered in service. However, it will enable us to determine new mechanisms that could be encountered for applications at very low pH for example. Two main mechanisms will be identified such as the well-known Sulfide Stress Cracking that have been previously reproduced by cathodic charging and the less usual Stress Corrosion Cracking assisted by preferential dissolution.

Chapter I:
Bibliographic review

Chapter I: Bibliographic review	17
1. Description of (super)-martensitic stainless steels	21
1.1. Introduction	21
1.2. Composition	21
1.2.1. Major elements: Fe-C-Ni-Cr	21
1.2.2. Secondary elements: Mn-Mo-Ti	25
1.2.3. Relations of equivalence.....	25
1.3. Microstructure of supermartensitic stainless steels.....	27
1.3.1. α' martensite	27
1.3.2. γ austenite	27
1.3.3. Martensitic transformations.....	28
1.3.4. Austenite/martensite interface	31
1.3.5. Carbide precipitation	31
1.4. Heat treatment applied to SMSS for oil & gas applications.....	32
1.4.1. Standard profile imposed by NACE MR0175	32
1.4.2. Austenite stability as a function of tempering temperature and composition.....	34
2. Cracking of (super)-martensitic stainless steels.....	35
2.1. Introduction	35
2.2. Crack initiation	36
2.2.1. Initiation by pitting	36
2.2.2. Initiation by chemical depassivation	37
2.2.3. Initiation by mechanical defects.....	38
2.2.4. Initiation in presence of H ₂ S	38
2.3. Adsorption, absorption and desorption of hydrogen.....	39
2.3.1. Hydrogen formation	39
2.3.2. Hydrogen adsorption.....	40
2.3.3. Hydrogen absorption or recombination.....	40
2.3.4. Hydrogen desorption.....	40
2.3.5. Influence of H ₂ S	41
2.4. Interactions between hydrogen and metal	42
2.4.1. Diffusible hydrogen.....	42
2.4.2. Trapped hydrogen	43
2.4.3. Equilibrium between diffusible and trapped hydrogen	45
2.4.4. Hydrogen diffusion and trapping measured by electrochemical permeation	45
2.5. Crack propagation.....	46
2.5.1. Various forms of cracking	46
2.5.2. Various mechanisms of Hydrogen Embrittlement (HE) and crack propagation.....	48
2.6. Use of Stress Corrosion Cracking tests to reproduce cracking susceptibility	50
2.6.1. Different type of tests.....	50
2.6.2. Different types of environments	50
2.7. Parameters influencing the resistance to hydrogen embrittlement	50
2.7.1. Metallurgical parameters	50
2.7.2. Other parameters	53
3. Summary and objectives	56

1. Description of (super)-martensitic stainless steels

1.1. Introduction

Stainless steels are essentially Fe based Fe-Cr-Ni-C alloys containing at least 11%Cr. Starting from this Cr-content, a stable Cr-rich oxide film can spontaneously form. This oxide forms a passive layer, about 3-5 nm thick [8], which protects the alloy from the environment. The most common classifications of stainless steels are based on their microstructure or their major alloying element.

Basic martensitic stainless steels are essentially Fe-Cr-C alloys with Cr contents not exceeding 13% and with medium or high (up to 1,2 wt%) carbon contents. AISI 410 is a classic example of this family of steels. The requirement of enhanced corrosion resistance, in particular that to Sulfide Stress Cracking (SSC) in environments containing H₂S and CO₂ combined with high mechanical properties requirements led to the development of Ni-containing martensitic steels in order to extend the γ field of the phase diagram to higher Cr contents. Such steels, often designated as supermartensitic, in which Cr contents can reach 16-18%, combined with very low C, are used in oil & gas industries [9] because of the combination of high mechanical properties coupled with both good corrosion resistance and low prices as compared to austenitic or superduplex grades [10]. These alloys are used in the quenched and double tempered state [3]. It is considered that forming fine grains of retained austenite inserted between martensite laths (see next section) enables ensuring a good toughness.

One of principal microstructural requirements for Fe-Cr-Ni martensitic steels is to limit the presence of δ -ferrite and σ phase. Indeed, the δ -ferrite has a detrimental influence on corrosion resistance and on the hot-working of the material [7]. The σ phase is formed near ferritic grain boundaries and leads to a brittle behavior of the alloy [7]. One is thus searching for a single phase austenitic structure at high temperature which enables (theoretically) reaching a single phase martensitic structure after quenching. At the same time, hot working behavior of the material is strongly improved if the high-temperature microstructure is purely austenitic.

Mechanical properties, corrosion resistance and microstructure are defined by both the composition and the heat treatments performed. In this part, we will describe the composition of martensitic stainless steels and their microstructure. Later, we will study their behavior regarding corrosion.

1.2. Composition

1.2.1. Major elements: Fe-C-Ni-Cr

As indicated above, martensitic stainless steels are mainly composed of Fe, Cr, C and Ni. First, we will describe relevant binary phase diagrams in order to analyze phases potentially present in the microstructure of steels. Then, we will see, using the ternary phase diagram Fe-Cr-Ni, more representative of the investigated alloy, how Ni additions modify the microstructure of Fe-Cr alloys.

Because of high Cr and low C contents in supermartensitic stainless steels, the Fe-C phase diagram shown in Figure 4 is of little utility to study microstructures of martensitic stainless steels.

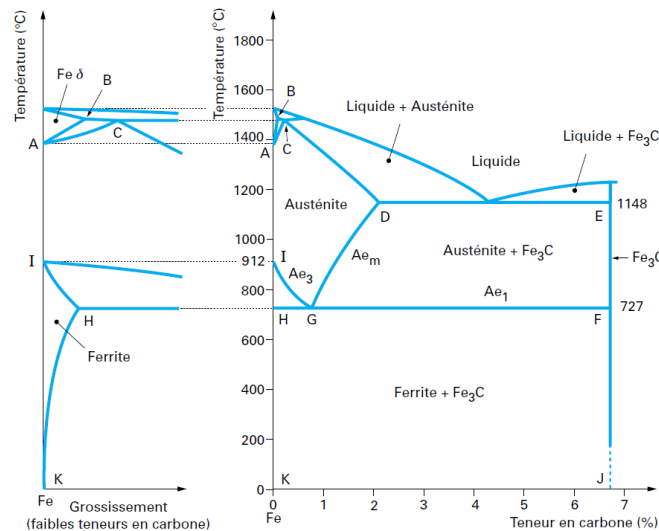


Figure 4 - Fe-C phase diagram [11]

Basic information on phases present in martensitic (Fe-Cr-C) stainless steels can be obtained from the binary Fe-Cr equilibrium diagram (Figure 5a). As previously mentioned, δ -ferrite has a negative impact on corrosion properties. According to the binary Fe-Cr phase diagram, a purely martensitic microstructure can only be obtained with Cr contents lower than 11 wt.%, which is close to the minimum required to guarantee the corrosion resistance of the steel. At the same time, the two phase $\gamma + \delta$ region is very narrow in binary Fe-Cr. Figure 5b shows that C (and N) strongly enlarge the $\gamma + \delta$ domain but without extending the single phase austenite loop. Additions of C (and N) allow increasing the Cr content, but the final microstructure will always contain δ ferrite. The entire C will not remain in solid solution. Indeed, it will form precipitates (see next section) with elements such as Cr or Ti. Carbide precipitates may cause galvanic corrosion [12]; consequently their presence in the microstructure should be limited. This is particularly valid in the case of service in strongly corrosive environments for which the use of Fe-Cr-C steels cannot provide a satisfactory solution. Nevertheless, even if a high carbon content could be accepted, increasing Cr above 25 wt.% might lead to the formation of the sigma phase at low temperature. This phase must be avoided because it causes brittle failures [7]. The presence of this phase limits the Cr content to less than 25% in such alloys.

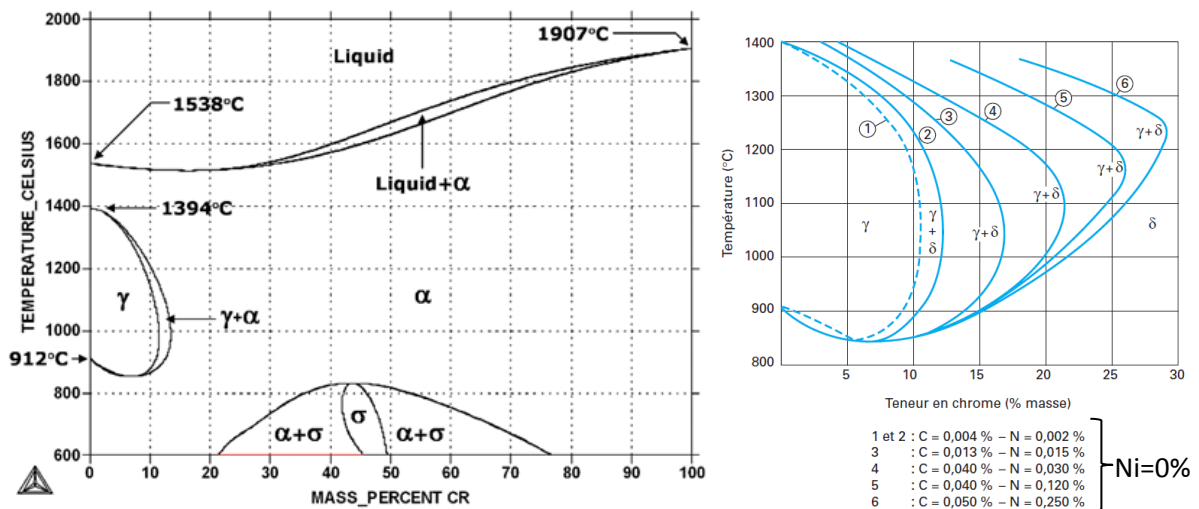


Figure 5 (a) and (b) - Fe-Cr diagram: influence of C and N on the γ -loop [13]

For the above reasons, the addition of gamma-forming elements like Ni (Figure 6) is necessary if higher Cr contents are required to improve corrosion properties. Furthermore, alloying with Ni decreases the A_{c1} temperature, leading to an easier partial re-austenization during tempering. Addition of Ni (>5 wt.%) also enables avoiding the δ ferrite at high temperature.

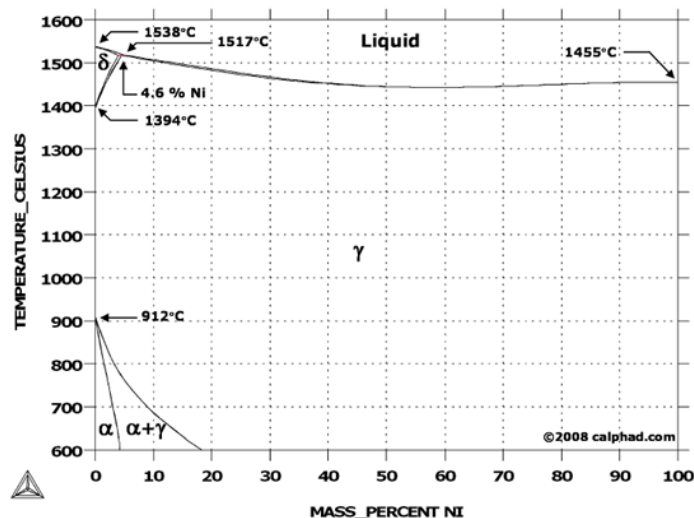


Figure 6 - Fe-Ni phase diagram [14]

The basic objective of microstructure design is thus to reach a single austenitic phase domain at high temperature in order to obtain pure martensite after quenching. According to Figure 7, which shows the isothermal section of the ternary Fe-Cr-Ni phase diagram at 900°C, a single FCC field is possible to be obtained at elevated temperature (900°C in Figure 7) for a wide range of Cr/Ni ratios.

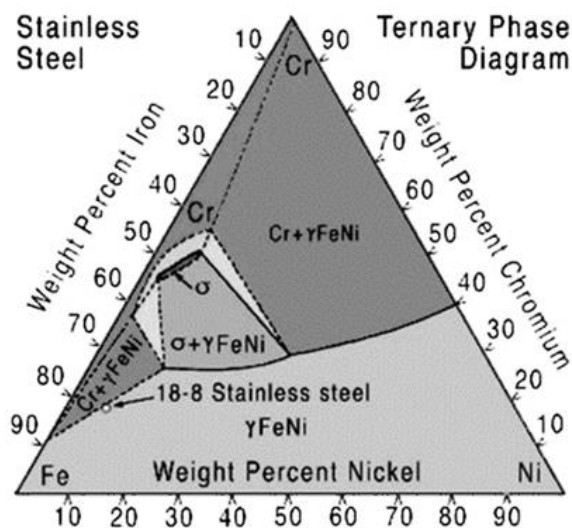


Figure 7 - Isothermal section of the ternary phase diagram Fe-Cr-Ni at 900°C

The domain of stability of the austenitic region obviously varies with temperature (Figure 8). Approximate microstructures at 1000°C and 1200°C are shown in Figure 8 as a function of Cr and Ni contents. As the Cr content must be greater than 11-13% for corrosion purposes and in order to get a single austenitic microstructure at high temperature, the Ni content has to be around at least 5 wt.% in supermartensitic stainless steels.

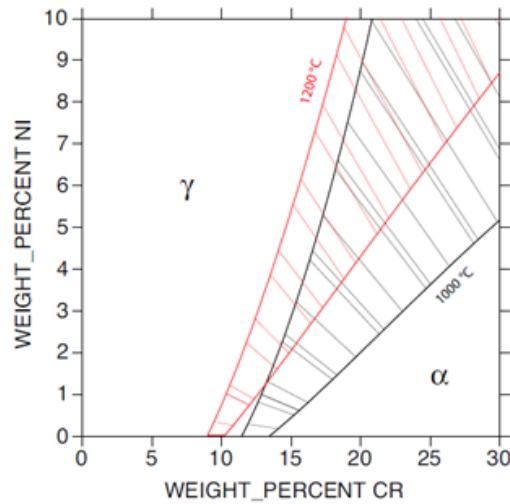


Figure 8 - Microstructure as a function of Cr and Ni content [14]

In Ni containing martensitic stainless steels the joint effect of Cr and Ni can be investigated through ternary phase diagrams (Figure 9) or pseudo-binary phase diagrams (Figure 10).

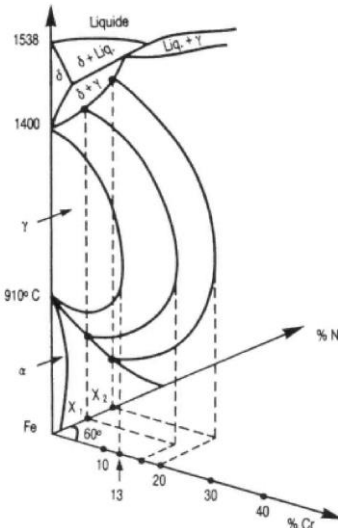


Figure 9 - Ternary phase diagram Fe-Cr-Ni [15]

Ternary phase diagrams being quite complicated to exploit, the influence of Ni on the stability of the austenitic domain as a function of both Cr content and temperature, is most frequently represented on pseudo-binary phase diagrams.

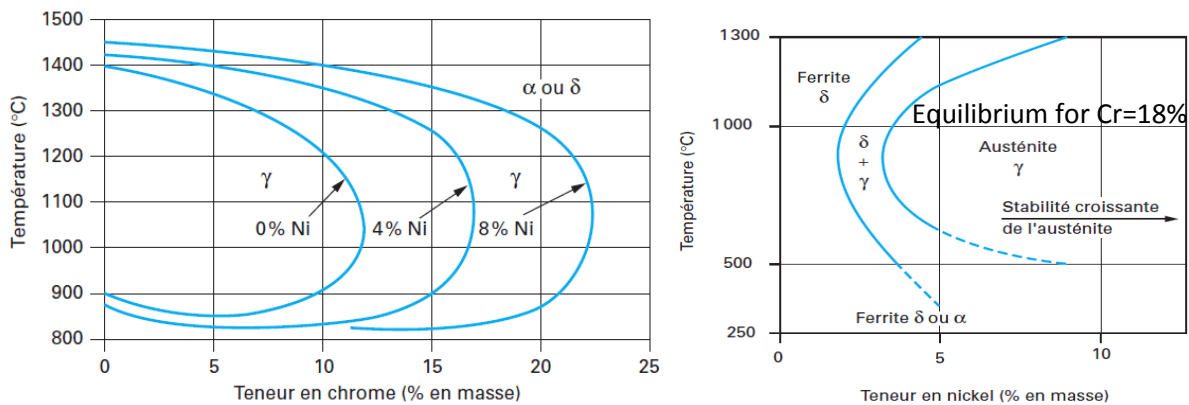


Figure 10 - Pseudo-binary phase diagrams [13]

The austenitic domain increases when Ni-content increases, limiting the risk of δ ferrite formation, even when the Cr-content increases. Furthermore, one can see the influence of Ni on the temperature of formation of austenite. Indeed, as already mentioned, Ni additions decrease the A_{C1} temperature. Consequently, if one of the objectives of tempering is to transform a part of martensite into reverted austenite, this operation is possible at lower temperatures, obviously reducing the energy cost.

1.2.2. Secondary elements: Mn-Mo-Ti

Mn is an element often added for economic reason in order to replace Ni. Indeed, similar to Ni, Mn favors the austenitic domain and is less expensive [16]. Mn is known to form precipitates with S (already present in iron ore) which is beneficial with respect to intergranular brittleness but harmful with respect to corrosion properties. Indeed, MnS particles can both act as hydrogen traps leading to a local increase in the concentration of hydrogen at the matrix/MnS interface and also accentuate galvanic corrosion [12]. The remaining amount of Mn has to be limited as it strongly decreases M_s and M_f temperatures and might result in difficulties in achieving fully martensitic microstructure after quenching.

Mo is added in order to improve corrosion properties in acid environments [7]. It also acts on the precipitation behavior of carbides. It decreases the solubility of C in the matrix and favors carbide precipitation. However, it also increases the temperature of formation of carbides. It can also precipitate to form intermetallic particles with negative impact on mechanical properties. It is also used for the resistance at high temperature of the alloy.

Ti is usually added in a very small quantity in order to avoid the formation of Cr carbides [17]. Indeed, the affinity of C with Ti is greater than the one with Cr, hence C preferentially combines with Ti in order to form TiC precipitates. Their repartition within the matrix is more homogeneous than Cr-containing carbides [17]. By adding Ti, one would reduce the extension of chromium depleted areas (see next section), increasing corrosion resistance.

1.2.3. Relations of equivalence

Alloying elements in stainless steels are commonly divided in two categories, which are the elements favoring the α phase (called α -formers) and the ones favoring the γ phase (called γ -formers). Main α -forming elements in stainless steels are Cr and Mo and main γ -forming elements are Ni, Mn and C.

In order to easily represent microstructures of steels at room temperature, several empiric formulas were proposed. According to their α -former or γ -former character, the compositions of alloying elements are grouped in numbers called Cr_{eq} and Ni_{eq} respectively. The diagram representing the microstructure of stainless steels after welding and subsequent cooling as a function of Ni_{eq} and Cr_{eq} is called the Schaeffler diagram, for a given cooling rate. Different formulas were proposed to calculate Cr and Ni equivalent.

Initially, Schaeffler (1949) defined these parameters for welded materials by the following formulae [18]:

$$Cr_{eq} = \%Cr + \%Mo + 1.5\%Si + 0.5\%Nb$$

$$Ni_{eq} = \%Ni + 30\%C + 0.5\%Mn$$

In 1981, Harries [19] took into account more elements and proposed another definition of Cr and Ni equivalent:

$$Cr_{eq} = \%Cr + 1.5\%Mo + 2\%Si + 5\%V + 1.75\%Nb + 5.5\%Al + 1.5\%Ti + 0.75\%W$$

$$Ni_{eq} = \%Ni + 30\%C + 0.5\%Mn + 0.3\%Cu + 25\%N$$

In 1982, Suutala [20] determined other relations between the final microstructure and the numbers Cr and Ni equivalent by formulas:

$$Cr_{eq} = \%Cr + 1.21\%Mo + 0.48\%Si + 0.14\%Nb + 2.2\%Ti + 0.72\%Ta + 2.27\%V + 2.48\%Al$$

$$Ni_{eq} = \%Ni + 0.11\%Mn - 0.0086\%Mn^2 + 24.5\%C + 18.4\%N + 0.44\%Cu + 0.41\%Co$$

Based on these concepts of Cr and Ni equivalent, Feithiger in 1990 [21] defined the minimum Ni_{eq} necessary to obtain a pure austenitic structure as a function of composition:

$$Ni_{eq,min} = 1.1813\%Cr + 1.5\%Mo + 0.48\%Si - 11.85$$

However, when the alloy contains nitrogen, ESPY's formulas are preferentially used in place of Schaeffler's ones:

$$Cr_{eq} = \%Cr + \%Mo + 1.5\%Si + 0.5\%Nb + 5\%V + 3\%Al$$

$$Ni_{eq} = \%Ni + 30\%C + 0.87 + 0.33\%Cu + 30(\%N - 0.045)$$

A rough prediction of the microstructure after fast cooling is possible from diagrams using various definitions of Cr_{eq} and Ni_{eq} , as shown in Figure 11 for Schaeffler formulas.

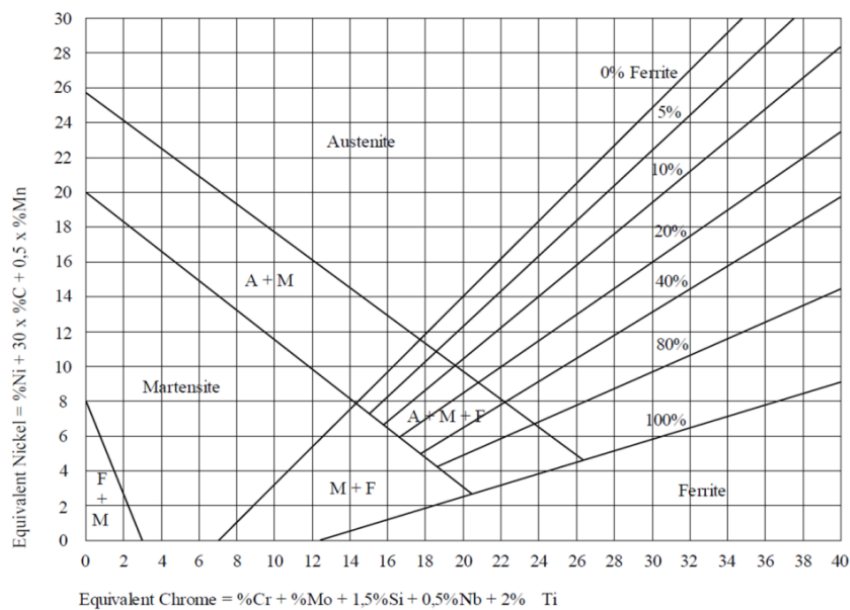


Figure 11 - Schaeffler diagram [18]

1.3. Microstructure of supermartensitic stainless steels

1.3.1. α' martensite

The martensitic transformation occurs without diffusion. The BCC lattice is deformed to a degree depending on the carbon content. The lattice can be transformed from cubic (cell parameter a_0) to tetragonal (cell parameters a and c):

$$\begin{cases} a \text{ (nm)} = a_0 \text{ (nm)} - 0.015 * \%C \text{ (wt\%)} \\ c \text{ (nm)} = a_0 \text{ (nm)} + 0.115 * \%C \text{ (wt\%)} \end{cases}$$

However, this lattice transformation occurs only above a critical carbon content [15].

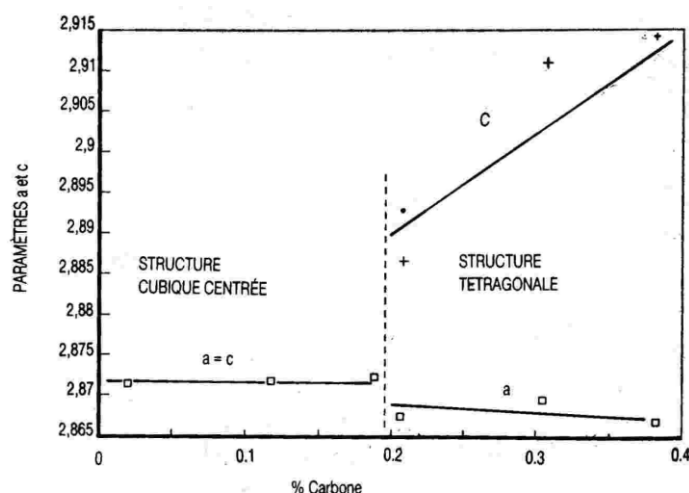


Figure 12 - Martensite lattice as a function of carbon content [15]

Hence, for low carbon contents, the martensitic structure remains entirely body-centered cubic (BCC) which is usually the case for supermartensitic stainless steels.

Two different morphologies of martensite are possible: plate-shaped or lath-shaped. Plate-shaped martensite has a lenticular form which enables accommodating stresses consecutive to transformation, while lath-shaped martensite are grouped in packets. However, if $\%C < 0.6$ (in wt.%), martensite will preferentially be lath-shaped with a habit plane corresponding to $\{111\}$ plane of parent austenite [15].

1.3.2. γ austenite

Within the case of lath-shaped martensite, austenite is located between laths. Austenite presence may result from two distinct mechanisms: it remains after quenching (residual austenite) if the temperature is not low enough or it is formed during tempering if the temperature of tempering is higher than A_{c1} (reverted austenite at high temperature and retained austenite on the material cooled down to the room temperature). The quantity of retained austenite formed during tempering can be expressed as a function of the Larsen-Miller parameter P by [22]:

$$P = 10^{-3} * T \text{ (in K)} * (20 + \log[t \text{ (in hours)}])$$

This austenite can be (just) meta-stable, depending on its composition, and can be transformed into martensite by stress or strain induced martensitic transformation (SIMT), see next section.

Retained austenite increases the toughness of the alloy but it can also act as hydrogen trap because hydrogen solubility is higher in austenite than in martensite.

1.3.3. Martensitic transformations

Since martensitic transformation occurs without any diffusion, the composition of the martensite formed will be the same as the composition of the parent austenitic phase. If one calls $G^A(T)$ and $G^M(T)$ the free energies of austenite and martensite respectively at the temperature T , the difference of energy is:

$$\Delta G^{A \rightarrow M}(T) = G^M(T) - G^A(T)$$

The transformation implies the creation of a new interface with the additional energy, called $\Delta G_{A/M}$, which is required to form this interface. The total energy needed for the transformation is thus:

$$\Delta G_{tot}(T) = \Delta G^{A \rightarrow M}(T) + \Delta G_{A/M}(T)$$

One can obtain the martensitic structure by different processes. The first one and most known, is to quench the material from the monophasic austenitic domain. This transformation is spontaneous. The temperature at which the martensitic transformation begins (by quenching or cooling) is called the martensitic start temperature, noted M_s , and depends essentially on the composition. It also depends on the austenite grain size and on the yield strength [23]. Several formulas were proposed to establish the relation between the composition and M_s . The differences in M_s , obtained by different empirical formulas, are within the range $\pm 50^\circ\text{C}$ [24], which indicates that there is no precise method to determine the temperature of spontaneous martensitic transformation.

$$M_s = 1302 - 42\%Cr - 61\%Ni - 33\%Mn - 28\%Si - 1667(\%C + \%N)$$

$$M_s = 540 - 497\%C - 6.3\%Mn - 36.3\%Ni - 10.8\%Cr - 46.6Mo$$

This temperature corresponds to the one for which the transformation is spontaneous, i.e. when the total energy variation is null.

$$\Delta G_{tot}(M_s) = 0$$

$$|\Delta G^{A \rightarrow M}(M_s)| = |\Delta G_{A/M}(M_s)|$$

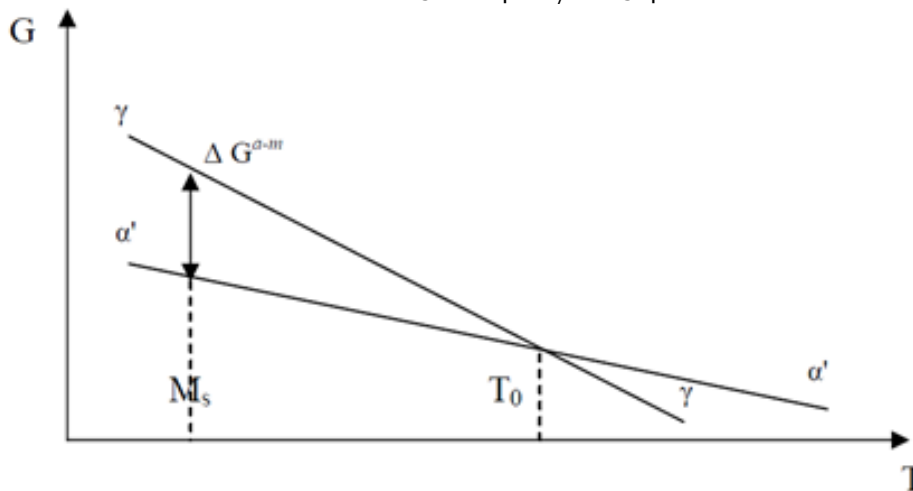


Figure 13 - Gibbs free energies of austenite and martensite as a function of temperature [25]

The total martensitic transformation by quenching or cooling is achieved at a temperature called M_f which is usually around 150°C below M_s . When M_f is lower than room temperature, a sub-zero treatment at a temperature lower than 0°C (usually -80°C) may be realized in order to eliminate the remaining residual austenite.

In first approximation, by neglecting the deformation, the amount of martensite formed during quenching (V_m) only depends on the temperature at the end of quenching T_q and can be expressed by the Koistinen & Marburger equation [26] (note that this equation gives 80% of martensite after quenching at T_q 150°C below M_s and 96% of martensite after quenching at T_q 300°C below M_s):

$$V_m = 1 - \exp(-0.011 * (M_s - T_q))$$

Although the composition of steels at the temperature of austenitization and during quenching is generally supposed homogeneous, it may be locally modified through the effect of intergranular segregation of alloying elements, the role of Si being particularly worth mentioning. As shown by Stolarz [27], Si segregates easily to grain boundaries and this effect is in particular responsible for the transpassive corrosion of stainless steels [27]. Kinetic calculations [27] indicate that 90% of equilibrium intergranular concentration at 800°C is completed within 1 second! Consequently, even for a fast cooling from austenitization temperature, austenite grain boundaries are enriched in Si, with a potentially strong effect on M_s and M_f temperatures.

Figure 14 presents the CCT diagram for a martensitic stainless steel containing 13%Cr. It shows that the critical cooling rate resulting in no residual austenite is of approximately 15°C per minute. This means that the quenching rate is not really critical for these alloys and that quite low cooling rate allows obtaining 100% martensitic structures. For example, oil cooling enables reaching cooling rates of around 300°C per minute, which is sufficiently fast. As mentioned above, local intergranular residual austenite can still persist due to Si segregation during quenching.

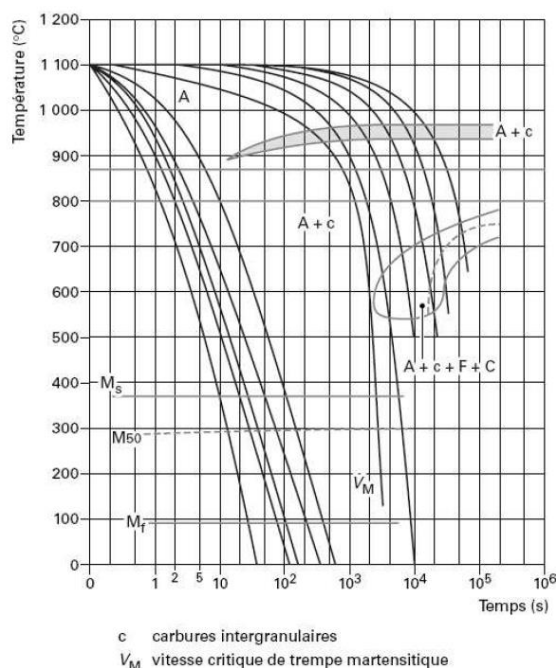


Figure 14 - CCT diagram for a martensitic stainless steel containing 13%Cr [28]

Another way to form martensite is to apply an external stress to austenite. This mechanism is called Stress or Strain Induced Martensitic Transformation (SIMT). The thermodynamic approach of this mechanism is schematically illustrated in Figure 15.

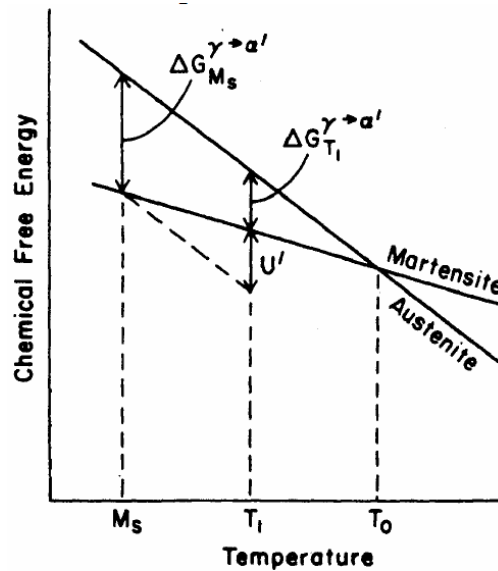


Figure 15 - Gibb's free energies of austenite and martensite as a function of temperature: effect of an external constraint [29]

The principle is that an external energy U' (in this case, given by mechanical straining) can assist the chemical driving force. The energy can be expressed as a function of stress by the formula [30]:

$$U' = \frac{1}{2} s_0 \sigma \sin(2\theta) \pm \frac{1}{2} \varepsilon_0 \sigma (1 + \cos(2\theta))$$

where σ represents the applied stress, s_0 and ε_0 are constants and θ is the angle between the stress axis and the normal of the habit plane.

Alternatively, the ability of austenite to resist to SIMT is described by the temperature M_{d30} introduced by Angel in 1954 [31]. It is the temperature where 50% martensite will form at 30% true strain. This temperature, like M_s , is function of the composition (in wt%):

$$M_{d30} = 413 - 462 (\%C + \%N) - 9.2\%Si - 8.1\%Mn - 13.7\%Cr - 9.5\%Ni - 18.5\%Mo$$

Higher M_{d30} temperatures result in less stable austenite phase. However, this temperature is not a threshold value and only takes into account the global strain and SIMT starts at temperatures significantly higher than M_{d30} . Moreover, controversies exist about the role of stress and strain in initiating SIMT. Although most experimental data indicate that SIMT takes place above a threshold of a macroscopic plastic strain [32], Das et al. [33] argue that a wide range of results supports the predominant role of stress over plastic strain.

The above controversy is mostly due to the fact that SIMT is implicitly correlated with macroscopic values of stress and strain. However, it is well documented [34] that, at a microscopic scale, SIMT sets off in zones with high stress concentrations which are generated by plastic deformation (intersection of slip bands under monotonic loading, interactions between slip bands and grain boundaries in fatigue).

Trapped hydrogen in austenite is also known to influence the resistance to SIMT. It has been showed on metastable austenitic stainless steels that hydrogen reduced the amount of SIMT [35].

1.3.4. Austenite/martensite interface

At the interface between austenite and martensite, one finds an invariant crystallographic plane called habit plane. Following crystallographic relations between austenite and martensite were identified in the literature [36]:

Bain	$(010)_\gamma \parallel (010)_{\alpha'} \text{ and } [001]_\gamma \parallel [101]_{\alpha'}$
Kurdjumov and Sachs (KS)	$(111)_\gamma \parallel (110)_{\alpha'} \text{ and } [1\bar{1}0]_\gamma \parallel [1\bar{1}1]_{\alpha'}$
Nishiyama-Wasserman (NW)	$(111)_\gamma \parallel (110)_{\alpha'} \text{ and } [0\bar{1}1]_\gamma \parallel [001]_{\alpha'}$

1.3.5. Carbide precipitation

In martensitic stainless steels, the carbon content must remain low in order to limit the formation of carbides in association with Cr. As seen in Figure 16, at a carbon content of 0.05% and for Cr content above 7%, the expected carbide is $M_{23}C_6$ [37]. They are preferentially formed at prior austenitic grain boundaries and within the martensitic phase. The $M_{23}C_6$ precipitation kinetics is particularly fast at temperatures around 650-700°C [37].

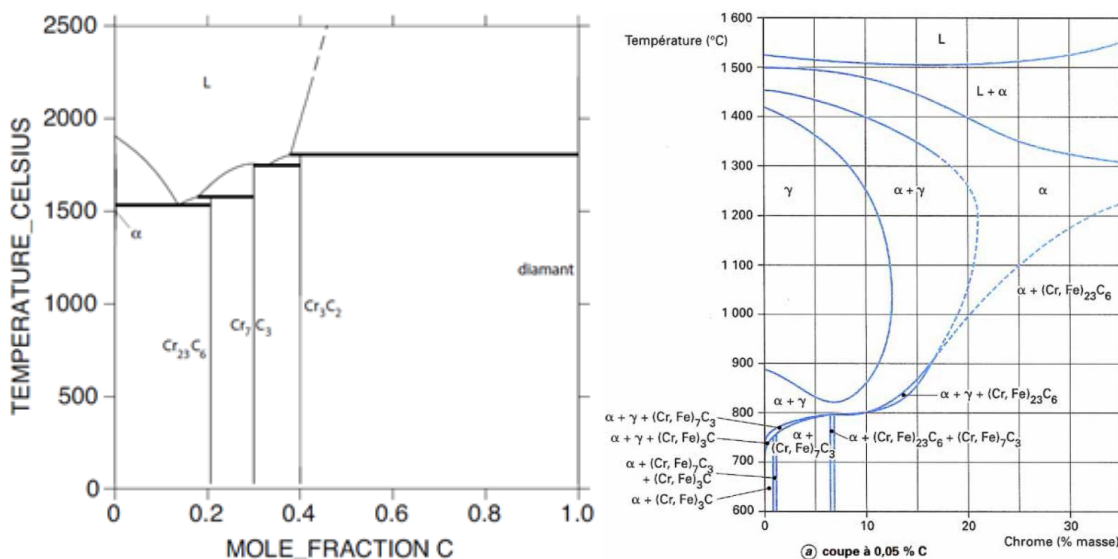


Figure 16 - Chromium carbides in steels [14]

As Cr diffusion rate is low, Cr depleted areas will locally form, decreasing the corrosion resistance of the alloy. Indeed, to be considered as stainless steels, alloys must contain at least 11% Cr. However, if carbides are small enough, depleted areas are not observed due to the sufficient homogenization. Quenching the alloy in oil can be helpful to avoid the formation of Cr carbides.

1.4. Heat treatment applied to SMSS for oil & gas applications

1.4.1. Standard profile imposed by NACE MR0175

To be certified NACE, according to the standards [38], for Oil&gas applications in presence of H₂S, “Low-carbon, martensitic stainless steels [...] shall have a maximum hardness of 23 HRC and shall be:

- 1) austenitized at 1010°C (1850°F) minimum, then air- or oil-quenched to ambient temperature,
- 2) tempered at 649°C to 690°C (1200°F to 1275°F), then air-cooled to ambient temperature, and
- 3) tempered at 593°C to 621°C (1100°F to 1150°F), then air-cooled to ambient temperature.”

The heat treatment profile corresponding to this standard is given in Figure 17 [39].

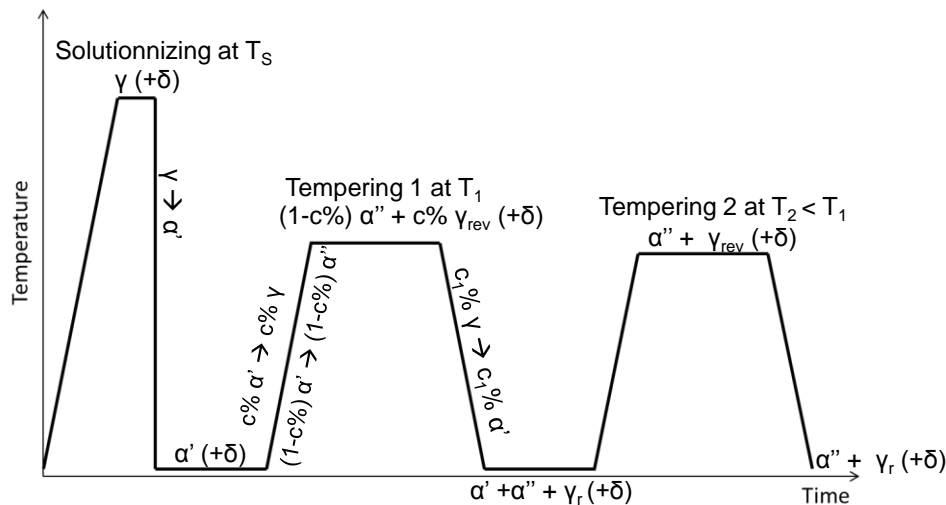


Figure 17 - Schematic representation of the standard heat treatment profile corresponding to the NACE standards

The first step, called austenitization (or solutionnizing) must be done at a temperature high enough to transform the whole microstructure into austenite. This is a necessary condition for obtaining a fully martensitic microstructure on quenching. It also enables to homogenize the alloy and to dissolve any precipitates present prior to treatment. Some amount of δ phase may be present at high temperature and, in this case, it will be retained after quenching at room temperature. This ferrite is stable at T_1 and T_2 and will therefore not be transformed.

After quenching, the martensite is called “fresh martensite” (α') and is characterized by high hardness (mainly depending on carbon content) and relatively poor ductility. A tempering treatment is thus applied in order to relax stresses and to transform a part of martensite into austenite (reverted austenite at the tempering temperature), a part of which will remain stable after cooling to room temperature (retained austenite γ_R). Consequently, hardness is decreased and toughness increased, this effect being mainly attributed to partial transformation of fresh martensite into retained austenite [40].

One can thus understand that the tempering temperature must be higher than the temperature of formation of austenite, called A_{c1} temperature (dependent on the composition). Different formulas exist:

$$\begin{aligned}
 A_{c_1} &= 310 + 35\%Cr + 3.5(\%Cr - 17)^2 + 60\%Mo + 73\%Si + 170\%Nb + 290\%V \\
 &\quad + 620\%Ti + 750\%Al + 1400\%B - 250\%C - 280\%N - 115\%Ni - 66\%Mn \\
 &\quad - 18\%Cu \\
 A_{c_1} &= 850 - 1500(\%C + \%N) - 50\%Ni - 25\%Mn + 25\%Si + 25\%Mo + 20(\%Cr - 10)
 \end{aligned}$$

Hence, $T_1 > A_{c_1}$ has to be applied. However, it is usual that the formation of austenite begins at a temperature lower than A_{c_1} determined by the empiric formulas [41]. This can be due either to the effect of carbide precipitation during heating or due to composition heterogeneities. Carbide precipitation leads to a local decrease of Cr content. Consequently, A_{c_1} will decrease locally and an anticipated formation of austenite will take place. Similarly, a local increase in Ni will lead to a decrease in A_{c_1} . Such local phenomena make delicate the use of empiric formulae which take into account exclusively global compositions.

The austenite formed at tempering temperature is called “reverted austenite”. During the cooling, the reverted austenite can partially transform into fresh martensite depending on the temperature at the end of cooling and on its stability (see next part). The part of the reverted austenite, remaining after cooling, i.e. the part stable at room temperature, is called “retained austenite”.

The second tempering treatment is considered necessary to temper the fresh martensite potentially formed during the previous cooling and/or to form more retained austenite. This treatment must be realized at a lower temperature than the first one. The principle is the same as the previous one. The main objective is to avoid, as far as possible, the formation of fresh martensite which hardens the material and decreases the corrosion resistance [42].

One can thus suppose that if no fresh martensite is formed during the first tempering, the second one will be useless, at least if elimination of fresh martensite is its only purpose. Indeed, one of the utilities of the second treatment is to temper fresh martensite, potentially formed during the first one.

However, elimination of fresh martensite does not seem to be the only purpose of this second heat treatment. Indeed, as reported by Wang et al. [43], for a low carbon 13Cr-4Ni SMSS, the material resists better to stress induced martensitic transformation in the elastic domain when a second heat treatment is applied. The second tempering also affects the morphology of retained austenite which tends to become more globular [43]. When a second tempering treatment is applied, the $S(\text{train})\text{IMT}$ would occur more easily in the plastic domain leading to a delay of the necking and thus a more uniform plastic deformation.

Moreover, this second treatment is industrially applied as a security. Indeed, steels are particularly sensitive to corrosion in the non-heat-treated form. Since a strict temperature control is difficult, the second treatment is applied at a slightly lower temperature to ensure that no fresh martensite is present in the final material.

The result of tempering is a fine austenite phase (few dozens of nm) present between the martensite laths. This microstructure offers an enhanced ductility and toughness [44]. Depending on the composition of the alloy and on the temperatures applied during treatments, the volume fraction of retained austenite can vary from 0% to 30%.

1.4.2. Austenite stability as a function of tempering temperature and composition

Too high tempering temperatures, i.e. well above A_{C1} , must be avoided because it would result in the formation of unstable austenite which transforms into fresh martensite during cooling. Indeed, austenite formed during tempering is not always stable. The evolution of the percentage of retained austenite is presented in Figure 18:

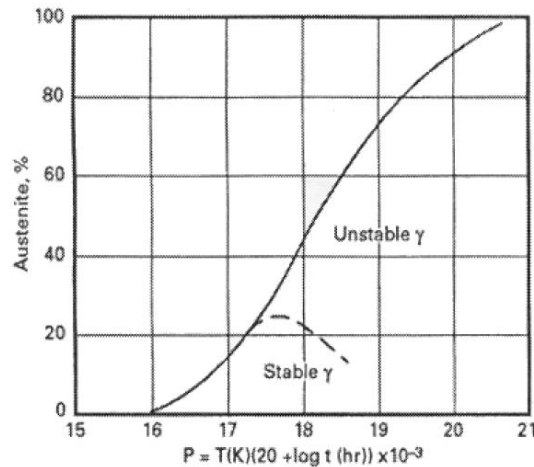


Figure 18 - Effect of the tempering treatment (Temperature (°C) and time (hours)) on the stability of reverted austenite in a 13Cr-4Ni-0.5Mo stainless steel [45]

Thibault et al. [46] observed that, between 600°C and 630°C, all reverted austenite will keep stable during cooling and thus become retained austenite in a 13%Cr-4%Ni stainless steel; which means that the reverted austenite formed at such temperatures is stable.

This stability can be explained by the enrichment of austenite in Ni (Ni diffuses over a distance of the order of some dozens of nanometers, towards newly formed austenitic grains) that increases its stability by lowering M_s . One would expect that the higher the tempering temperature the higher the amount of retained austenite will be. However, at temperatures higher than 630°C (for the steel investigated in [41]), the volume of reverted austenite is higher and, as the Ni content is fixed, the enrichment is not sufficiently high to make the austenite stable at room temperature. Hence, there is an optimum temperature (T_{opt}) at which the volume of the retained austenite is maximal. For temperatures lower than T_{opt} , the volume of reverted and retained austenite is lower but this reverted austenite formed is very stable due to a sufficient enrichment in Ni. On the contrary, for temperatures higher than T_{opt} , the volume of reverted austenite will be higher, so the Ni enrichment will be lower, and consequently the retained austenite fraction will be lower because some of the reverted austenite formed during tempering will be transformed into fresh martensite during cooling.

2. Cracking of (super)-martensitic stainless steels

2.1. Introduction

In this part, we will describe the phenomena involved in the environmentally assisted cracking of stainless steels. It is admitted that damage occurs in two steps: initiation of a surface defect and propagation of a crack from this defect which leads to failure [47]. We will describe these two stages separately, first the crack initiation followed by the hydrogen entrance (if any), then the crack propagation.

First of all, we need to define the ambiguous term of crack initiation. In this study, we will call crack initiation the phenomenon which leads to the sufficiently long destabilization of the passive film that makes possible the development of cracks. This destabilization can be either local, as in the case of pits, or global in the case of the dissolution of the passive film. The different phenomena included in this definition are:

- The variations of composition of the material which generates galvanic coupling, preferential pitting sites or preferential hydrogen adsorption sites.
- The composition of the environment assisted pit formation or passive film dissolution.
- The surface state of the material which can be modified by the application of the mechanical loading.

Then, the crack initiation is function of the ability of the alloy to repassivate [48]. Indeed, if the passive film is destabilized during a short time, cracks will not be able to form and the phenomenon leading to this depassivation will not be called initiation because it is not stable.

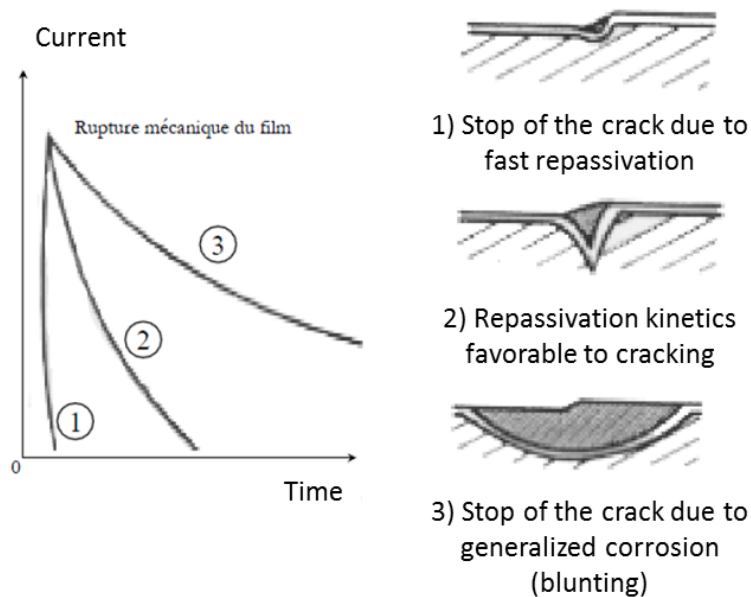


Figure 19 - Influence of the repassivation kinetics on the crack initiation [48]

2.2. Crack initiation

2.2.1. Initiation by pitting

The most known and most observed crack initiation phenomenon in Oil & Gas environments is pitting, which is a localized corrosion phenomenon.

The pitting resistance of an alloy can be determined by the Pitting Resistance Equivalent Number (PREN) given by the relation:

$$PREN = \%Cr + 3.3\%Mo + 16\%N$$

When working with multi-phase alloys and according to the literature [49] [50], it is more convenient to define different pitting resistance numbers for the different phases of the alloy. This is the case of duplex stainless steels whose austenitic and ferritic phases have different PREN:

$$PREN_{\alpha} = \%Cr + 3.3\%Mo$$

$$PREN_{\gamma} = \%Cr + 3.3\%Mo + 16\%N - \%Mn$$

Cracks can initiate at the bottom of pits [51] due to their geometry which leads to stress concentration. In this case, the pit acts as a micro notch. On another hand, the composition of the environment can be modified inside a pit. Indeed, an acidification can occur, leading to a chemical dissolution which can assist crack initiation (and propagation).

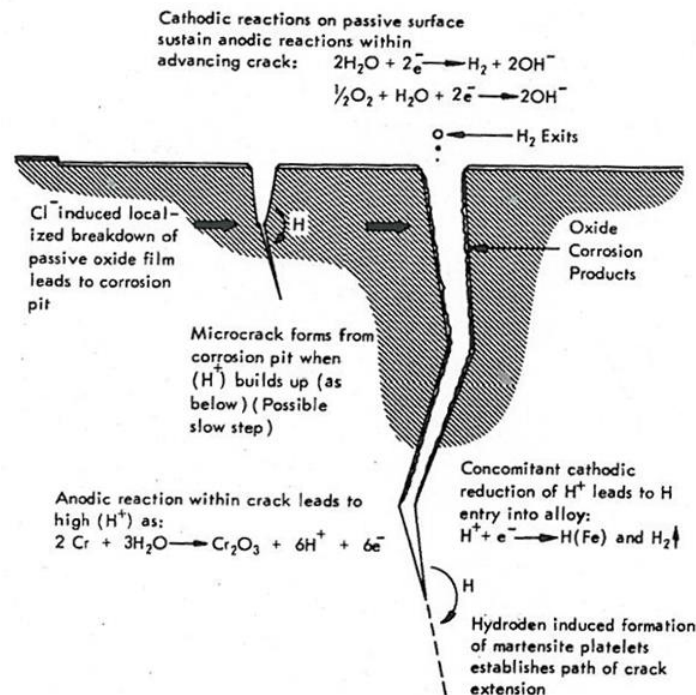


Figure 20 - Mechanism proposed by Rhodes showing crack initiation by pitting and modification of the pH deep down into pits and cracks [51]

2.2.2. Initiation by chemical depassivation

The microstructure of quenched and tempered SMSS is composed of two major phases, FCC and BCC with different compositions due to partitioning of alloying elements. As described in the previous section, this effect is at the origin of the stabilization of the gamma phase. It is also observed in duplex stainless steels [52] and leads to the presence of two corrosion peaks on polarization curves (Figure 21). Furthermore, according to the pH of the environment, only one peak (associated to the dissolution of the gamma phase) or two peaks (dissolution of both alpha and gamma phases) are observed [52].

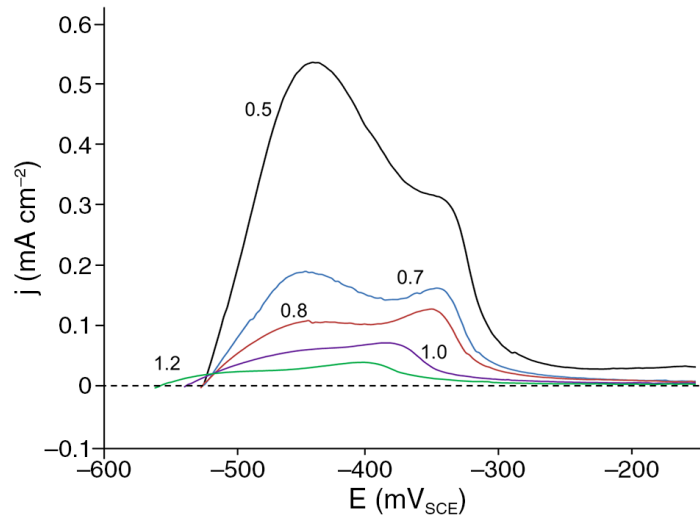


Figure 21 - Example of depassivation as a function of pH on a duplex stainless steel [52]

Once one or both phases are depassivated, corrosion defects can form by preferential dissolution of one phase and constitute sites of crack initiation. The proton reduction reaction close to these sites constitutes a source of hydrogen that can participate in the embrittlement of one of phases of the material. Actually, the phase in a cathode situation is likely to be weakened by the evolution of hydrogen at its surface (Figure 22). This hydrogen is formed by the cathodic reaction that protects this phase.

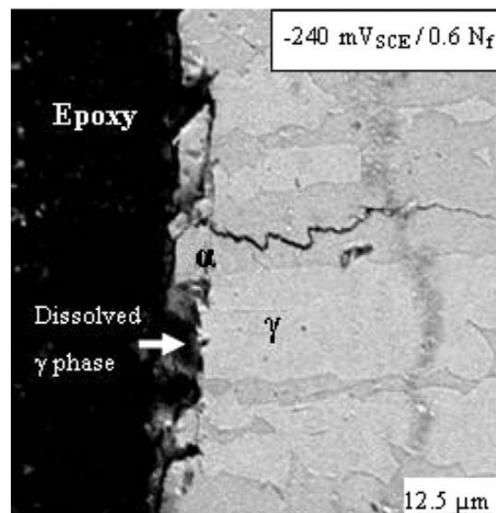


Figure 22 - Cross section of a duplex stainless steel showing preferential dissolution on austenite and crack initiation due to hydrogen embrittlement on ferrite [53]

2.2.3. Initiation by mechanical defects

When the passive film is chemically stable in the given environment and when no pitting occurs, cracks can initiate on defects of mechanical origin. Indeed, Serre et al. [54] observed slip bands at the surface of a duplex stainless steel at a very low plastic deformation (0,2%). Considering the differences between the two phases which compose SMSS, local plastification can occur even within the macroscopic elastic domain.

Furthermore, it has been showed by Mary et al. [55] that microplasticity begins earlier in the soft phase than in the hard phase (at respectively 54% and 76% of their yield strength in the investigated case).

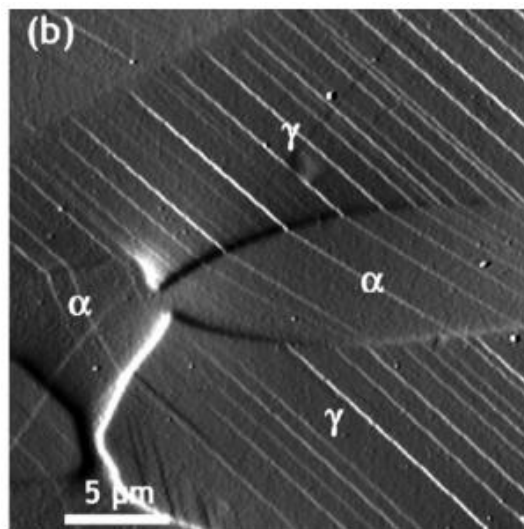


Figure 23 - Different types of slip bands observed at the surface of a duplex stainless steel deformed at 1.8% [54]

2.2.4. Initiation in presence of H₂S

H₂S is known to act on hydrogen entrance and crack propagation due to its capability to form protons and to inhibit hydrogen recombination. However, it also has a little (but non negligible) impact on crack initiation. Indeed, H₂S is known to increase the depassivation pH (pH_d) [56]. The depassivation pH of SMSS has been measured between 1.5 and 2.0 without H₂S. However, in presence of H₂S, this pH is expected to be higher [56], which is a reason that explains the limitation of the use of SMSS for oil & gas applications [3]. Figure 24 summarizes the influence of H₂S on both, the anodic dissolution and the depassivation pH.

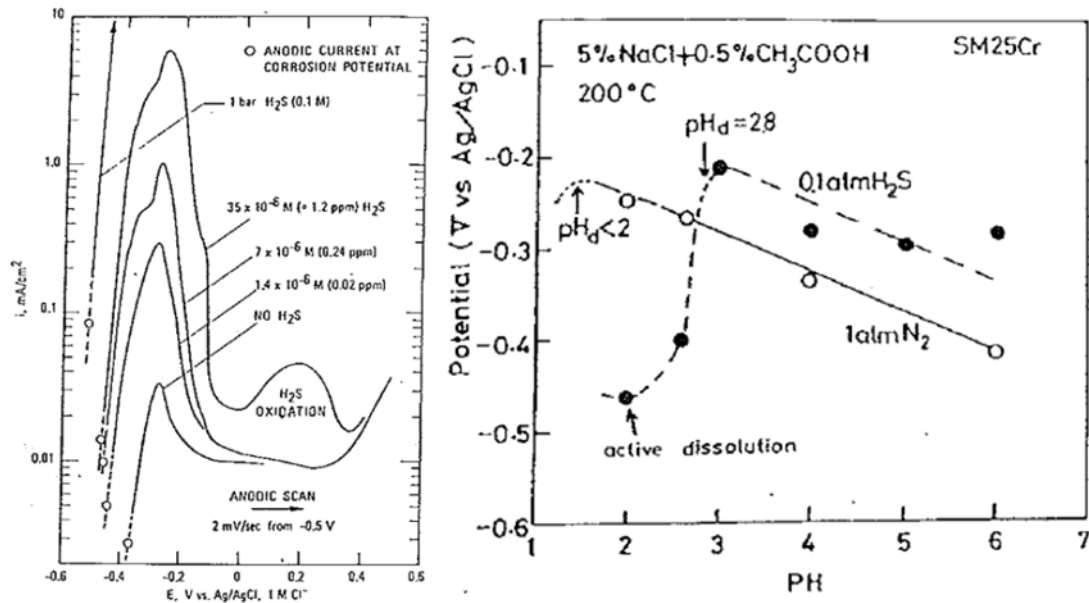


Figure 24 - Influence of H₂S content on the anodic dissolution (left [57]) and influence of its presence on the depassivation pH (pH_d) (right [58])

The presence of sulfur in the solution and at the metal surface (coming from the decomposition of H₂S) is also known to accelerate the anodic dissolution of the passive film [59] as seen in Figure 25 [60].

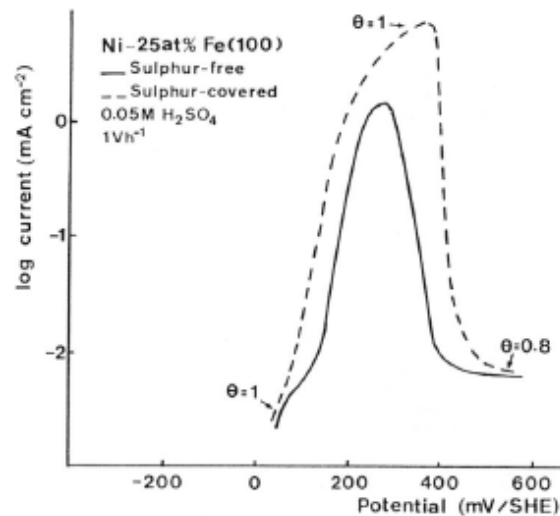
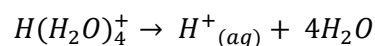


Figure 25 - Influence of the presence of adsorbed sulfur in the anodic dissolution [60]

2.3. Adsorption, absorption and desorption of hydrogen

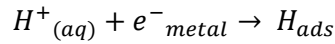
2.3.1. Hydrogen formation

Proton formation in the environment is possible following different mechanisms. Protons may be generated by chemical reactions of another species (such as H₂S for example, see next section) or they can come from a cathodic reaction. The mechanism of hydrogen charging by cathodic reaction has been extensively studied [61] [62]. According to these authors, the first step consists in the creation of a "free" proton by desolvation of the oxonium ion:



2.3.2. Hydrogen adsorption

Once these protons are generated, they can be adsorbed at the surface of the metal and react with valence electrons of the material. This reaction is known as the Volmer equation:



2.3.3. Hydrogen absorption or recombination

Adsorbed hydrogen can then be either absorbed or recombined on the surface to produce H_2 which bubbles off when dissolved H_2 has reached the saturation. This hydrogen gas (H_2) is not dangerous for the material. The recombination of hydrogen can be expressed by different reactions. The most known are the Tafel's reaction and the Heyrovsky's reaction [63]:

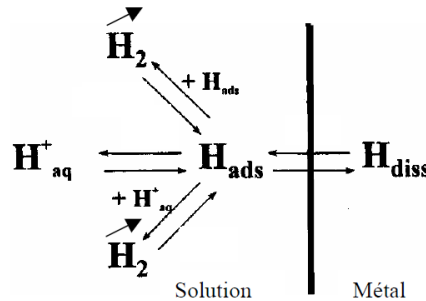
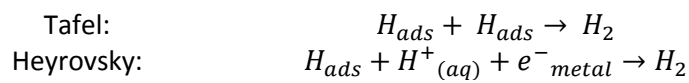
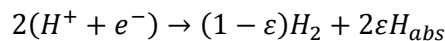
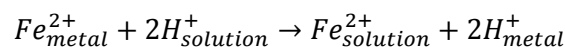


Figure 26 - Schematic representation of hydrogen charging [63]

However, these reactions are not complete. Indeed, a part of hydrogen ϵ is absorbed, the remaining being recombined.



Another theory of hydrogen penetration exists and has been developed by Crolet [64]. This theory is called the direct protonic transfer, and consists in a cation-exchange between two phases (the metal and the solution):

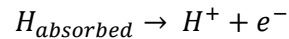


One must notice that, according to this theory, hydrogen is present in the material as a proton and not as atomic hydrogen. Indeed, hydrogen is an element that tends to give electrons contrary to interstitial elements such as carbon for example [64].

2.3.4. Hydrogen desorption

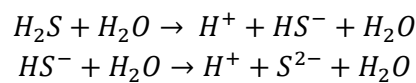
As explained previously, once hydrogen is present in the environment, it can penetrate inside the material by adsorption and then absorption. However, this absorption cannot be infinite. Indeed, the equilibrium is established between the amount of hydrogen present in the environment and the quantity of hydrogen absorbed inside the material [65]. Consequently, if the concentration of hydrogen inside the material becomes too high with respect to the concentration in the environment, a phenomenon of desorption will take place in order to re-equilibrate both concentrations (inside and outside the metal). Diffusible hydrogen will be able to escape from the

bulk to compensate the lack of hydrogen outside. Here again, as for absorption, several mechanisms of desorption are proposed. The simplest one is the direct exchange:

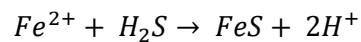


2.3.5. Influence of H₂S

The difference between isolated proton H⁺ and proton coming from H₂S lies in the fact that the kinetics of both processes are not the same. Indeed, kinetics of hydrogen absorption is increased when H₂S is present in the environment because H₂S acts as catalyst for hydrogen penetration inside the metal. H₂S is considered as dangerous for metals because it acts as source of protons. Indeed, in presence of water, H₂S will dissociate in water forming an acidic and corrosive environment containing protons according to the reactions:



In acid environments, H₂S is stable as seen in Figure 27. It can thus react with water to form a layer of iron sulfide FeS according to the equation:



The exact composition of the layer can change as a function of pH, the partial pressure of H₂S and the environment. One can thus observe following types of layers: FeS, FeS₂, Fe₇S₈ or Fe₉S₈. Moreover, in presence of other elements, a layer of different composition can be formed. It has been showed that, for stainless steels containing Ni, the most stable layer that tends to be formed is NiS [66].

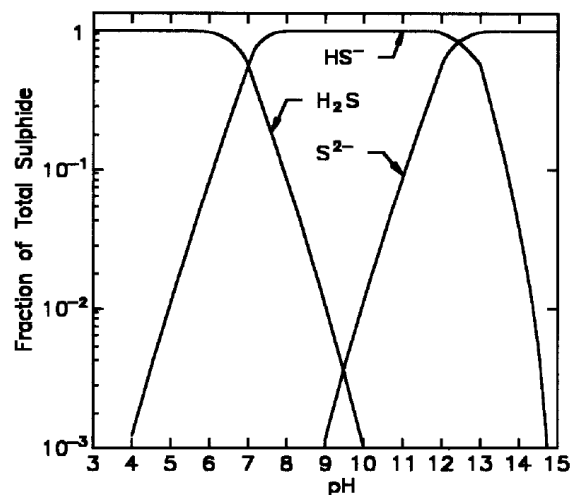


Figure 27 - Stability of H₂S as a function of pH [67]

H₂S is considered as dangerous because it acts as a reservoir of protons which, by penetrating into the material by electrochemical reactions, induce material brittleness. Indeed, one considers that H₂S is adsorbed in the same sites as hydrogen, avoiding hydrogen recombination and thus favoring hydrogen entrance [68]. Another theory considers that H₂S lowers the energy gap between adsorbed hydrogen and metal [69].

H₂S also influences hydrogen desorption. A new approach based on HS⁻ as a catalyst for hydrogen entrance and exit has been developed by Crolet [64]:



This approach is schematically explained in Figure 28.

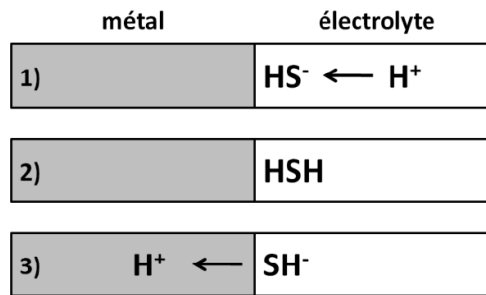


Figure 28 - Schematic representation of the direct protonic transfer approach [64]

2.4. Interactions between hydrogen and metal

Once absorbed inside the structure, hydrogen can evolve differently inside the material. Indeed, according to its energy, hydrogen can be either in solid solution or trapped inside particles, at lattice defects or in one of phases of multiphase materials [70]. Hydrogen in solid solution can diffuse and it is thus called diffusible hydrogen as opposed to trapped hydrogen.

Indeed, because of its small size (with a radius of $0.53 \times 10^{-10} \text{m}$) and low mass, the mobility of hydrogen in metallic material is high [71] and it can diffuse easily from interstitial site to another by jumping from one site to another. This theory has been confirmed by Jiang and Carter [72] with the “ab initio” calculation of diffusion. Nevertheless, interstitial sites available in bcc or fcc structures are too small to contain a hydrogen atom without distortion of the surrounding lattice, and cause a positive change in volume. That is why its diffusion into a region surrounding a defect is controlled by hydrostatic stress gradients, the hydrogen atoms fitting more easily into the stretched lattice where its chemical potential is lower [73].

2.4.1. Diffusible hydrogen

2.4.1.1. Diffusion in concentration gradient

The driving force for hydrogen diffusion is the concentration gradient. Indeed, given that hydrogen penetrates by the surface, the concentration of hydrogen is higher near the surface than in the bulk. This concentration gradient will thus always exist.

The flux of hydrogen inside the material coming from the difference of concentration can be expressed by Fick’s laws. At a given temperature T , the flux J_m is expressed (in atoms/ m^2/s) by the formula:

$$J_m = -D \vec{\nabla} C + \frac{D C V_h}{RT} \vec{\nabla} \sigma_h$$

where D is the diffusion coefficient in the considered phase (see Table 4), V_h is the molar volume of hydrogen, σ_h represents the hydrostatic stress and C represents the concentration of free hydrogen (without taking into account the trapped hydrogen, see next part).

Hydrogen diffusion coefficients in steels are given in Table 4, with a remarkable difference of six orders of magnitude between martensite and austenite.

Table 4 - Diffusion coefficient of hydrogen in different microstructures of steels

	Ferrite α	Austenite γ	Martensite α'
Diffusion coefficient at 25°C (in m ² /s)	9.5x10 ⁻⁹	2.1x10 ⁻¹⁶	10 ⁻¹⁰

In the case of a biphasic microstructure composed of martensite and retained austenite, and by considering it as a composite, the apparent macroscopic diffusion coefficient can be expressed by [74]:

$$\frac{1}{D} = \frac{(1 - f_{\gamma})}{D_{\alpha'}} + \frac{f_{\gamma}}{D_{\gamma}}$$

where D is the macroscopic diffusion coefficient, f_{γ} the fraction of retained austenite and D_{γ} and $D_{\alpha'}$ are the diffusion coefficients of austenite and martensite respectively, however this simple formula is of little interest for SMSS because the actual spatial distribution of the retained austenite is too complex with respect to the assumptions at the origin of this formula.

2.4.1.2. Short circuit diffusion along grain boundaries

The diffusion mechanism mentioned before is a classical lattice diffusion mechanism that does not take into account 1D or 2D defects such as dislocations or grain boundaries. On such defects of the material, diffusion is supposed to be faster [75]. However, this effect is difficult to be quantified because it is strong only when the diffusion in the bulk is slow, that is to say, typically for austenitic structures (see Table 4). That is why faster diffusion has been clearly demonstrated in austenitic grain boundaries for example.

2.4.1.3. Hydrogen transport by dislocations

Hydrogen can be dragged by mobile dislocations. Hydrogen is attracted by the stress field of dislocations due to its small size. Then, it can follow the movement of dislocations. The flux of hydrogen is thus increased by this phenomenon because dislocations usually move faster than hydrogen alone [76]. However, this theory cannot be applied for long-range diffusion [77]. Furthermore, the association between hydrogen and dislocation leads to a relaxation of the elastic stresses due to a formation of a plastic field. This plastic field leads to the formation of new point defects and dislocations. These newly formed dislocations can in turn drag hydrogen. In consequence, these two effects (transport of hydrogen and creation of dislocations) may accelerate crack propagation [78].

2.4.2. Trapped hydrogen

In opposition to diffusible hydrogen, hydrogen can be immobilized at particular sites of the microstructure and it is then called trapped hydrogen. The presence of traps is usually considered dangerous for the resistance to embrittlement. Indeed, the phenomenon of trapping induces an increase of the hydrogen solubility inside the material which might be considered as beneficial, however, the continuous hydrogen uptake will eventually result in its overconcentration. This local

overconcentration may cause damages such as blisters for example. In order to be able to control such local effects, the nature of traps must be identified.

Traps can be characterized by their energy and their localization.

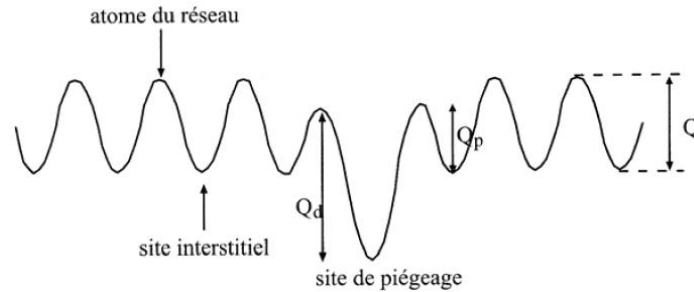


Figure 29 - Schematic representation of the potential energy of a hydrogen atom in the lattice [79]

Depending on the interaction energy between the trap and hydrogen itself, the trap is called reversible or irreversible. Some examples of binding energies are summarized in Table 5 [80].

Table 5 - Binding energies of hydrogen with different microstructural defects [80]

	Binding energy (in eV/at)	
	Ferritic steels	Austenitic steels
Dislocation	0.20 - 0.58	0.10 - 0.20
Grain boundary	0.10 - 0.58	0.10 - 0.20
Void	0.46 - 0.54	0.20 - 0.42
Cavity	0.28 - 0.96	0.41 - 0.53
Interfaces (precipitates, inclusion)	MnS: 0.29 - 0.57	
	AlN: 0.48 - 0.58	
	Fe ₃ C: 0.57 - 0.84	
	TiC: 0.95	

The number of hydrogen traps (N_T) can be related to the plastic strain by a formula established from experiments on α ferrite carried out by Kummick and Johnson and numerically expressed by Sofronis and McMeeking [81]:

$$\log_{10}(N_T) = 23.26 - 2.33 \exp(-5.5 * \epsilon_p)$$

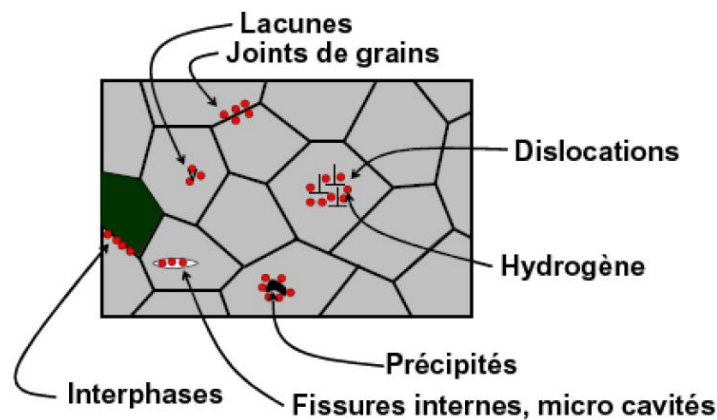


Figure 30 - Schematic representation of hydrogen traps [82]: grain boundaries, dislocations, precipitates, interphases, voids or cavities

2.4.3. Equilibrium between diffusible and trapped hydrogen

Both populations of hydrogen (in the lattice and trapped) are in equilibrium. If one notes C_T and C_L the concentrations of trapped hydrogen and hydrogen in the lattice respectively, one can find the relation [70]:

$$C_T = \frac{N_T}{1 + \frac{N_L}{K_T * C_L}}$$

where K_T is the equilibrium constant, N_T and N_L the number of sites per unit volume.

2.4.4. Hydrogen diffusion and trapping measured by electrochemical permeation

To study hydrogen diffusion in metal, one uses the electrochemical permeation technique. The principle of this technique is to generate a concentration gradient of hydrogen between two sides of a thin metallic specimen. This technique was developed by Devanathan and Stachurski [83]. The concentration gradient is created by the application of either a cathodic current or potential at the entry side and an oxidation potential at the exit side.

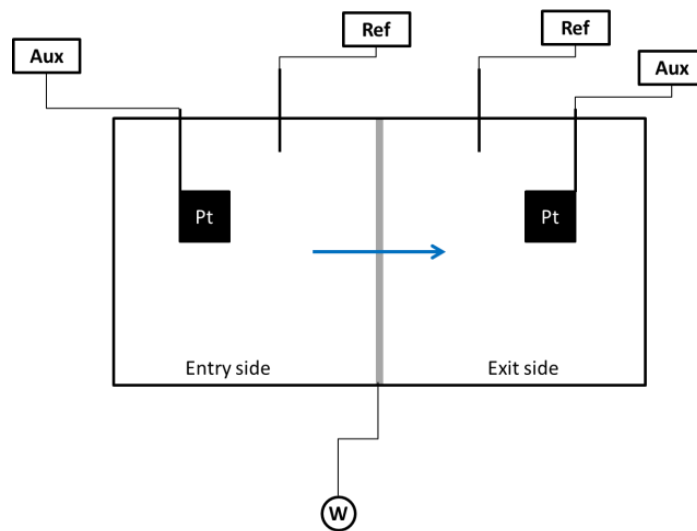


Figure 31 - Schematic representation of electrochemical permeation cells

As shown in Figure 31, the experimental setup is composed of two cells. On the exit side, the solution used is usually 0.1M NaOH deaerated with nitrogen. Auxiliary electrodes are platinum plates and reference electrodes are calomel electrodes (SCE). The work electrode is the thin sample of tested steel. The sample is polished on both sides then either both sides or only one side are/is covered with palladium.

The hydrogen flux detected at the exit side can be expressed by the relation [84]:

$$\frac{J(e, t)}{J_{max}} = \frac{2e}{\sqrt{\pi Dt}} * \sum_{n=0}^{\infty} \exp\left(-\frac{(2n+1)^2 * e^2}{4Dt}\right)$$

where e is the sample thickness, t the time and D the apparent diffusion coefficient. This coefficient can be determined experimentally using the curve presented in Figure 32.

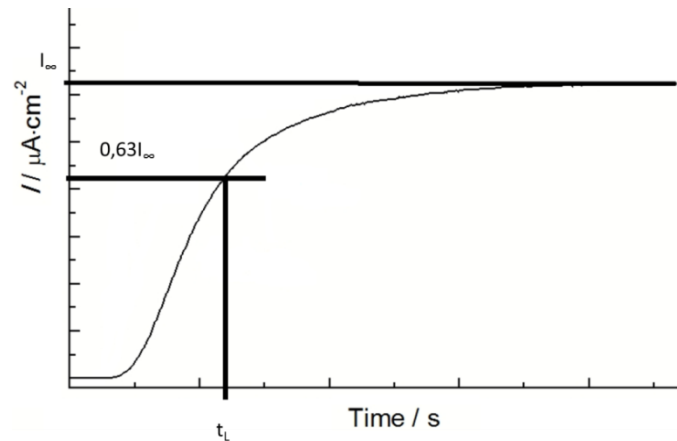


Figure 32 - Hydrogen permeation curve obtained

$$D = \frac{e^2}{6t_L}$$

2.5. Crack propagation

Different forms of environmentally assisted cracking can be encountered, depending on the material-environment combination and as a function of applied stress. In this part, we will mainly describe embrittlement forms and mechanisms likely to occur in presence of corrosive environments containing H₂S.

2.5.1. Various forms of cracking

2.5.1.1. Stress Corrosion Cracking (SCC)

Stress Corrosion Cracking (SCC) is the term that usually describes the crack formation and growth in a corrosive environment. It leads to a brittle failure in materials which are supposed to be ductile under purely mechanical loading. It usually corresponds to a combination of anodic and cathodic phenomena.

SCC can only occur if all of the following conditions are verified:

- Tensile stress (either residual or external)
- Presence of aqueous corrosive environment

2.5.1.2. Hydrogen Sulfide Cracking (HSC) and Sulfide Stress Cracking (SSC)

Sulfide Stress Cracking (SSC) is the cracking mechanism resulting from the combination of a tensile stress and corrosive environment containing H₂S in a sufficient amount. The stress can be either residual stress or service stress. It is admitted by NACE standards [3] that SSC is limited to steels whose hardness is of at least 22 HRC. SSC is a cathodic phenomenon such as Hydrogen Embrittlement and a particular case of Hydrogen Sulfide Cracking (HSC).

From a macroscopic point of view, sulfide stress cracks always initiates at the surface of the material and crack propagation follows a path perpendicular to the loading axis [85]. Failure through HSC/SSC clearly involves different mechanisms than damage under simple mechanical loading which usually initiates at 45° regarding the loading axis.

In the case of SSC H_2S is considered to increase the rate of corrosion and/or hydrogen entry by poisoning the hydrogen recombination at the surface of the metal. In fact, as shown in Figure 33, for a steady state permeation current, the sensitivity to SSC only depends on the amount of hydrogen absorbed by the material and not on the presence or absence of H_2S . The increased severity associated with H_2S containing environments might then result from a poisoning of the hydrogen recombination.

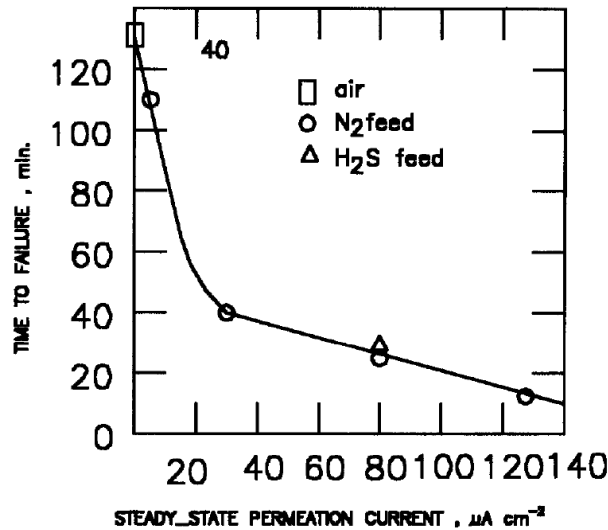


Figure 33 - Time to failure as a function a steady state permeation current with and without H_2S on AISI 4130 during tensile tests under applied potential [67]

In presence of H_2S , hydrogen absorption is favored due to the poisoning of the surface by either FeS or NiS layers. Indeed, as mentioned previously [59], the adsorbed sulfur increases the anodic dissolution rates which enable formation of metallic sulfurs.

Permeation current and anodic dissolution are more important when H_2S is present which can explain that H_2S environments are more severe than other ones. One can thus consider that the embrittlement is proportional to the hydrogen flux entering the material, this one being obviously higher in presence of H_2S due to the adsorption of sulfur at the metal surface [60].

As previously described, once absorbed hydrogen diffuses to sites where internal stress is the highest (grain boundaries or intermetallic particles for example). Such sites can become the initiation sites of brittle cracks under applied or residual stress.

SSC in high strength steels (yield strength > 700 MPa) usually leads to intergranular fractures. On the contrary, for lower strength steels (yield strength < 700 MPa) fractures are generally transgranular. The influence of the yield strength on the cracking mode can be explained by Davidenkov diagrams [86].

The sensitivity to SSC increases with an increasing partial pressure of H_2S and a decreasing pH [44].

2.5.1.3. *Hydrogen Induced Cracking (HIC)*

Hydrogen Induced Cracking (HIC) is a form of hydrogen embrittlement linked to trapped hydrogen. Indeed, in this form of embrittlement, cracking occurs near hydrogen traps such as precipitates or, more often, MnS particles. Cracking results from the pressure increase due to the accumulation of molecular hydrogen in the trap. This increase of the pressure leads to an increase of the local stress leading to crack initiation. Contrary to SSC, this form of embrittlement does not require the application of an external loading, but it requires an important amount of trapped hydrogen in order to reach the threshold internal pressure [87]. However, in precipitate-free supermartensitic stainless steels, precipitates could not be the initiation sites of HIC cracks, but, if one considers the retained austenite as a trap and that it can store enough hydrogen, γ_R may be regarded as a potential crack initiation site.

2.5.1.4. *Stress Oriented Hydrogen Induced Cracking (SOHIC)*

Stress Oriented Hydrogen Induced Cracking (SOHIC) corresponds to the accumulation of cracks formed by HIC perpendicularly to the direction of applied stress (either residual or external). The macroscopic failure corresponds to the link between each blister created by HIC. This form of hydrogen embrittlement is a mix between SSC and HIC because it requires both applied stress and trapped hydrogen. For the same reason as HIC, this phenomenon will probably not be observed in supermartensitic stainless steels.

2.5.1.5. *Cracking assisted by dissolution*

Dissolution along the crack path can also influence the crack propagation path as it has been shown in Duplex Stainless Steels [88]. Staehle [48] proposed a model of anodic dissolution where the capability to initiate and propagate cracks is dependent on the repassivation kinetic. Furthermore, it has been observed that the cracking path is not only dependent on the solution but also on the composition of the alloy [89].

2.5.2. Various mechanisms of Hydrogen Embrittlement (HE) and crack propagation

Different theories were developed in order to explain different forms of cracking observed experimentally. In this part we will thus describe some of the mechanisms that are susceptible to occur in supermartensitic stainless steels.

2.5.2.1. *Adsorption Induced Dislocation Emission (AIDE)*

Adsorption Induced Dislocation Emission (AIDE) mechanism is associated with hydrogen adsorbed at the surface of the material and has been proposed by Lynch [90] [91]. Adsorbed hydrogen can assist the nucleation and emission of dislocations by decreasing the surface energy. Hydrogen adsorbed at the crack tip enables the emission of dislocations in the plastic domain and accelerates crack propagation.

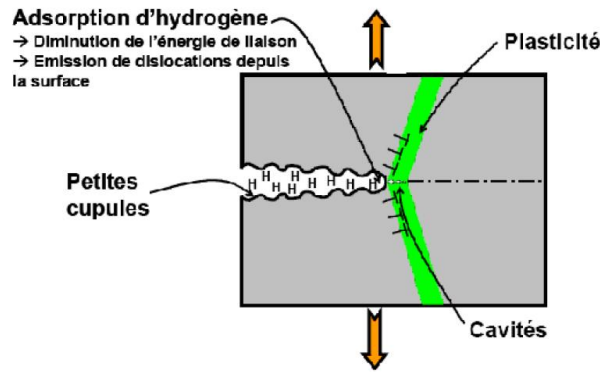


Figure 34 - Schematic representation of AIDE [82] showing hydrogen adsorption at the crack tip leading to the decrease of the binding energy and to the emission of dislocations from the crack tip

2.5.2.2. *Hydrogen Enhanced Localized Plasticity (HELP)*

Hydrogen Enhanced Localized Plasticity (HELP) mechanism is founded on the relation between hydrogen and dislocations. Indeed, hydrogen is supposed to increase the dislocation mobility [92]. This effect is mainly observed on some specific slip systems. When this phenomenon occurs at the crack tip, it leads to an increase of the local concentration of dislocations, subsequent localized shearing and finally the decrease of the macroscopic ductility of the material.

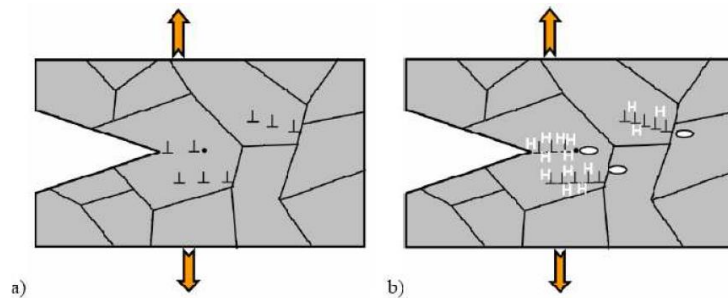


Figure 35 - Schematic representation of HELP [82] showing the increase of dislocation concentration at a crack tip

2.5.2.3. *Hydrogen Enhanced DEcohesion (HEDE)*

Hydrogen Enhanced DEcohesion (HEDE) mechanism has been proposed by Troiano in 1960 [93] and then improved by Oriani [70]. This mechanism is essentially associated with HIC and SOHIC types of cracking. Indeed, this model supposes that trapped hydrogen leads to a reduction of the energy of cohesion, reducing in the same time the energy needed to create a new surface and leading to an easier propagation of the crack. As previously mentioned, in SMSS, traps are not precipitates but rather retained austenite grains (see later).

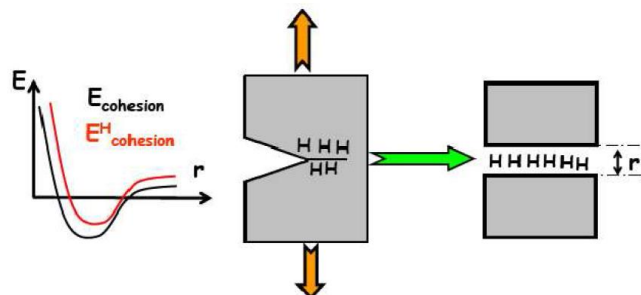


Figure 36 - Schematic representation of HEDE [82] showing opening of an interface due to the reduction of the cohesive energy consecutive to hydrogen trapping

2.5.2.4. *Selective dissolution*

There is no specific mechanism of selective dissolution in dual phase material. But it has been found in Duplex Stainless Steels [52] that the composition heterogeneities are at the origin of preferential dissolution of one phase. The other phase protects cathodically the first one, being the site of cathodic reaction creating hydrogen at its surface. This hydrogen can enter this specific phase and initiate cracks through one of the previously mentioned hydrogen embrittlement mechanisms.

2.6. Use of Stress Corrosion Cracking tests to reproduce cracking susceptibility

2.6.1. Different type of tests

Several modes of solicitations can be used to reproduce cracking susceptibility of metallic materials. There are three principal categories of tests:

- Mechanical tests with imposed deformation: “U-bend” samples or “4 point bending” samples are immersed in the environment after straining in air. Time to failure is the criterion of material resistance. In these tests, it is difficult to know the stress state of the samples and then a reference test is needed.
- Mechanical tests at constant load: A constant load is applied to a sample (for example using O-ring machine) immersed in the test solution. According to NACE standards, the material is considered resistant if its time to failure exceeds 720 hours under well specified corrosion and mechanical loading conditions. A threshold value of the applied stress in the specific environment can thus be determined.
- Mechanical tests at constant strain rates, also called Slow Strain Rate Tensile tests (SSRT): The sample is deformed at a constant strain rate in the corrosive environment. All these tests lead to failure, and the elongation at failure and the aspect of the fracture surfaces enable characterizing the severity of embrittlement. This type of test is the most adapted to study crack propagation mechanisms.

2.6.2. Different types of environments

Different environments can be used during SCC tests: acid, base or neutral environments. The main objective is here to reproduce the industrial environment in terms of severity and mechanisms involved in the environmentally assisted cracking phenomena. The most known is the synthetic sea water containing high amounts of chlorides. A typical basic environment is 0.1M NaOH that enables via the reduction of water, the formation of adsorbed hydrogen as compared to acid environments. Acid environments are the most frequently used for Oil&Gas applications.

2.7. Parameters influencing the resistance to hydrogen embrittlement

2.7.1. Metallurgical parameters

The resistance to hydrogen embrittlement is not determined exclusively by environmental conditions but also by metallurgical factors (composition, microstructure) and surface conditions.

Surface conditions:

Surface conditions play an important role in hydrogen embrittlement because they influence hydrogen adsorption and absorption. Furthermore, SSC cracks can initiate on surface defects. For example, cracks can initiate on corrosion pits or mechanical defects.

Composition:

Resistance to hydrogen embrittlement obviously depends on the composition of the alloy. Indeed, some elements are detrimental for corrosion resistance properties while others are beneficial.

For example, if the alloy contains more than 0.2% of Cu, a protective film can be formed in environments with $\text{pH} > 4$. Indeed, Cu quickly combines with S forming a protective film. However, this film is dissolved if pH is lower than 4 [94].

Grain boundary decohesion is favored by phosphorous. This element segregates to grain boundaries and can lead to intergranular fracture. Furthermore, intermetallic particles are also considered as critical. Indeed, they act as hydrogen traps leading to a local increase in hydrogen content and as stress concentration areas. The concentration of stress is more important for elongated particles which are thus considered as the most critical intermetallic particles than circular ones. Consequently, brittle particles may act as crack initiation zones and the size of cracks will obviously directly depend on that of particles. MnS particles are considered particularly dangerous because of their large size, elongated shape and the tendency to form sites of galvanic coupling.

Microstructure:

Microstructure also impacts resistance to hydrogen embrittlement because some phases can store more hydrogen than others (see Table 6). Coudreuse [95] determines a classification of steel microstructures as a function of their resistance to hydrogen embrittlement. From left to right the resistance to hydrogen embrittlement increases:



Fresh microstructures are detrimental because of their high hardness. On the other side, tempering results in stress release and homogenization of the microstructure which increases the resistance to embrittlement.

The microstructure of SMSS depends on the whole thermo-mechanical history of the alloy. The amount of retained austenite in a supermartensitic stainless steels is supposed to influence the resistance to hydrogen embrittlement. This is essentially due to the difference in hydrogen solubility in martensite and in austenite (Table 6). In pure ferritic or pure martensitic alloys, the solubility is close to 0 at room temperature whereas for austenitic microstructures the solubility is much higher due to the larger interstitial sites in FCC lattice [96]. Hence, austenitic grains can act as hydrogen traps.

Table 6 - Hydrogen solubility in the different phases of steels

	Ferrite α	Martensite α'	Austenite γ
Solubility at 20°C (in wt. ppm)	$\sim 10^{-4}$	$\sim 10^{-3}$	$\sim 10^{-1}$

On the other hand, the hydrogen content in the material is often underestimated when calculated by standard procedures (such as the electrochemical permeation test presented previously). Indeed, such tests are based on measurements of the flux of hydrogen across the surface of the sample. But, hydrogen contained in retained austenite will not have sufficient time to diffuse out of the sample during these tests. The measure of hydrogen trapped inside the alloy will thus be underestimated [97]. Consequently, the amount of hydrogen trapped in the microstructure have to be measured by high temperature outgassing using thermal desorption spectroscopy or by a complete melting and subsequent analysis.

Martensitic steels with a high martensite fraction after quenching are more resistant to SSC than martensitic steels with residual austenite after quenching because less traps are present in the microstructure (Figure 37) [98]. The complete martensitic transformation after quenching is thus an objective that can be reached by adapting the composition of the alloy or the quenching.

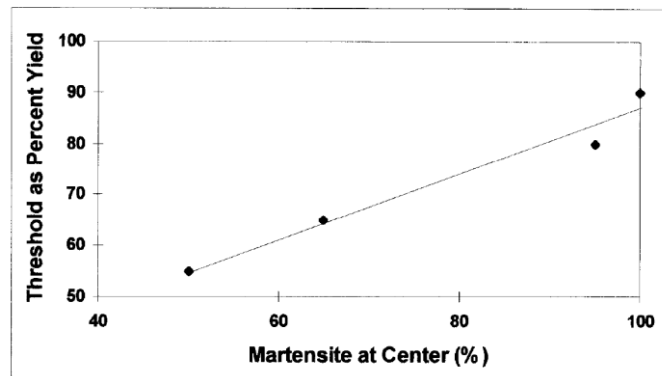


Figure 37 - Threshold stress for SSC as a function of the percentage of martensite after quenching on AISI 4130 [98]

As previously mentioned, the retained austenite formed during tempering of SMSS may transform into fresh martensite during plastic straining (at a crack tip for example) and since austenite is expected to contain more hydrogen than martensite (see Table 6), hydrogen will be released inside the newly formed martensite, leading to an oversaturation of hydrogen in the martensitic phase. For example, in a study performed by Cabanillas et al. [99], the initial fraction of austenite (before straining) was 11% while it decreased to 7.5% after 5% straining. Knowing that hydrogen content is typically of 2 ppm in a pure martensitic microstructure and 10 ppm in a martensitic microstructure containing retained austenite [99], one can see that the transformation of austenite to martensite will lead to an increase of hydrogen content in α' . Solheim et al. [100] applied the above hydrogen concentrations to Oldens' model and found that the critical stress to failure drops from 1525 MPa for a pure martensitic microstructure containing 2 ppm of hydrogen to 787 MPa for a pure martensitic microstructure containing 10 ppm of hydrogen (coming from retained austenite that has transformed into martensite during straining).

To summarize, one can thus see that the fraction of retained austenite, its stability regarding SIMT and the presence of fresh martensite are key microstructural parameters for the study of the resistance to hydrogen embrittlement in SMSS.

2.7.2.4. *Aggressiveness of the environment : Influence of pH, p_{H_2S} , CO_2 and chlorides*

Environment can be classified in different categories:

- Sweet service
- Sour service
- Acid gas

Sweet gas:

Sweet gas is defined as an environment containing hydrocarbons and CO_2 in presence of water. The biggest threat in this environment is due to general corrosion. Indeed, CO_2 acidifies the water leading to a degradation of the passive film.

Sour gas:

Sour gas is defined as an environment containing hydrocarbons and H_2S in presence of water. For carbon and low alloy steels, the threshold value for H_2S in sour gas is $p_{H_2S} \leq 0.0030$ bars. However, this limit must also be a function of the acidity of the environment. Indeed, contaminants, such as chlorides for example, act as catalyst leading to an increase of the corrosion kinetics due, for example, to an easier crack initiation and/or propagation.

Acid gas:

Acid gas is defined as an environment containing hydrocarbons, CO_2 , H_2S and also contaminants such as chlorides.

In order to visualize the coupled effect of H_2S and acidity, a plot called severity diagram may be used (Figure 39). SSC sensitivity increases with a decreasing pH and an increasing partial pressure of H_2S . Indeed, if pH decreases, more protons H^+ are available in the environment; and, as seen previously, equilibrium exists between absorbed protons and protons in the environment. Hence, a decrease of the pH leads to an increase of absorbed hydrogen decreasing the resistance to SSC. Furthermore, the quantity of absorbed hydrogen also increases with the pressure of H_2S .

Naturally, the severity diagram depends on the type of embrittlement considered because cracking mechanisms are not the same as seen previously.

It is thus necessary to deal with different types of diagrams. Figure 39-a shows the diagram for SSC, as defined in the standard ISO 15156 by the NACE [3] while Figure 39-b shows a partial diagram made by Kittel et al [103] for HIC.

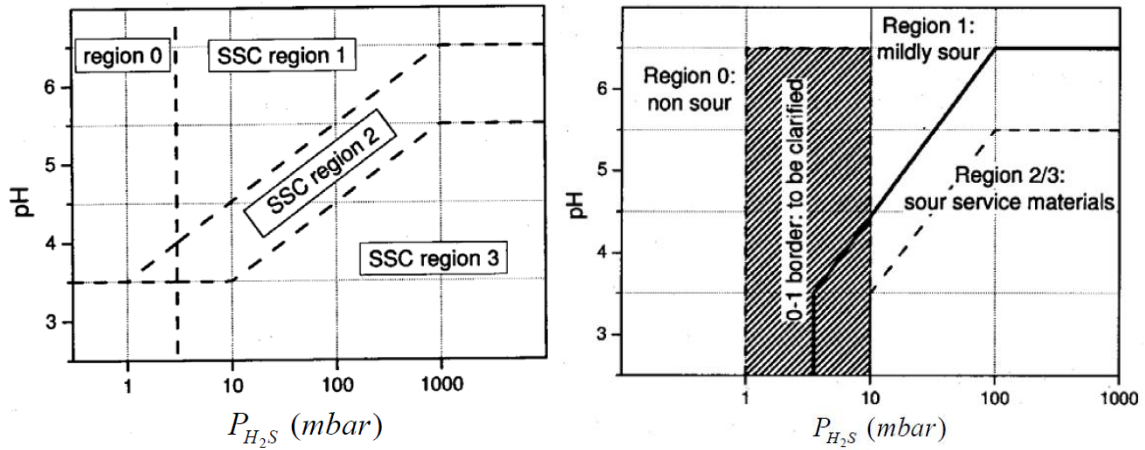


Figure 39 - Severity diagram regarding SSC (left) and HIC (right)

The plot is divided in different regions. Region 1 corresponds to the sweet service region described previously while region 3 corresponds to the sour service domain. This diagram is based on both experimental studies and industrial feedbacks on platforms.

As mechanisms for SSC and HIC are not the same, it is necessary to define another diagram for HIC damage (Figure 39-b). A study performed by Kittel et. Al. [103], limited to pipeline steels, indicates the differences between both types of embrittlement. However, this diagram is not complete and frontiers must be defined more accurately by further experiments.

These diagrams are used in order to help choosing the right alloy as a function of environmental conditions. However, as explained previously, even if environment is the most impacting criterion, several other parameters must be taken into account.

Furthermore, the pH of the environment depends on the pressure of H_2S as presented in Figure 40:

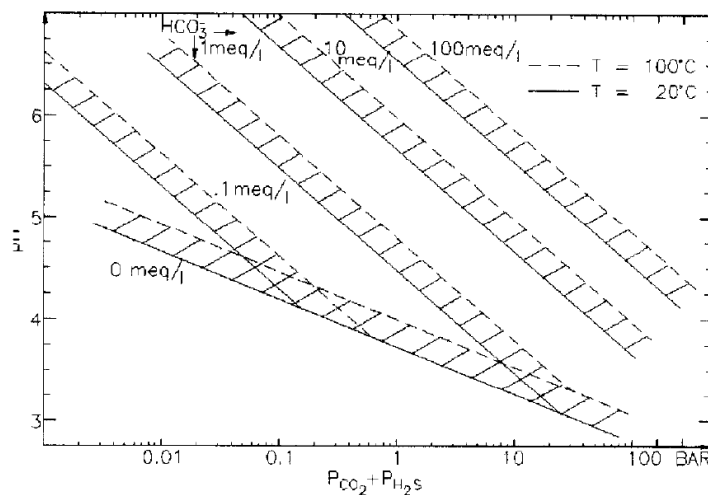


Figure 40 - Influence of the pressure of H_2S on the pH [67]

3. Summary and objectives

The literature review presented above emphasizes the complexity of microstructures of quenched and tempered supermartensitic stainless steels. These microstructures are multiphase ones and their main components are tempered martensite (α'') and retained austenite (γ_R). The morphology is that of lath martensite, with γ_R situated at α'' interlath positions and at former austenitic grain boundaries. Such type of microstructure yields mechanical properties which fit with the requirements of NACE standards for Oil&Gas applications. Nevertheless, rare cases of failure in service were observed in past years [104] and the mechanisms involved in material damage are not always fully understood. It is certain, however, that crack initiation and propagation in hydrogenating 'Oil&Gas' environments are closely related to the microstructural features of alloys. Both principal phases of SMSS, α'' and γ_R , are characterized by a radically different behavior with respect to hydrogen (solubility, mobility ...). Moreover, phase transformations under mechanical loading (SIMT) cannot be excluded, in particular in regions with high stress concentration, including the crack tip. This may affect the hydrogen distribution within the microstructure and influence the sensitivity of the steel to environmentally-assisted cracking.

As seen all along this Chapter and per analogy with Duplex Stainless Steels (DSS), especially concerning their dual phase microstructure and their applications, the first approach to cracking mechanisms can be similar for SMSS and DSS. Within the literature concerning the use of DSS in the Oil&Gas industry, it can be found that several cracking mechanisms can be involved in acid environments such as Stress Corrosion Cracking (SCC), Hydrogen Embrittlement (HE) or Sulfide Stress Cracking (SSC) for examples. The third Chapter of this work will thus be focused on the study of two mechanisms (SCC and HE) in acid environments. To do so, Slow Strain Rate Tensile tests (SSRT) are used under the application of specific potentials determined by the electrochemical study of our alloy Virgo™38.

As previously mentioned, one of the particularity of Oil&Gas media is the presence of H_2S which provides a very high hydrogen activity that can lead to embrittlement following local or general depassivation. This very high hydrogen activity can be reproduced by poisoned solutions such as the one used in the fourth Chapter of this study. This Chapter is also devoted to the study of the influence of the microstructural elements such as retained austenite content and precipitation on the resistance to Hydrogen Embrittlement.

However, the results of tests presented in Chapters III and IV did not enable identifying crack initiation mechanisms that occurred in service conditions. The fifth Chapter of this thesis is focused on the study of our alloy in presence of H_2S in order to get closer to the industrial environments. In this Chapter, we will compare the failures obtained with the mechanisms previously identified (Chapter III and IV) and conclude on the most impacting parameters on the sensibility to environmentally assisted cracking. The role of pitting corrosion, which appears as the preferential crack initiation mechanism, will also be discussed.

Chapter II:
Metallurgy and mechanical behavior of Virgo™38

Chapter II: Metallurgy and mechanical behavior of Virgo™38	57
1. Metallurgy of Virgo™38.....	61
1.1. Composition and metallurgy of the industrial alloy	61
1.2. Influence of heat treatments on the microstructure.....	67
1.2.1. Microstructure of re-austenitized samples and influence of the sub-zero treatment after oil-quenching	67
1.2.2. Influence of tempering on the retained austenite content.....	70
1.2.2.1. Influence of the tempering temperature	70
1.2.2.2. Influence of the tempering holding time at 620°C.....	75
1.2.2.3. Influence of the second tempering treatment.....	75
1.2.3. Influence of tempering on carbide precipitation	77
2. Mechanical behavior of Virgo™38.....	81
2.1. Influence of the direction of sampling in industrially forged material	81
2.2. Mechanical behavior as a function of heat treatment applied	82
2.2.1. Tensile properties of Virgo™38 in different microstructural states	82
2.2.2. Impact toughness of Virgo™38 in different microstructural states	84
2.2.3. Relationships between microstructure and the 0.01% yield stress in Virgo™38.....	85
2.3. Mechanical stability of retained austenite after industrial heat treatment.....	91
2.4. Summary	97

This Chapter is devoted to the study of Virgo™38 microstructures obtained in different tempering condition (T, t). The analysis includes the precipitation of carbides which is not frequently taken into account in low carbon SMSS. The results of tensile tests in air are then used to interpret the observed variations of the yield stress and to identify the corresponding strengthening mechanisms. Finally, the behavior of Virgo™38 with respect to stress induced martensitic transformation (SIMT) is investigated. All the analyses are performed starting from and as received alloy (named industrial Virgo™38) re-austenitized quenched and sub-zero heat treated.

1. Metallurgy of Virgo™38

1.1. Composition and metallurgy of the industrial alloy

Virgo™38, a 16Cr-4Ni low-carbon supermartensitic stainless steel (Table 7), is a nominally precipitation-free alloy belonging to the GE Oil&Gas portfolio. As previously mentioned, it is used for the construction of centrifugal compressor impellers working in sour environments rich in CO₂ and H₂S. To be safely used in accordance with previously mentioned requirements of the NACE standard MR0175 [3] and internal BHGE standards, this alloy has to satisfy strict conditions in terms of fracture toughness (HRC<28) associated with a minimal proof stress of 620MPa. As for other SMSS, these requirements can be fulfilled in Virgo™38 through microstructure design under strictly controlled conditions, aiming to obtain a two phase structure composed of tempered martensite α'' and retained austenite γ_R in sufficiently high volume fraction and located between martensite laths. This type of microstructure is obtained by sub-zero quenching and double tempering as mentioned in Chapter I, the tempering parameters (temperature and time) being decisive.

Table 7 - Chemical composition (wt %) and mechanical properties of Virgo™38 after quenching and double tempering

%C	%Cr	%Ni	%Mn	%Si	%Cu	%Mo	%P	YS (MPa)	UTS (MPa)	HRC
0.035	15.2	4.63	0.64	0.34	0.10	0.07	0.018	>620	>780	<28

Optimal tempering parameters are very sensitive to the chemical composition and they must be individually adjusted for each grade. That is why, in this chapter, we will study the influence of the heat treatment parameters on the final microstructure of Virgo™38. In addition to that, the stability of the microstructure obtained through optimized tempering may be affected by the presence of stresses of any origin. The transformation of retained austenite to fresh martensite (Stress Induced Martensitic transformation or SIMT) may affect the material resistance with respect to environmentally induced damage. Indeed, the optimized tempering produces retained austenite with a M_s point close to room temperature, what makes it particularly sensitive to stress induced martensitic transformation (SIMT). While SIMT was extensively described in single phase austenitic steels [105] and, more recently, in duplex stainless steels [106], only very little information concerning the stability of retained austenite in SMSS is available [43]. This phenomenon may potentially play a decisive role in environmentally assisted damage of SMSS. Indeed, even if the optimized microstructure has a required level of fracture toughness it may be seriously altered through transformation of retained austenite to fresh martensite. The fact that SIMT is very likely to occur at the tip of cracks initiated in critical regions of components concerned is thus particularly dangerous with respect to the material integrity.

After austenitization ($T > 1000^\circ\text{C}$), the alloy is quenched in oil to room temperature. To ensure that no residual austenite remains after quenching, a sub-zero treatment is applied. The first tempering is carried out slightly above the A_{c1} temperature in order to form the targeted fraction of reverted austenite, expected to remain stable after cooling to room temperature. The role of second tempering, applied according to NACE guidelines at a slightly lower temperature than the first one, is to transform small fractions of fresh martensite which risk to be formed during cooling after first tempering if its parameters are not perfectly controlled. Indeed, presence of fresh martensite in the final microstructure should be avoided in order to guarantee the required retained austenite fraction of at least 20%, responsible for the required fracture toughness.

Prior to observations, samples were grounded using SiC papers up to P4000 (2min for each paper) and electrolytically polished using a 6% solution of perchloric acid in ethanol at a tension of 25V during 90s.

Figure 41 shows the optical micrograph of Virgo™38 in as-received (sub-zero quenched and double tempered) state. In the following, this state provided by BHGE will be called "industrial state". It reveals prior austenitic grains of 20-30 μm average diameter with a lath structure typical for martensitic microstructures and elongated grains of δ -ferrite with a volume fraction of <5%.

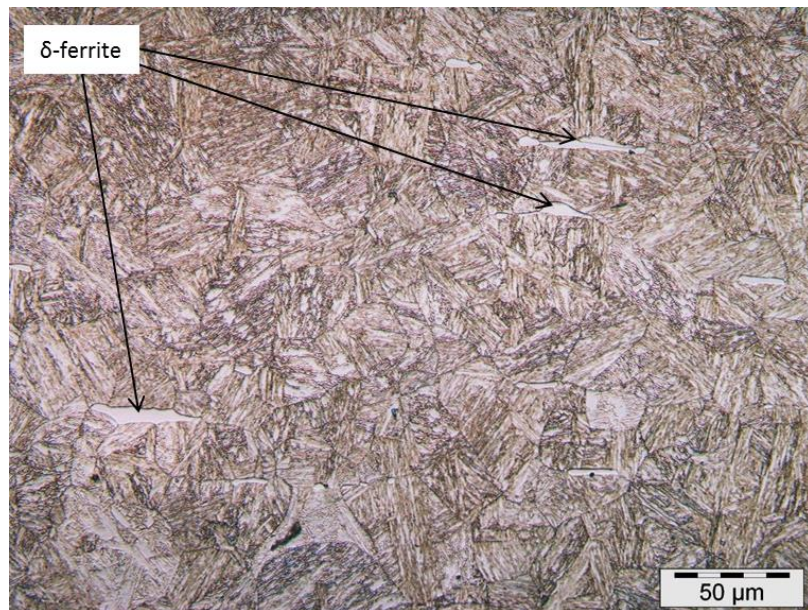


Figure 41 - Optical micrograph of Virgo™38 (sub-zero quenched and double tempered state) after electro-polishing and Vilella's etching: lath structure inside prior austenitic grains and δ -ferrite (<5%)

The XRD analysis (Figure 42) reveals the presence of approximately 22% of retained austenite γ_r within the structure of the steel. TEM observations show (Figure 43) that γ_r is formed between primary martensite laths. The width of austenite laths does not exceed 200nm. The surface area of austenite measured on the TEM micrograph of Figure 43-a is of $25 \pm 2\%$, compatible with XRD estimations. The XRD diffractogram of Figure 42 clearly indicates that the martensite formed in Virgo™38 is cubic bcc. This observation matches literature data according to which no tetragonal distortion is likely to be observed for carbon contents lower than 0.2 wt% [15].

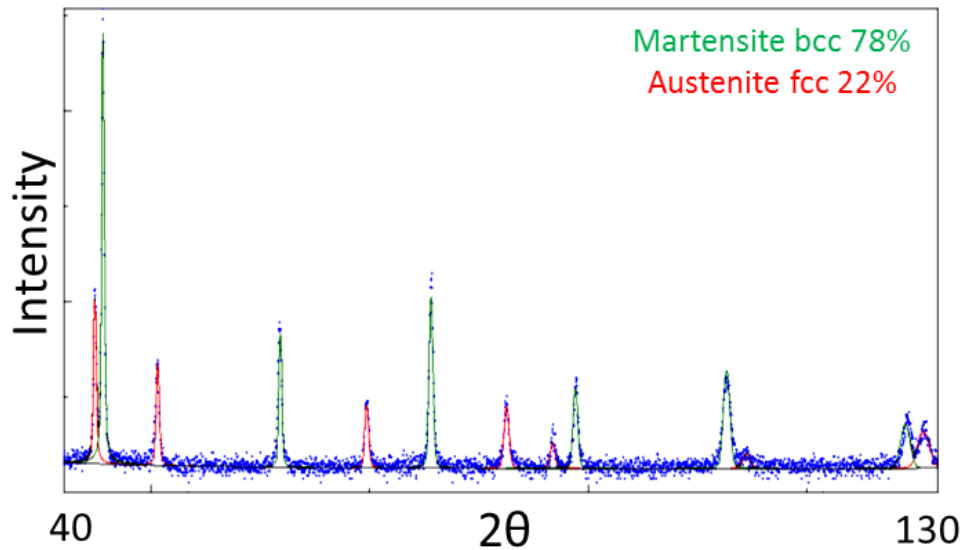


Figure 42 - Phase composition (XRD) of Virgo™38 after industrial heat treatment showing BCC martensite (78%) and FCC retained austenite (22%)

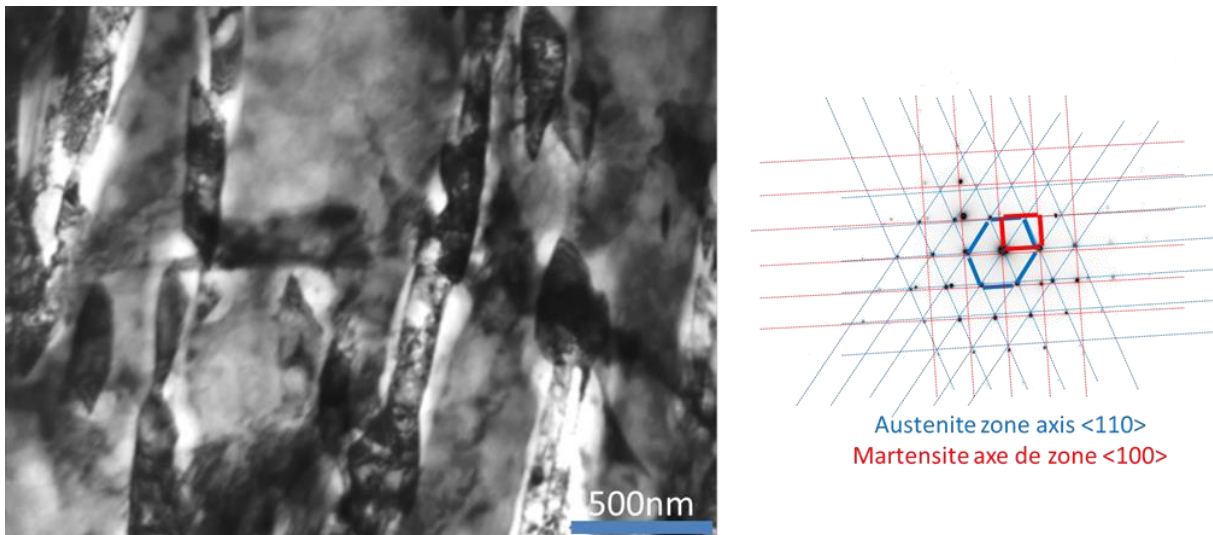


Figure 43 - TEM micrograph of Virgo™38 (industrial state): the retained austenite appears as dark laths situated between clear martensite ones and relation of orientation

As shown in Figure 43-b the martensite laths and retained austenite grains have been identified to be oriented following the Nishiyama-Wasserman relation.

The EBSD phase map of Figure 44 shows the retained austenite distribution at the micrometric scale. The alignment of FCC regions clearly follows the orientation of laths, as well as this of prior austenite grain boundaries. However, a strong difference of the size of FCC regions is observed, some of austenite grains being much larger than laths visible at the TEM micrograph of Figure 43.

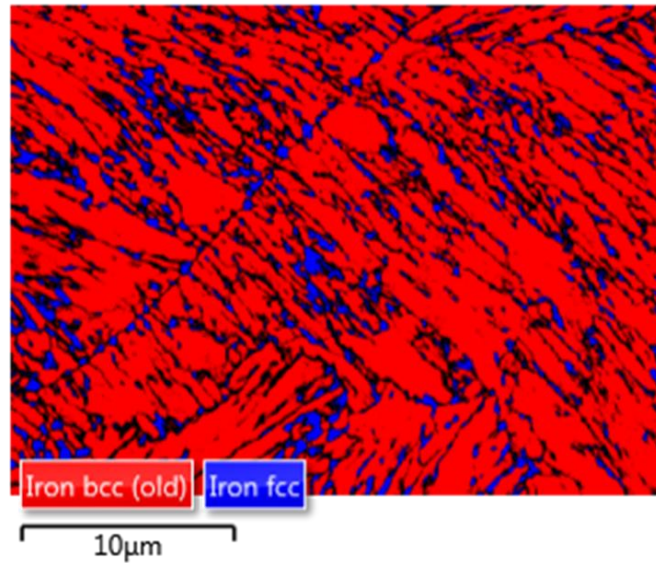


Figure 44 - EBSD map of industrial Virgo™38 (quenched, sub-zero treated and double tempered microstructure): retained austenite distribution

The formation of retained austenite occurs during tempering and is associated with a significant migration of atomic species between the principal phases, BCC and FCC. The most significant is Ni partitioning, followed by that, much weaker, of Mn (Figure 45). This process leads to a significant enrichment of Ni and Mn in the austenite, with direct consequences on its stability at room temperature (see next section). Indeed, according to the M_s formula used for this family of steels:

$$M_s(^{\circ}\text{C}) = 540 - 497C - 6.3\text{Mn} - 36.3\text{Ni} - 10.8\text{Cr} - 46.6\text{Mo}$$

the increase of Ni content in FCC up to 9-10% shifts M_s to room temperature and prevents fresh martensite formation during cooling after tempering, which is one of the goals of the optimized treatment of the alloy.

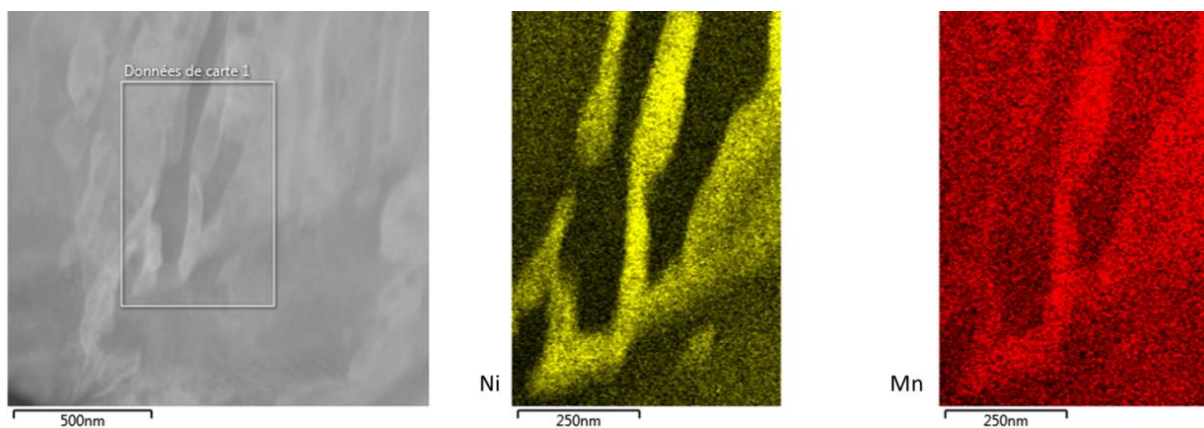


Figure 45 - TEM image and EDX maps showing qualitative Ni and Mn partitioning effect between austenite (bright phase on the TEM image on the left) and martensite (dark phase on the TEM image). EDX maps indicate enrichment of austenite in Ni and Mn.

The quantification of Cr, Ni and Mn contents by TEM-EDX gives an average content of 10.33%Ni, 1.24%Mn and 13.33%Cr in retained austenite and 1.84%Ni, 0%Mn and 14.88%Cr in tempered martensite.

Furthermore, TEM-EDX maps clearly show Cr-rich precipitation which occurs close to prior austenite boundaries and within martensite as shown on Figure 46 and Figure 47. The precipitate size does not exceed 20nm in diameter and globally their distribution in the microstructure is not homogeneous, most of interfaces being totally precipitate-free. We note that Cr-rich regions associated with carbides present slightly higher Mn concentrations. Because of their distribution, mainly within prior austenite grain boundaries, these carbides are not supposed to have a significant effect on the elastic limit.

The optimized microstructure of Virgo™38 appears therefore as a morphologically complex one, composed of two major phases:

- tempered martensite α'' , containing 15%Cr and 2%Ni, with a volume fraction of around 75%
- retained austenite γ_r , containing 13%Cr and 11%Ni, with a volume fraction of around 25%

and

- δ -ferrite (<5%)
- mixed (Cr, Mn) carbides ($M_{23}C_6$, according to [41]) (<1%)

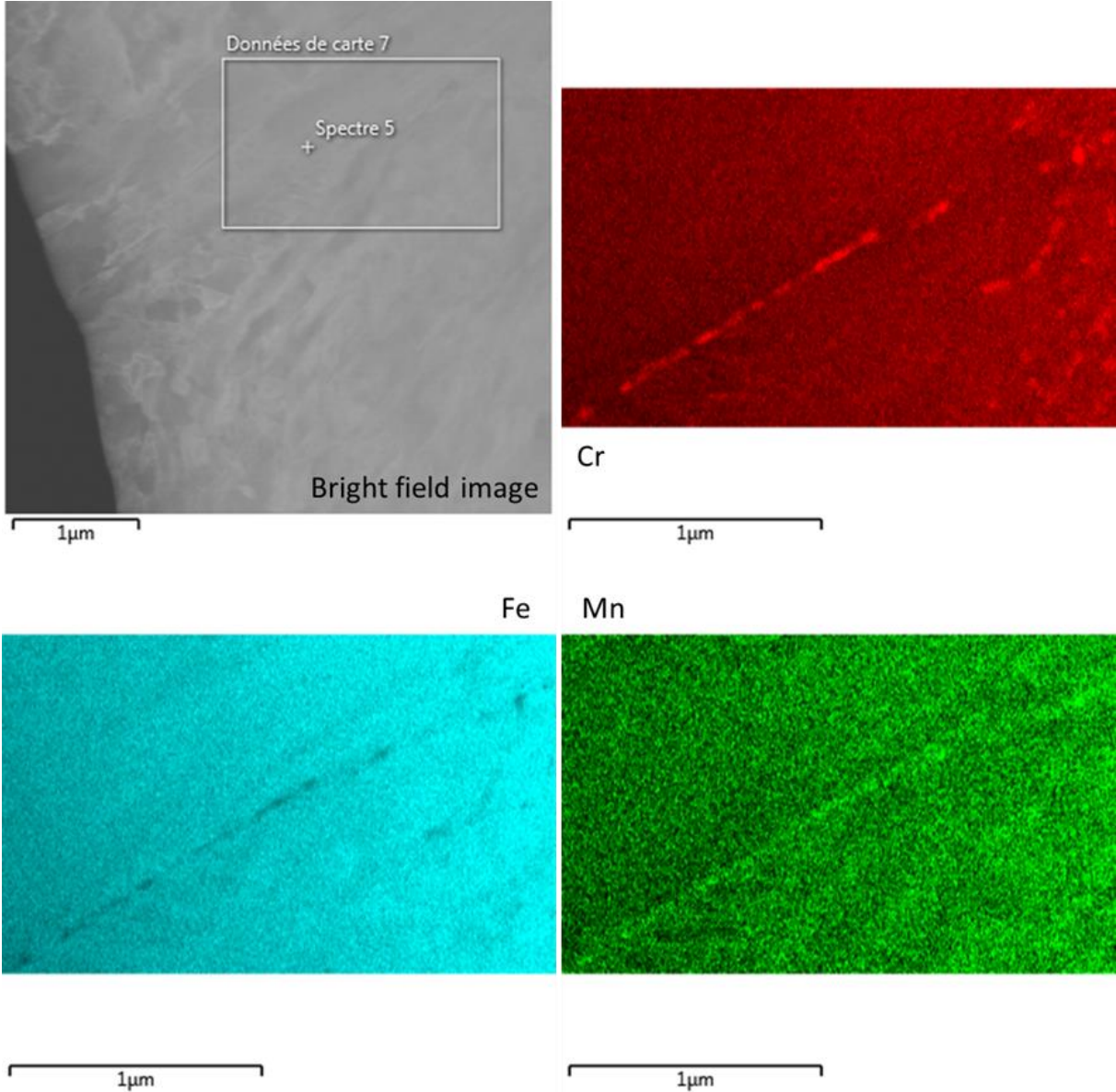


Figure 46 - TEM image and EDX maps showing Cr-rich precipitation close to former austenitic grain boundary in industrially heat treated Virgo™38

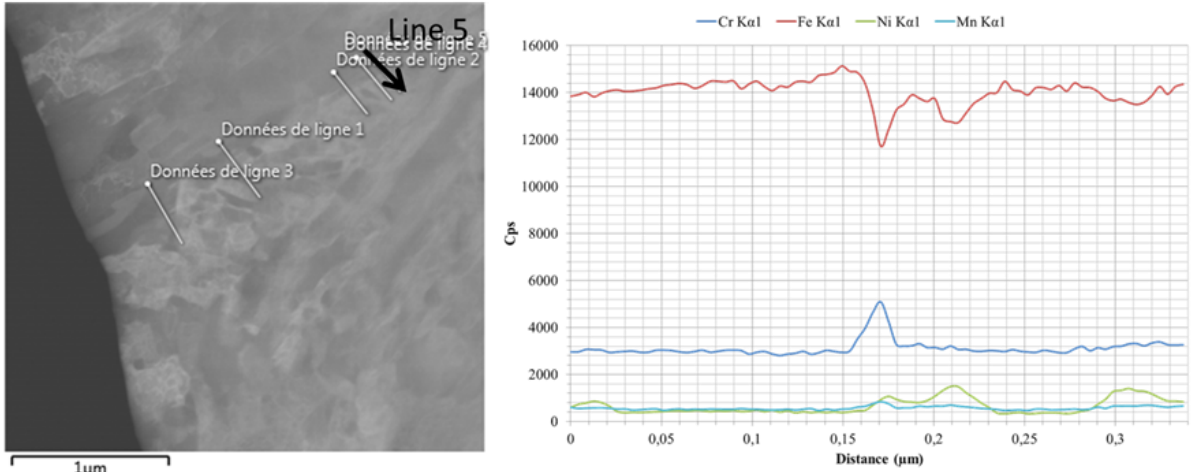


Figure 47 - EDX line-scan across the grain boundary presented in Figure 46 showing Fe, Cr, Ni and Mn profiles: carbide precipitation inside austenitic grain boundary and Ni enrichment in retained austenite

1.2. Influence of heat treatments on the microstructure

1.2.1. Microstructure of re-austenitized samples and influence of the sub-zero treatment after oil-quenching

In order to investigate the effect of heat treatment on the microstructure, samples of as-received alloy were re-austenitized at 1020°C during 15min and then oil quenched to room temperature. The resulting microstructure is presented in Figure 48. Even if the presence of potential residual austenite (indexed at 0.03%) cannot be totally excluded, the FCC phase is not detected through XRD measurements (Figure 49). Its volume fraction is thus certainly below 2%.

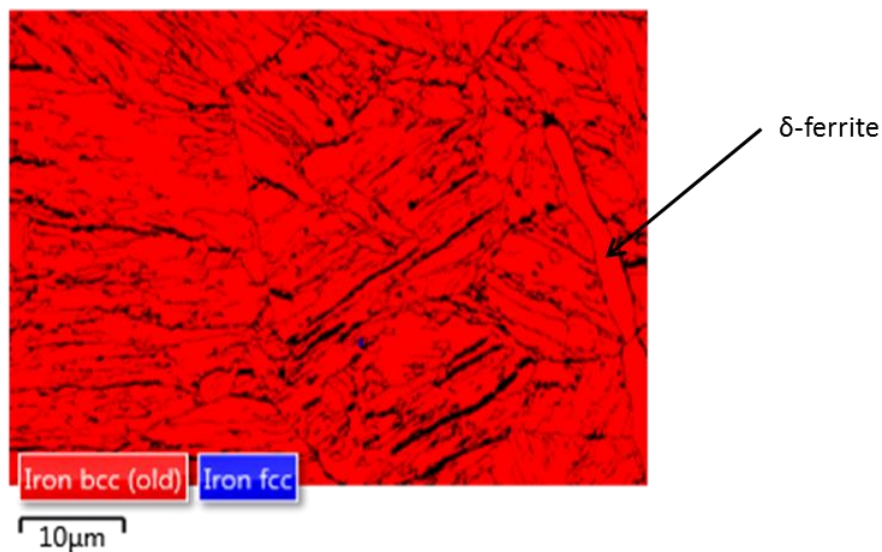


Figure 48 - EBSD phases map of re-austenitized and oil quenched sample showing martensite lathes, δ -ferrite and potentially residual austenite. Non-indexed areas (large dark areas) can potentially be attributed to the presence of another phase (FCC?)

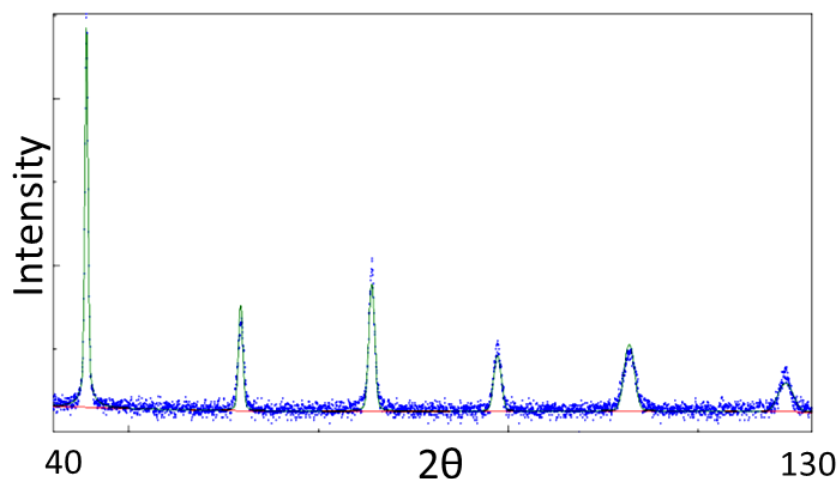


Figure 49 - X-Ray diffractogram obtained from a re-austenitized and oil-quenched sample showing the presence of a single BCC phase

In order to ensure a full transformation of residual austenite into martensite and to go closer to industrial heat treatment other samples were sub-zero treated after oil-quenching. The resulting microstructure is presented in Figure 50. EBSD analysis does not reveal any FCC phase and this result

is supported by XRD measurements presented in Figure 51. It can thus be concluded that residual austenite fraction is below 2%, the detection limit of the technique.

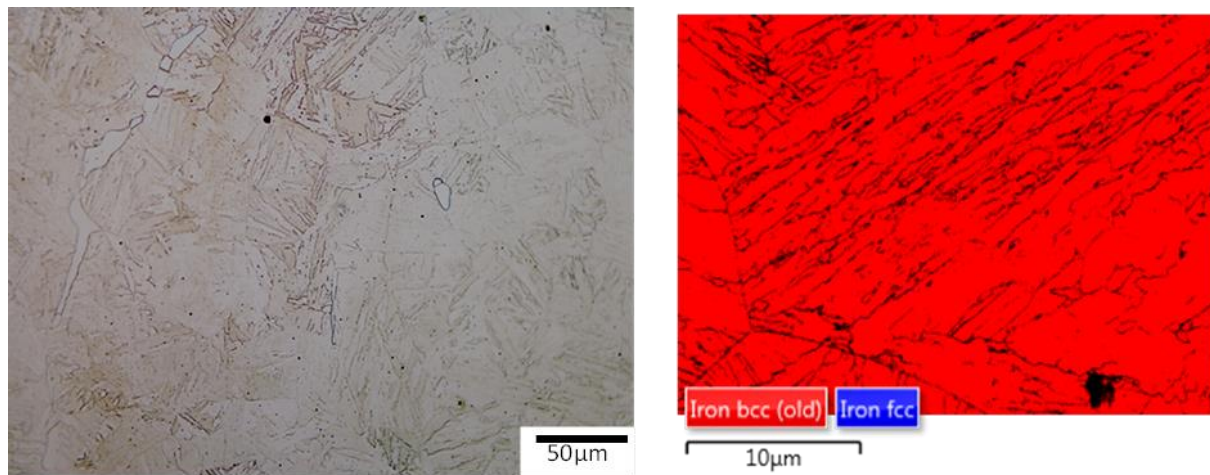


Figure 50 - Optical microscopy (Villela's etching) and EBSD phase map of re-austenitized, oil quenched and sub-zero treated microstructure

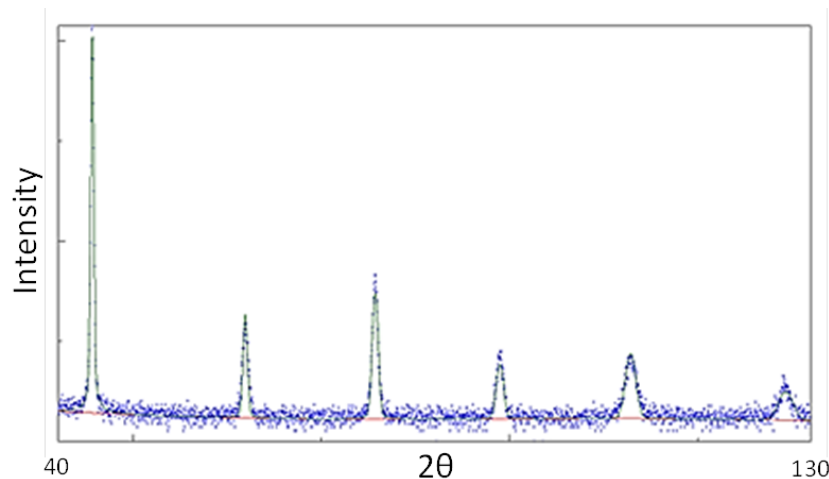


Figure 51 - X-Ray diffractogram obtained from a re-austenitized, oil-quenched and sub-zero treated sample showing the presence of a single BCC phase

For the following part of the work the sub-zero treatment will thus systematically be applied after quenching in order to complete the martensitic transformation and limit the presence of residual austenite, especially close to former austenitic grain boundaries. Indeed, as seen in Figure 52, one can see the presence of a thin layer - potentially a residual austenite close to a (former?) austenitic grain boundary which remains non transformed after quenching. However, because of the magnetism of the material, observations were difficult to perform even when tilting the sample and consequently EDX profiles could not be collected.

This thin layer, imagined as residual austenite, could be due to silicon segregation during quenching [107]. Although the grain boundary enrichment factor of Si in austenite does not exceed 20 [107], Si may have a significant effect on local M_s temperature ($-7.5Si$ to $-14.5Si$, according to different sources), in particular when it is combined with Ni enrichment of boundaries. A local decrease of M_s of a few tenths K is thus potentially possible, making impossible a full transformation of thin zones around austenitic grain boundaries. We will investigate, in the following chapters, the consequences of this effect on the material behavior in corrosive environments. If however, the

austenite surrounding grain boundaries (and the boundaries themselves) remained non transformed, its volume fraction would be of approximately 0.05vol% (for the grain diameter of 20 μ m), thus very difficult to detect.

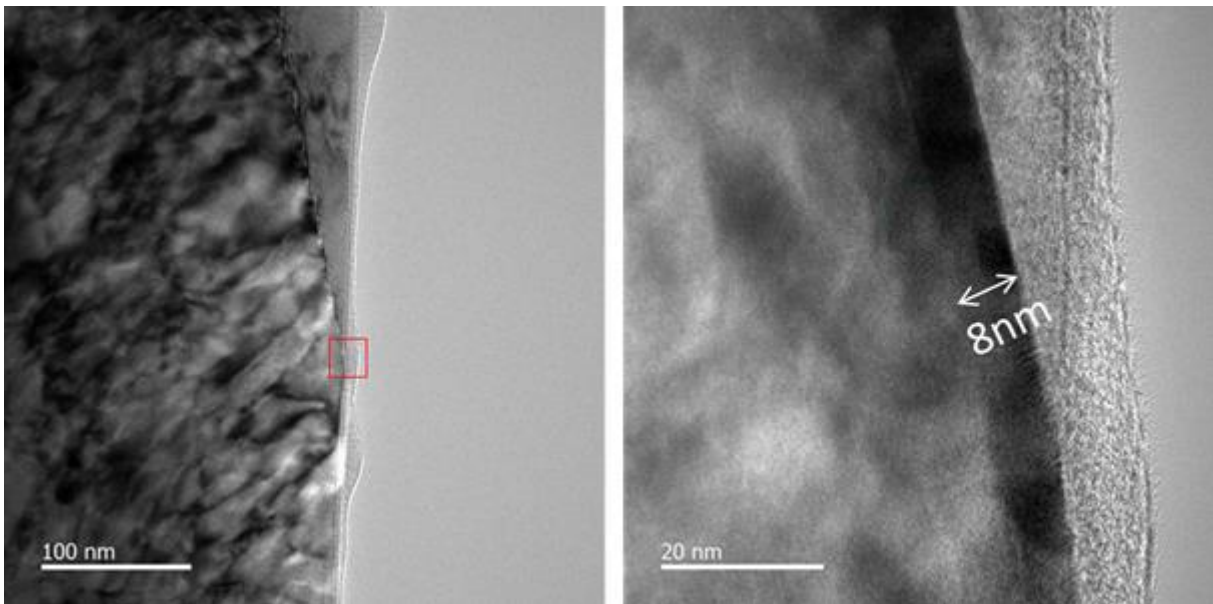


Figure 52 - TEM bright field image of the quenched sample showing a potential second phase of less than 10nm thick close to the former austenitic grain boundary

Prior to tempering, the temperatures of phase transitions were estimated by dilatometry on a re-austenitized, oil-quenched and sub-zero treated industrial specimen. Dilatometric test was carried out between room temperature and 1020°C at a heating rate of 10°C/min. After maintaining during 15min at 1020°C, the sample was cooled down to room temperature at a cooling rate of 5°C/min (Figure 53).

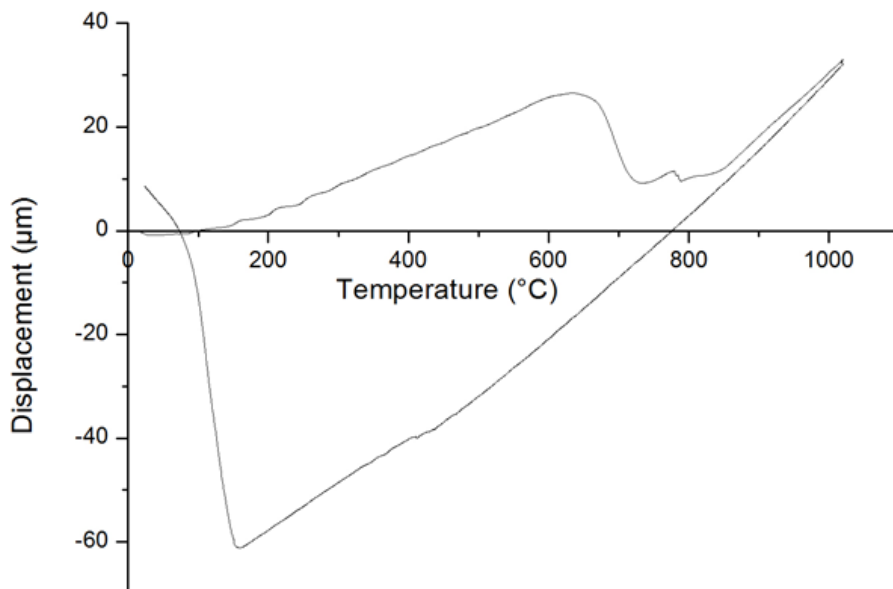


Figure 53 - Dilatometric measurements on Virgo™38 after re-austenitization at high temperature, oil-quenching and sub-zero treatment

According to Figure 53, the heating peak appears at approximately 620°C, however a slope change can already be observed slightly below 600°C. A_{c1} could thus be estimated close to 600°C,

while M_s is situated at approximately 165°C. Since the test had been stopped at room temperature, it was not possible to obtain a precise value of M_f , the latter one being evidently lower than 20°C. We note that estimated A_{c1} and M_s temperatures are in accordance with the values given by the empirical formulas below:

$$A_{c1} (\text{°C}) = 850 - 1500(C+N) - 50Ni - 25Mn + 25Si + 25Mo + 20(Cr-10) \approx 620\text{°C}$$

$$M_s (\text{°C}) = 540 - 497C - 6.3Mn - 36.3Ni - 10.8Cr - 46.6Mo \approx 175\text{°C}$$

In the following sections, the terms of “quenched samples” and “quenched state” will be used to design samples in the re-austenitized oil-quenched and sub-zero treated state.

1.2.2. Influence of tempering on the retained austenite content

1.2.2.1. Influence of the tempering temperature

Starting with a purely martensitic structure after austenitization, oil-quenching and sub-zero treatment, tempering treatments at temperatures between 580°C and 660°C during 2 hours followed by air cooling were carried out. This temperature range was defined according to the results of dilatometric tests. The objective was to obtain microstructures with different volume fractions of retained austenite. The retained austenite fractions were measured by X-ray diffraction (XRD) using a Panalytical X'Pert diffractometer. The volume fractions of martensite and austenite were then determined by the Rietveld method [108] [109] using the free software MAUD. This technique does not require external calibration and gives accurate austenite content provided its volume fraction exceeds 2 volume percent. This technique can be used because the tested samples have no preferential texture as determined by XRD. However, the retained austenite content is underestimated with such technique. A strict procedure of metallographic preparation (as described in the next section and in appendix 1) was applied to avoid stress induced martensitic transformation (SIMT) at the sample surface during polishing. The reverted austenite fractions (i.e. the amount of austenite at different tempering temperatures, at the end of temperature 'plateau' of two hours) were also measured through in situ XRD measurements inside a HTK16 furnace. Furthermore, ThermoCalc® calculations were performed in order to predict the chemical composition of reverted austenite formed at different temperatures.

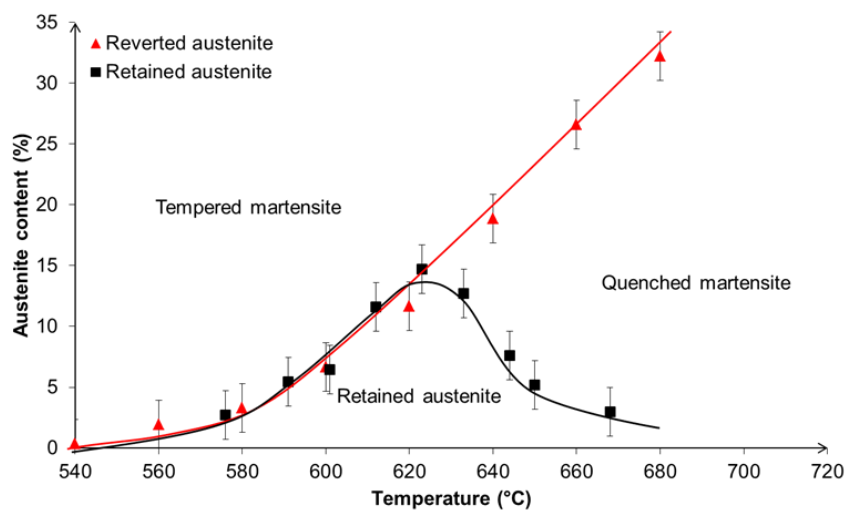


Figure 54 - Reverted and retained austenite fractions as a function of tempering temperature. Reverted austenite fraction constantly increased while retained austenite fraction presents a peak at around 620°C.

In situ XRD measurements at the end of 2h tempering period presented in Figure 54 indicate that reverted austenite (γ_{rev}) volume fraction progressively increases from approximately 2% at 560°C to 32% at 660°C. The effective Ac_1 point should thus be situated between 540 and 560°C. Up to tempering temperature of 620°C, the reverted austenite formed remains stable after subsequent cooling to room temperature (Figure 54) and the resulting microstructure after cooling is composed of tempered martensite α'' and retained austenite γ_R , the corresponding volume fractions being obviously dependent on tempering temperature.

During tempering, nickel tends to accumulate in austenite grains so that its average concentration within this phase increases. However, this effect depends on volume fraction of reverted austenite, i.e. on the tempering temperature. In fact with high volume fractions of reverted austenite, its enrichment in nickel is less important. Since the stability of reverted austenite depends on its average Ni content, the final amount of retained austenite is indirectly function of tempering temperature. For this reason, a maximum of retained austenite fraction is supposed to be observed for an intermediate tempering temperature depending on the composition of the steel [110] and was clearly confirmed in Figure 54. This partitioning effect of alloying elements was clearly demonstrated in industrial samples (see Figure 45).

According to the Marshall's formula below (and to any other empiric M_s estimations), the increase of Ni content in γ lowers M_s and hence stabilizes austenite at lower temperatures.

$$M_s (^{\circ}C) = 540 - 497C - 6.3Mn - 36.3Ni - 10.8Cr - 46.6Mo$$

Therefore, the maximal retained austenite content is reached when M_s of the reverted austenite is close to room temperature. This obviously depends on Ni content in γ_{rev} i.e. on the tempering temperature. This effect accounts for the presence of the tempering temperature peak at which a maximal retained austenite fraction is present in the microstructure after cooling to room temperature.

The equilibrium composition of the reverted austenite was simulated for different tempering temperatures using the ThermoCalc® software. The results concerning Cr and Ni contents in α'' and γ_{rev} are shown in Figure 55. One can see that the values obtained after quantitative EDX analysis on Figure 45 and Figure 47 are in accordance with the ones obtained from the ThermoCalc® simulations of Figure 55 after a tempering treatment at 620°C, close to the temperature of the first tempering applied industrially.

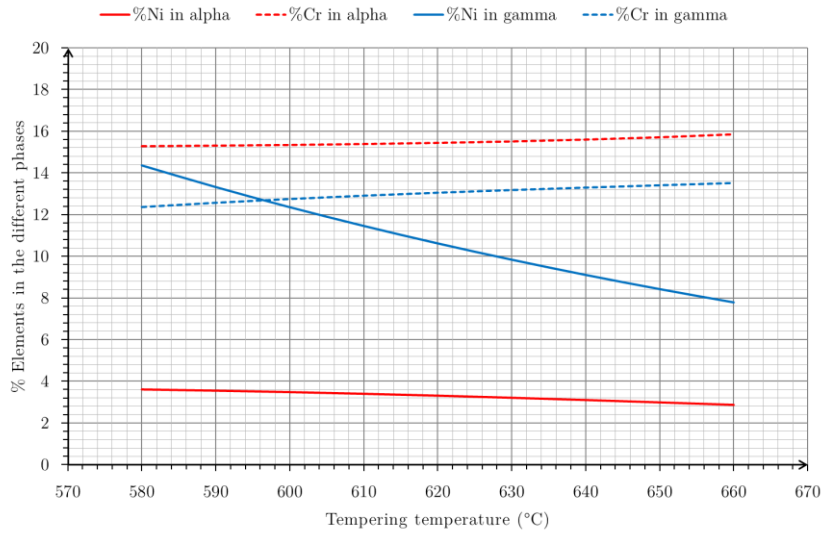


Figure 55 - ThermoCalc® simulation of equilibrium compositions of tempered martensite and reverted austenite in Virgo™38, versus tempering temperature

This change of composition as a function of tempering temperature obviously leads to the increase of M_s temperature as illustrated in Figure 56. More precisely, the predicted M_s becomes equal to room temperature for tempering temperature of 618°C which is perfectly compatible with experimental data of Figure 54.

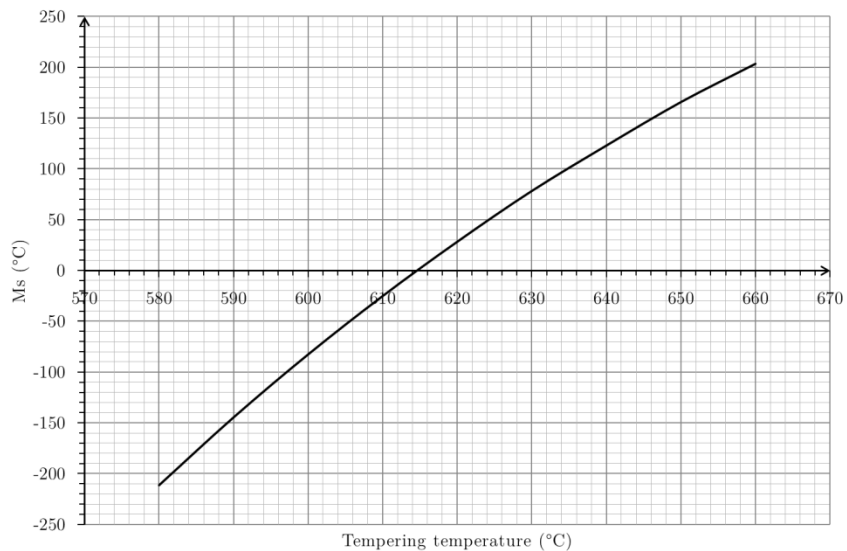


Figure 56 - M_s temperature in reverted austenite as a function of tempering temperature for equilibrium compositions calculated by ThermoCalc® and given in Figure 55

It should be emphasized that the retained austenite obtained after tempering close to the peak temperature is likely to be strongly unstable with respect to SIMT, with potential consequences on mechanical properties of the material (see next sections).

For tempering temperatures above 620°C (when M_s of the reverted austenite becomes higher than room temperature), a part of reverted austenite, increasing with T , transforms back into martensite on cooling so that the final microstructure contains in fact three phases with different compositions and properties: tempered martensite α'' , retained austenite γ_r and secondary fresh martensite α'_f .

Because of the expected negative impact of fresh martensite on fracture toughness, the temperature of first tempering should thus not exceed 620°C. For a 2h single tempering treatment, the maximal volume fraction of retained austenite (stable at room temperature) is of 14.7% according to Figure 54.

The different microstructures obtained after the first tempering treatment of 2 hours are presented on EBSD maps of Figure 57. Tempering at 580°C produces limited amount of retained austenite (3.5% γ_r), mainly at former austenite grain boundaries. At the peak temperature of 620°C (14.7% γ_r), retained austenite distribution is rather homogenous across the microstructure and the EBSD map of Figure 57-c coincides with TEM observations of Figure 43. Finally, only small isolated FCC regions persist after tempering at higher temperatures. The retained austenite seems to be destabilized first close to the former austenitic grain boundaries (where they were formed originally) which, once again, could indicate potential composition heterogeneities in this area (Si segregation for example). Indeed, after tempering at 640°C during 2 hours (Figure 57-d), the retained austenite is only located between the martensitic lathes while it is not explicitly detected at the grain boundaries.

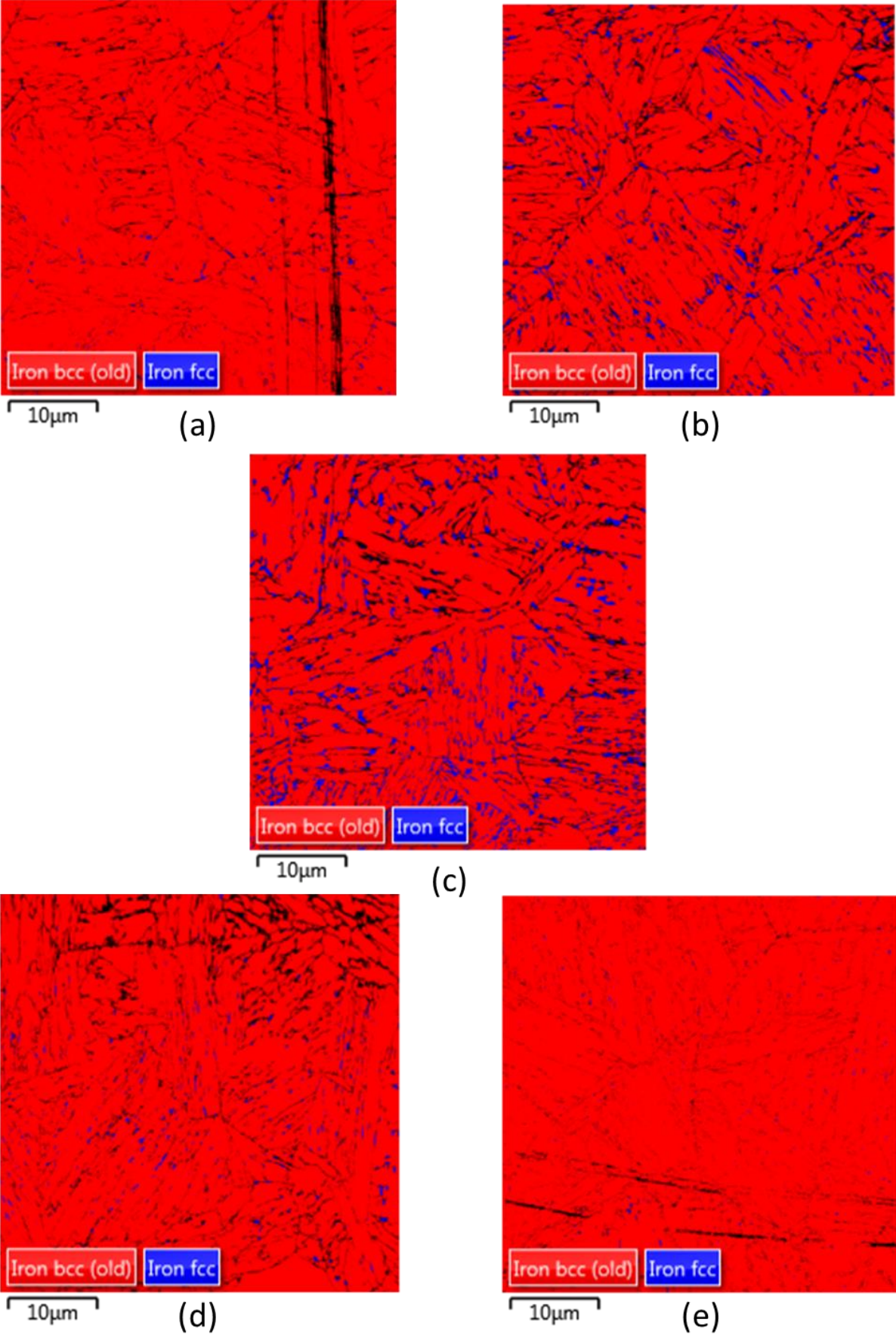


Figure 57 - EBSD maps of samples QT580-2h (a), QT600-2h (b), QT620-2h (c), QT640-2h (d) and QT660-2h (e) showing retained austenite distribution

1.2.2.2. Influence of the tempering holding time at 620°C

We have seen previously that the maximal retained austenite fraction was obtained by tempering at a temperature of 620°C during 2 hours. However, for a holding time of 2 hours, “only” 14.7% of retained austenite was obtained while the industrial treatment produces between 20% and 30%, considered necessary to guarantee the required fracture toughness.

The results of XRD analyses showing the retained austenite contents after tempering treatments at 620°C during up to 48 hours are presented in Figure 58.

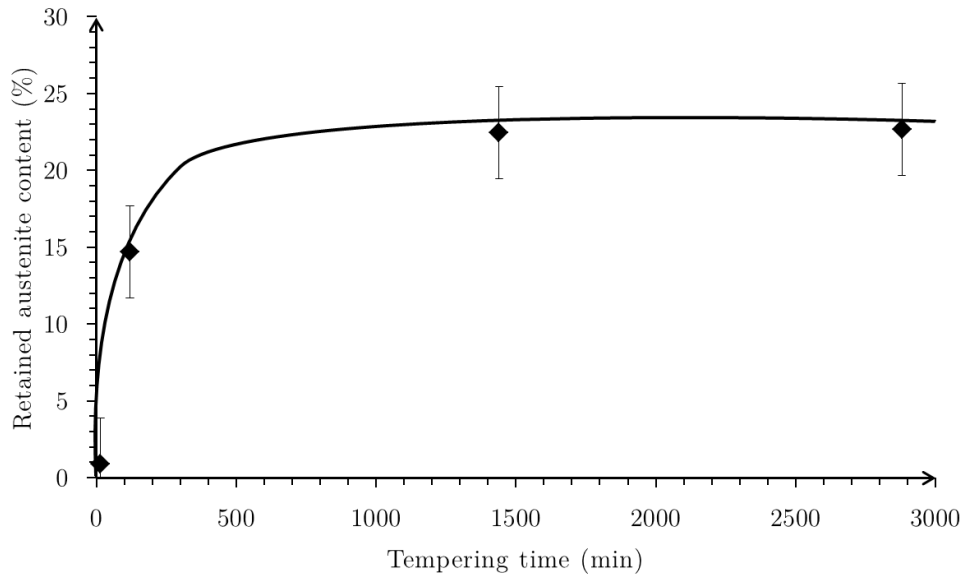


Figure 58 - Evolution of the retained austenite fraction measured by XRD after air cooling as a function of tempering holding time for a tempering temperature of 620°C

As visible in Figure 58, the tempering time of 2 hours is not long enough to produce the equilibrium amount of austenite at 620°C. That means that the retained austenite contents presented in Figure 54 are systematically lower compared to the ones obtained industrially (where durations are calibrated in order to obtain saturation of retained austenite).

1.2.2.3. Influence of the second tempering treatment

The NACE standards [3] impose the use of SMSS in quenched and double tempered state. However, as explained previously, the second tempering treatment is not supposed to have any influence on the retained austenite content if the first one is performed up to saturation at the retained austenite peak. To check this postulate, we performed a second tempering treatment at 600°C during 2h and 48h on two samples after the first tempering at 620°C during 2h and 48h respectively.

If the retained austenite content is not equal to the saturated one (for example after 2h at 620°C where we get 14.7% of retained austenite), the second tempering treatment at 600°C during 2h enables increasing the retained austenite content. However, if the first tempering is performed up to saturation (for example after 48h at 620°C where we get around 23% of retained austenite), the second one at 600°C during 48h does not influence the retained austenite content.

One can see on EBSD maps of Figure 59 that the difference of retained austenite content between double tempering during 2h+2h and 48h+48h is a result of a more pronounced growth of austenite in interlath position (equivalent diameters of 171nm and 228nm respectively). Moreover, the 48h+48h double annealing leads to a significant growth of some austenitic regions which become larger than a few μm and so clearly above the width of initial martensite laths. According to literature review [43], the second tempering treatment is also supposed to increase the resistance to SIMT in SMSS. It also enables a more efficient tempering of the martensite.

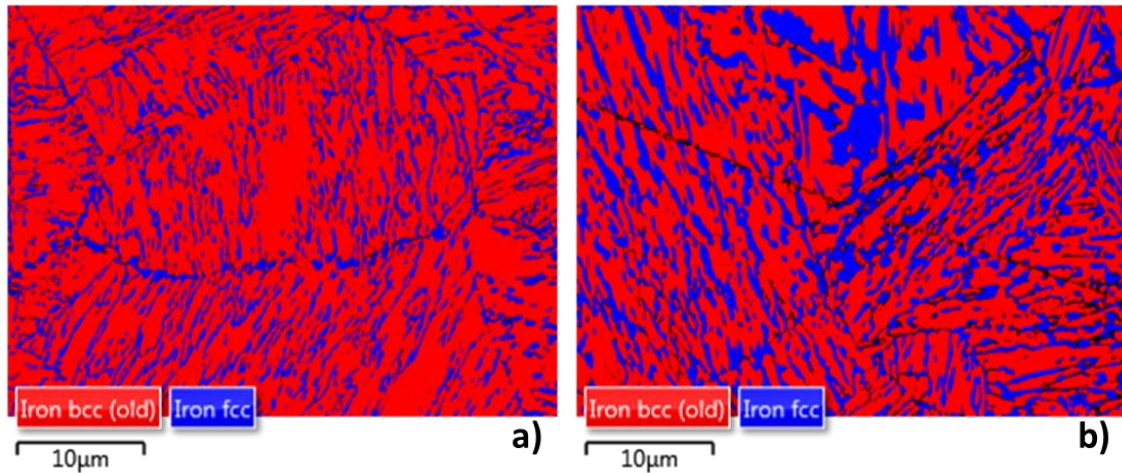


Figure 59 - Evolution of the retained austenite grain size after double tempering at 620°C and 600°C during 2h+2h and 48h+48h

As determined by XRD, applying a second tempering treatment at 600°C during 2h after a first one at 620°C during 2h enables increasing the retained austenite content from 14.7% to 16%. We can thus see that, in the case of non-saturation after the first tempering treatment, the second tempering treatment enables forming more retained austenite. Furthermore, performing a second tempering treatment at 600°C during 48h after a first treatment at 620°C during 48h does not change the retained austenite content (23% in each case) as the saturation in retained austenite was already achieved.

One can conclude that, if the first tempering treatment is performed at the peak temperature and long enough to produce equilibrium microstructure, the second treatment is not necessary, at least from the point of view of the retained austenite content. We have also seen that width of retained austenite laths increased during tempering, which can indicate that Ni diffusion limits the formation of austenite in first steps. The formation of retained austenite and the supposed composition profile can be summarized in Figure 60.

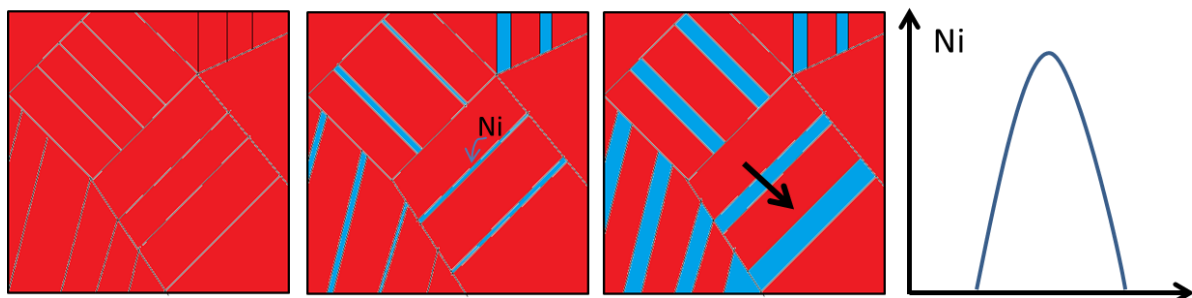


Figure 60 - Schematic representation of austenite formation during tempering and resulting Ni repartition in austenite (richer at the center of grains than on boundaries) potentially influencing its stability

1.2.3. Influence of tempering on carbide precipitation

As seen during the presentation of the industrial heat treated grade, carbide precipitation takes place in Virgo™38. In this part, we will focus on the influence of the heat treatment on the precipitation.

ThermoCalc® simulations using Prisma 2015b were performed for a model alloy (Table 8) in order to predict the precipitation behavior of Virgo™38. The simulations were performed for tempering at 500°C, 550°C, 580°C, 620°C and 660°C up to 24 hours, separately for BCC and FCC phases. The equilibrium volume fraction of $M_{23}C_6$ carbides given by ThermoCalc® is of 0.78vol.% for all temperatures between 500°C and 660°C. Prisma simulations allow taking into account the kinetic aspect of precipitation.

Table 8 - Composition of model Virgo™38 used for the simulation of $M_{23}C_6$ precipitation using Prisma

	Fe	Cr	Ni	C
Wt. %	Base	15.5	4.5	0.04

Even if literature data collected on the same industrial alloy [41] report the presence of some $M_{23}C_6$ in the austenite, Prisma simulations predict that carbide precipitation is nearly exclusively in the BCC phase. Indeed, as shown in Figure 61-a no precipitation is supposed to occur in retained austenite (maximal fraction of $10^{-8}\%$ after 5 hours treatment). These calculations are also in agreement with the observations performed within this work (Figure 46).

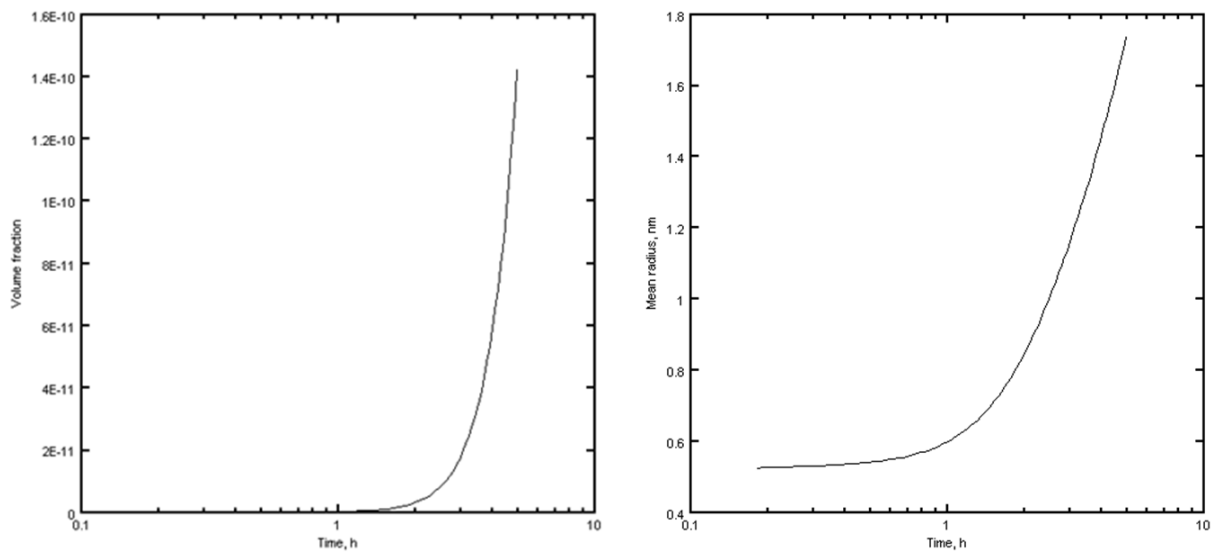


Figure 61 - Results of the Prisma simulations in retained austenite at 620°C showing: a) volume fraction vs time and b) mean radius vs time

$M_{23}C_6$ precipitation is thus supposed to occur in the martensite (and at former grain boundaries) as it has been observed experimentally on Figure 46 and as shown on the Prisma simulations of Figure 62. The final volume fraction calculated by Prisma at 620°C (slightly lower than 0.8%) corresponds to the one obtained for the simulations at the equilibrium performed on ThermoCalc®.

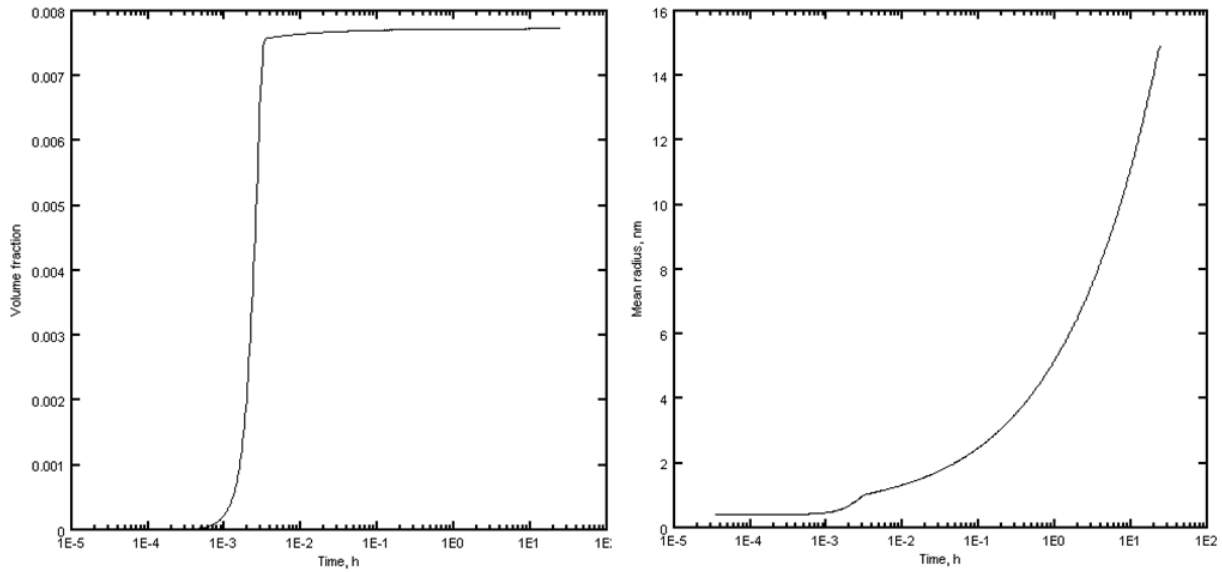


Figure 62 - Results of the Prisma simulations in the BCC phase at 620°C showing: a) volume fraction vs time and b) mean radius vs time

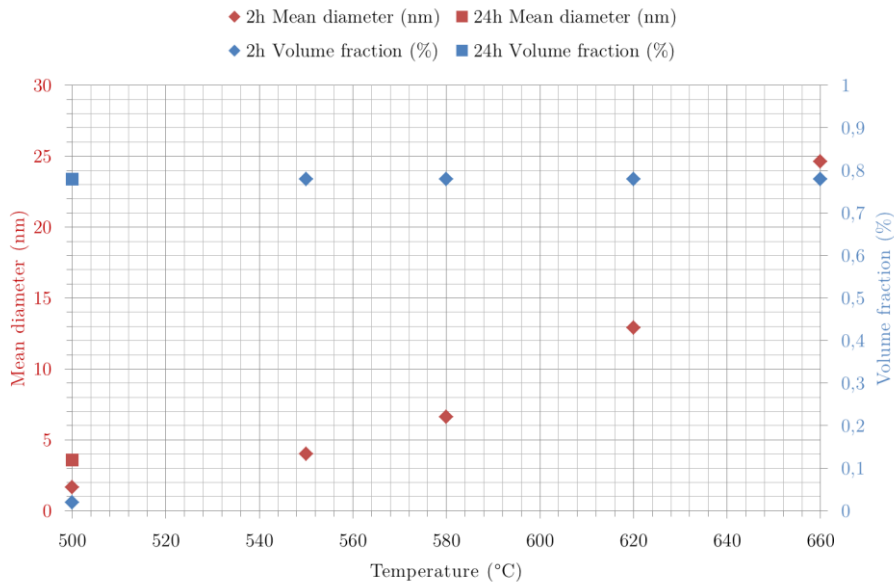


Figure 63 - Results of the Prisma simulations for $M_{23}C_6$ precipitation in the BCC phase of model Virgo™38 after 2 and 24 hours at different temperatures

Kinetic aspects of simulated carbide precipitation are presented in Figure 63 and Figure 65. The data of Figure 62 show that the equilibrium volume fraction of carbides is reached after less than 10s at 620°C. After this time, carbide coalescence is predicted, leading to the increase of particle radius from 1nm at 30s to 14nm after 24h. At 500°C, the tempering must be of at least 10 hours (Figure 64 and Figure 63) to reach the maximal volume fraction of carbide.

It may thus be concluded that (nearly) all carbon atoms present in solid solution after quenching may be consumed to form $M_{23}C_6$ precipitates during tempering between 500°C and 660°C.

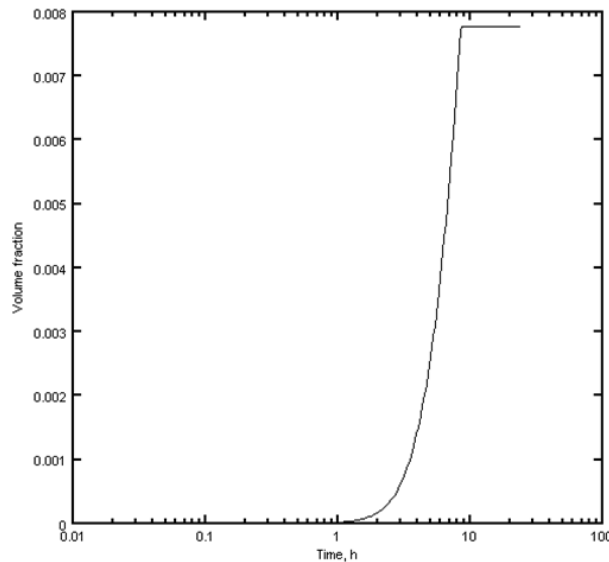


Figure 64 - Precipitation kinetic at 500°C showing that equilibrium volume fraction is reached after at least 10 hours treatment

While tempering at all applied temperatures produces the same $M_{23}C_6$ volume fraction (provided sufficiently long tempering time), the average size of precipitates increases when temperature increases as seen on Figure 63. Increasing the tempering time also enables increasing the precipitates size as seen on Figure 65.

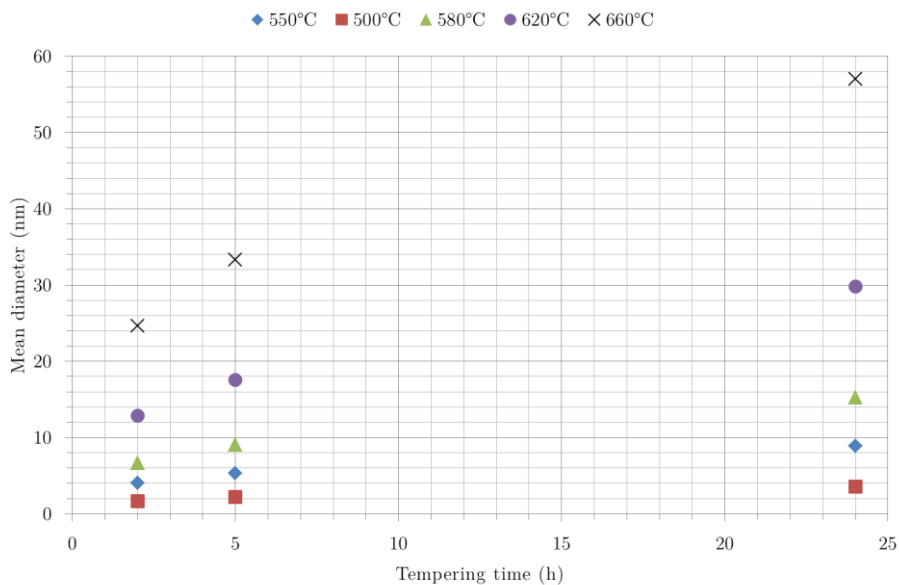


Figure 65 - Results of the Prisma simulations for precipitates size in BCC phase of model Virgo™38 as a function of the tempering time for different tempering temperatures

A treatment between 2 and 5 hours at the peak temperature of 620°C gives the volume fraction of $M_{23}C_6$ precipitates of 0.78% with the simulated average diameter of 14-18nm which is coherent with TEM observations realized on the industrial heat.

However, if the alloy had to be optimized in order to get the maximal yield stress, tempering at low temperature (500°C) during at least 10 hours should be recommended. In such conditions, the volume fraction of particles reaches the equilibrium one (around 0.8%) and their average diameter does not exceed 4nm. However, such a treatment might result in a drastic decrease of toughness.

In this section, we attempted to simulate carbide precipitation in Virgo™38 with Prisma for different tempering treatments (temperature, time) using a simplified alloy composition (Fe-Cr-Ni-C). One of the limits of our approach is that we decided to perform calculations using a model alloy which is much simpler than the complex industrial material described previously. Another limitation of the simulation is that Prisma does not predict the heterogeneous distribution of the precipitates, for example at former austenitic grain boundaries. We have seen that precipitation does not occur in retained austenite contrary to what is mentioned in the literature [41] but only within the bulk BCC martensite as observed in our TEM experiments on the same alloy. If this prediction is valid, it also contributes to the heterogeneous aspect of the precipitation, in particular at higher tempering temperatures with high volume fraction of reverted austenite.

With respect to the treatment at 620°C, close to the one realized in industrial practice, we can conclude that the results of the simulations are in a good agreement with those obtained experimentally. We could certainly obtain a finer (and probably more homogeneous) population of precipitates for lower tempering temperatures. These precipitates would be more efficient in terms of mechanical properties while considering the Orowan mechanisms, as it will be discussed in the next section. However, it must be emphasized that the optimization of Virgo™38 is essentially realized to maximize its fracture toughness and not its yield stress.

2. Mechanical behavior of Virgo™38

2.1. Influence of the direction of sampling in industrially forged material

According to the internal specifications, tensile specimens (geometry given in Figure 96, Chapter III) should be taken in the tangential direction directly from the forged and heat treated impeller. However, due to the number of samples needed for this study and to ensure that all samples are taken from the same impeller to have strictly the same composition during all the studies, it has been chosen to take the samples in the radial direction (Figure 66). To demonstrate that the mechanical properties and the microstructure are the same in both directions, three tensile tests have been performed on samples oriented radially and tangentially and the results are presented in Figure 67.

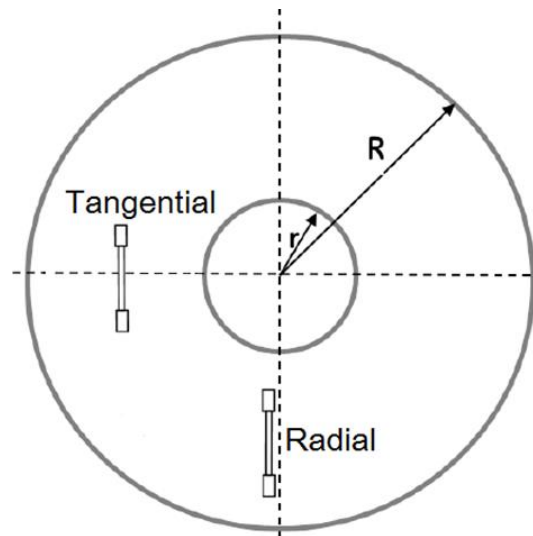


Figure 66 - Schematic representation of an impeller: sample out-taking in the tangential and radial directions

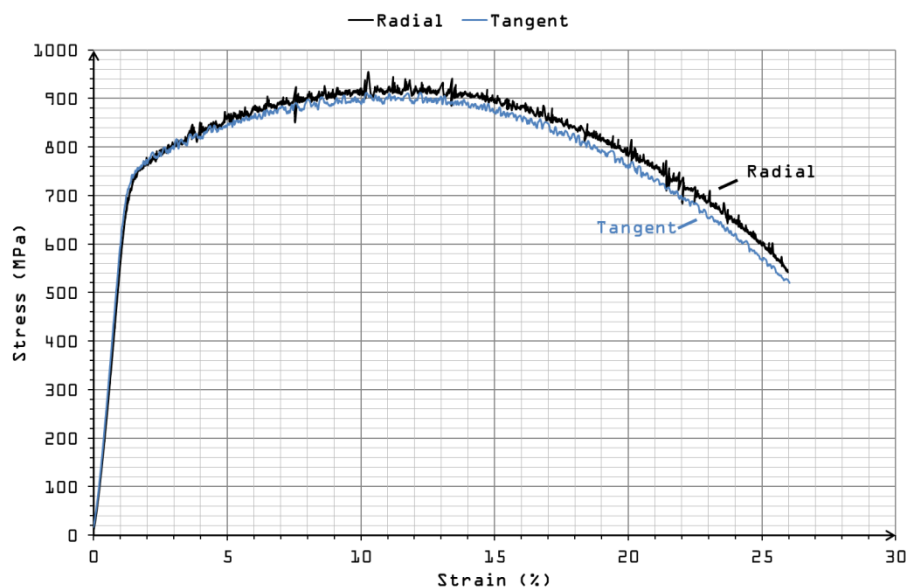


Figure 67 - Tensile curves of Virgo™38 for radial and tangential sample orientation (air, 10^{-5} s^{-1})

The microstructures and retained austenite contents are also the same in both directions. For the rest of the study, it was thus decided to machine all samples in the radial direction.

2.2. Mechanical behavior as a function of heat treatment applied

2.2.1. Tensile properties of Virgo™38 in different microstructural states

Tensile tests in laboratory air were realized on Virgo™38 samples after different heat treatments in order to study the influence of the tempering parameters on the mechanical behavior. All the specimens (except the industrial and quenched ones) are in a single tempered state after re-austenitization and sub-zero quenching as described in part I of this Chapter.

In Figure 68, tensile curves of seven different Virgo™38 microstructures are presented. The industrial heat treatment is taken as the reference. The re-austenitized, oil-quenched and sub-zero treated state (called quenched state as previously mentioned) is the first step for all the other single tempering treatments. Five combinations of temperature and time (Table 9) were studied in order to highlight different hardening phenomena to be discussed in the next section.

Table 9 - Combination of time and temperature of tempering treatment for the study of the mechanical properties

Temperature of tempering treatment (in °C)	Time of treatment (in hours)
200	24
500	24
580	2
620	2
660	2

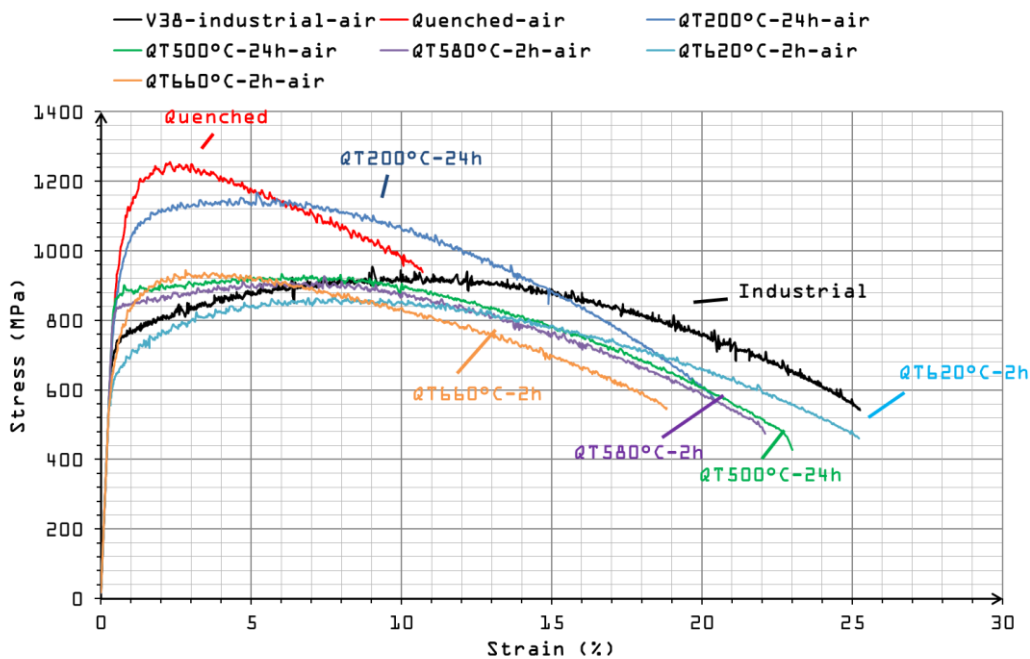


Figure 68 - Tensile curves of Virgo™38 after different heat treatments (air, strain rate of $10^{-5} s^{-1}$)

Tensile properties of Virgo™38 in different microstructural states are summarized in Table 10.

Table 10 - Summary of the 0.01% yield stresses, 0.2% proof stresses, UTS, elongations at UTS and at failure and reduction in area for the different heat treatments performed on Virgo™38

Heat treatment applied	0.01% yield stress (MPa)	0.2% proof stress (MPa)	Elongation at failure E_p (%)	UTS (MPa)	Elongation at UTS (%)	RA (%)
Industrial (reference)	570	735	25	920	9.5	75
Quenched	680	1020	10.2	1240	2	43
QT200°C-24h	660	930	20	1140	4	72.1
QT500°C-24h	730	870	22.5	930	6.5	73.2
QT580°C-2h	720	835	22	910	7	74
QT620°C-2h	490	640	25	860	8	74.2
QT660°C-2h	520	710	18.5	935	3	65.2

In the following discussion, the stress corresponding to the plastic strain of 0.01% will be considered as the ‘elastic limit’, while the terms of ‘yield stress’ and ‘proof stress’ are relative to the 0.2% threshold.

In the industrial state (black curve in Figure 68), the 0.01% yield stress is of 570 MPa, to be compared with the 0.2% proof stress equal to 735 MPa. The elongation at failure is 25%. As mentioned before, all following treatments were realized on the industrial heat of Virgo™38, the first step being re-austenitization and oil-quenching and sub-zero treating (Q).

In the quenched state (red curve), the yielding starts at 680 MPa and is followed by an important strain hardening which can be associated with the increase of the dislocation density in a quasi-single phase BCC structure. The 0.2% proof stress is of 1020 MPa and the elongation at failure reduced to 10.2%.

Annealing at 200°C during 24 hours (dark blue curve) does not significantly change the shape of the initial part of the tensile curve as compared with the quenched state. The 0.01% yield stress is slightly reduced (660 vs 680 MPa) and a pronounced strain hardening is observed. The 0.2% proof stress is of 930 MPa which is 100 MPa less than in the quenched state, probably due to some recovery during annealing at 200°C. This allows a more extended phase of plastic consolidation due to multiplication of dislocations. Differences in the shapes of the stress-strain curves for quenched state and tempered at 200°C appear for higher strains. Indeed, tempering at 200°C during 24 hours extends the tensile curve to larger elongations, so that failure occurs for a plastic strain of 20%.

Tempering at 500°C during 24 hours and 580°C during 2 hours (green and purple curves respectively) leads to a significant change in the shape of the tensile curves, as compared with the previous ones. First of all, for these two states, yielding starts at a higher stress (730 MPa and 720 MPa respectively) than for the quenched state. The 0.2% proof stresses are 870 MPa and 835 MPa respectively. Strain hardening occurs at a very low rate in both cases. The ductility does not change a lot compared with the 200°C treatment - failures occur for plastic strains of 22.5% and 22% respectively for 500°C and 580°C annealing.

Increasing the annealing temperature to 620°C (light blue curve), corresponding to the maximal retained austenite content, results in a strong decrease of the 0.01% yield stress (490 MPa), associated with a slight increase of elongation at failure (25%). The 0.2% proof stress is of 640 MPa. Simultaneously, the shape of the curve changes compared with annealing at lower temperatures. Indeed, in this case, we observe a progressive strain hardening which contrasts with the tensile behavior after treatments at 500°C and 580°C. The 0.01% yield stress after this annealing is the lowest among all tested microstructure. Since annealing at 620°C produces the maximal retained austenite content (here corresponding to only 2h tempering so 14.7%), it seems coherent to correlate the minimal $\sigma_{0.01}$ and $\sigma_{0.2}$ values with the high γ_R volume fraction. We will see however (section 2.2.3), that this intuitive correlation does not reflect the properties of phases present in the microstructure of Virgo™38.

Finally, the 0.01% yield stress after annealing at 660°C (orange curve) slightly increases compared with the previous one (620°C / 2 hours). The yielding starts at 520 MPa in this case and the 0.2% proof stress is of 710 MPa. Strain hardening is also more pronounced and the form of the tensile curve approaches that observed after 200°C/24h tempering.

We also mention that all the tensile tests performed in air, even in the re-austenitized and quenched state, produced entirely ductile fractures.

In summary, the best combination of high 0.01% yield stress and elongation at failure is clearly obtained after annealing treatments at temperatures below the peak of retained austenite (Figure 54) while the peak treatment at 620°C produces a microstructure with the lowest yield stress and without a significant increase of elongation. Although the microstructure obtained through annealing at 660°C contains a large amount of fresh martensite (>25%) and only 3% of retained austenite (Table 11), its 0.01% yield stress remains low. An interpretation of this unattended behavior will be given in section 2.2.3, through the analysis of different hardening mechanisms likely to operate in the microstructure of Virgo™38.

2.2.2. Impact toughness of Virgo™38 in different microstructural states

Charpy impact tests in laboratory air and at room temperature were realized on Virgo™38 samples after different heat treatments in order to study the influence of the tempering parameters on the fracture toughness. The heat treatment parameters chosen were the same as described previously (Table 9) except 200°C/24h annealing which was not tested.

The specimen geometry corresponds to the smallest sub-size specimen recommended by ASTM E23, which means they have a total length of 55mm, a 5x5mm² cross section and a 1-mm-deep 45° notch with a root radius of 0.25mm (Figure 69).

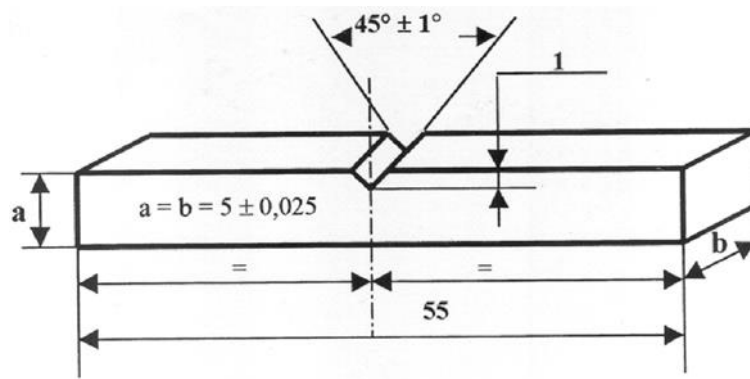


Figure 69 - Sample geometry used for Charpy impact tests corresponding to the smallest sub-size specimen recommended by ASTM E23

Results shown in Figure 70 indicate that the peak of impact toughness coincides with that of retained austenite (Figure 54). Note that the absolute value of impact toughness in quenched state (115) is very high for martensitic structure.

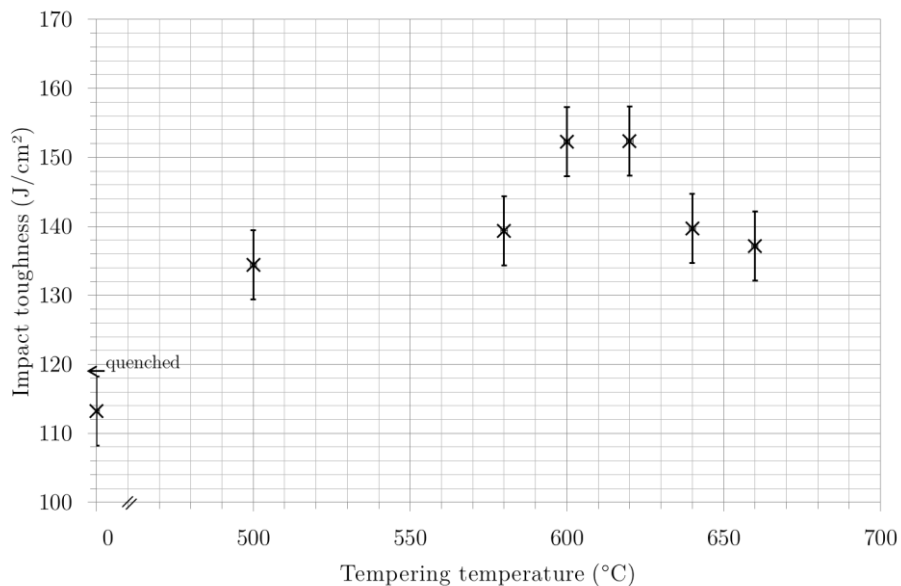


Figure 70 - Charpy impact toughness measured at room temperature for different heat treatment showing the highest impact toughness for high retained austenite content

2.2.3. Relationships between microstructure and the 0.01% yield stress in Virgo™38

Heat treatments realized on Virgo™38 result in significant microstructure modifications operating essentially at the nanoscopic scale. Table 11 presents different elements of microstructure present in the material after five annealing treatments applied (as described previously). All phase contents are given in weight percent, except for $M_{23}C_6$, expressed in volume percent. Delta-ferrite (about 5 vol.%) is present in all microstructures presented in Table 11 and will not be taken into account in the following analysis.

Table 11 - Microstructural elements present in the material after different tempering treatments

	0.01% yield stress $\sigma_{0.01}$ (MPa)	Fresh or Tempered martensite α''	Interstitial C in α'	Secondary fresh martensite α'_f	Interstitial C in α'_f	Retained austenite γ_R	Interstitial C in γ_R	$M_{23}C_6$ (d) [nm]
(0) Q	680	✓ ≈100% (F)	✓					
(1) QT200/24	660	✓ ≈100% (T)	✓					
(2) QT500/24	730	✓ ≈100% (T)						✓ (3.5) ≈0.8%
(3) QT580/2	720	✓ ≈97% (T)				✓ ≈3%	✓	✓ (6.5) ≈0.8%
(4) QT620/2	490	✓ ≈84% (T)				✓ ≈15%	✓	✓ (13) ≈0.8%
(5) QT660/2	520	✓ ≈70% (T)		✓ ≈27%	✓	✓ ≈3%	✓	✓ (25) ≈0.8%

Virgo™38 is a low carbon supermartensitic stainless steel containing 0.04 wt.% C. The martensitic microstructure formed during quenching is thus purely BBC with C atoms in oversaturated solid solution [15]. Nevertheless, according to Prisma simulations discussed above, some amount of carbide precipitation during oil quenching cannot be totally excluded. When annealed, $M_{23}C_6$ carbides can be formed as reported in the literature [37] and as observed in this study (Figure 46 and Figure 47), at least for the optimized industrial heat treatment. Prisma simulations previously realized (1.2.3) showed that annealing between 500°C and 660°C leads to the $M_{23}C_6$ precipitation up to saturation volume fraction (≈0.8%). This means that the BCC matrix becomes nearly carbon free. This effect appears as decisive with respect to the mechanical resistance (yield stress) and it must be put in relationship with the carbide size and distribution.

In the following, we will propose a semi-quantitative correlation between the 0.01% yield stress of the material after different heat treatments and its microstructure, using classical models of crystal strengthening. In a polycrystalline alloy such as Virgo™38, at least four contributions to the yield stress must be taken into account:

- “Work hardening” (dislocation density)
- Solid solution strengthening
- Precipitation hardening
- Grain refinement (Hall-Petch law)

At the first view, the grain size contribution to the elastic limit is likely to play a very important role in Virgo™38 given the dimensions of BCC and FCC laths (Figure 43). However, it is important to note that the grain size variation as expressed by the Hall-Petch relationship acts on the 0.2% proof stress and NOT (or very little) on the physical elastic limit. So, 0.2% proof stress measurements (and micro-hardness tests - in fact a complex integration between yield stress and deformation up to 8%) reflect material properties in the initial part of the plastic range and no direct extrapolation can be made toward the physical yield stress.

The physical elastic limit, defined as the shear stress necessary to let a dislocation glide over the strongest local obstacle present in a grain of a polycrystalline material [111], being very difficult to determine experimentally, we propose to consider the stress producing a plastic strain of 0.01% as the physical yield stress σ_{el} (Table 10 and Table 11).

The “**work hardening**” contribution acts across the generic

$$\Delta\tau_{\Delta} \approx \frac{\sigma_{\Delta}}{2} \approx 0.4\mu b\sqrt{\rho} \quad (i)$$

relationship, where ρ represents the dislocation density of the considered microstructure, $\mu \approx 80\text{GPa}$ is the shear modulus and $b \approx 0.25\text{nm}$ is the Burger’s vector. According to literature data, the value of ρ exceeds 10^{15}m^{-2} in the fresh martensite [112] but it is obviously supposed to decrease during tempering. Data collected on Fe-Cr martensitic steels [113] reveal that ρ may decrease by one order of magnitude after annealing at 750°C during one hour and two orders of magnitude after 100 hours.

The value of $\Delta\tau_{\Delta}$ results mainly from diffuse and attractive interactions between dislocations. The effect of thermal activation on such obstacles is weak. Consequently, this kind of obstacle remains nearly unaffected by temperature (below $0.3T_M$).

Solid solution strengthening may be expressed by:

$$\Delta\tau_S \approx \frac{\sigma_S}{2} \approx \frac{Q_0}{2b^3}\sqrt{C} \quad (ii)$$

where Q_0 ($\approx 1.4 \cdot 10^{-19}\text{J}$ for carbon atoms in BCC) is the interaction energy between solute atoms and dislocations and C is the atomic fraction of considered solute. In quenched Virgo™38, carbon is the only element able to produce a significant hardening, but its real effect (if any) depends, as we will see, on the importance of the “work hardening” or precipitation hardening. Unlike $\Delta\tau_{\Delta}$, the solid solution contribution (ii) depends strongly on thermal activation. The expression of Eq. ii represents the maximal effect at 0K and, since the transition temperature is of approximately 400K, its effective value at room temperature is considerably smaller.

Precipitates likely to improve the mechanical resistance of Virgo™38 are essentially (Cr-Mn-Fe) $M_{23}C_6$ carbides. $M_{23}C_6$ being not coherent with the BCC matrix, the **precipitation hardening** at temperatures below $0.3T_M$ can only occur through Orowan’s looping mechanism:

$$\Delta\tau_P \approx \frac{\sigma_P}{2} \approx 0.75 \frac{\mu b}{L} \quad (iii)$$

where L is the average distance between precipitates in the slip plane and is related to their volume fraction V_V and radius r through:

$$L \approx r \sqrt{\frac{2\pi}{3V_V}} \quad (\text{iv})$$

According to the “strongest obstacle criterion” for localized obstacles to dislocation slip [111], it is necessary to check which of these two effects, dislocation density (Eq. i) or solid solution strengthening (Eq. ii), is more likely to occur in the microstructures (0) and (1) (Table 11), which are the only ones which do not contain carbide precipitates. Putting a dislocation density of 10^{15}m^{-2} (which is certainly underestimated) and carbon concentration into the corresponding equations, it becomes clear that the contribution of solid solution strengthening is much weaker than that of work hardening in quenched Virgo™38.

$$\sigma_S = \frac{Q_0}{b^3} \sqrt{C} \approx 250 \text{MPa} \text{ versus } \sigma_\Delta = 0.8\mu b \sqrt{\rho} \approx 510 \text{MPa}$$

Considering that, we can now estimate the dislocation density in the microstructure (0) i.e. quenched state, by Eq. (i), which is found close to:

$$\rho_Q = \frac{\sigma_Q^2}{0.64\mu^2 b^2} \approx 1.8 * 10^{15} \text{m}^{-2}$$

a value which is coherent with literature data on Fe-Cr martensitic steels [113].

Using data from Table 10, it is also possible to get an idea about the effect of low temperature tempering (200°C/24h) on ρ . It appears that only a slight decrease of dislocation density occurs during this treatment:

$$\frac{\rho_{Q200}}{\rho_Q} = \frac{\sigma_{Q200}^2}{\sigma_Q^2} \rightarrow \rho_{Q200} \approx 0.94\rho_Q$$

also in a good agreement with literature [114].

Before analyzing the effect of tempering between 500°C and 660°C on dislocation density, we remark that microstructures (2) to (5) in Table 11 all contain $M_{23}C_6$ precipitates with the same volume fraction (0.78%) but with very different sizes, which gives a strengthening of:

$$\begin{aligned} \sigma_P &\approx 1.5 \frac{\mu b}{L} \approx \frac{1.83}{r} && \text{if all precipitates contribute} \\ \sigma_P &\approx 1.5 \frac{\mu b}{L} \approx \frac{1.29}{r} && \text{if 50\% of precipitates contribute} \end{aligned}$$

The second approximation takes into account the fact that a significant fraction of precipitates may be located at former austenite grain boundaries, in particular for higher tempering temperatures, and that their impact on the elastic limit is negligible.

Let's start this analysis by microstructure (5) annealed at 660°C during 2 hours where the particle radius exceeds 12nm. Moreover, a significant fraction of precipitates is located at former austenitic grain boundaries and they have no impact on mechanical resistance. Supposing that 50% of the particles (with a radius of 12nm) could contribute to the physical elastic limit, their strengthening effect does not exceed 100MPa which is much smaller than the expected effect of dislocation density. Even by taking into account the contribution of all the precipitates, the corresponding strengthening is negligible (only 150MPa). In agreement with the "strongest obstacle criterion", we can thus estimate the dislocation density in tempered martensite of microstructure (5) by supposing the elastic limit of secondary fresh martensite similar to that of quenched martensite $\sigma_{\alpha'}$. Indeed, this microstructure is composed of approximately 70% of tempered martensite α'' and nearly 30% of secondary fresh martensite α'_f (Table 11), the 3% of retained austenite being neglected in this analysis. A simple mixture law, which is supposed to describe approximately the evolution of yield stress of two phase aggregates [115], gives:

$$\sigma_{\Delta 660, \alpha''} = \frac{\sigma_{el660} - 0.3 * \sigma_{\alpha'}}{0.7} \approx 450MPa$$

with associated dislocation density in tempered martensite of:

$$\rho_{Q660, \alpha''} \approx 7.9 * 10^{14} m^{-2}$$

Similar as for microstructure (5), the effect of dislocation density is also dominant in microstructure (4), for which 15% of retained austenite γ_R are present after cooling to room temperature. Supposing the elastic limit of martensite (85%) tempered at 620°C/2h similar to that calculated after 660°C/2h (i.e. 450MPa), we can estimate the elastic limit of retained austenite by a simple mixture law:

$$\sigma_{\Delta, \gamma_R} = \frac{\sigma_{el620} - 0.85 * \sigma_{\alpha''}}{0.15} \approx 710MPa$$

Surprisingly, it is higher than that of quenched martensite (Table 10). Although intuitively a value smaller than that of tempered martensite would be expected, the result of our estimation is in agreement with qualitative TEM observations of Figure 43 which suggests a higher dislocation density in retained austenite compared with tempered martensite. This result confirms indirectly that the elastic limit in both α' and γ_R is essentially due to high dislocation densities and not, or very little, to the presence of C in solid solution.

Physical elastic limits of microstructures (2) and (3) are nearly the same and higher than that observed in the quenched state. The only possible explanation is precipitation hardening by $M_{23}C_6$ carbides. Unlike for treatments at 620°C and 660°C, the particles are very fine (see Table 11) and they are the strongest obstacles to dislocation slip. Equation (iii) gives the elastic limit of around 740MPa for the microstructure (2) supposing that only 50% of all particles are present inside martensitic laths. It would exceed 1000MPa if all carbide particles contributed to the material's strength. Even if there is a large degree of uncertainty about the real distribution of carbide precipitates, there is no doubt that the high 0.01% yield stress in microstructures (2) and (3) can only be explained through precipitation strengthening. These two microstructures (2) and (3), whose mechanical resistance is due to precipitation strengthening, are also characterized by tensile curves with much slower strain hardening than those corresponding to other microstructures (Figure 68).

A similar effect of precipitation hardening on the yield stress and on strain hardening in quenched and precipitation hardened states was reported by Oehlert and Atrens [116] in the case of two low alloyed martensitic steels. The 0.01% yield stress increases after tempering as compared with the quenched microstructure, while the 0.2% proof stress is higher after quenching. The same tendency was observed in Virgo™38 (Table 10).

In summary:

- We could estimate dislocation densities in quenched and tempered martensite and in retained austenite to be $1.8 \cdot 10^{15} \text{m}^{-2}$; $7.9 \cdot 10^{14} \text{m}^{-2}$ and $2.0 \cdot 10^{15} \text{m}^{-2}$ respectively
- Strengthening by dislocation networks appears to be the principal mechanism in quenched Virgo™38, but also after annealing at 200°C, 620°C and 660°C
- Hardening of Virgo™38 after annealing at 500°C/24h and 580°C/2h is due to fine M_{23}C_6 precipitation
- The 0.01% yield stress of retained austenite is comparable with that of quenched martensite (710MPa vs 680MPa)
- In a two phase microstructure composed of tempered martensite and retained austenite, γ_R is the harder phase (710MPa vs 450MPa)

Because of necessary simplifying assumptions concerning the microstructure and the basic mixture law used to predict the behavior of two-phase aggregates, all the estimations presented above indicate the tendencies, but cannot be considered as exact quantitative predictions.

In view of the results discussed above, the conventional interpretation, supposing retained austenite to be the weakest phase of the alloy, must be revised. The combination of a high yield stress and impact toughness is probably due to a combination of tempered martensite with a low yield stress (which is responsible for impact toughness) and a hard retained austenite which enables reaching the required yield stress of the alloy.

The additional argument which strengthens the above conclusion results from a comparison of two samples composed of tempered martensite and retained austenite and in which carbide influence on the yield stress may be neglected. Indeed, in the industrially treated sample, γ_R content ($\approx 22\%$) is significantly higher than that observed after laboratory tempering at 620°C during 2 hours ($\approx 15\%$). The higher 0.01% yield stress measured in the industrial microstructure (570 versus 490MPa) can only be explained if retained austenite is the "hard" phase" of the quasi-biphasic aggregate.

As mentioned previously, the **"grain size effect"**

$$\sigma_{GS} = \sigma_0 + \frac{k}{\sqrt{d}} \quad (v)$$

does not bring a direct contribution to the physical elastic limit. Moreover, it would be difficult to introduce it in a discussion about the evolution of 0.2% proof stress as a function of heat treatment applied. The first reason is that the Hall-Petch constants, in particular σ_0 , reflect the properties of a given matrix (similar dislocation densities, solute concentrations, presence of precipitates...). This is NOT a situation of Virgo™38 after different annealing treatments. Secondly, grain size is delicate to define in lath-like microstructures. Moreover, if the lath width is chosen as 'd', the corresponding distances are close to the limit at which breakdown of Hall-Petch law is frequently observed [117].

2.3. Mechanical stability of retained austenite after industrial heat treatment

This analysis was performed on an industrial grade in the industrial quenched and double tempering state with the initial retained austenite content of 22vol%, see Table 7 for its chemical composition and Figure 44 for its microstructure.

The maximum of retained austenite content shown in Figure 54 is directly related to the chemical composition of reverted austenite, in particular its nickel content as previously explained. The increasing instability of reverted austenite after treatments at $T > 620^\circ\text{C}$ is thus a consequence of the increase of the M_s point, which exceeds room temperature. Per analogy and as shown by ThermoCalc® simulations, the M_s temperature is very close to room temperature for reverted austenite formed at 620°C (Figure 56). In such conditions, the energy provided by applied stress can easily disturb the stability of retained austenite and induce martensitic transformation.

Stress induced martensitic transformation was investigated using three techniques:

- X-ray diffraction during and after uniaxial tests (tensile and compressive) with different amounts of homogeneous plastic deformation using in situ measurements
- EBSD observations aiming to detect local aspects of SIMT
- Semi-quantitative analyses after heavy local plastic strain (mechanical polishing, phase composition close to the fracture surface)

At first, the sensitivity of Virgo™38 with respect to stress induced martensitic transformation (SIMT) was investigated using uniaxial compression tests at room temperature. All samples were in as received industrial microstructural state and the retained austenite fractions were calculated by XRD using the Rietveld method between each compression steps on a polished section. The simplicity of this method (compression and XRD measurements) allowed getting the first idea about the kinetics of SIMT in Virgo™38.

The plot of Figure 71 shows that a considerable amount of plastic strain is necessary to obtain a measurable effect on the retained austenite content and that even for $\epsilon_p = 7.5\%$, the transformation is far from being completed (10% remaining v_R).

No differences between tempered martensite, non-tempered martensite and martensite formed by SIMT are observed in XRD patterns. This means that their structure is the same, at least from the crystallographic point of view.

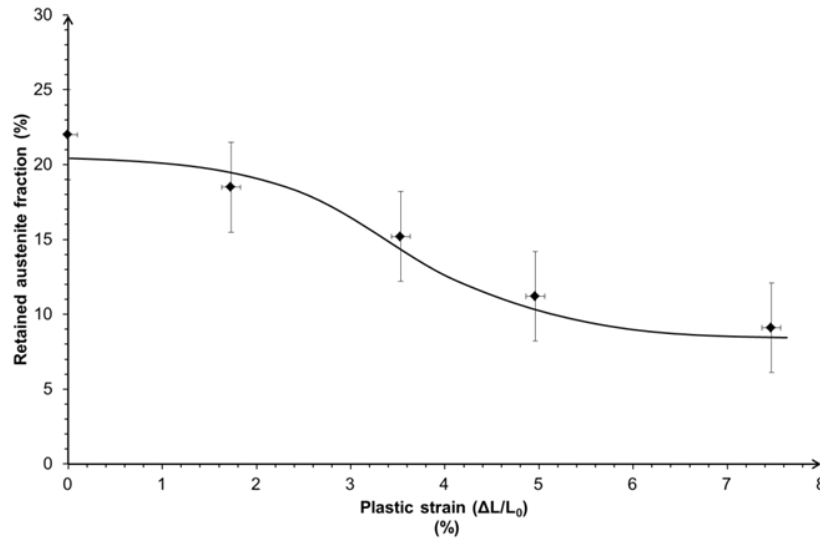


Figure 71 - Retained austenite fraction calculated by XRD using the Rietveld method as a function of plastic deformation applied by compression tests

The results of Figure 71 fit well with Olson’s and Cohen’s [118][119] model proposed to predict SIMT kinetics. They made the assumptions that α'-martensite is nucleated at the shear band intersections and that the fraction of martensite formed during the SIMT is continuous function of the strain applied. In our case, based on their study and by extrapolating for SMSS and in order to take into account the initial retained austenite content, the fraction of austenite was defined as:

$$f_{\gamma} = f_{\gamma_0} e^{-\beta(1-e^{-\alpha\varepsilon})^{4.5}}$$

The best fitting parameters of the previous curve are $\alpha=0.5$ and $\beta=1$. α describes the rate of the shear band formation while β represents the probability that the martensite nucleates at these intersections. We will see that SIMT in Virgo™38 rather starts at ('gamma/alpha') interlath boundaries than on slip band intersections. However, in both cases local manifestation of plasticity and associated stress concentrations are responsible for setting off the transformation. The use of Olson’s and Cohen’s equations appears therefore as justified.

The effect of plastic strains under tensile loading was investigated using XRD measurements on in-situ deformed samples. Tensile tests were carried out using a tensile machine presented in Figure 72, designed and fabricated in the laboratory.

X-ray measurements of retained austenite fractions are plotted in Figure 73 versus plastic strain. The results are similar to those collected from compression tests (Figure 71). A clear decrease is noted as a function of increasing plastic deformation. However, the transformation starts for smaller plastic strains, the final amount of transformed austenite is smaller and the shape of the curve is exponential. These apparent differences might be due to a different behavior during traction and compression. Indeed, the Olson’s and Cohen’s law is not applicable in this case, and the applied law can be the Ludwigson’s and Burger’s law [120][121]. We also note that no measurable transformation of retained austenite was detected in the elastic domain of the tensile curve.

$$\frac{1}{f_{\gamma}} - \frac{1}{f_{\gamma_0}} = \frac{k_p}{p} * \varepsilon^p$$

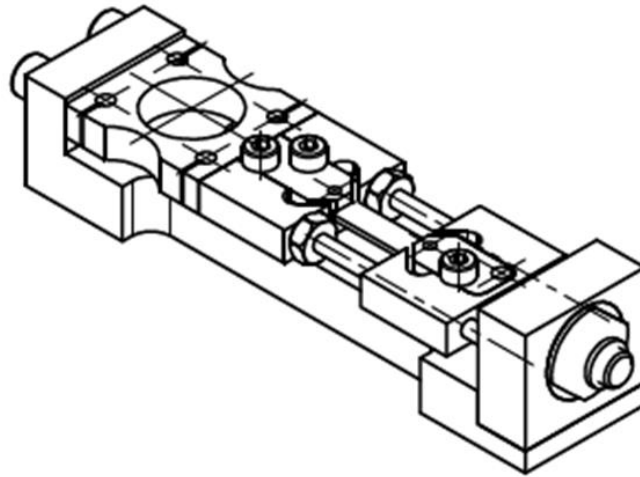


Figure 72 - Homemade tensile machine used for tensile test and constant load inside a Panalytical X'Pert diffractometer

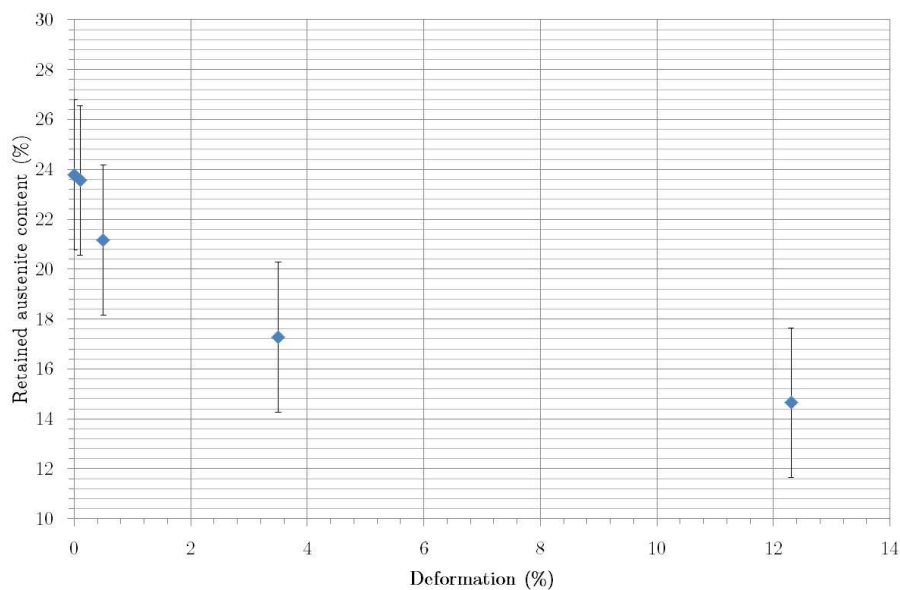


Figure 73 - Retained austenite fraction calculated by XRD using the Rietveld method as a function of deformation applied by in situ tensile tests

To investigate local aspects of SIMT, in situ measurements under tensile stress by EBSD were carried out. For this study, a tensile machine provided by Kammrath and Weiss was used.

The results are presented in Figure 74 for tensile stresses of 560 (elastic range, 98% of 0.01% yield stress) and 735 MPa (corresponding to 0.2% proof stress). Although no quantitative conclusions can be drawn because of a very high fractions of “zero solutions” (Table 12), a look at two former austenite grains in the lower part of EBSD maps indicate that SIMT takes place through thinning of γ_R laths. This suggest that α''/γ_R interfaces are the preferred sites for nucleation of stress induced martensite. This mechanism is possible if plastic deformation starts in martensite whose elastic limit is lower than that of retained austenite. This generates high local stresses at interfaces with retained austenite which remains elastic or much less plastically deformed.

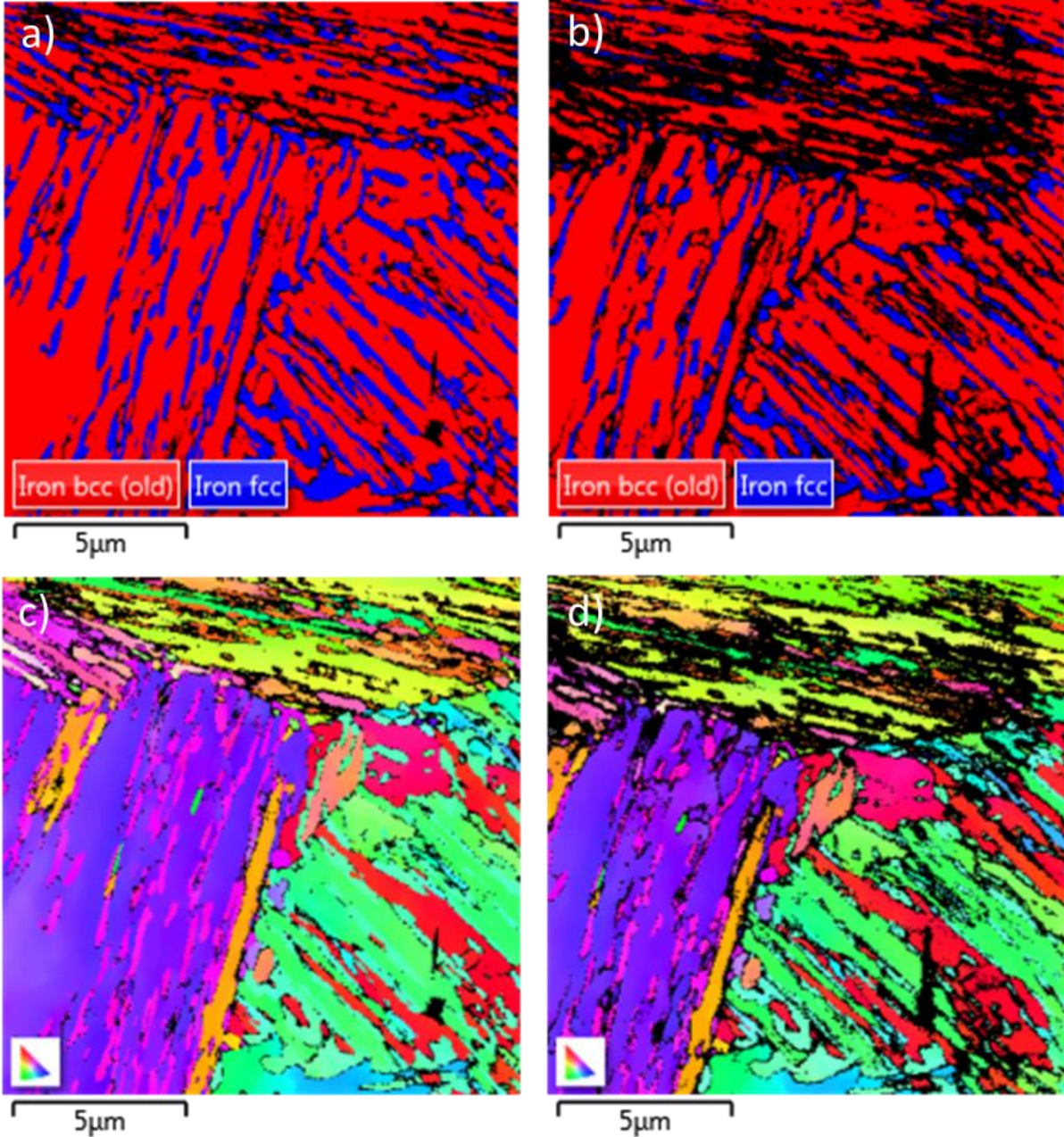


Figure 74 - EBSD maps (a and b) and inverse pole figures (c and d) of samples deformed at 560MPa (a and c) and at 735MPa (b and d) inside SEM showing SIMT phenomenon (IPF, red (001) green (101) blue (111))

Table 12 - Unindexed fraction and phase fractions of retained austenite and martensite obtained by EBSD analysis

	Phase Fraction (%) at 560 MPa	Phase Fraction (%) at 735 MPa	Phase Fraction (%) at 880 MPa (after necking maps performed on another area)
Iron bcc	66.52	55.14	73.09
Iron fcc	20.61	10.92	3.31
Zero Solutions	12.86	33.94	23.60

Since large macroscopically homogeneous plastic strains (at least up to 12%) do not bring SIMT to its term, we analyzed the effect of large local strains on the phase composition of Virgo™38.

First, we used X-ray diffraction to investigate the effect of surface preparation techniques on the amount of austenite in the surface layer (Figure 75). Local strains induced by metallographic preparation appear to provide enough mechanical energy to set off stress induced martensite transformation. Moreover, the volume fraction of retained austenite in the surface layer (6.5%) is much smaller than the one measured after tensile and compression tests up to respectively 12% and 7.5%. Clearly, mechanical polishing leads to SIMT in Virgo™38. Consequently, the phases proportion at the surface may be very different from that of the bulk. This can only be avoided by following a strict procedure of surface preparation (appendix 1). All samples described in the previous section were analyzed after electropolishing of at least 90s in a 6% solution of perchloric acid in ethanol at a tension of 25V after mechanical polishing up to P4000.

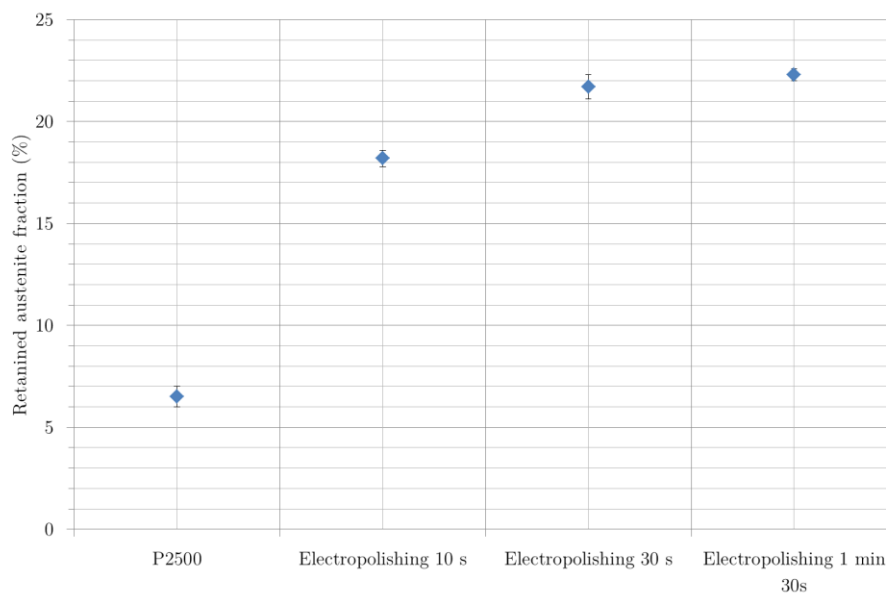


Figure 75 - Influence of the metallographic preparation on the retained austenite content measured by X-Ray Diffraction

Finally, X-ray diffraction analysis was performed at the tensile fracture surface of Virgo™38 after industrial heat treatment ($E_p=25\%$). No FCC is detected in this case, which means that austenite fraction must be lower than 2%, the detection limit of the method. Consequently, large local stresses may allow a nearly full transformation of retained austenite by SIMT. These large local stresses are difficult to be estimated in this case, but taking into account the depth of analyze on the fracture surface (some μm) one can consider that it only corresponds to snatched ligaments at that the equivalent deformation is higher than 100%.

The results presented above clearly demonstrate the sensitivity of Virgo™38 to stress induced martensitic transformation (SIMT). The results of different tests give information about threshold conditions for SIMT, its kinetics and preferred transformation sites in a complex microstructure of Virgo™38.

First of all, no SIMT is detected under macroscopically elastic stresses. X-ray diffraction results show that a macroscopic plastic strain of at least 0.5% is necessary to obtain a measurable (of the order of 2 vol.%) decrease of the retained austenite content (Figure 71 and Figure 73).

Under homogeneous plastic strain (tensile or compressive) and until necking sets off (tensile curve) i.e. up to $\epsilon_p \approx 12\%$, SIMT leads to a transformation of not more than 50% of γ_R (Figure 71 and Figure 73). These observations demonstrate that although M_s of retained austenite is close to room temperature, SIMT is not easy to take place as expected in a multiphase microstructure of Virgo™38.

A possible explanation is the difference in elastic limits of two principal phases of the alloy, tempered martensite and retained austenite. We saw in the previous section that γ_R is considerably harder than α'' so that plastic deformation is likely to start in the martensite while the retained austenite remains in the elastic domain. Consequently, it is not surprising that a considerable amount of macroscopic plastic strain is necessary to initiate SIMT of the retained austenite.

The above assumption matches with local aspects of SIMT in Virgo™38, as observed by EBSD (Figure 74). The transformation appears to take place through thinning of austenite (inter-)laths, suggesting that α''/γ_R interfaces are preferred sites of SIMT initiation. High local stresses at such interfaces are possible when one of the phases (α'' in this case) is plastically deformed, while the other one (γ_R in this case) remains elastic (Figure 76).

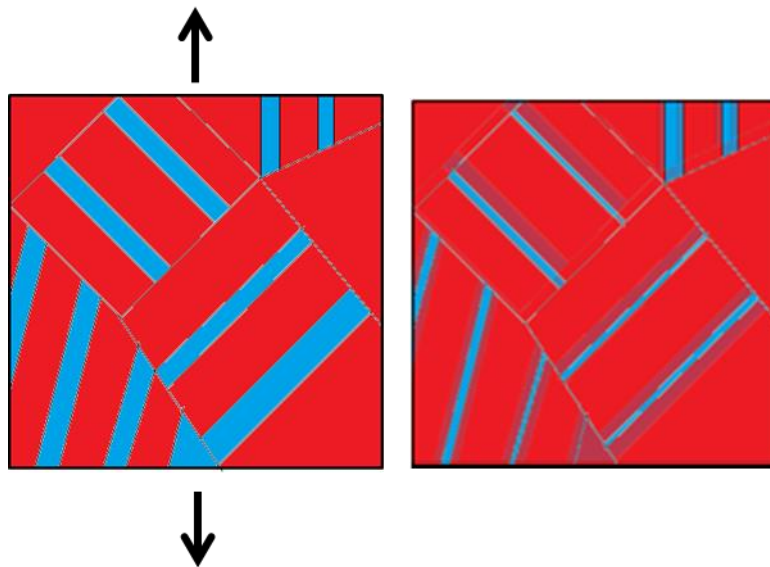


Figure 76 - Schematic representation of SIMT in Virgo™38 leading to retained austenite refining

Finally, observations realized after heavy local deformation (mechanical polishing, fracture surface) demonstrate that it is possible to bring the transformation nearly to the end.

In summary, under “in field” conditions proper to Virgo™38 applications, SIMT is not likely to play a role in massive components, except in regions of geometrically induced stress concentrations. However, two other types of local effects should be taken into consideration:

- Local plastic strains due to surface finishing, if they induce local plasticity
- Heavy stress concentrations at crack tips (when cracking due to environmentally induced damages occurs), associated with large local plastic strains. Complete transformation of retained austenite might be possible in front of a propagating crack changing radically the microstructural environment for propagation (see next Chapters).

2.4. Summary

The principal results of a microstructural study of Virgo™38 in different metallurgical states, associated with tensile test data, may be summarized as follows:

The microstructure of the as-received (“industrial”) heat of Virgo™38 is mainly composed of approximately 78% of BCC phases (essentially tempered martensite α' , but also a small amount of δ -ferrite, <5vol.%) and 22% of retained austenite γ_R . The microstructure contains less than 1 vol% of carbide precipitates ($M_{23}C_6$), mainly located at former austenite grain boundaries and in BCC. This microstructure is obtained after a standard procedure of heat treatment composed of a sub-zero quenching and double tempering.

Laboratory tests showed that the first step of the industrial heat treatment, a sub-zero quenching, produces a fully BCC microstructure. However, FCC→BCC transformation might remain uncompleted in intergranular zones, because of Si and Ni segregation to boundaries, likely to occur very rapidly during quenching, as previously observed in austenitic stainless steels.

Tempering treatments realized during 2 hours at temperatures between 500°C and 660°C on sub-zero treated samples reveal the peak of retained austenite at 620°C. This classical result is explained by partitioning of alloying elements, in particular Ni, between FCC and BCC phases and the resulting variation of M_s point of reverted austenite γ_{rev} . Consequently, the retained austenite (γ_R) is potentially very sensitive to stress induced martensitic transformation (SIMT) because its M_s point is close to room temperature.

Carbide precipitation in martensite is possible at all tempering temperatures applied and, according to thermodynamic calculations on a simplified Fe-Cr-Ni-0.04%C composition, the equilibrium volume fraction of 0.78% is achieved after 2 hours treatments between 580°C and 660°C. However, for tempering at 500°C, the holding time must exceed 10 hours. The average particle size obviously decreases when tempering temperature decreases.

The tensile behavior of Virgo™38 in air depends very strongly on tempering temperature. We identified two basic hardening mechanisms which can account for the elastic limit of the material. In the quenched state and after tempering at 200°C and above 620°C, the dislocation density (in a quasi-single phase BCC quenched alloy or in a two phase BCC/FCC aggregate after tempering) is the principal hardening factor. For tempering within the range between 500°C and 580°C, carbide precipitation becomes the dominating mechanism. This precipitation at 500°C and 580°C leads to the highest 0.01% yield stress values observed in this study, associated with a very good ductility.

Although Virgo™38 belongs to the family of nominally “precipitate-free” stainless steels, $M_{23}C_6$ carbides are present in all tempered microstructures. However, their effect on mechanical properties seems to be negligible for tempering temperatures close to the peak of retained austenite (around 620°C) and above. This is due to the large size (with respect to the Orowan strengthening mechanism) of carbide particles and their preferred location at former austenite grain boundaries. However, a fine precipitation produced during tempering at temperatures between 500°C (3nm) and 580°C (6nm) leads to a significant particle strengthening effect through Orowan looping.

Thus, from a purely metallurgical point of view and using the terminology proper to precipitation hardened alloys, the industrially targeted Virgo™38 microstructure is an “over-aged” one, while “peak aging” conditions (high elastic limit associated with high ductility) would correspond to treatments at lower temperatures (500-580°C). However, it is necessary to be reminded that NACE specifications for Oil&Gas applications do not aim to maximize the elastic limit as it will be discussed in following Chapters.

The estimation of different contribution to the elastic limit of our alloy shows that the optimized microstructure may be considered as a semi-biphasic aggregate composed of tempered martensite and retained austenite (for tempering temperatures above 600°C, carbide precipitation does not contribute to the material strengthening). In opposition to what is generally admitted, retained austenite, and not tempered martensite, is the "hard" phase of the aggregate. This is perfectly confirmed by comparing 0.01% yield stresses of samples treated in industrial conditions and laboratory tempered at 620°C during two hours. The higher 0.01% YS measured in the industrial sample may be explained as resulting from the higher γ_R content.

As expected, SIMT occur in the industrially optimized microstructure of Virgo™38. The amount of stress induced martensite increases with plastic deformation and approximately half of the initial amount of retained austenite is transformed into martensite by applying a homogeneous plastic strain of about 10% (corresponding approximately to UTS). This can only occur under high stress concentrations induced by local manifestations of plasticity like intersections of slip bands or interactions of slip bands with interlath boundaries. Such high local plastic strains can also be achieved in case of uncontrolled surface preparation and contribute to crack initiation and also in the vicinity of propagating cracks, consequently SIMT has to be taken into account in the analysis of environmentally assisted cracking mechanisms in SMSS.

Chapter III:
Hydrogen Embrittlement and Stress Corrosion
Cracking of Virgo™38 in acid environments

Chapter III: Hydrogen Embrittlement and Stress Corrosion Cracking of Virgo™38 in acid environments	99
1. Depassivation of Virgo™38 studied by an electrochemical approach	103
1.1. Experimental procedure	103
1.2. Depassivation study of Virgo™38 without loading	104
1.3. Depassivation study of Virgo™38 under constant load	107
1.4. Parameters influencing depassivation of Virgo™38	108
1.4.1. Influence of composition heterogeneities	108
1.4.1.1. Influence of Cr content.....	108
1.4.1.2. Influence of Ni content.....	109
1.4.2. Influence of applied load	110
1.5. Interpretations of the depassivation of Virgo™38.....	111
2. Experimental methods	118
3. Hydrogen embrittlement of industrial Virgo™38 during SSRT tests	122
3.1. Conditions of the tests	122
3.2. Study of industrial Virgo™38 under cathodic charging in different acid environments.....	123
3.3. Conclusions on HE under cathodic charging in acid environments	131
4. Stress Corrosion Cracking of industrial Virgo™38 during SSRT tests	133
4.1. Conditions of the tests	133
4.2. SCC behavior of Virgo™38 under applied potential.....	134
4.2.1. SSRT tests at a potential in the active dissolution domain of martensite.....	134
4.2.2. SSRT tests at a potential in the active dissolution domain of retained austenite.....	136
4.3. Conclusions on SCC tests under applied potential in acid environment	139
5. Conclusions	140

1. Depassivation of Virgo™38 studied by an electrochemical approach

1.1. Experimental procedure

One of the parameters influencing cracking susceptibility of passive materials is the resistance of the passive film. Several causes of instability, both chemical and mechanical, can affect the resistance of the passive film. The influence of alloying elements on the passivation of stainless steels was extensively studied by XPS and Auger [122][123][124]. Usually, in stainless steels, the passive film is enriched in Cr at the interface between metal and oxide, while hydroxides are concentrated at the interface between oxide and environment [125][126]. Most studies showed that addition of alloying elements such as Mo improved the resistance to the chemical depassivation, across mechanisms like insertion of chlorides in the film.

In this work, the resistance to chemical depassivation of Virgo™38 was studied by potentiodynamic measurements. These experiments were performed on one hand without applying mechanical stresses and on the other hand under constant load. Cylindrical tensile specimens with 4mm diameter were used for tests under applied stress (see Figure 96 later in this chapter) while specimens for electrochemical measurements without mechanical loading were machined as discs of 10mm in diameter. All specimens were prepared by successive mechanical polishing down to ¼µm diamond paste and finishing with colloidal silica. As mentioned in Chapter II, no stress induced martensitic transformation (SIMT) of the retained austenite was detected after this procedure at the surface of samples. All specimens were degreased with acetone and aged in air at least 24 hours before the tests in order to ensure the reproducibility of conditions for in-air passive layer building.

Solutions used for the potentiodynamic measurements were composed of deionized water containing 30g/L NaCl and 0.4g/L sodium acetate. These solutions were purged with CO₂ and acidified with HCl 24h before the tests. pH was re-controlled directly before starting the tests. Potential and current were recorded using a potentiostat PGP201 coupled with the software VoltaMaster 4. All the experiments were performed at room temperature. The working electrode was immersed during 15min in the solution and the open circuit potential (OCP) was recorded. Then, a scan at 1mV/s was performed from -50mV/OCP until the current density reached 1.5mA/cm². For the polarizations under constant load, the samples were loaded at 750MPa (corresponding to 0.2% proof stress) and put in contact with the solution 15min later, after the stress had reached a stable value of approximately 720MPa (i.e. 95% of the proof stress) after relaxation of around 30MPa.

Experiments without loading on quenched and industrial specimens were performed in an in-house designed electrochemical cell showed in Figure 77.

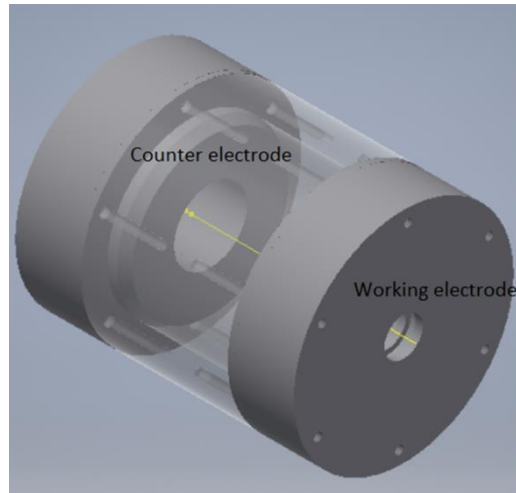


Figure 77 - Electrochemical cell designed for potentiodynamic tests without applied stress

The counter electrode (CE) was a platinum sample of 7cm² and the reference electrode was a saturated calomel electrode (SCE). The work electrode (WE) for tests without mechanical stresses is inserted in a hole of 10mm in diameter and protected from crevice corrosion using silicon paste at its borders. The real surface exposed to the solution is measured by optical microscopy before each test. The SCE electrode was inserted between CE and WE. Experiments without loading were performed on quenched and industrial specimens while experiments under constant load were performed only on industrial specimens. Experiments under constant load were performed in O-rings cell instrumented with the same electrochemical material as presented previously (PGP 201 potentiostat and software VoltaMaster 4).

1.2. Depassivation study of Virgo™38 without loading

By analogy with Lean Duplex Stainless Steels (LDSS) and due to the partitioning effect of alloying elements on the industrial alloy after tempering, according to the results presented in Chapter II, a splitting of the dissolution peak (activity peak) while lowering the pH of the solution may be expected [52][127][128]. Since specimens in the quenched state are purely martensitic, we expect the emergence of a single activity peak while lowering the pH of the solution. The amount of two major elements (Cr and Ni) for three phases: martensite obtained by quenching α' , tempered martensite α'' and retained austenite γ_R were calculated using ThermoCalc® and are recalled in Table 13.

Table 13 - Chemical compositions of major elements in fresh martensite, tempered martensite and retained austenite according to ThermoCalc® after different heat treatments (quenched and industrial)

	%Cr	%Ni
Fresh martensite α'	15.5	4.5
Tempered martensite α''	15.5	3
Retained austenite γ_R	13	11

Because there is a significant difference between Cr and Ni contents in retained austenite and tempered martensite, it is expected to observe two different depassivation behaviors for both phases on the industrial specimens, as observed on LDSS [52].

Figure 78 represents the polarization curves obtained at different pH to analyze the electrochemical behavior and determine the depassivation pH (pH_D) of industrial Virgo™38 without mechanical loading in acid environments.

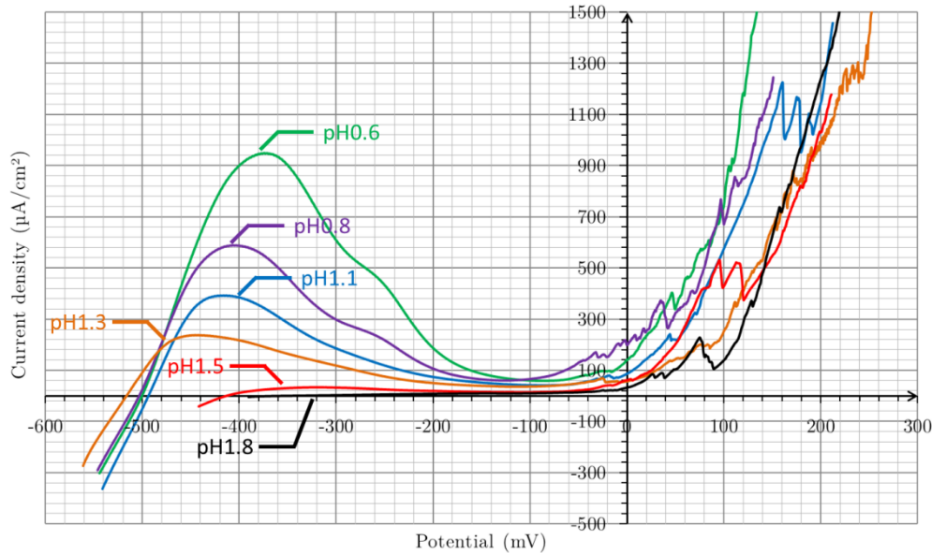


Figure 78 - Potentiodynamic measurements performed at different pH without mechanical loading on Virgo™38 at industrial state ($\alpha'' + \gamma_R$ phases) in 30g/l NaCl + 0.4g/L NaCH₃COO solution acidified with HCl

By gradually decreasing pH, one can see the formation of an activity peak with an increasing maximal current density at the peak. Depassivation pH, defined as the pH corresponding to the critical current density, which is considered to be of the order of magnitude of 10 μ A/cm² for stainless steels [129][130], is around pH=1.6. As expected by comparison with duplex stainless steels [52][127][128], at lower pH and particularly below pH=1.5, two peaks of activity separated by 100 to 150 mV appear on the curves.

To identify the phases corresponding to each of the activity peaks, samples were immersed in the solution at pH=0.6 (where current intensities associated to the two peaks are maximal) during 24h at the potentials corresponding to the two activity peaks (-400mV/SCE and -280mV/SCE) [52]. Figure 79 presents the SEM micrographs of the corroded surfaces which highlight the selective dissolution of one of both phases, according to the potential applied.

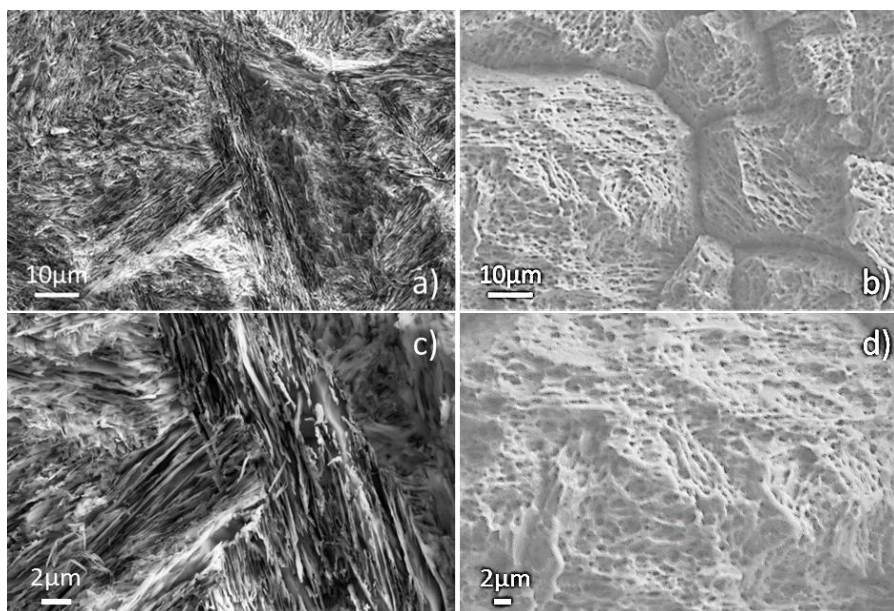


Figure 79 - SEM micrographs after preferential dissolution test in the solution at pH=0.6: a) and c) 24h at -400mV/SCE showing the dissolution of α'' and b) and d) 24h at -280mV/SCE showing the dissolution of γ

Chapter III: Hydrogen Embrittlement and Stress Corrosion Cracking of Virgo™38 in acid environments

Figure 79-a-c and Figure 79-b-d show the surface aspect of specimens observed after expected selective dissolution by maintaining the potential at values corresponding to the two potentials of activity peaks respectively. After maintaining a potential equal to -280mV/SCE , only martensite was left in the surface, while after maintaining a potential equal to -400mV/SCE , only retained austenite was observed. In the latter case the distance between flat austenite grains corresponds to the average thickness of dissolved martensite grains. Moreover, Figure 79-b illustrates intense dissolution of regions corresponding to prior austenite grain boundaries. This effect may obviously be due to the formation of reverted austenite in these regions during tempering, but at the same time it might result from the presence of non-transformed residual austenite during oil quenching, as suggested in Chapter II.1.2.1 (Figure 52). The dissolution rate of prior boundaries clearly appears to be higher than that of lath austenite, which may result from a local small difference of chemical composition between both austenitic regions, consecutive to intergranular segregation occurring during quenching at temperatures above M_s . The observations of selective dissolution are consistent with the results obtained on LDSS [52] where the peak of Cr-enriched phase (α phase) is more cathodic while the activity peak of the γ phase is more anodic. In addition, by increasing pH up to 1.5, the α peak disappears showing a passivated state of the martensite while retained austenite still remains active but with a significantly lower corrosion rate. Ultimately, the particular electrochemical behavior of DSS can be extended to Virgo™38 stainless steel, which do not have a single pH_D but one for each of its phase, namely 1.6 for retained austenite and 1.5 for tempered martensite.

As seen previously, Cr content is more important in tempered martensite than in retained austenite and as it has a very cathodic potential ($E[\text{Cr}/\text{Cr}^{2+}] = -992\text{mV/SCE}$ [131]), it is not surprising to see that the most cathodic peak corresponds to the phase containing the highest amount of Cr. Similarly, the activity peak corresponding to more noble potentials is associated to the dissolution of retained austenite.

Unlike in tests on the two-phase alloy, reported above polarization tests performed on quenched α' phase alloy reveal a single activity peak for pH below 1.5 as seen in Figure 80.

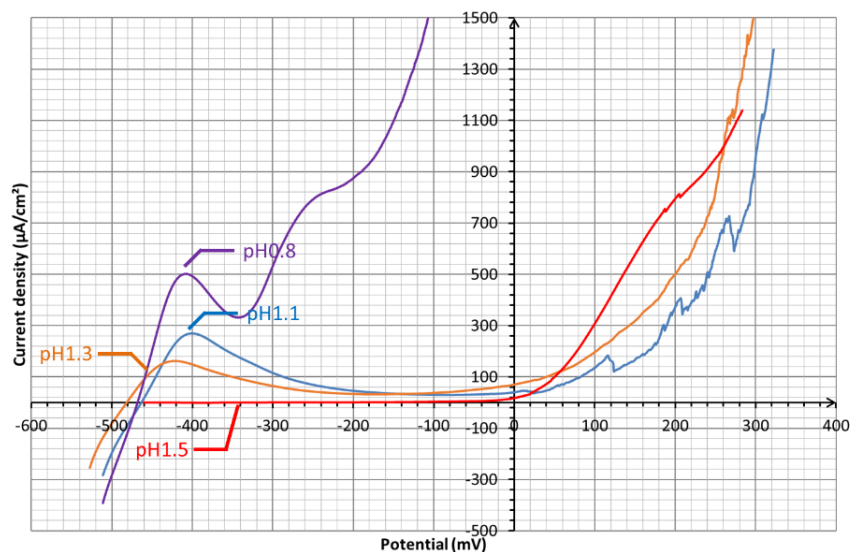


Figure 80 - Potentiodynamic measurements performed at different pH without mechanical loading on the re-austenitized and quenched specimens in $30\text{g/l NaCl} + 0.4\text{g/l NaCH}_3\text{COO}$ solution acidified with HCl. Test at $\text{pH}=0.8$ developed crevice corrosion under the seal but did not influence the measure of the single corrosion peak

The current densities recorded at the activity peaks for each phase of industrial alloy (measured by deconvolution of the activity peaks) and at the unique activity peak of the alloy in the quenched state are presented in Figure 81.

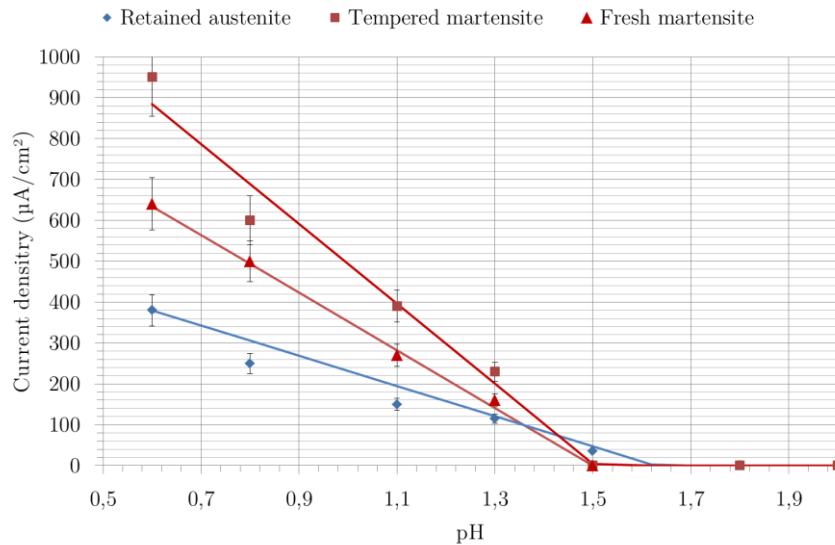


Figure 81 - Current densities measured at the activity peaks at different pH without loading: comparison between fresh martensite obtained by quenching after re-austenitization, tempered martensite and retained austenite

The depassivation pH and the slopes of the curves (representing the effect of pH on corrosion rate) for the three phases are presented in Table 14 where are recalled the Cr and Ni contents for each phase.

Table 14 - Depassivation pH and slope measured on Figure 81 for the different phases without mechanical charging

	pH _D	%Cr	slope (µA/cm ² /pH)	%Ni
Fresh martensite α'	1.5	15.5	-705	4.5
Tempered martensite α''	1.5	15.5	-980	3
Retained austenite γ _R	1.6	13	-370	11

Fresh and tempered martensites have the same depassivation pH (pH_D close to 1.5), which is explained by the fact that they contain the same amount of Cr. The formation of a protective and stable film would be possible only when the chromium concentration in the film exceeds 50% of overall cations, which makes it possible to effectively inhibit the oxidation and dissolution of iron [132][133]. In addition, it was shown that the rate of repassivation of Fe-Cr binary steel increases with the chromium content of the alloy. The depassivation pH of retained austenite is higher, equals to 1.6 due to lower Cr content. The difference of the evolution of the dissolution rates as a function of pH (slopes of the curves) can be explained by the Ni content. Both effects will be discussed later.

1.3. Depassivation study of Virgo™38 under constant load

The same procedure of potentiodynamic measurements was applied for tests under constant load on O-ring machine on the industrial microstructure containing 22% of retained austenite. The stress applied corresponds to 0.2% proof stress (around 750MPa). Figure 82 represents current densities recorded at the activity peaks for each phase as previously done for tests without mechanical loading.

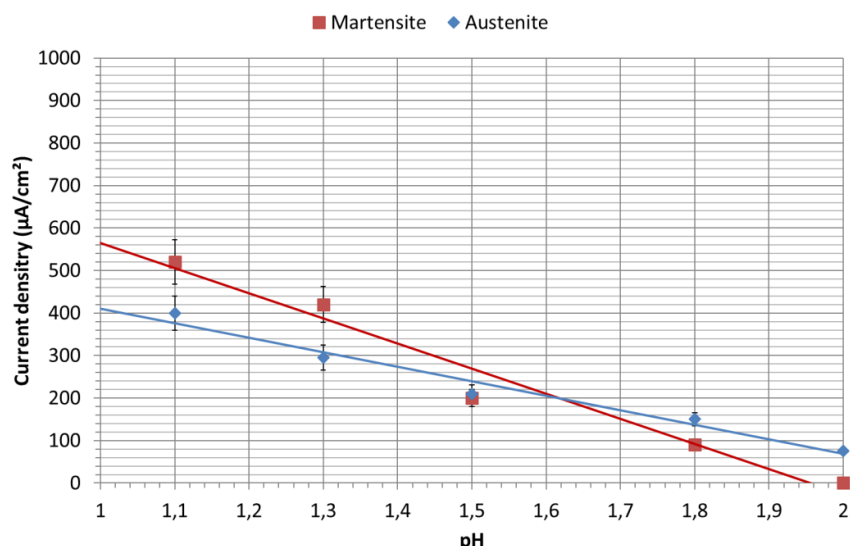


Figure 82 - Current densities measured at the activity peaks at different pH under a 750MPa constant stress

In Table 15 are reported the depassivation pH, the slope of current density vs pH curves and Ni and Cr contents. Depassivation occurs for higher pH in tests under constant load than without loading. As in the previous case, the Cr-rich tempered martensite is depassivated for lower pH than retained austenite.

Table 15 - Depassivation pH and slope measured on Figure 82 for the different phases under constant load

	pH _D	slope (µA/cm ² /pH)	%Cr	%Ni
Tempered martensite α''	1.9	-590	15.5	3
Retained austenite γ _R	2.2	-340	13	11

By comparing Table 14 and Table 15, one can see that the pH effect appears less marked under constant load in tempered martensite than without mechanical stresses applied while it is similar for retained austenite in both conditions.

1.4. Parameters influencing depassivation of Virgo™38

1.4.1. Influence of composition heterogeneities

1.4.1.1. Influence of Cr content

As mentioned previously and as visible in Figure 83, the depassivation pH (pH_D) decreases with increasing Cr content. Indeed, the pH_D has already been observed to decrease with the increasing Cr content in LDSS [52]. It is also important to note that the pH_D is shifted towards higher values in presence of applied stress. This shift is more important in retained austenite than in tempered martensite.

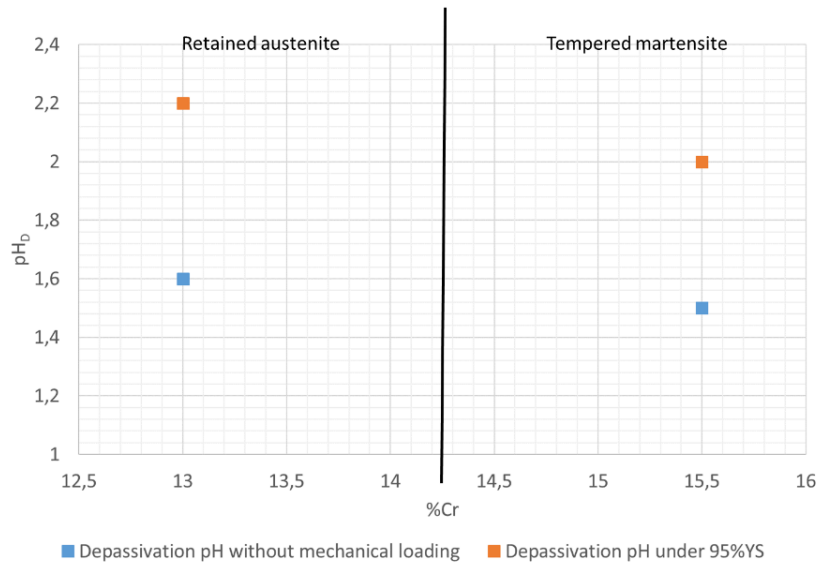


Figure 83 - Influence of the Cr content on the depassivation pH measured with and without stress applied

The difference in depassivation pH_D between both phases is thus explained by the variation of the Cr content due to the partitioning of alloying elements during the tempering treatment. Indeed, Cr is the element known to form the passive film, it is thus not surprising to see that it influences its stability in acid solutions.

The Cr content also has an influence on the position of the activity peak. Indeed, as Cr has a very cathodic potential ($E[Cr/Cr^{2+}] = -992\text{mV/SCE}$ [131]) compared to iron ($E[Fe/Fe^{2+}] = -688\text{mV/SCE}$ [131]), the peak corresponding to the dissolution of the phase rich in Cr (tempered martensite in our case) is supposed to be located at more cathodic potential. This shift has been observed experimentally in Figure 78 and confirmed by SEM observations after potentiostatic measurements presented in Figure 79.

Since Virgo™38 is used in sour environments containing H_2S for some of its application, it would be necessary to determine the influence of H_2S partial pressure on the depassivation mechanisms. Richoux et. al. [56] showed that the presence of H_2S does not influence the mechanism itself but shifts the depassivation pH towards higher values.

1.4.1.2. Influence of Ni content

According to the literature data [52], the corrosion rate decreases when the Ni content increases. To check this relationship in Virgo™38, two polarization curves at same pH are compared in Figure 84. In this figure, we can compare the peaks which correspond to the dissolution of the quenched and tempered martensites respectively. Both phases contain the same amount of Cr (15.5 wt%) but a significantly different Ni content (4.5 wt% in quenched martensite vs 3 wt% in tempered martensite). The current density at the activity peak is lower when Ni content is more important. Note also that the actual surface that contributes to the corrosion peak is higher in the quenched state containing 100% of martensite, as opposed to the industrial state where martensite occupies only 78% of the tested surface. Even with its higher surface, the intensity of its peak is significantly lower.

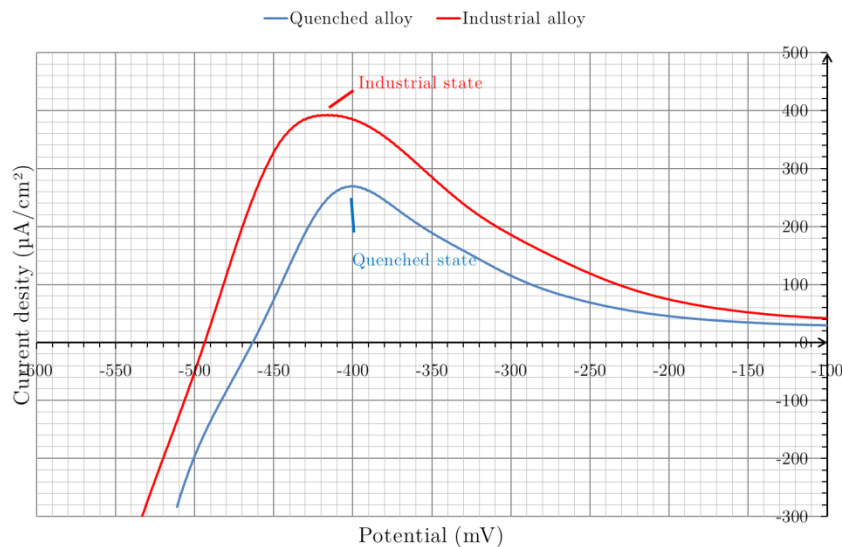


Figure 84 - Comparison of potentiodynamic polarization curves of quenched and industrial alloy at pH=1.1 showing the influence of Ni content on the intensity of the corrosion peak: beneficial effect of Ni

As for Cr, Ni content has also an influence on the position of the activity peak. Indeed, Ni has a more anodic potential ($E[\text{Ni}/\text{Ni}^{2+}] = -498\text{mV/SCE}$ [131]) compared to iron ($E[\text{Fe}/\text{Fe}^{2+}] = -688\text{mV/SCE}$ [131]). The peak corresponding to the dissolution of the phase richer in Ni (retained austenite or quenched martensite compared to tempered martensite in our case) is supposed to be located at a more anodic potential. This difference can be seen in two cases: between quenched and tempered martensite in Figure 84 or between retained austenite and tempered martensite in Figure 78.

As previously mentioned, Ni content has also an influence on the evolution of the dissolution rates as a function of pH (slopes of the curves in Figure 81 and Figure 82) as seen in Table 16.

Table 16 - Influence of the Ni content on the effect of the pH of the corrosion rate with and without stress applied

	Effect of the pH on the dissolution rate measured without loading ($\mu\text{A}/\text{cm}^2/\text{pH}$)	Effect of the pH on the dissolution rate measured under 95%YS ($\mu\text{A}/\text{cm}^2/\text{pH}$)
3wt% Ni	980	590
4.5wt%Ni	705	/
11wt%Ni	370	340

The higher the Ni content, the less important the effect of the pH on the dissolution rate. This observation is in a good agreement with the previous one. The application of a constant load decreases the effect of the pH on the dissolution rate, especially for low Ni content, which could indicate a possible new mechanism activated. Apparently, pH is not the only parameter which influences the depassivation in this case.

1.4.2. Influence of applied load

We can see in Figure 85 that the application of a constant load close to the 0.2% proof stress increases the corrosion rates (current densities at the maximum of activity peaks) for both phases. The gap between curves is more important for retained austenite, which indicates that the increase is more significant in this phase as seen previously.

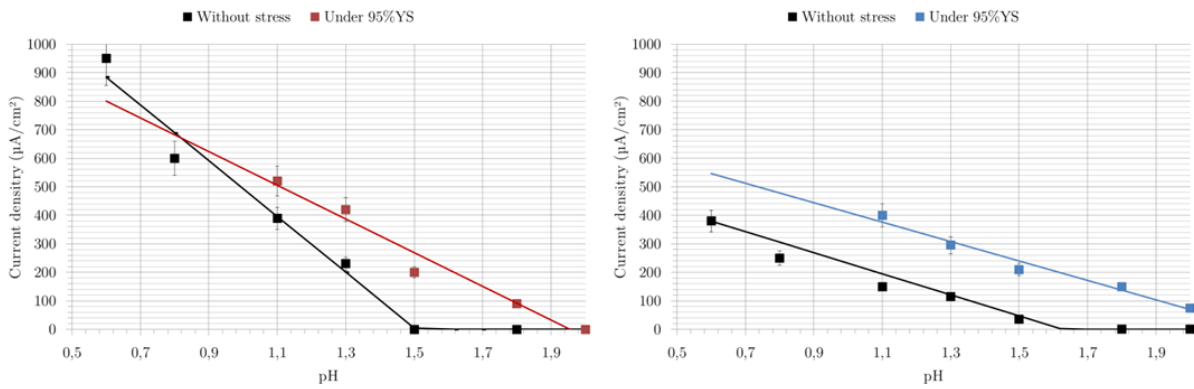


Figure 85 - Influence of the constant stress applied on the current densities measured at the activity peaks as a function of pH for tempered martensite (left) and retained austenite (right)

The higher destabilization of retained austenite under mechanical loading compared to martensite could be due to:

- the emergence of shear bands at the surface of retained austenite being more detrimental than at the surface of tempered martensite
- a less stable passive film at the surface of retained austenite
- a different composition of the passive film of retained austenite

1.5. Interpretations of the depassivation of Virgo™38

The emergence of shear bands in retained austenite can potentially be observed by AFM, providing the use of extremely sharp tips. In fact, due to the dimension of austenite grains (a few hundreds of nm), the study of the emergence of plastic bands at the surface has appeared more challenging than initially envisaged and we were not able to demonstrate whether slip bands effectively appeared first on martensite as expected from mechanical analysis in Chapter II, where austenite was suggested as a mechanically stronger phase.

The passive film composition and thickness at the surface of individual grains of the retained austenite can only be studied by performing Auger measurements as this methods provides the required lateral resolution of some dozens of nanometers, however it does not provide the useful information about chemical bonds. Alternatively, on much larger areas containing hundreds of grains, XPS spectroscopy is certainly the most suitable method. Several bibliographic studies deal with passive film nature and thickness on duplex stainless steels where partitioning mechanism also occurs. Since microstructure size scale is larger in DSS the differences in composition between alpha and gamma phases are less pronounced. On the whole there is only a limited consensus on actual physico-chemical properties of passive films on such two-phase alloys.

Some authors analyzed the effect of static stresses and plastic strains on the corrosion kinetics of metallic materials [134][135][136][137]. Their conclusions converge in the sense that elastic stresses shift the corrosion potential, and that plasticity accelerates the dissolution rates in an order of magnitude higher than that caused by elastic stresses. At the beginning of 1990s, Gutman [138] formalized, using a thermodynamic approach, the effects of mechanical stresses and plastic strains on the mechano-electrochemical potential of materials in aqueous environments. Directly related to the kinetics of anodic and cathodic reactions, the potential shift was based on the influence of elasto-

Chapter III: Hydrogen Embrittlement and Stress Corrosion Cracking of Virgo™38 in acid environments

plastic effects on what was compiled as the mechanochemical potential. The model considers the elastic effects to be governed by the hydrostatic component of the applied stresses and the plastic deformation effects to be governed by the piling-up of dislocations on the surface in contact with the electrolyte. All these effects could be at the origin of the higher destabilization of the retained austenite in Virgo™38.

As already suggested, it is possible to study the passive film composition and thickness through XPS analyzes. Before presenting our results, let's imagine possible scenarios. In a first hypothesis, based on the composition differences between tempered martensite (15.5%Cr) and retained austenite (13%Cr) in industrially heat treated Virgo™38 (Table 13), one would expect that Cr content of the passive film at the surface of retained austenite would be lower than that at the surface of tempered martensite. Cr would probably be replaced by Fe (as Ni is usually not found in the passive film of stainless steels) leading to a more porous passive film with a higher thickness. This first hypothesis is schematically presented in Figure 86 for both microstructures presented previously (quenched and industrial, where black dots represent very small carbides).

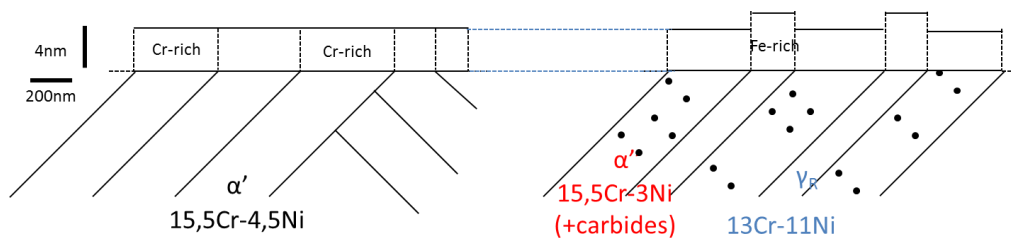


Figure 86 - Schematic representations of microstructures and hypothetical relative thickness of passive films on the quenched (left) and industrial (right) microstructure: first hypothesis. We suppose a thicker passive film at the surface of retained austenite due to its potential enrichment in Fe. In opposition, the passive film at the surface of quenched and tempered martensites would be Cr-rich due to the high Cr content of these phases. In overall, the resulting thickness would be higher in the industrial state than after quenching.

To check this hypothesis, XPS measurements were performed on both metallurgical states using mirror polished samples. The spectra obtained are presented in Figure 87. To improve graphical representation, a constant of 80 000 counts/s is added after the measurements on the industrial sample.

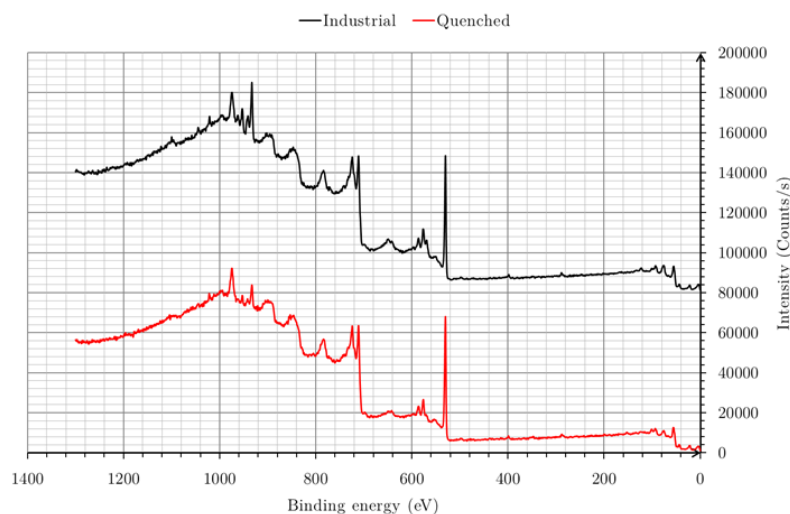


Figure 87 - XPS spectra obtained after measurements on quenched and industrial Virgo™38 mirror polished and cleaned 1min using ion cleaner. Some qualitative differences can be noticed, consequently quantitative analysis has to be performed.

It is difficult to visually distinguish differences on these survey spectra (Figure 87). For this reason, complementary angular resolved analyses were performed on Fe and Cr peaks. An example of the spectrum obtained is presented in Figure 88.

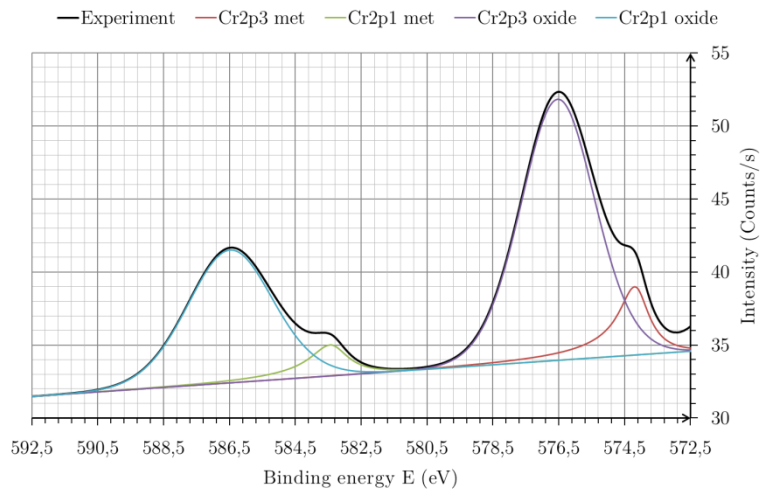
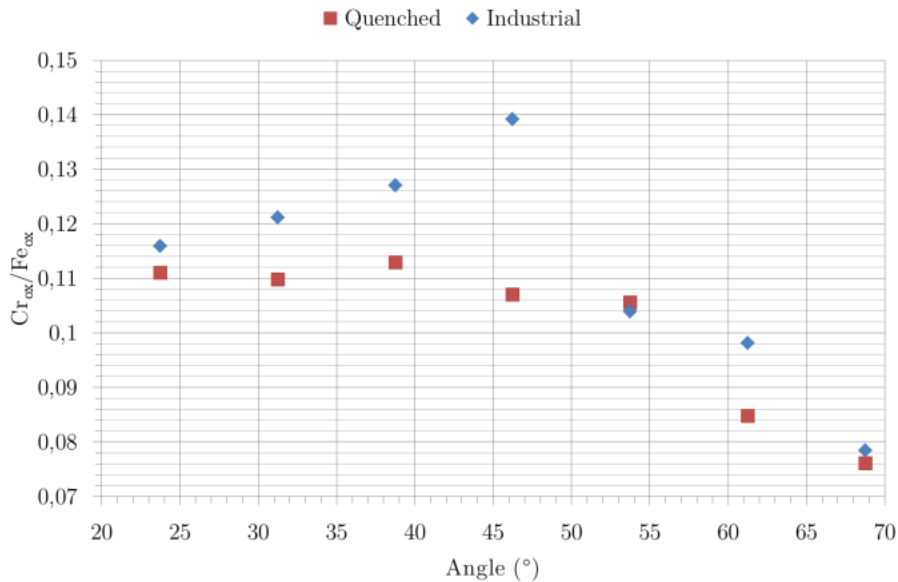


Figure 88 - XPS spectrum of Cr peaks in the range 572-592eV obtained after measurements on industrial Virgo™38 with a detection angle of 23.75° showing the decomposition of the spectra in two peaks: metallic and oxide

One can clearly see two doublets: Cr $2p^{1/2}$ on the left and Cr $2p^{3/2}$ on the right. Peaks corresponding to the oxide are of much higher intensities than those corresponding to metal (small shoulders on the right, at 574 and 583.5eV). We can thus, by a decomposition of these peaks, determine the intensities of both contributions and give quantitative results on the composition of the passive films (Figure 89).



a)

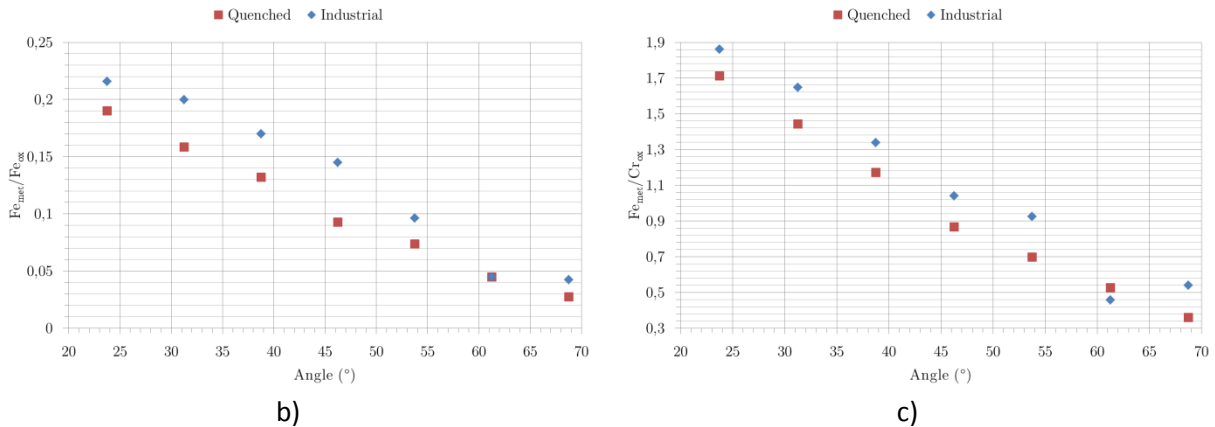


Figure 89 - Ratios of intensity determined after XPS measurements: a) Cr_{ox}/Fe_{ox} , b) Fe_{met}/Fe_{ox} and c) Fe_{met}/Cr_{ox}

Figure 89-a shows that Cr_{ox}/Fe_{ox} ratio in the quenched sample is constant as a function of the detection angle (with respect to the normal to the surface) up to 55° and then decreases which indicates the presence of two oxide layers. The layer at the metal/oxide interface (with stronger contribution at low angles) is a Cr-rich oxide. A Fe-enriched layer is present at the top of the oxide. After industrial heat treatment, this ratio is slightly increasing up to 55° (this tendency is rather unusual and could not be interpreted) and then is decreasing, as on quenched state, which indicates a Cr enrichment at the metal/oxide interface and, once again, the presence of a Fe-enriched layer at the top of the oxide. Moreover, there is more Cr in the passive film after industrial heat treatment than in the quenched state. This higher Cr content could be due to a thinner Fe enriched passive film at the surface. Figure 89-b and Figure 89-c just indicate that it is easier to see metallic iron for all angles on industrial alloy; therefore the oxide film on industrial alloy is thinner (in average), which is not coherent with the previous assumption. Furthermore, Figure 90 confirms that the passive film is thinner after industrial heat treatment as compared to the quenched state.

Consequently, our first hypothesis, even if apparently sound, was not confirmed by experimental observations. The possible reason is the omission of non-identified factors decisive with respect to the composition of passive films.

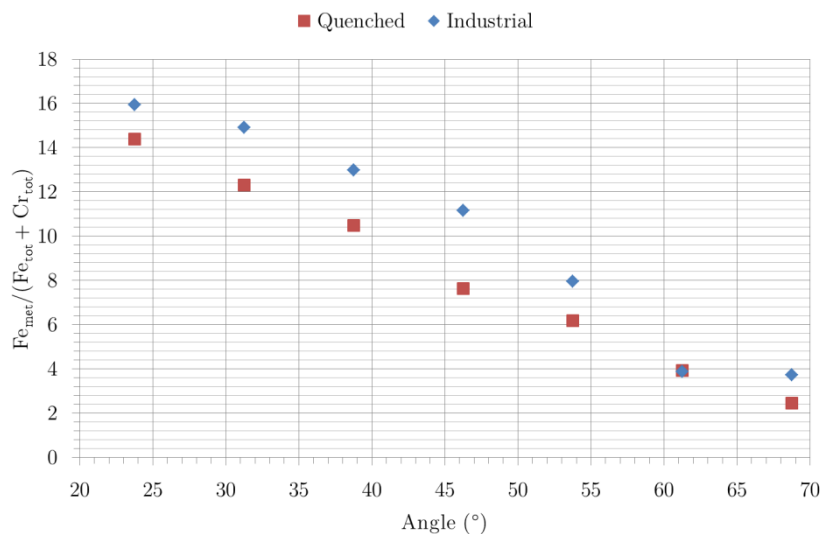


Figure 90 - Metallic iron relative intensities determined after XPS measurements showing systematically higher values for industrial state. It indicates a thicker passive film in the quenched state.

In fact, even if their Cr content is the same, there is a strong difference between fresh martensite of the quenched specimen and tempered martensite of the industrial alloy. The former is characterized by a high dislocations density while the latter contains fewer dislocations and consequently fewer short circuits for preferential diffusion towards the surface. Moreover, quenched martensite contains carbon atoms in oversaturated solid solution while the BCC lattice of tempered martensite is nearly carbon free. As seen in Chapter II, the dislocations density of retained austenite in the industrial specimen is similar to that of quenched martensite.

The second hypothesis is thus an accelerated diffusion of Fe atoms by dislocations in quenched martensite and retained austenite that would increase the Fe content in the passive film of these two phases (Figure 91) and consequently a faster kinetics of their growth resulting in a higher thickness of these two phases as compared to tempered martensite for the same oxidation time. Furthermore, as their dislocations density is almost the same, the relative thickness of the passive films at the surface of quenched martensite and retained austenite might be analyzed with respect to the difference in diffusion coefficients between BCC (fast diffusion) and FCC (comparatively slow diffusion). Following this concept, higher diffusivity in BCC quenched martensite would result in easier Fe access to the oxide, as opposed to the retained austenite, where, the lower Fe diffusion coefficient would let this film be thinner. Finally, as dislocation density is lower in tempered martensite, this effect of accelerated iron transportation by dislocation can be neglected. Consequently, the passive film would be Cr-rich and the resulting oxide thickness would be smaller.

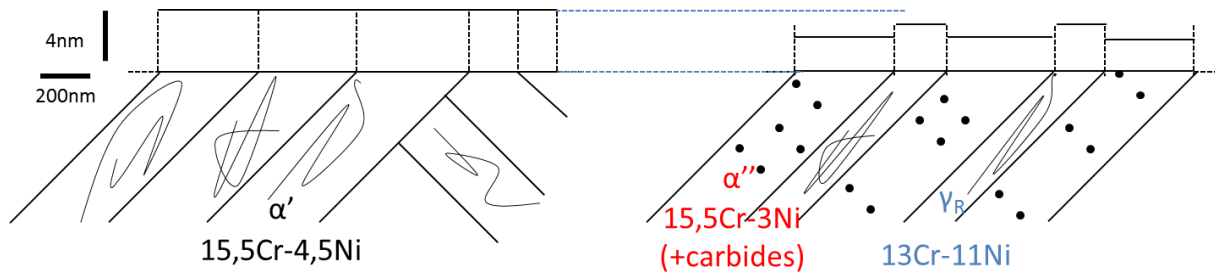


Figure 91 - Schematic representations of microstructures and hypothetical relative thickness of passive films on the quenched (left) and industrial (right) microstructure according to the second hypothesis. We suppose now that the thicker passive film at the surface of quenched martensite and retained austenite is due to the accelerated diffusion of Fe atoms due to dislocations. The passive film at the surface of tempered martensite (78%) is thinner due to its low dislocations density as compared to retained austenite (22%). The resulting total passive thickness as observed by XPS would thus be lower as compared to the quenched state.

According to this hypothesis, the resulting thickness of the passive film on the industrial alloy should be lower, as a consequence of a reduced amount of accelerated Fe diffusion in tempered martensite. Consequently Cr would preferentially oxidize in this phase and form a more compact oxide film. The resulting composition would thus appear richer in Cr.

This second hypothesis matches much better with all XPS measurements presented previously, namely:

- a thicker passive film in the quenched state as compared to the industrial state
- an apparent enrichment in Cr after industrial heat treatment due to lower Fe diffusion
- an heterogeneous composition of the passive film in the industrial state

The composition heterogeneities within the passive layers thickness of the three phases considered can be represented as follow (Figure 92):

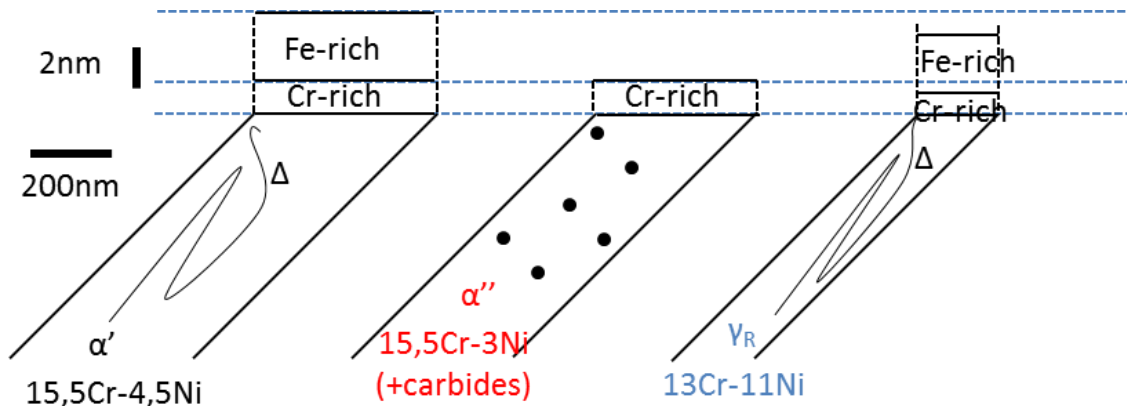


Figure 92 - Schematic representations of the hypothetical relative thickness of passive films on the three phases according to the second hypothesis. We suppose that the Cr-rich layers at the surface of quenched and tempered martensites are equivalent due to the same Cr content in the bulk. The Fe-rich layer at the surface of quenched martensite would be due to its high dislocations density. These assumptions explain the relatively higher Cr content measured by XPS in the industrial state, which actually corresponds to a lower Fe content of the passive layer in this state. The Cr-rich layer at the surface of retained austenite would be thinner due to its lower Cr content in the bulk and a Fe-rich layer would be present due to a high dislocations density.

The relative arrangement of oxide layers could be confirmed or infirmed by performing subsequent SIMS experiments or only cations analysis by high lateral resolution Auger analysis on individual austenite and martensite grains.

The second hypothesis also matches with the experimental data of electrochemical measurements considering that only the Cr rich layer influences the depassivation behavior, namely:

- a thinner and less resistant internal passive film at the surface of retained austenite due to a lower Cr content leading to a 'high' depassivation pH
- equivalent Cr rich passive films (a relatively thicker than that of retained austenite) at the surface of quenched and tempered martensites leading to a lower depassivation pH

This second hypothesis apparently appears to be in contradiction with the AFM mapping presented in Figure 93 on an industrially heat treatment specimen of Virgo™38 mirror polished and aged in air. Indeed, one can see that the passive film at the top of martensite is significantly thicker than the one at the top of retained austenite. However, one must indicate that this difference, in fact in relative altitude of the austenite with respect to the martensite, might result from the polishing procedure rather than from the difference in absolute thickness of oxides above these two phases.

Consequently, the second hypothesis based on accelerated iron diffusion towards surface through high density dislocation network in both fresh martensite and retained austenite, lower Cr/Fe ratio in the film and consequently its poorer quality therefore higher thickness, results in a coherent interpretation of all XPS measurements. In particular, passive film on austenite grains is interpreted as composed of a relatively poor in chromium "Cr(not-so)-rich layer" at the alloy-oxide interface and Fe-rich relatively thick overlayer. Such a passive film must be less resistant than passive films developed on both martensites, as clearly demonstrated by depassivation measurements.

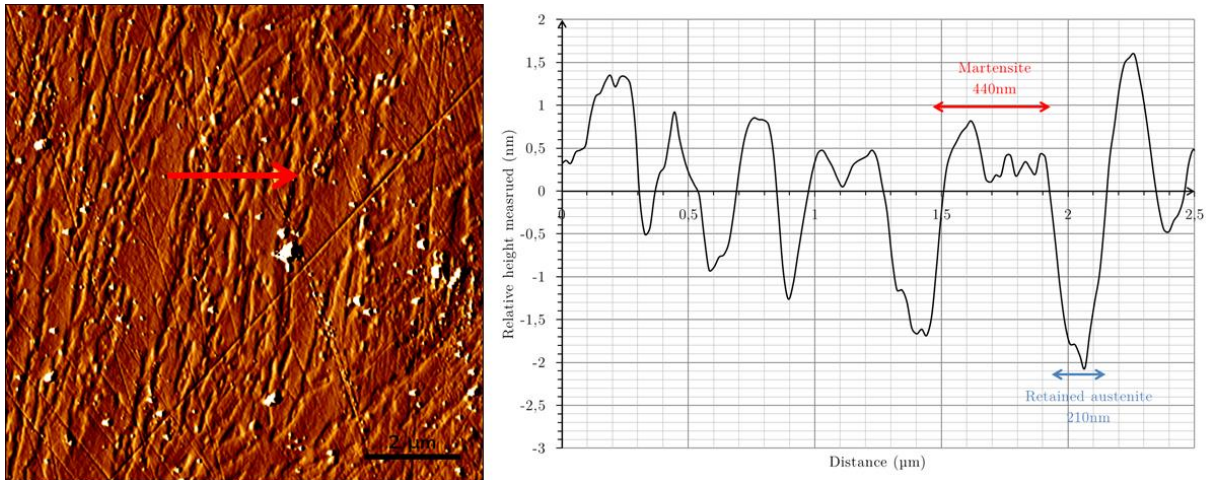


Figure 93 - AFM mapping on mirror polished industrial Virgo™38 aged in air showing that retained austenite is lower than martensite

2. Experimental methods

As mentioned in Chapter I, there are different types of mechanical tests to study the effect of aggressive or hydrogenating environments on materials. In this study, Slow Strain Rate Tensile tests (SSRT) have been chosen since they allow studying both the crack initiation and propagation. Historically, this type of test has been introduced in Stress Corrosion Cracking (SCC) studies because it has been demonstrated that strain rate rather than stress is the main factor that governs the synergetic effects between plastic deformation at a crack tip and the aggressive environment. Stainless steels are very sensitive to environmentally assisted cracking under applied potential during Slow Strain Rate Tensile tests (SSRT). Mechanisms involved can be different according to the potential applied. Indeed, for passive alloys such as SMSS, either SCC or HE is possible according to the applied potential as seen in Figure 94.

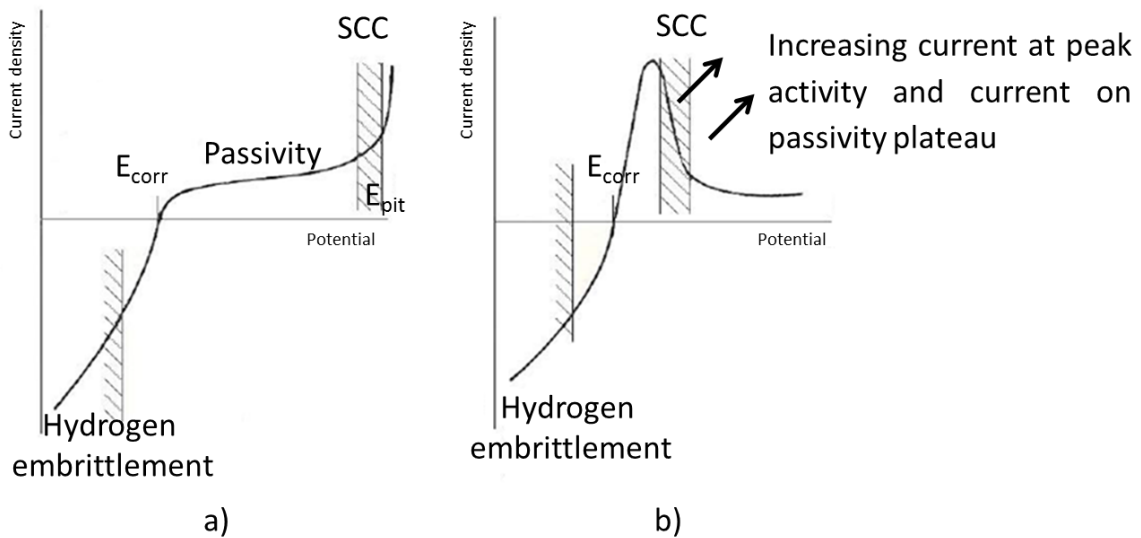


Figure 94 - Domains where SCC and HE are predominant in stainless steels (adapted from [139])
 a) Passive alloy in an environment where $\text{pH} > \text{pH}_0$
 b) System with loss of passivity (for $\text{pH} < \text{pH}_0$)

In SCC domains, passive films are thermodynamically stable but the repassivation kinetic is too slow to prevent crack initiation either by pitting or preferential dissolution.

In order to study both HE and SCC of Virgo™38, two acid environments with different compositions were used (Table 17). The studied potential, either applied cathodic potential or Open Circuit Potential (OCP), were chosen in order to change the mechanism as explained in the following.

Table 17 - Compositions of the different acid environments used during SSRT tests under cathodic charging to study HE of Virgo™38

	Sodium chloride (NaCl) content (g/L)	Sodium acetate (NaCH ₃ COO) content (g/L)	pH (compound used to adjust)	Purging gas	Applied potential (mV/SCE)	OCP (mV/SCE)
Solution 1	30	0	3.5 (CH ₃ COOH)	N ₂	-1200	-455
Solution 2	30	0.4	1.5 (HCl)	CO ₂	-1200	-415

All SSRT tests were performed at different strain rates at room temperature after solution purging during 12h prior to loading. Strain rate is known to be one of basic factor in SCC, as reported by McIntyre et al [140]. According to Parkins [141] there is a critical frequency of the breakdown of the passive film that favors cracking. Indeed, if the applied strain rate is too high compared to electrochemical reactions kinetics, the damage will be only mechanical and will lead to ductile failures while if the applied strain rate is too low, the mechanical effect on depassivation will not be sufficient and passive film will have time to reform. Thus, a competition between repassivation and dissolution can explain the presence of a critical strain rate for anodic SCC phenomenon. However, for hydrogen embrittlement the decrease of the strain rate leads to a decrease of the ductility. The influence of the strain rate on the embrittlement is summarized on Figure 95 for both mechanisms.

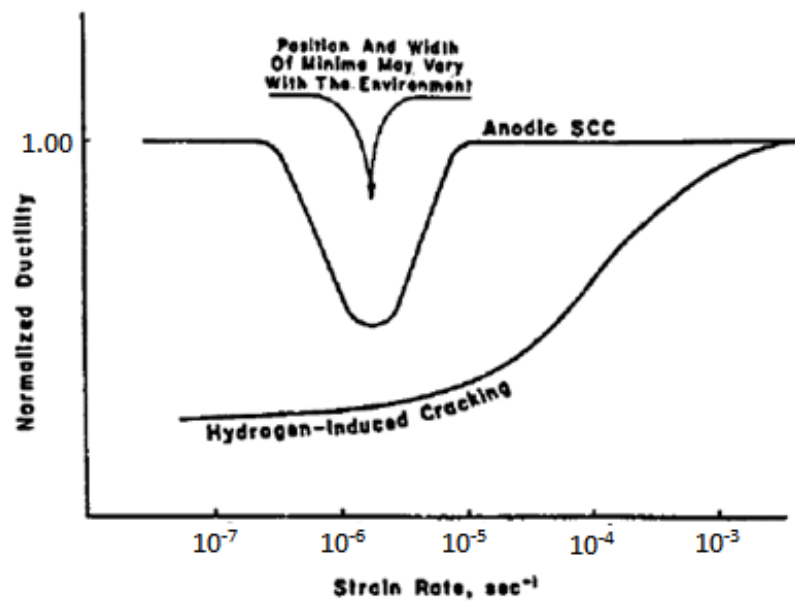


Figure 95 - Influence of the applied strain rate during SSRT test on the embrittlement of a stainless steel by SCC or HE [140]

As studied in Chapter II-2, the samples are taken in the radial direction of the forged impeller. Cylinders of 9mm in diameter are taken by electro-erosion and then machined using a conventional lathe. The geometry of samples is given in Figure 96.

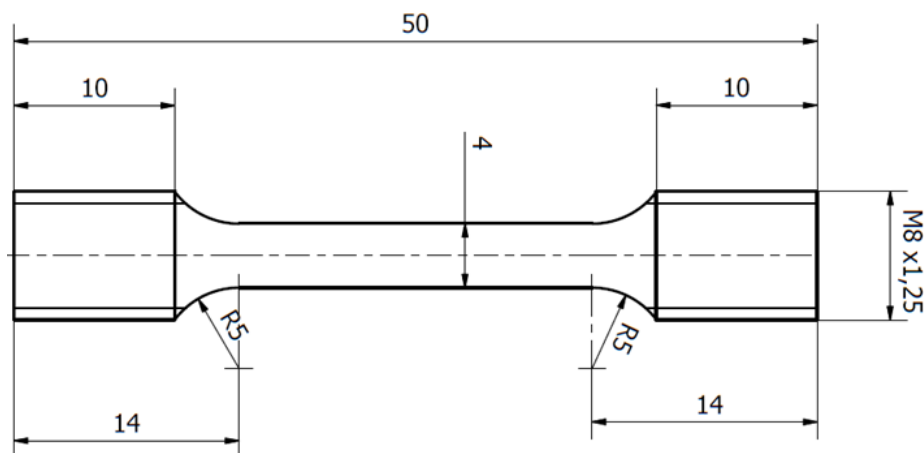


Figure 96 - Geometry of samples used for the SSRT tests under cathodic charging

Chapter III: Hydrogen Embrittlement and Stress Corrosion Cracking of Virgo™38 in acid environments

After machining the roughness of the surface is $0.8\mu\text{m}$. Before the tests, samples were manually polished down to $1\mu\text{m}$ using a conventional lathe, grinding papers and diamond pastes. Figure 97 represents the sample surface after polishing. One can see that samples still have some scratches but these ones are not perpendicular to the tensile direction and have limited depth. Only one sample has been tested by optical profilometer (Figure 97). On this sample, a maximum difference of 600nm has been measured corresponding to the roughness of $0.01\mu\text{m}$ which is far below the values imposed by the NACE TM0177 standard ($0.81\mu\text{m}$).

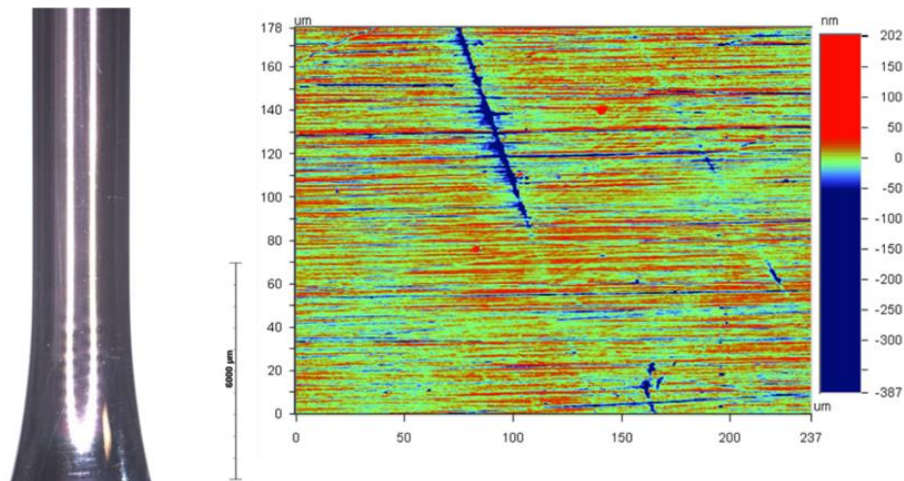


Figure 97 - Surface state previous to the tests:
a) optical microscopy (magnification bar is $6000\mu\text{m}$) and b) profilometer mapping near a scratch

After polishing, each sample is cleaned with ethanol and acetone in an ultrasonic bath and its diameter is measured both by optical microscopy and using a digital caliper.

Slow strain rate tensile tests were performed at École des Mines de Saint-Étienne (France) using a Schenck tensile machine coupled with the Wavematrix software (see Figure 98). The recorded parameters are the load, the displacement using a LVDT captor and either the potential (for OCP measurements) or the current (for tests at constant potential) using a PGP 201 potentiostat. The sample is electrically isolated from the tensile machine by fixing tools made of zirconium oxide.

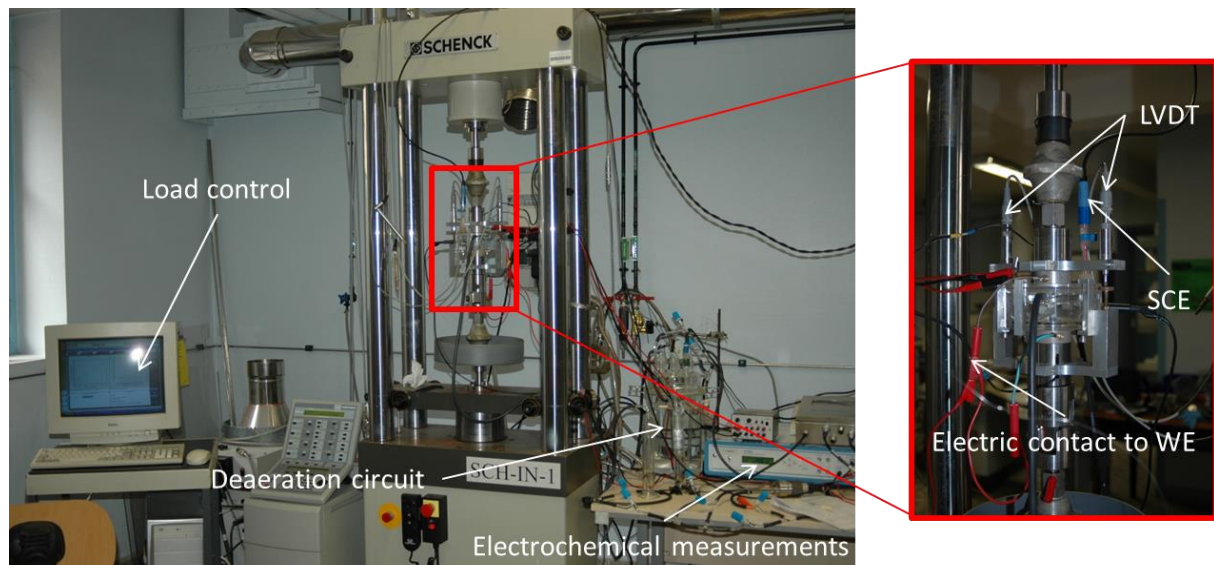


Figure 98 - Slow strain rate tensile tests (SSRT) setup used at École des Mines in Saint-Étienne (France)

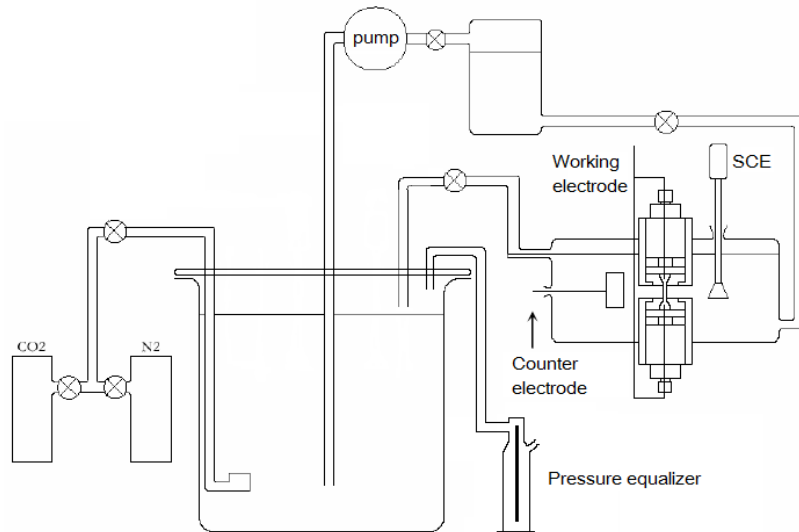


Figure 99 - Schematic representation of the solution circuit for the slow strain rate tensile tests

The solution is purged with a gas (either nitrogen or carbon dioxide) during 12h. The sample is then installed on the tensile machine in the cell and pre-charged at 0,2kN. This cell is purged with the gas during 30min before inserting the solution using a pump. For the tests under cathodic charging, the potential is applied directly when all three electrodes are immersed in the solution and the tensile tests starts directly at a nominal strain rate of 10^{-6}s^{-1} or 10^{-7}s^{-1} . After the test, the samples are dismantled as soon as possible, cleaned with ethanol and observed by SEM. The final diameter close to the fracture surface measured by optical microscopy enables calculating the reduction in area RA (also called Z%) and the ratio of area reduction RAR:

$$RA (\%) = \frac{D^2 - D_f^2}{D^2} * 100$$

where RA is the reduction in area, D the initial diameter and D_f the final diameter at the fracture location.

$$RAR (\%) = \frac{RA_E}{RA_A} * 100$$

where RA_E is the reduction in area in environment and RA_A is the reduction in area in air.

The plastic elongation E_p is measured on the tensile curves and the reduction of plastic elongations RE_p is calculated:

$$RE_p (\%) = \frac{E_A - E_E}{E_A} * 100$$

where E_E is the plastic elongation in environment and E_A is the plastic elongation in air.

3. Hydrogen embrittlement of industrial Virgo™38 during SSRT tests

3.1. Conditions of the tests

First, we focus on the study of Hydrogen Embrittlement of Virgo™38 under cathodic potential applied in the acid environments presented in the previous section. The polarization curves in both solutions are presented in Figure 100 and show a large cathodic domain.

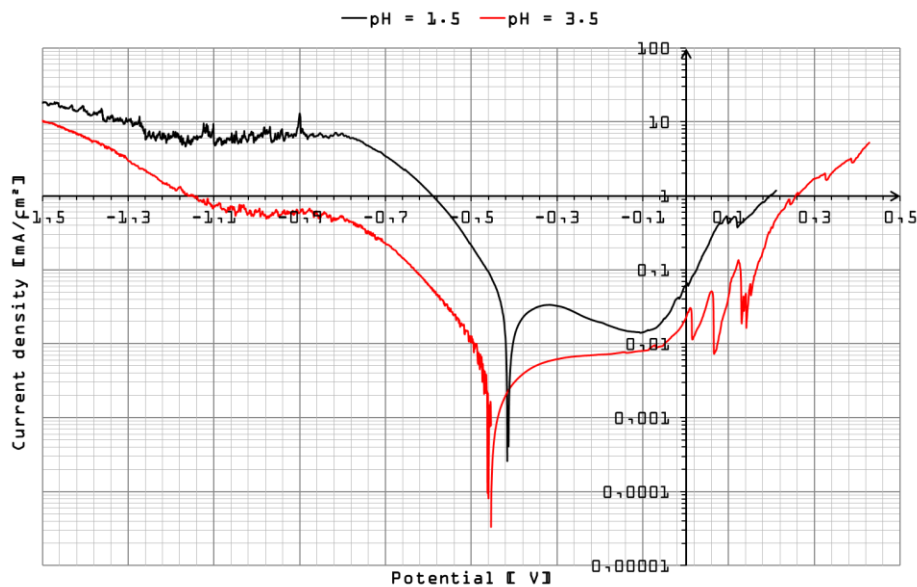


Figure 100 - Polarization curves at 1mV/s in both solutions (pH=1.5 and 3.5) showing a large cathodic domain

A unique potential of -1200mV/SCE has been chosen in order to be positioned far in the cathodic region to ensure the highest hydrogen activity possible in these environments in order to obtain hydrogen embrittlement of Virgo™38. By applying a static potential of -1200mV/SCE, cathodic current of proton discharge is higher for the environment at pH=1.5 than for the one at pH=3.5. Indeed, in this range of cathodic potentials, the current density of protons discharge is dependent on their number and their renewal by diffusion towards the electrode, which increases at lower pH.

3.2. Study of industrial Virgo™38 under cathodic charging in different acid environments

The stress strain curve obtained for test in solution 1 under cathodic polarization at a strain rate of 10^{-6}s^{-1} is presented in Figure 101 and compared to a reference test performed in air at 10^{-5}s^{-1} .

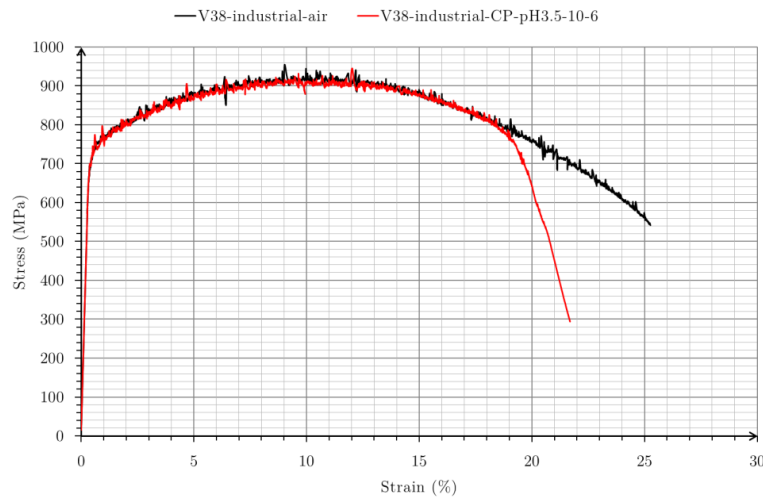


Figure 101 - Tensile curve of Virgo™38 after SSRT tests under cathodic charging at -1200mV/SCE in a solution containing 30g/L NaCl at $\text{pH}=3.5$ (adjusted with acetic acid) purged with N_2 and at a strain rate of 10^{-6}s^{-1} compared to test in air at 10^{-5}s^{-1}

The two curves overlap perfectly up to the final rupture where specimen under hydrogen charging shows reduced necking. The reduction in area measured for the test under cathodic polarization is of 47% compared to 75% in air, which gives a ratio of area reduction of 63%. The reduction of plastic elongation is of 14%. For these environmental conditions comparable to cathodic protection with a medium hydrogen activity, the material presents a ductile macroscopic behavior which contrasts with intergranular fractures observed in service or in environments containing H_2S (see Chapter V).

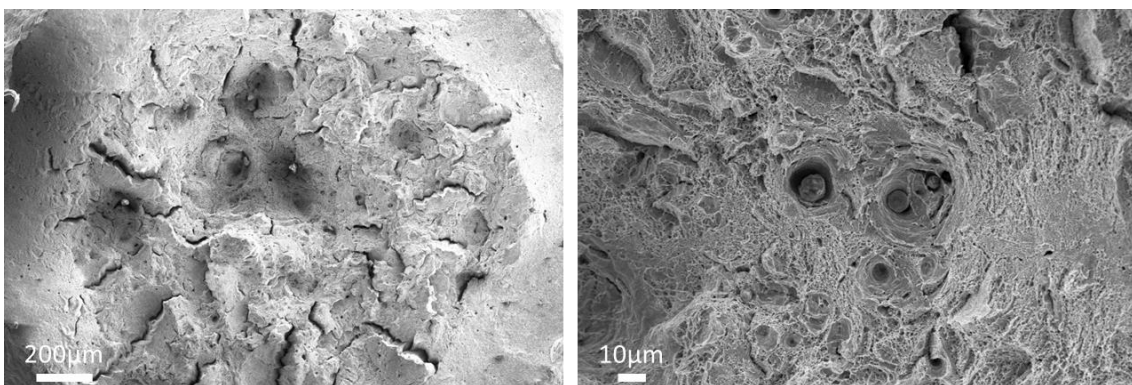


Figure 102 - Fracture surface of Virgo™38 after SSRT test in air at 10^{-5}s^{-1} showing ductile behavior with dimples and particles rich in Al and Ti

Figure 102 shows the fracture surface of specimen tested in air. Typical ductile fracture in cup with circular shear lips is observed. Dimples are present in the central part of the surface while several ruptures by shear are connected with the peripheral zone. These characteristic features indicate an in volume damage by growth of microcavities in the core of the specimen during the necking to final rupture.

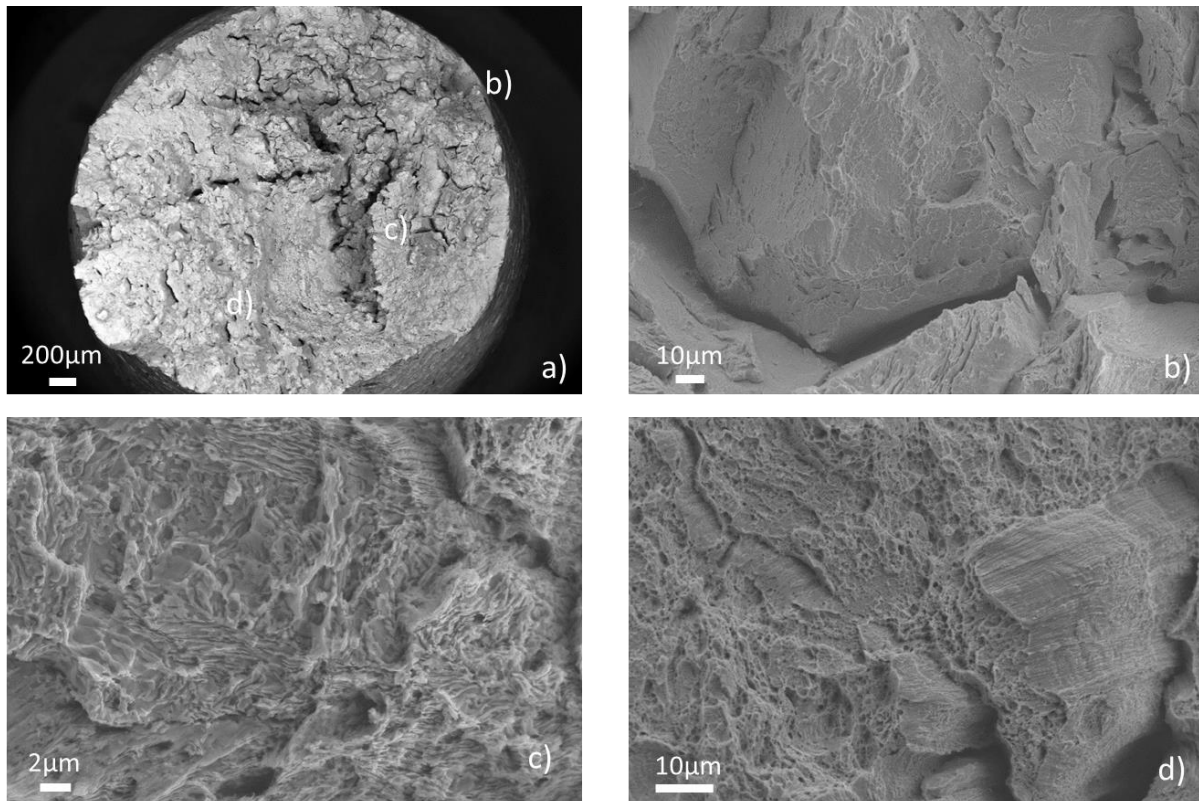


Figure 103 - Fracture surface of Virgo™38 after SSRT test at a strain rate of 10^{-6}s^{-1} and under cathodic charging at -1200mV/SCE in a solution containing 30g/L NaCl at $\text{pH}=3.5$ (adjusted with acetic acid) purged with N_2

- a) Overview of the fracture surface
- b) Detailed image of the crack initiation area (on the right side of a)) showing nearly intergranular failure
- c) Detailed image showing small "chemical etching" on the fracture surface
- d) Ductile region

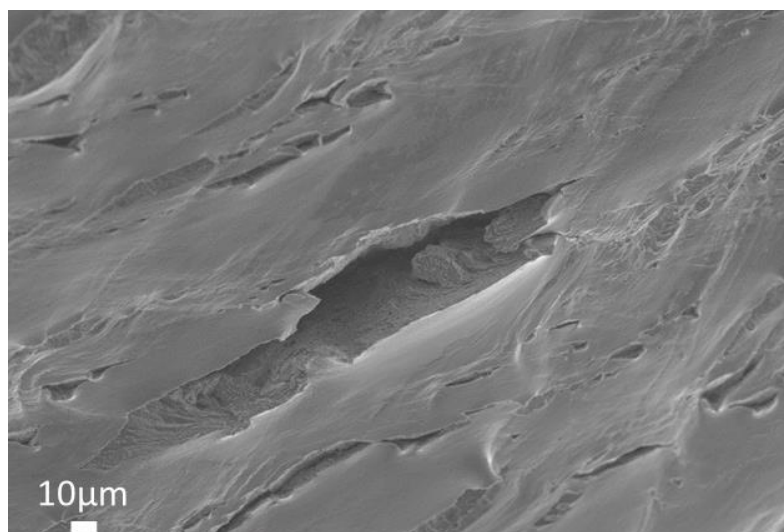


Figure 104 - Barrel surface of Virgo™38 after SSRT test at a strain rate of 10^{-6}s^{-1} and under cathodic charging at -1200mV/SCE in a solution containing 30g/L NaCl at $\text{pH}=3.5$ (adjusted with acetic acid) purged with N_2 showing several secondary cracks with dimples inside

Fracture surface of specimen tested at cathodic potential is presented on Figure 103. Even if some nearly intergranular areas are visible on the fracture surface close to the initiation site on Figure 103-b, the major part of the fracture surface is ductile with dimples. As the fracture surface was exposed to the environment at Open Circuit Potential at the end of the test (during cleaning) it can be observed some areas where dissolution occurred. The mechanism of 'preferential dissolution' will be discussed in section 4 of this Chapter. These conditions are not sufficiently aggressive to reproduce failures that occurred in service. Indeed, at a pH higher than the depassivation pH, the passive film is stable and reform quickly under plastic deformation limiting the entry of hydrogen. Nonetheless, crack initiation occurs on surface (Figure 104) and crack path seems to follow a near-grain boundary region but with a ductile mode of propagation (Figure 103-c and -d).

To increase the brittle character of cracking, it has been chosen to increase hydrogen activity by decreasing the pH of the solution down to the pH_D . The purging gas has been changed from N_2 to CO_2 in order to buffer the pH during the SSRT tests. In this solution (solution 2), the passivity of the material is deteriorated; the domain of passivity is reduced and the current on the plateau is increased. Two tests were performed, one at OCP and the other at cathodic potential of -1200mV/SCE . The strain rates were 10^{-6}s^{-1} in both cases. The stress strain curves obtained are presented in Figure 105 and compared to a reference test performed in air.

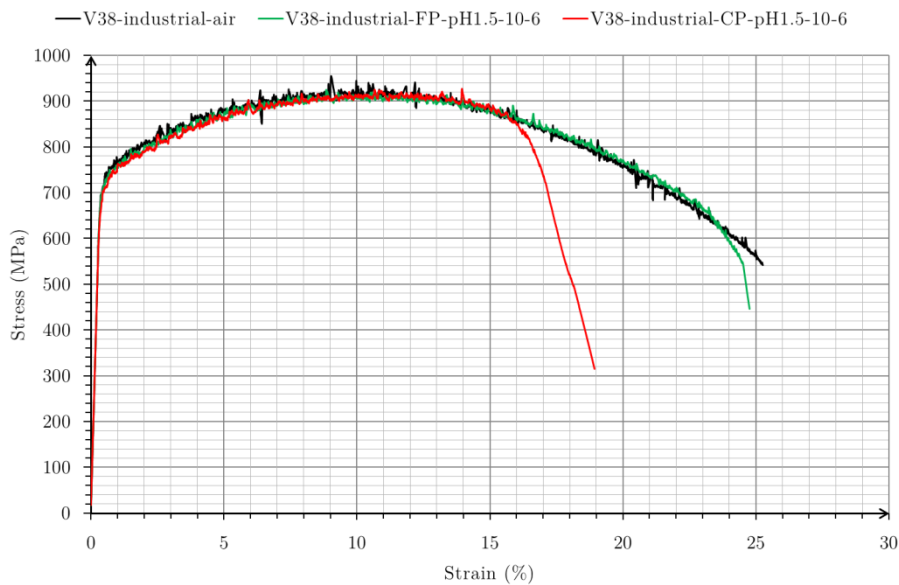


Figure 105 - Tensile curves of Virgo™38 tested at a strain rate of 10^{-6}s^{-1} under open circuit potential (FP, green curve) and cathodic charging at -1200mV/SCE (CP, red curve) in a solution containing $30\text{g/L NaCl} + 0.4\text{g/L}$ sodium acetate at $\text{pH}=1.5$ (adjusted with HCl) purged with CO_2

The results at OCP show that these conditions do not lead to crack initiation. The resulting stress-strain curve (green curve in Figure 105) is perfectly overlapped with the one obtained after the test in air. The fracture surface obtained after the test at OCP shows a failure in cup with dimples (Figure 106-b). Some areas present features of preferential dissolution (Figure 106-c and Figure 107). Neither the hydrogen activity (and its consequences on embrittlement once entered) nor the localized dissolution were sufficient to initiate cracks at this strain rate, even for pH lower than the depassivation pH.

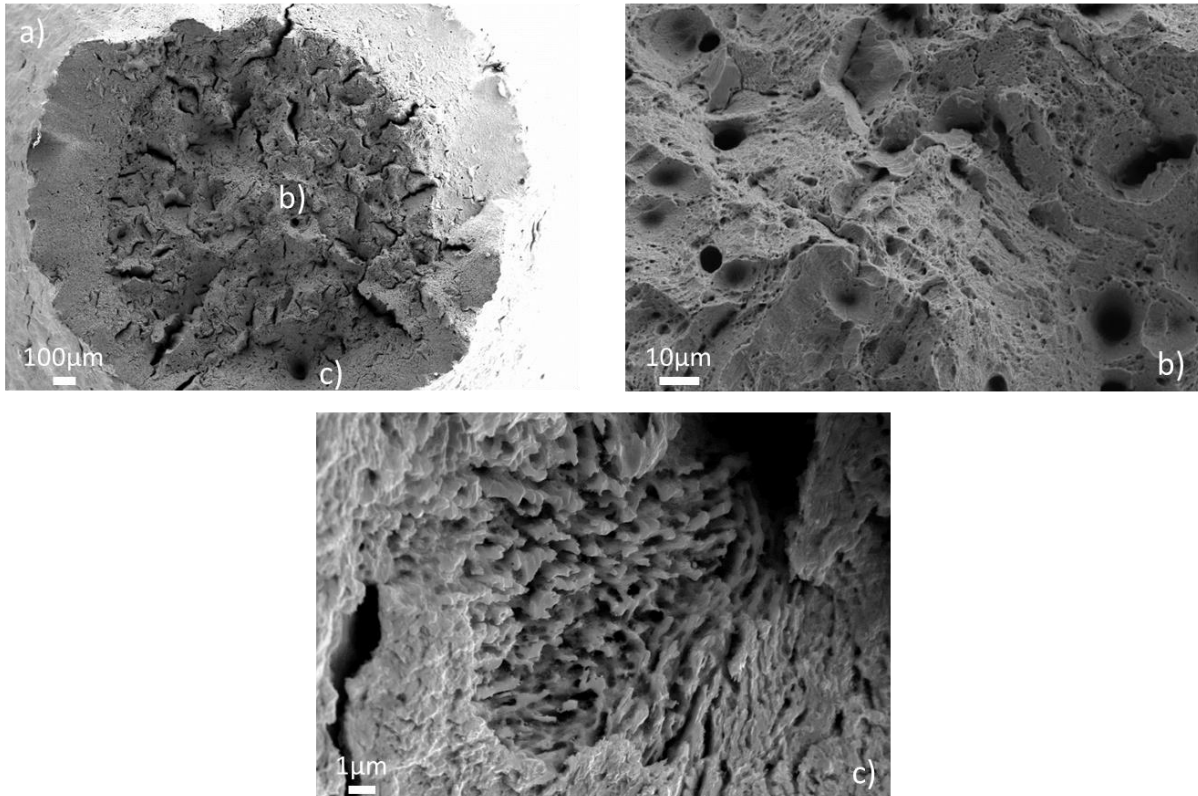


Figure 106 - Fracture surface of Virgo™38 after SSRT test at a strain rate of 10^{-6} s^{-1} and at Open Circuit Potential in a solution containing 30g/L NaCl + 0.4g/L sodium acetate at pH=1.5 (adjusted with HCl) purged with CO_2
a) Overview of the fracture surface showing ductile behavior with dimples
b) Detailed image showing dimples
c) Detailed image showing preferential dissolution on the fracture surface

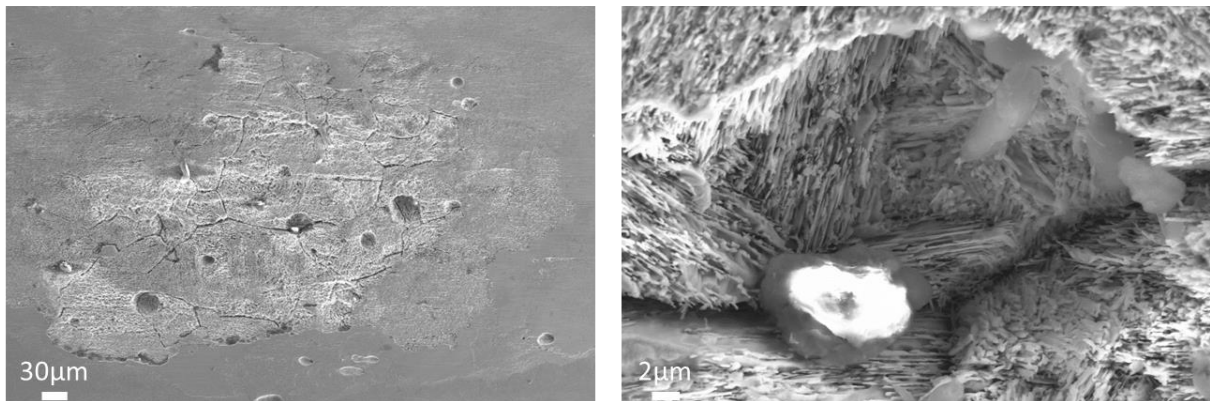


Figure 107 - Barrel surface of Virgo™38 after SSRT test at a strain rate of 10^{-6} s^{-1} and at Open Circuit Potential in a solution containing 30g/L NaCl + 0.4g/L sodium acetate at pH=1.5 (adjusted with HCl) purged with CO_2 showing marks of preferential dissolution and oxide formation at the surface

As in the previous case, the potentials of both phases are different (see section 1) and selective dissolution is observed on the fracture surface (Figure 106-c) and all along the barrel surface on patches (Figure 107). This suggests that the passive film was locally destabilized. However, the kinetics of dissolution remains too slow to lead to critical defect formation and brittle failure. This synergy between preferential dissolution and plastic deformation corresponds to Stress Corrosion Cracking phenomenon and will be studied in part 4 of this Chapter.

The increase of hydrogen activity by applying a cathodic potential leads to a lower elongation at failure ($E_p=19\%$, $RE_p=24\%$) and reduction in area ($Z%=24\%$, $RAR=32\%$), which is almost half of the value obtained in the solution at $pH=3.5$ (solution 1). Transgranular brittle crack initiations on the surface were observed (Figure 108 and Figure 109). Their maximum depth is about 400 to 500 μm . Once again, fracture occurs after necking (Figure 105) in a state of maximum strain hardening, which finally means that under these electrochemical conditions embrittlement is very limited and that Virgo™38 can withstand harsh cathodic charging conditions, even at low pH.

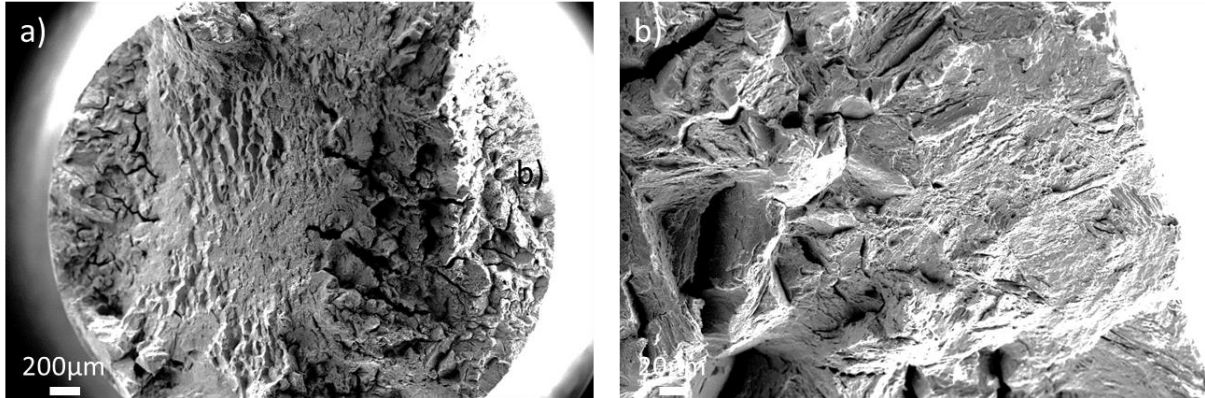


Figure 108 - Fracture surface of Virgo™38 after SSRT test at a strain rate of $10^{-6} s^{-1}$ and under cathodic charging at $-1200mV/SCE$ in a solution containing 30g/L NaCl + 0.4g/L sodium acetate at $pH=1.5$ (adjusted with HCl) purged with CO_2
a) Overview of the fracture surface

b) Detailed image showing transgranular mode of cracking close to one of the crack initiation area



Figure 109 - Barrel surface of Virgo™38 after SSRT test at a strain rate of $10^{-6} s^{-1}$ and under cathodic charging at $-1200mV/SCE$ in a solution containing 30g/L NaCl + 0.4g/L sodium acetate at $pH=1.5$ (adjusted with HCl) purged with CO_2 showing several secondary cracks

The test performed under cathodic potential reveals a limited brittle area with a transgranular mode of failure on Figure 108. This limited crown is attributed to the moderate hydrogen flux reached in these conditions and to the duration of the test.

Chapter III: Hydrogen Embrittlement and Stress Corrosion Cracking of Virgo™38 in acid environments

We have seen that the embrittlement is still limited at pH=1.5 for a strain rate of 10^{-6}s^{-1} . According to what has been presented before, not only hydrogen activity influences the embrittlement in the HE domain. Indeed, a lower strain rate should increase the HE by letting time to hydrogen to diffuse within the material. The stress strain curves obtained for the tests in solution 2 under OCP and cathodic polarization at a strain rate of 10^{-7}s^{-1} are presented in Figure 110 and compared to a reference test performed in air.

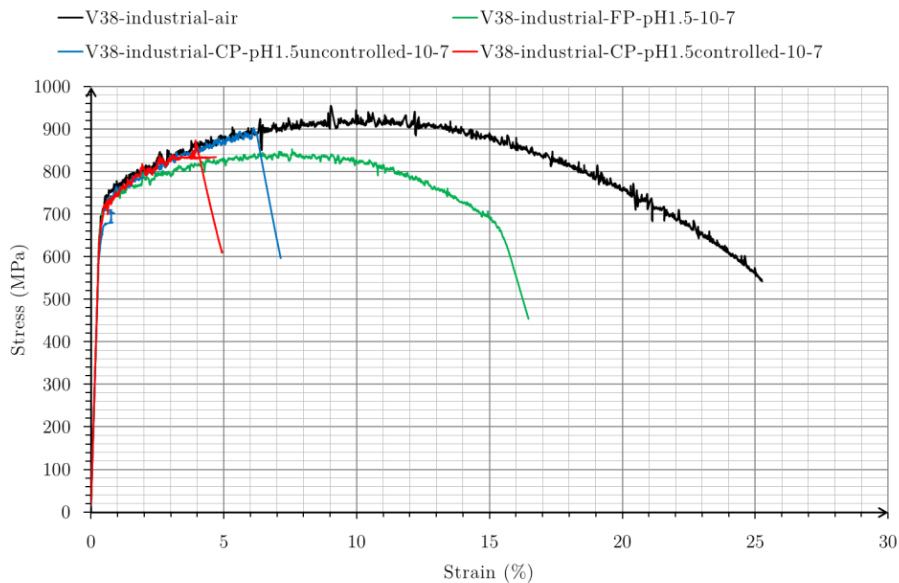


Figure 110 - Tensile curves of Virgo™38 under open circuit potential (FP, green curve) and cathodic charging at -1200mV/SCE (CP) in a solution containing 30g/L NaCl + 0.4g/L sodium acetate at pH=1.5 (adjusted with HCl) purged with CO₂ and at a strain rate of 10^{-7}s^{-1} with and without controlling the pH drift (red and blue curve respectively)

The test at OCP at a strain rate of 10^{-7}s^{-1} presents a stress-strain curve (green curve in Figure 110) below the reference test in air due to a harsh generalized corrosion reducing the cross section during the tensile test. The specimen reveals generalized corrosion with marks of preferential dissolution both on the fracture surface (Figure 111) and barrel surface (Figure 112). The intergranular grooves observed could be associated with the dissolution of retained austenite localized at former austenitic grain boundaries, as seen in part 1 of this Chapter (Figure 79). Another interpretation of corrosion grooves may be attempted on the basis of the idea of incomplete martensitic transformation of intergranular regions of austenite, presented in section 1.2.1. If austenite grain boundaries persist after quenching as a consequence of segregation of silicon and possibly other elements, the dissolution rate of corresponding regions might be faster due to differences in chemical composition with respect to the bulk and due to the atomic structure of boundaries. However, no identification of the dissolved phase was performed in this sample to validate or reject this assumption.

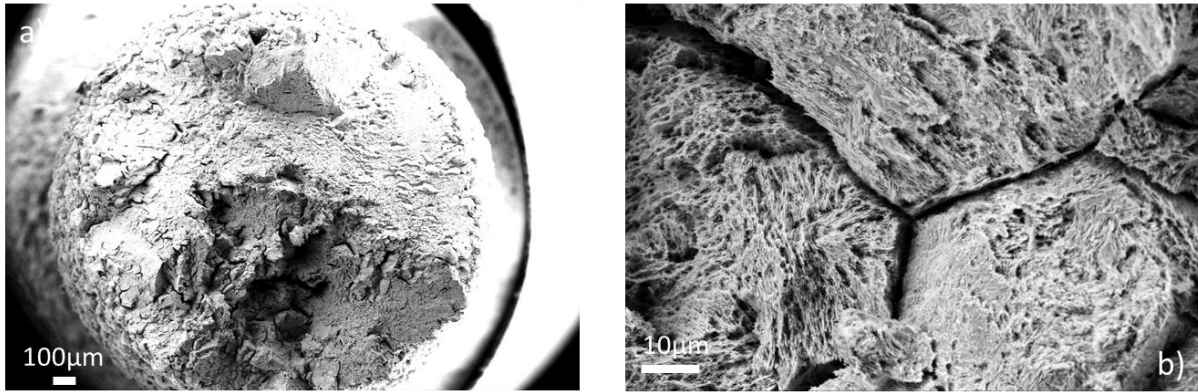


Figure 111 - Fracture surface of Virgo™38 after SSRT test at a strain rate of 10^{-7} s^{-1} and at Open Circuit Potential in a solution containing 30g/L NaCl + 0.4g/L sodium acetate at pH=1.5 (adjusted with HCl) purged with CO_2
a) Overview of the fracture surface showing ductile behavior with dimples
b) Detailed image showing preferential and intergranular dissolutions on the fracture surface

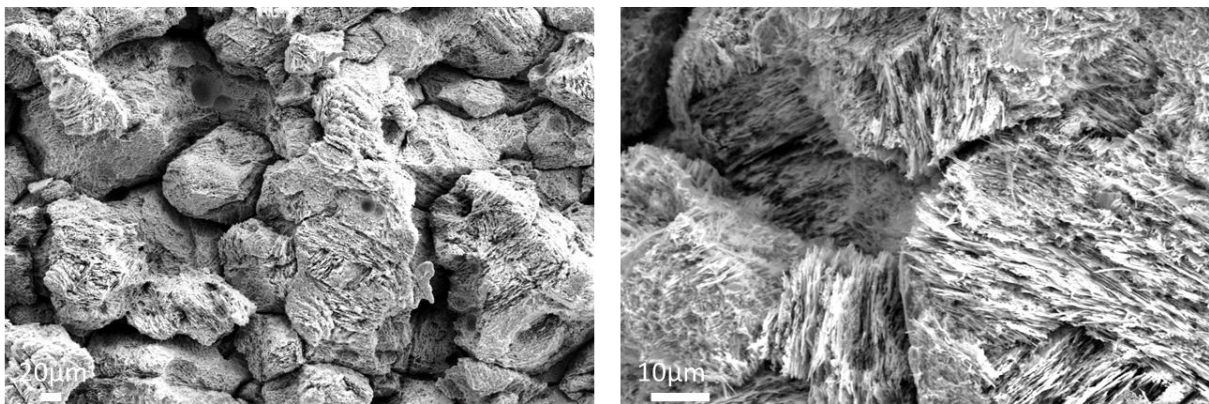


Figure 112 - Barrel surface of Virgo™38 after SSRT test at a strain rate of 10^{-7} s^{-1} and at Open Circuit Potential in a solution containing 30g/L NaCl + 0.4g/L sodium acetate at pH=1.5 (adjusted with HCl) purged with CO_2 showing generalized intergranular corrosion and preferential dissolution

Two tests were performed under cathodic polarization because we noticed a pH drift all along the first test. Indeed, pH increased up to 4.61 during 11.5 days in the first test. A pH monitoring was installed and the pH was maintained between 1.5 and 1.6 by adding HCl during the second test under cathodic charging. The reduction in area measured for the tests under applied cathodic potential are of 8% and 6.5% respectively, which gives a ratio of area reduction of 11% and 9% while it is 36% of reduction in area and 48% of ratio of area reduction for the test at OCP. The reductions of plastic elongations are 72% and 82% for tests under cathodic charging and 36% for the test at OCP, respectively.

At OCP and 10^{-7} s^{-1} , the mechanism involved is probably SCC assisted by dissolution (or generalized corrosion) because we notice a decrease of 0.2mm in diameter during the test, which explains that the 0.2% proof stress and UTS are lower than in air. However, we can notice that the test at OCP at 10^{-7} s^{-1} (Figure 110) is more brittle than the one at 10^{-6} s^{-1} (Figure 105), which is in contradiction with what was presented before [140], namely that the most critical strain rate for SCC is supposed to be 10^{-6} s^{-1} . This mechanism will be discussed in the following part of this Chapter.

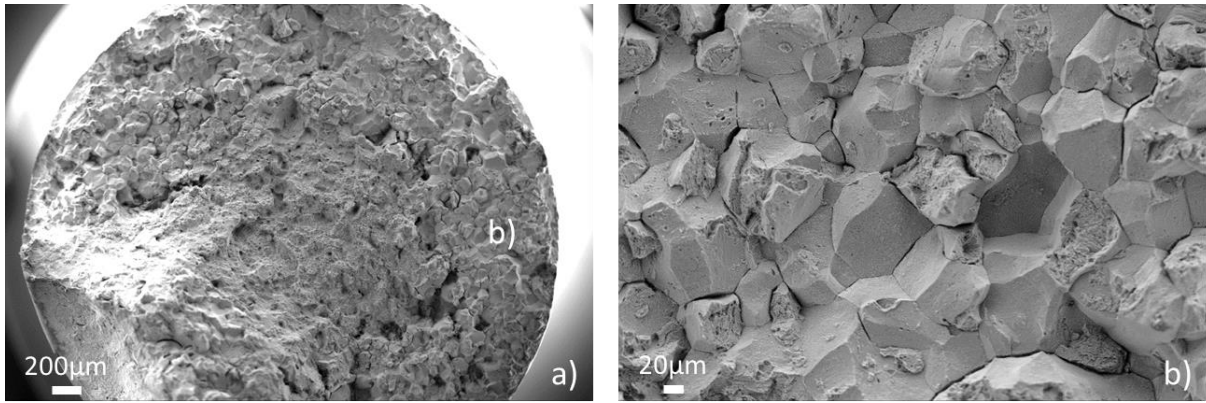


Figure 113 - Fracture surface of Virgo™38 after SSRT test at a strain rate of $10^{-7} s^{-1}$ and under cathodic charging at -1200mV/SCE in a solution containing 30g/L NaCl + 0.4g/L sodium acetate at pH=1.5 (adjusted with HCl) purged with CO₂ without controlling the pH drift
a) Overview of the fracture surface
b) Detailed image showing mixed intergranular and transgranular modes of cracking

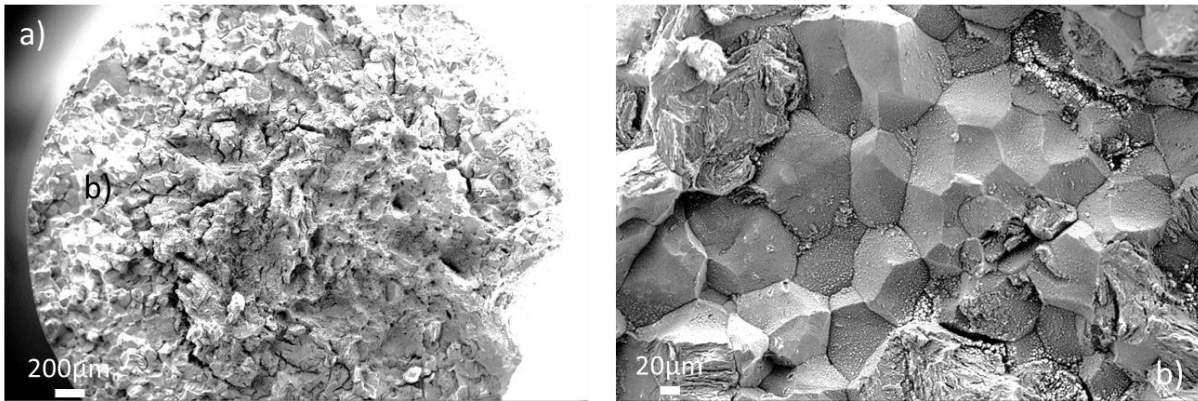


Figure 114 - Fracture surface of Virgo™38 after SSRT test at a strain rate of $10^{-7} s^{-1}$ and under cathodic charging at -1200mV/SCE in a solution containing 30g/L NaCl + 0.4g/L sodium acetate at pH=1.5 (adjusted with HCl) purged with CO₂ with the control of the pH drift
a) Overview of the fracture surface
b) Detailed image showing mixed intergranular and transgranular modes of cracking

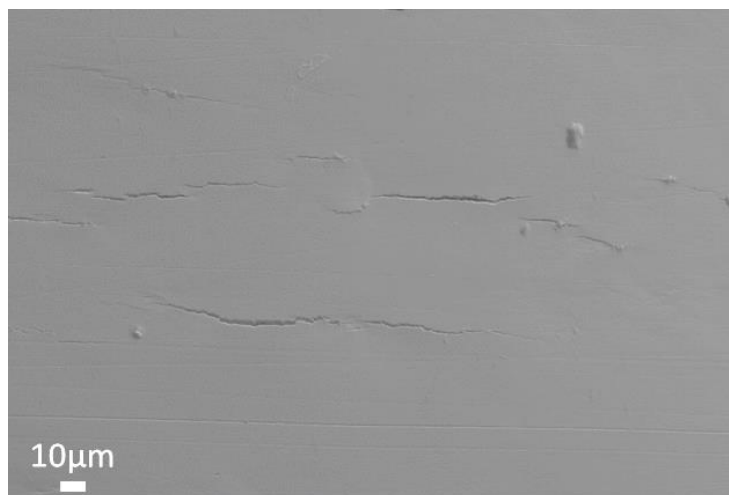


Figure 115 - Barrel surface of Virgo™38 after SSRT test at a strain rate of $10^{-7} s^{-1}$ and under cathodic charging at -1200mV/SCE in a solution containing 30g/L NaCl + 0.4g/L sodium acetate at pH=1.5 (adjusted with HCl) purged with CO₂ with the control of the pH drift showing several secondary cracks

Both tests under cathodic charging show a brittle mixed intergranular-transgranular behavior. The difference is that the heart of the ductile fracture in the case of unmonitored pH is larger than in the other case. The brittle crowns were 865µm and 930µm respectively which could be explained by the pH variation decreasing the hydrogen activity during the test under unmonitored pH. Moreover, numerous secondary intergranular cracks are visible at fracture surfaces. They might result from the deflection of crack trajectory at triple points.

A third test under cathodic charging has been interrupted at a stress level corresponding to 0.2% proof stress, i.e. 750MPa. The observation of barrel surface shows that cracks initiate within the nominally macroscopic elastic domain (Figure 116). However, it must be emphasized that 0.01% yield stress for this microstructural state of Virgo™38 is of 570MPa, so that the applied stress corresponds to a plastic deformation which cannot be neglected. According to estimations performed in Chapter II, the elastic limit is significantly lower in tempered martensite (≈450MPa) than in retained austenite (≈710MPa). For this reason, tempered martensite is certainly exposed to heavier plastic strains, in particular when the macroscopic plasticity is low, what may have consequences on crack initiation conditions.



Figure 116 - Barrel surface of Virgo™38 after SSRT interrupted at 0.2% proof stress test at a strain rate of $10^{-7}s^{-1}$ and under cathodic charging at -1200mV/SCE in a solution containing 30g/L NaCl + 0.4g/L sodium acetate at pH=1.5 (adjusted with HCl) purged with CO₂ with controlling the pH drift showing several secondary cracks

3.3. Conclusions on HE under cathodic charging in acid environments

The reductions in area and the reduction in plastic elongations for all the HE tests are summarized in Table 18.

Table 18 - Reduction in area RA, ratio of area reduction RAR, plastic elongations E_p and reduction of plastic elongation RE_p measured on the different specimens after HE tests

	RA (%)	RAR (%)	E _p (%)	RE _p (%)
Reference (air)	75	100	25	0
CP-pH=3.5-10 ⁻⁶	47	63	21.5	14
FP-pH=1.5-10 ⁻⁶	75	100	24.5	2
CP-pH=1.5-10 ⁻⁶	24	32	19	24
FP-pH=1.5-10 ⁻⁷	36	48	16	36
CP-pH=1.5-10 ⁻⁷	8	11	7	72
CP-pH=1.5-10 ⁻⁷ with pH control	6.5	9	4.5	82

Chapter III: Hydrogen Embrittlement and Stress Corrosion Cracking of Virgo™38 in acid environments

The results shown in Table 18 confirm that the supermartensitic stainless steel Virgo™38 is more sensitive to HE at the strain rate of 10^{-7}s^{-1} than at 10^{-6}s^{-1} , at least for imposed cathodic potential of -1200mV/SCE.

In this part, we demonstrated that it is possible to obtain brittle failures by synergetic effects of hydrogen and plastic deformation. It was necessary to decrease and maintain the pH at 1.5 (corresponding to the depassivation pH) under cathodic charging in order to produce a sufficiently high hydrogen activity and allow hydrogen entry in the material. We can speak here about hydrogen embrittlement but a precise mechanism was not yet established.

For the tests at Open Circuit Potential, the failures were mainly due to mechanical damages at 10^{-6}s^{-1} without any initiation from the surface of the specimen. At 10^{-7}s^{-1} , both crack initiation and propagation are assisted by dissolution. The mechanism involved corresponds to anodic Stress Corrosion Cracking (ASCC), and is presented and detailed in the next part of this Chapter with dedicated experiments.

This first series of experiments under cathodic charging has allowed to reproduce some of main features of “in service” embrittlement and cracking of Virgo™38. A strong decrease in elongation and area reduction together with the evidence of large intergranular areas obtained under relatively high hydrogen activity (pH decreased down to 1.5) as compared to relatively low hydrogen activity (pH 3.5) indicate that HE plays a major role. Moreover the importance of H-plasticity interactions is underlined by a strong strain-rate effect while going down to 10^{-7}s^{-1} as indicated in the literature for this mechanism [140]. However, these conditions are certainly not fully representative of “in service” conditions due to the excessive pH decrease and in the same time only partly intergranular fractures were obtained. That is why we need to find conditions enabling to increase hydrogen fugacity. The low hydrogen fugacity is attributed to the too high hydrogen recombination at the sample surface as presented in Chapter I. In the following chapters we will thus focus on a pH range within service conditions (with some extra tests outside this range) which ensure sufficiently high H activity by adding H_2S (Chapter V). Furthermore, as one cause of limited embrittlement is identified to be the high recombination at the surface, we will focus on the effect of the addition of a recombination poison such as Na_2S (Chapter IV). For safety reasons, these tests will be performed in basic environments as they enable to reach very high hydrogen activity.

4. Stress Corrosion Cracking of industrial Virgo™38 during SSRT tests

4.1. Conditions of the tests

SCC under applied potential in acid environments in the active to passive transition region was widely studied in austenitic stainless steels [139] and has recently been successfully transposed to duplex stainless steels [88].

As for duplex stainless steels, SMSS presents two distinct corrosion peaks at pH=1.5 (corresponding to the depassivation pH of the alloy) and under mechanical loading as shown in Figure 117. Thus, it is theoretically possible to enhance the corrosion of one or the other phase by applying a particular potential, even if the potential difference is definitively small.

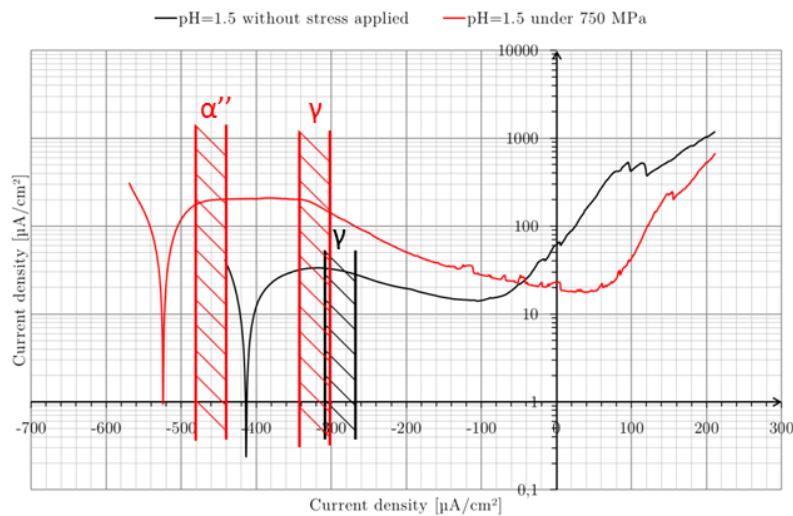


Figure 117 - Polarization curves of Virgo™38 in solution 2 showing two distinct domains favoring SCC initiation by anodic dissolution mechanism either in martensite or retained austenite

Thus, we decided to study the SCC behavior of Virgo™38 for two different applied potentials corresponding to the two domains revealed in Figure 117 and already discussed in section 1 of this Chapter (Figure 78, Figure 81 and Figure 82). The tests were performed at strain rates of 10^{-6}s^{-1} and 10^{-7}s^{-1} . The SCC behavior will only be studied in solution 2 at pH=1.5 as presented previously because it presents an active to passive transition region.

Table 19 - Conditions of the SCC tests on Virgo™38

	Potential applied (mV/SCE)	Targeted dissolved phase	Applied strain rate (s^{-1})
SCC test 1a	-480	Martensite	10^{-6}
SCC test 1b	-480	Martensite	10^{-7}
SCC test 2a	-350	Retained austenite	10^{-6}
SCC test 2b	-350	Retained austenite	10^{-7}

As mentioned above, there are two active to passive transition regions according to the pH and the applied mechanical loading. The analysis of the depassivation pH of each phase enables us to conclude that martensite is active at the more cathodic potential (in this case around -480mV/SCE) while retained austenite is active at the nobler anodic potential (-350mV/SCE in solution 2). This difference is due to the partitioning effect of the alloying elements described in Chapter II and discussed in section 1 of this Chapter.

4.2. SCC behavior of Virgo™38 under applied potential

4.2.1. SSRT tests at a potential in the active dissolution domain of martensite

First, we focus our attention on the preferential dissolution of the martensitic matrix. The stress strain curves obtained for the tests in solution 2 (Table 17) at the activity potential of martensite are presented in Figure 118.

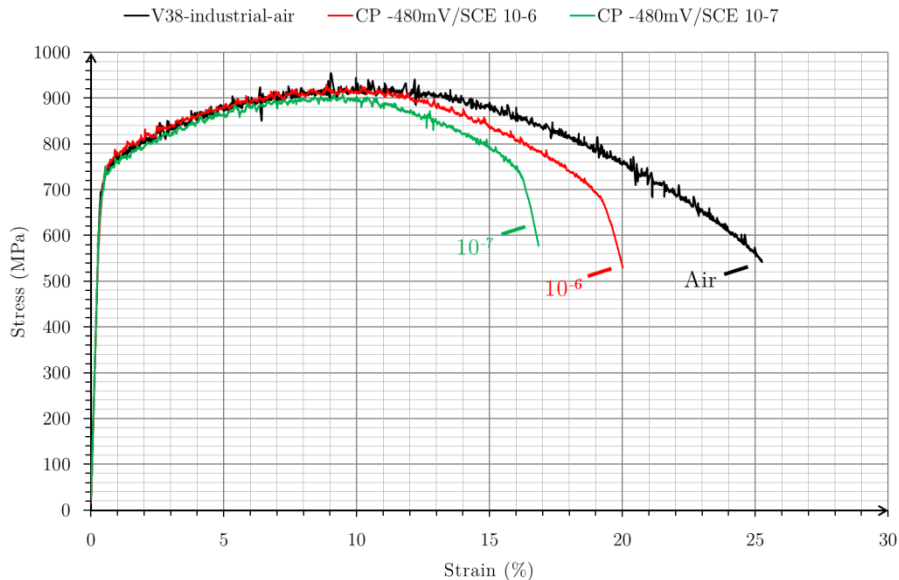


Figure 118 - Tensile curves of Virgo™38 under anodic potential of -480mV/SCE (corresponding to the martensite potential of activity) in a solution containing 30g/L NaCl + 0.4g/L sodium acetate at pH=1.5 (adjusted with HCl) purged with CO₂ and at a strain rate of 10⁻⁶s⁻¹ and 10⁻⁷s⁻¹ (red and green curves respectively)

The SSRT test at 10⁻⁶s⁻¹ shows a limited effect of environment as compared to tests under cathodic potential presented before. The reduction in area measured for this test is of 43%, which corresponds to a ratio of area reduction of 57%. The reduction of plastic elongation is of 24%. However, preferential corrosion is observed on the fracture surface (Figure 119) and a loss of thickness in diameter of this specimen, measured in an area not affected by necking far from the fracture surface, is measurable. Indeed, diameter decreased from 3.89mm to 3.75mm. The test at a strain rate of 10⁻⁷s⁻¹ shows a lower elongation to failure. Indeed, the reduction in area measured for this test is of 40%, which corresponds to a ratio of area reduction of 54% and the reduction of plastic elongation is of 36%. The diameter of the specimen is also significantly reduced by corrosion; it decreased from 3.90mm to 3.72mm. The reduction in diameter in both cases suggests the occurrence of generalized corrosion. Nevertheless, the fracture surface shows here again preferential dissolution features (Figure 120).

In both cases, failures occurred well after the UTS, in the necking region where triaxial state of stresses induces crack initiations perpendicular as well as parallel to the loading direction (Figure 119-a and Figure 120-a). Work hardening is well known to increase corrosion rates in steels [142] [143] [144]. At the microstructure scale, this increase is explained by the high dislocations density which disorganizes the state of surface and the sub-surface layers. The test at 10⁻⁷s⁻¹ which lasted longer shows a higher loss in diameter than at 10⁻⁶s⁻¹. This may be attributed to the longer exposure to conditions which produce generalized dissolution.

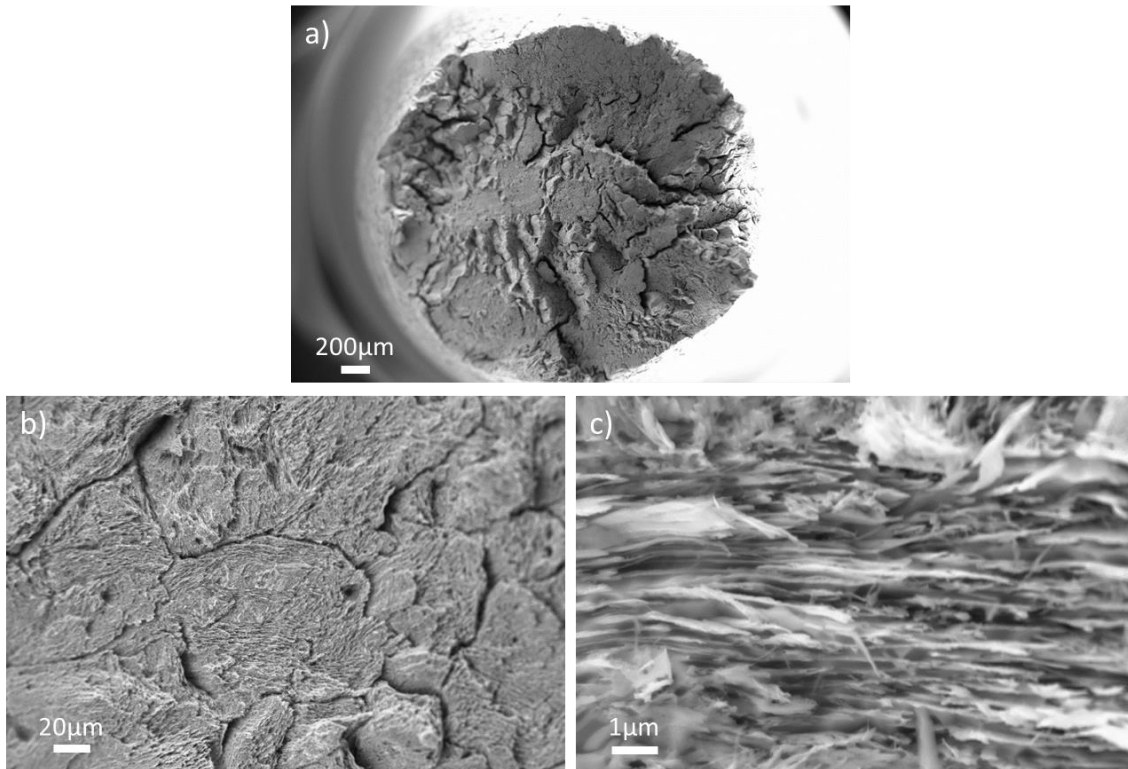


Figure 119 - Fracture surface of Virgo™38 after SSRT test at a strain rate of 10^{-6} s^{-1} and under cathodic charging at -480 mV/SCE in a solution containing $30 \text{ g/L NaCl} + 0.4 \text{ g/L}$ sodium acetate at $\text{pH}=1.5$ (adjusted with HCl) purged with CO_2
 a) Overview of the fracture surface

b) and c) Detailed images showing preferential dissolution on the fracture surface

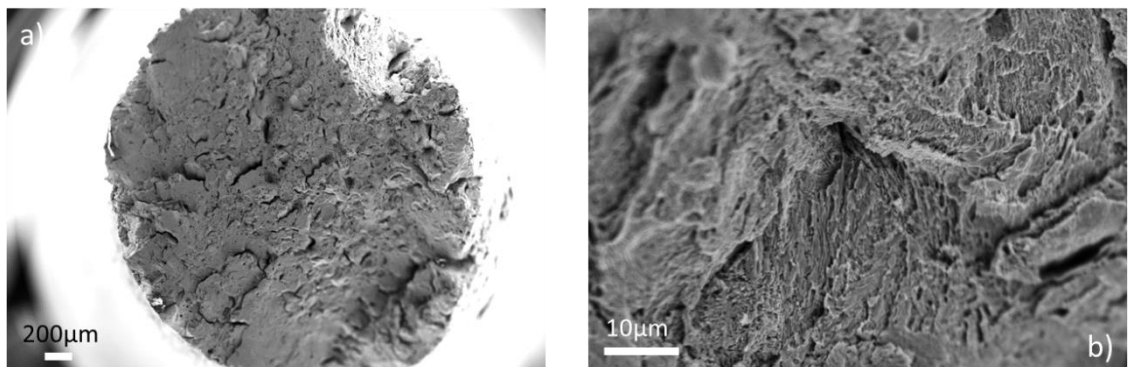


Figure 120 - Fracture surface of Virgo™38 after SSRT test at a strain rate of 10^{-7} s^{-1} and under cathodic charging at -480 mV/SCE in a solution containing $30 \text{ g/L NaCl} + 0.4 \text{ g/L}$ sodium acetate at $\text{pH}=1.5$ (adjusted with HCl) purged with CO_2
 a) Overview of the fracture surface

b) Detailed images showing preferential dissolution on the fracture surface

Careful examinations of the fracture surfaces and in the necking region show that the apparent generalized corrosion is the result of a succession of multiple preferential dissolution steps at different scales. At the scale of a few prior austenite grains an engraving of the former grain boundaries is observed, which could form critical defects for crack initiation (Figure 119-b). At higher magnification, Figure 119-c shows preferential dissolution of martensite laths leaving the retained austenite laths intact insofar as the austenite is cathodically protected by polarization at -480 mV/SCE . This preferential corrosion localized in one phase or in the vicinity of former austenitic grain boundaries is probably at the origin of critical defect formation. The actual mode of cracking seems to be mixed with transgranular and intergranular crack paths.

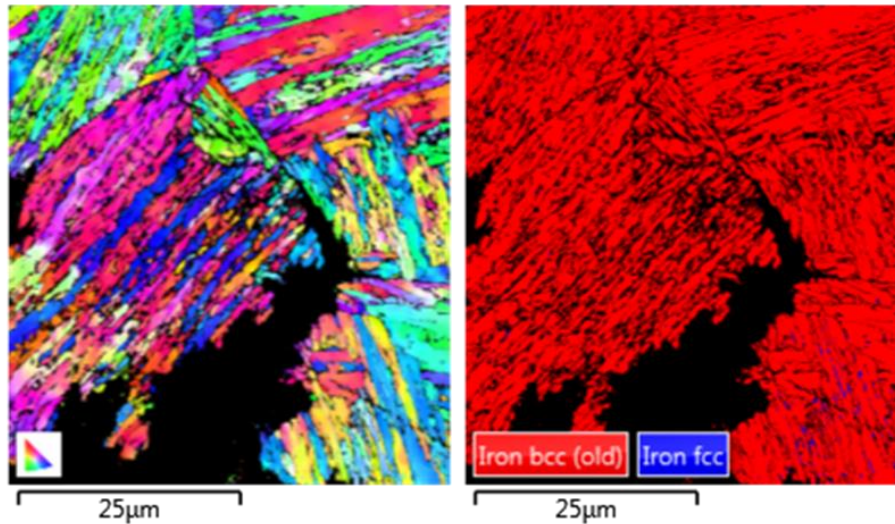


Figure 121 - EBSD mapping of a secondary crack after SCC test at -480mV/SCE (corresponding to the activity potential of martensite) in a solution containing 30g/L NaCl + 0.4g/L sodium acetate at pH=1.5 (adjusted with HCl) purged with CO₂

Figure 121 presents an EBSD map performed on a secondary crack. We can see that this crack propagates in an intergranular way in the portion analyzed. We can also see a lot of unindexed areas between martensitic laths. These areas do not correspond to the dissolution of retained austenite but rather to its transformation. Indeed, after more than 15% of elongation, the transformation of austenite to martensite is expected to occur at a level of 50% (see Chapter II, Figure 73).

4.2.2. SSRT tests at a potential in the active dissolution domain of retained austenite

Such as previously, we performed tests at the potential corresponding to the dissolution of retained austenite. The stress strain curves obtained for the tests in solution 2 (Table 17) at the activity potential of retained austenite are presented in Figure 122.

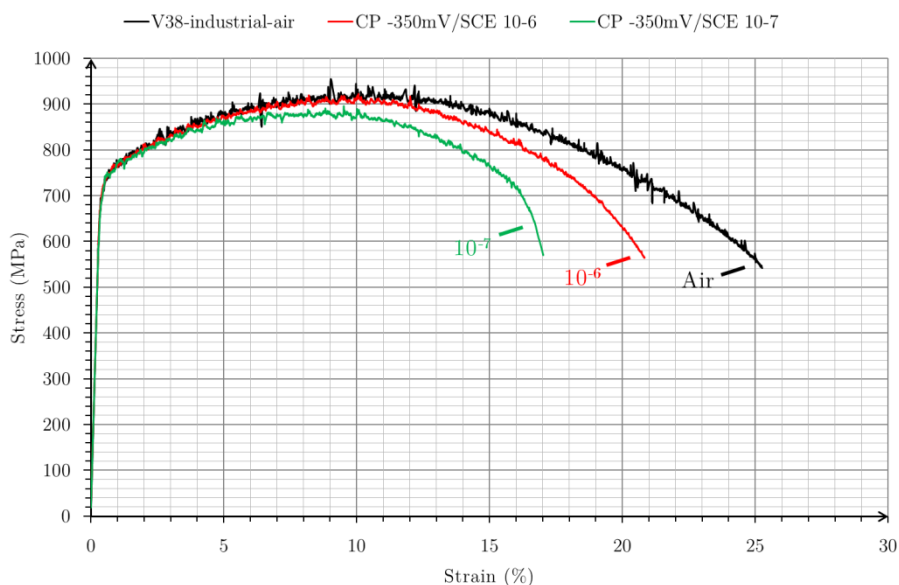


Figure 122 - Tensile curves of Virgo™38 under anodic charging at -350mV/SCE (corresponding to the activity potential of retained austenite) in a solution containing 30g/L NaCl + 0.4g/L sodium acetate at pH=1.5 (adjusted with HCl) purged with CO₂ and at a strain rate of 10⁻⁶s⁻¹ and 10⁻⁷s⁻¹ (red and green curves respectively)

Once again, the SCC test at a strain rate of 10^{-6}s^{-1} shows a significant elongation to failure as compared to hydrogen embrittlement tests presented before. Indeed, the reduction in area measured for this test is of 50%, which corresponds to a ratio of area reduction of 67%. The reduction of plastic elongation is of 18%. However, general corrosion is observed and the diameter of the specimens decreased from 3.90mm to 3.89mm far from the fracture surface in an area not affected by necking, which is coherent with a SCC mechanism associated with anodic dissolution. At a strain rate of 10^{-7}s^{-1} , the reduction in area is of 46%, which corresponds to a ratio of area reduction of 62% and the reduction of plastic elongation is of 34%. The diameter of the specimens decreased from 3.89mm to 3.85mm.

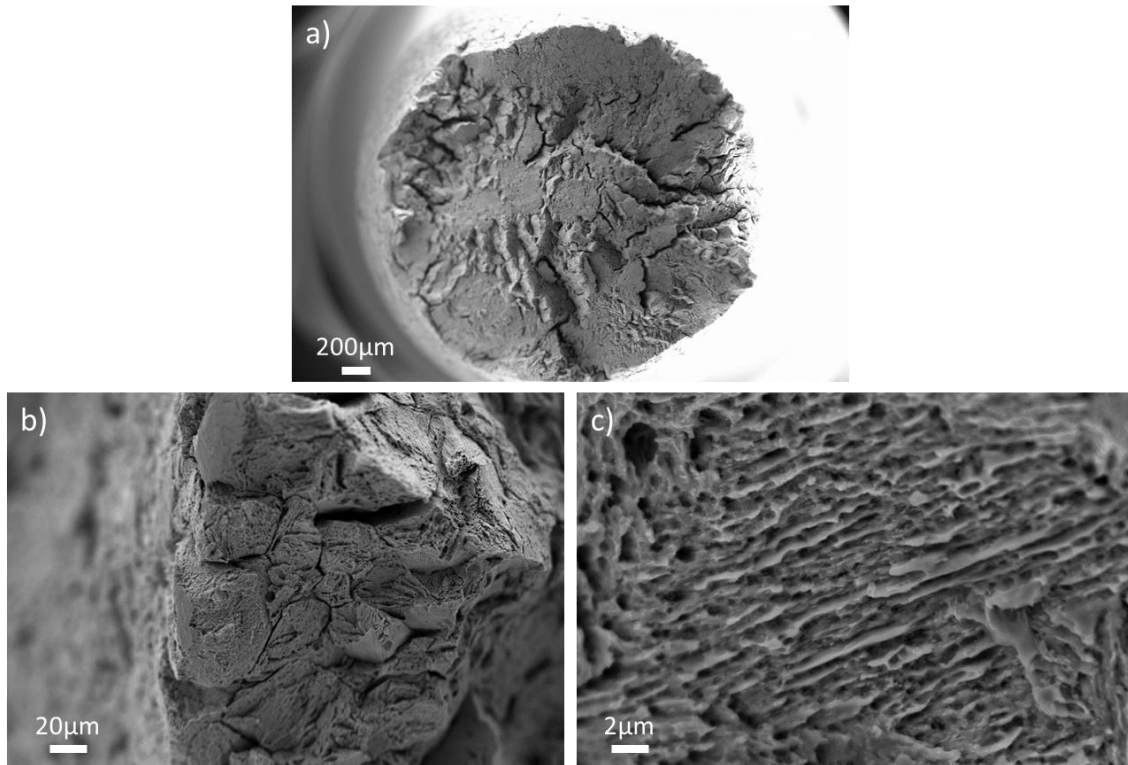


Figure 123 - Fracture surface of Virgo™38 after SSRT test at a strain rate of 10^{-6}s^{-1} and under cathodic charging at -350mV/SCE in a solution containing $30\text{g/L NaCl} + 0.4\text{g/L}$ sodium acetate at $\text{pH}=1.5$ (adjusted with HCl) purged with CO_2
 a) Overview of the fracture surface
 b) and c) Detailed images showing preferential dissolution on the fracture surface

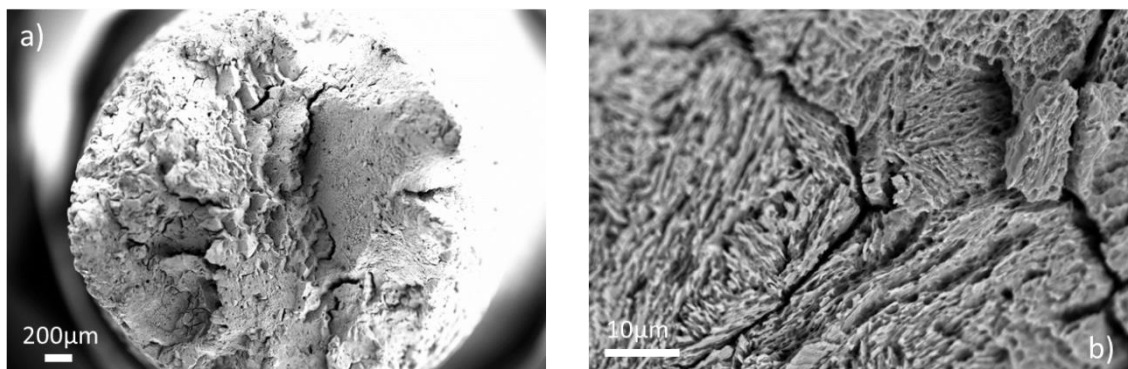


Figure 124 - Fracture surface of Virgo™38 after SSRT test at a strain rate of 10^{-7}s^{-1} and under cathodic charging at -350mV/SCE in a solution containing $30\text{g/L NaCl} + 0.4\text{g/L}$ sodium acetate at $\text{pH}=1.5$ (adjusted with HCl) purged with CO_2
 a) Overview of the fracture surface
 b) Detailed images showing preferential dissolution on the fracture surface

Chapter III: Hydrogen Embrittlement and Stress Corrosion Cracking of Virgo™38 in acid environments

Fracture surface examinations show here again crack initiations from the surface of the specimens despite significant elongation, beyond the necking of the specimen. The mode of propagation is mixed, showing transgranular cracks and intergranular crack paths identified by the granular appearance in some parts. Nevertheless, no facet of smooth grain boundary is observed for conditions explored. Careful examination at higher magnification (Figure 123-c) shows that, at this potential of -350mV/SCE, no lath of austenite is observed on the fracture surface. Surface reveals features of dissolution which draw the underlying martensite microstructure with numerous cavities of dissolution (Figure 123-c and Figure 124-b). Actually, the passivity of martensite is destabilized by plastic deformation and it also corrodes.

We can also observe in these conditions that grain boundary grooves appear; they could correspond to the dissolution of the retained austenite formed close to former austenitic grain boundaries.

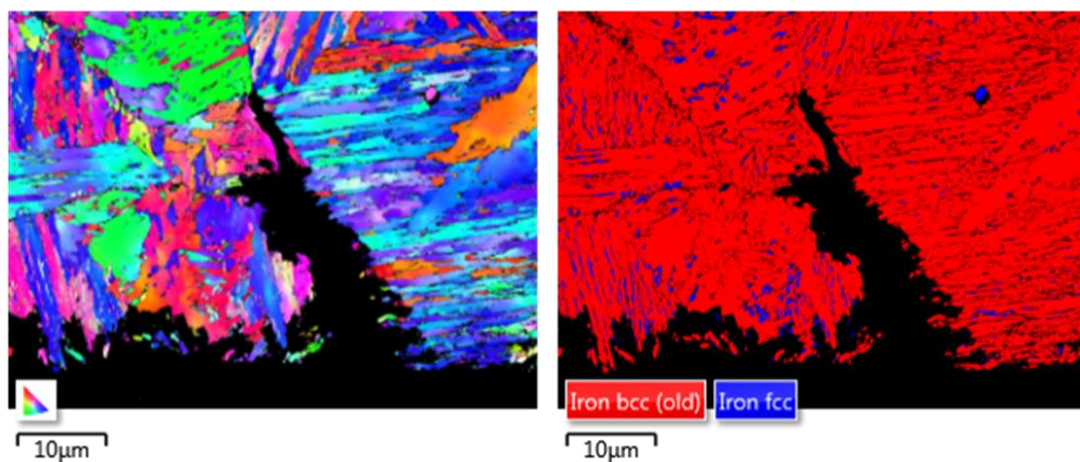


Figure 125 - EBSD mapping of a secondary crack after SCC test at -350mV/SCE (corresponding to the activity potential of retained austenite) in a solution containing 30g/L NaCl + 0.4g/L sodium acetate at pH=1.5 (adjusted with HCl) purged with CO₂ showing preferential dissolution of retained austenite

The EBSD maps presented in Figure 125 shows that cracks propagate following an intergranular path. It is also visible that dissolution occurred showing the dissolution of retained austenite and the formation of cavities in which martensite also dissolves.

4.3. Conclusions on SCC tests under applied potential in acid environment

The reductions in area and the reductions in plastic elongations for all the SCC tests are summarized in Table 20.

Table 20 - Reduction in area RA, ratio of area reduction RAR, plastic elongations E_p and reduction of plastic elongation RE_p measured on the different specimens after SCC tests

	RA (%)	RAR (%)	E_p (%)	RE_p (%)
Reference (air)	75	100	25	0
SSC test 1a at -480mV/SCE 10^{-6}	43	57	19	24
SSC test 1b at -480mV/SCE 10^{-7}	40	54	16	36
SSC test 2a at -350mV/SCE 10^{-6}	50	67	20.5	18
SSC test 2b at -350mV/SCE 10^{-7}	46	62	16.5	34

Surprisingly and contrary to what is presented in the literature for ASSC mechanism [140], elongations are smaller for tests at $10^{-7}s^{-1}$ than $10^{-6}s^{-1}$. This difference with the literature review can be due to the absence of H_2S . Indeed, H_2S increases the corrosion rate and, as mentioned previously, $10^{-6}s^{-1}$ is identified in the literature as the threshold strain rate that enables a competition between repassivation and dissolution in presence of H_2S . In our case, in absence of H_2S , the corrosion rate is expected to be lower (absence of H_2S) and thus the corresponding threshold strain rate is also expected to be lower.

In this part, we highlighted a cracking phenomenon different from the usual Hydrogen Embrittlement. Indeed, under actual service conditions, where the expected pH is at least of 3.0, the Anodic Stress Corrosion Cracking phenomenon is not observed because of the stability of the passive film at such pH level. However, while decreasing the pH under the depassivation pH, it is possible to observe ASSC. Even if this mechanism is less violent than Hydrogen Embrittlement, it would be dangerous to neglect it as it can also play a role in crack propagation under hydrogen embrittlement if the local pH is decreased.

5. Conclusions

Two mechanisms of environmentally assisted damage were detailed in this Chapter: Hydrogen Embrittlement under cathodic charging and Anodic Stress Corrosion Cracking under applied anodic potential at the peak of activity of each phase, both in acid environments at a pH below the depassivation pH under applied loading. The potentials applied for anodic SCC tests were chosen according to the depassivation study performed on Virgo™38 by potentiodynamic measurements.

The relatively low embrittlement obtained by applying cathodic potential shows that Virgo™38 is resistant to hydrogen embrittlement, even at very low pH out of specifications (as low as 1.5) in absence of H₂S. The conditions of hydrogen embrittlement tests are certainly not fully representative of “in service” conditions due to this excessive pH decrease necessary to obtain embrittlement. Even if hydrogen embrittlement tests show the highest embrittlement, hydrogen fugacity seems to be not sufficient to reproduce the in service failures. The following Chapter will be dedicated to the study of Hydrogen Embrittlement in an environment where hydrogen activity is higher. This environment will enable us to conclude on a possible mechanism of crack propagation in these conditions.

When the applied potential is close to the activity potential(s), it shows that Virgo™38 is not very sensitive to SCC insofar as a significant plastic deformation is necessary to the damage. One can conclude that, as indicated by the industrial feedbacks, Virgo™38 seems to be more sensitive to hydrogen embrittlement than to anodic stress corrosion cracking. The differences in activity potentials of both phases due to the partitioning effect studied at the beginning of this Chapter seem to be at the origin of a preferential dissolution of either retained austenite or tempered martensite. The resistance to anodic dissolution seems to be lower for tempered martensite than for retained austenite. At Open Circuit Potential (OCP) the mechanism involved seems to be Anodic Stress Corrosion Cracking leading to the dissolution of one or the other phase due to local microscopic coupling between these two phases. Even if the potential difference between the two constitutive phases is too small to talk about galvanic coupling, in the following of this work we will still use this term in order to simplify the explanations. This mechanism will be also observed in presence of H₂S in Chapter V of this study.

Chapter IV:
Hydrogen embrittlement of Virgo™38 in different metallurgical states under cathodic charging in an environment containing Na₂S

Chapter IV: Hydrogen Embrittlement of Virgo™38 in different metallurgical states under cathodic charging in an environment containing Na₂S..... 141

1. Definition of an environment with elevated hydrogen activity to reproduce hydrogen embrittlement observed in service	145
1.1. Composition of the environment containing Na ₂ S and conditions	145
1.2. Influence of the poison on the HE behavior of industrial Virgo™38.....	146
1.2.1. Reference tests in basic environment without poison.....	146
1.2.2. Influence of the addition of Na ₂ S on the hydrogen activity	147
1.3. Conclusions	153
2. Effect of the microstructure on the resistance to HE of Virgo™38.....	154
2.1. Reference metallurgical state: Virgo™38 impeller industrially heat treated	154
2.2. Influence of the amount of retained austenite on the resistance to HE of Virgo™38	158
2.2.1. Influence of the heat treatment.....	158
2.2.2. Influence of the pre-straining.....	167
2.3. An industrial case study: the Cover	169
2.3.1. Description of the material: composition, metallurgy and industrial failure	169
2.3.2. Behavior of the Cover during SSRT test under cathodic charging.....	170
3. Discussion	173
3.1. Summary of the results.....	173
3.2. Interpretation on the optimal amount of retained austenite in terms of its quantity and stability.....	174
3.3. Interpretation of the fracture mode.....	176
3.4. Proposed mechanisms of Hydrogen Embrittlement	178
3.4.1. Intergranular fractures	178
3.4.2. Transgranular fractures	180
3.5. Interpretation of the cracking of the Cover.....	180
3.5.1. Interpretation based on the retained austenite content and the fracture mode.....	180
3.5.2. Explanations based on the precipitation state on the Cover	182
3.5.3. Phosphorous Grain Boundary Segregation (PGBS) in the Cover	182
4. Conclusions	187

Definition of an environment with elevated hydrogen activity to reproduce hydrogen embrittlement observed in service

In this chapter, we will first (4.1) focus on the choice of a high hydrogen fugacity environment to substitute H₂S whose use in our laboratory is prohibited for administrative and security reasons. Our choice, namely NaOH + Na₂S is validated by permeations tests.

This environment will be used to study the influence of the microstructure on hydrogen embrittlement resistance of Virgo™38. A particular attention will be given to the role of retained austenite (4.2) and to the chemical composition (4.3) of former austenitic grain boundaries (where failure occurred in service).

1. Definition of an environment with elevated hydrogen activity to reproduce hydrogen embrittlement observed in service

1.1. Composition of the environment containing Na₂S and conditions

In order to study HE of Virgo™38 in more hydrogenating environment than those presented in Chapter III, SSRT tests in a basic (elevated pH) environment containing Na₂S as a poison to the recombination in H₂ gaseous (Table 21) were proposed. Indeed, according to some studies [145][146], Na₂S addition to NaOH solutions increases the brittleness of steels under cathodic polarization. These conditions correspond to high hydrogen activity. For example, authors have shown that for Armco iron, the hydrogen permeation fluxes measured under cathodic charging at -1300mV/SCE in a Na₂S containing environment (Table 21) are equivalent to those obtained in an environment at pH=4.5 under 1bar of pure H₂S at Open Circuit Potential (OCP) [147] which is closer to industrial conditions in terms of hydrogen activity compared to acid environments without poison presented in Chapter III.

Table 21 - Compositions of the environment containing poison used for SSRT tests under cathodic charging for HE of Virgo™38

	NaOH (mol.L ⁻¹)	Na ₂ S (mol.L ⁻¹)	pH before the test	Purging gas	Applied potential (mV/SCE)	OCP (mV/SCE)
Reference solution	0.1	0	13	N ₂	-1300	-350
Poisoned solution	0.1	0.02	12.3	N ₂	-1300	-370

All the tests were performed at room temperature at the unique strain rate of 10⁻⁷s⁻¹ and the solutions were purged 12h before starting the SSRT test. According to literature data [140] and following the results obtained in Chapter III, this lower strain rate causes more damaging than 10⁻⁶s⁻¹ regarding hydrogen embrittlement.

The same sample geometry and experimental setup as described in Chapter III was used for these tests. A very strict safety procedure was adopted in order to ensure that no H₂S can contaminate the atmosphere during the tests in the poisoned solution (Appendix 2).

1.2. Influence of the poison on the HE behavior of industrial Virgo™38

1.2.1. Reference tests in basic environment without poison

To ensure that the material behavior to be observed in this new environment is due to the addition of the poison (Na₂S) and not to NaOH, a reference slow strain rate tensile test was performed without poison in the 0.1M NaOH solution at a strain rate of 10⁻⁷s⁻¹ under cathodic charging at -1300mV/SCE (Figure 126).

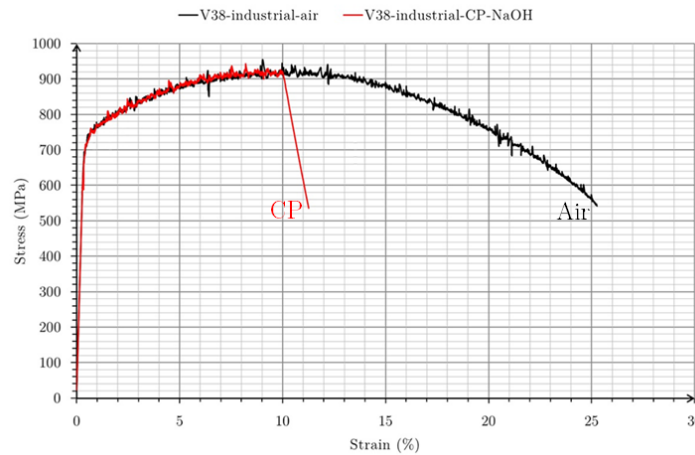


Figure 126 - Tensile curves of Virgo™38 in air (Air, black curve) and under cathodic charging (CP, red curve) at -1300mV/SCE in a solution containing 0.1M NaOH without Na₂S purged with N₂ and at a strain rate of 10⁻⁷s⁻¹

The area reduction measured after the test under cathodic charging in 0.1M NaOH solution is equal to 14%, which gives a ratio of area reduction of 18.7% with respect to the test in air. The reduction of plastic elongation is 56% with respect to the test in air. The embrittlement obtained in these conditions is less important than that measured at the same strain rates and under cathodic charging in acid environment, which can be interpreted by the origin of hydrogen. In alkaline solutions, the Hydrogen Evolution Reaction (HER) goes through the formation of the hydrogen intermediates H_{ads} formed via charge-induced discharge of water (H₂O + e⁻ → H_{ads} + OH⁻), the Volmer step. The main difference between the HER in acid and alkaline environments lies in the source of the hydrogen; while in acid electrolytes, active intermediates are formed from protons, in alkaline ones an additional activation process involving the dissociation of water is required to generate the H_{ads}, and limits the reaction rate. At equal charging conditions in terms of cathodic overpotential, the hydrogen charging efficiency is lower in alkaline solution.

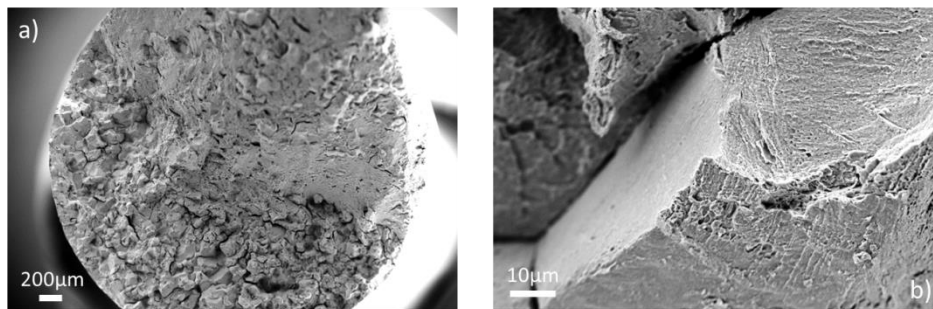


Figure 127 - Fracture surface of Virgo™38 after SSRT test at a strain rate of 10⁻⁷s⁻¹ and under cathodic charging at -1300mV/SCE in a solution containing 0.1M NaOH without Na₂S purged with N₂

- a) Overview of the fracture surface
- b) Detailed image showing mixed intergranular/transgranular mode of cracking

Definition of an environment with elevated hydrogen activity to reproduce hydrogen embrittlement observed in service

HE embrittlement of the material obtained under cathodic polarization both at low and high pH leads to the appearance of the intergranular mode of fracture with different aspects of the grains boundaries facets. As seen in Figure 127 the intergranular fracture occupies a large fraction of the fracture surface. At a higher scale, one can observe that grain boundaries facets show a more or less smooth surface. On the right of the grain, marks of ductility clearly appear, either in the form of emergence of slip lines or simply in the form of ductile tear with little dimples. On the contrary on the left of this grain, a smooth appearance predominates.

With regard to the elongation at failure, we can assume that straining in the reference solution does not produce a strong hydrogen embrittlement of Virgo™38. Nevertheless, the material is clearly affected by hydrogen effects that occur under these conditions at a high level of plastic deformation. Later, all the effects, even more deleterious on the embrittlement of the material, will thus be attributed to the addition of the poison Na_2S , by considering SSRT test in NaOH solution at a cathodic potential of -1300mV/SCE as the reference test.

1.2.2. Influence of the addition of Na_2S on the hydrogen activity

As previously mentioned, bibliographic studies indicate that the presence of Na_2S increases the hydrogen activity under cathodic charging [147]. To measure the influence of Na_2S addition on the hydrogen activity, permeation tests were performed in the poisoned solution using a Devanathan cell [83] presented in Figure 128.

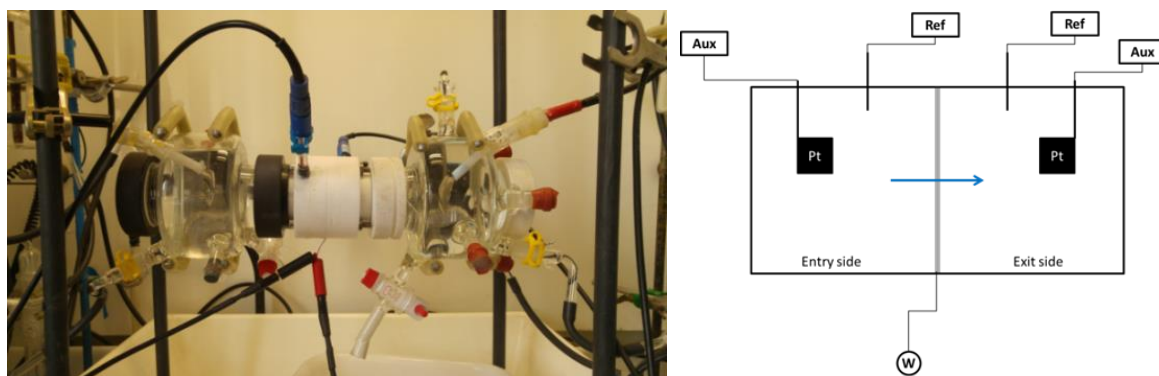


Figure 128 - Hydrogen permeation cells used at Ecole des Mines (left) and schematic representation (right)

The experimental setup is composed of two cells. On the exit side (detection side), the solution used was 0.1M NaOH deaerated with nitrogen while on the entry side (charging side) we used either the reference or the poisoned solution. In both parts, auxiliary electrodes are platinum plate and reference electrodes are calomel electrodes (SCE). The working electrode was a thin plate (around $300\mu\text{m}$ thickness) of Virgo™38 carefully polished (see Chapter II) on both faces. We considered that passive film of Virgo™38 is stable enough in the detection solution close to the OCP and that it can enable a good recombination of hydrogen; that is why we chose not to perform a palladium deposition at the exit side. On the exit side, the potential was maintained at -300mV/SCE , which is close to the OCP ($+50\text{mV/OCP}$) and thus enables a total hydrogen atom oxidation. In a first approach, we decided to apply a constant potential at the entry side in order to reproduce the same conditions as during SSRT tests. This experimental setup enables to determine the apparent diffusion coefficient and the apparent hydrogen concentration at the sample surface by plotting the detection current as a function of time as shown in Figure 129. Equations presented within the bibliographic review enable to determine the apparent diffusion coefficient and the apparent surface concentration.

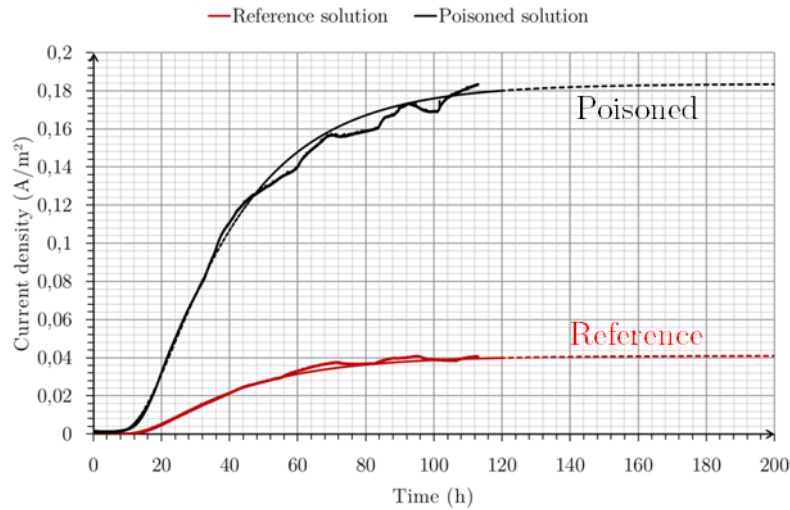


Figure 129 - Current density vs time measured at the exit side of the permeation setup during preconditioning treatment of the sample (Virgo™38 impeller industrially heat treated) at a constant applied potential of -1300mV/SCE at the entry side in both solutions (reference solution: red curves and poisoned solution: black curves)

The data of Figure 129 were used to determine the apparent hydrogen diffusion coefficients, by applying equations given within the bibliographic review (time lag method). The corresponding values are $8.7 \cdot 10^{-14} \text{ m}^2/\text{s}$ and $9.1 \cdot 10^{-14} \text{ m}^2/\text{s}$ in the reference solution and the poisoned one respectively. As expected, these values are close to each other because the hydrogen diffusion coefficient is not supposed to depend on the solution used but only on the microstructure. These values are also in agreement with the ones found in the literature on SMSS containing retained austenite [148]. The apparent hydrogen concentrations at the entry side were $1480 \text{ mol}\cdot\text{m}^{-3}$ and $6450 \text{ mol}\cdot\text{m}^{-3}$ respectively. These entry conditions finally set a larger hydrogen flow in the steel when it is polarized in solution containing Na₂S. A factor 4.6 is recorded between the respective current densities. This difference explains that the embrittlement obtained during SSRT tests in the poisoned solution is higher than in the reference solution (see later).

The hydrogen fugacity can be measured by permeation tests using a method described by Liu et al [149]. They measured permeability transients in order to determine parameters in the thermodynamic relationship between hydrogen activity and applied electrochemical potential (equation (i)) during charging considering that the electrolytic cathodic charging is the same as the gaseous hydrogen charging at a given temperature.

Under hydrogen cathodic charging at a constant potential E_C , the relation between the hydrogen fugacity f_H and the applied potential can be written as:

$$f_H = A * \exp\left(-\frac{\eta F}{\zeta RT}\right) \quad (i)$$

where A and ζ are the parameters function of the mechanism of cathodic discharge that can be determined by the method described by Liu et al [149], F is the Faraday constant, R the gas constant, T the absolute temperature and η is the overpotential determined at normal temperature and pressure by:

$$\eta[\text{V}] = E_{C/NHE} - E_H^0 = E_{C/SCE} + 0,244 + 0,0591 * \text{pH}_{\text{entry}}$$

Definition of an environment with elevated hydrogen activity to reproduce hydrogen embrittlement observed in service

By using the Sieverts law ($f_H = \left(\frac{C}{S}\right)^2$) and the relation between the hydrogen concentration at the entry face and the steady state current ($i_\infty = \frac{FDC}{e}$) [150] one can re-write equation (i) as [149]:

$$\ln(i_\infty) = \ln\left(\frac{FDS}{e}\right) + \frac{1}{2}\ln(A) - \frac{\eta F}{2\zeta RT} \quad (\text{ii})$$

Therefore, the parameters A and ζ can be evaluated experimentally from the relationship (ii) between η and i_∞ by varying the entry potential during the same experiment (applying transients). In the previous relation, D is the lattice diffusion coefficient which is significantly different from the apparent diffusion coefficient that can be determined by a unique transient. The successive transients have as a consequence to reduce the trapping effects which lead to partial increase or decrease of the cathodic polarization and a better determination of the lattice diffusion coefficient and real hydrogen concentration at the sample surface (Figure 130).

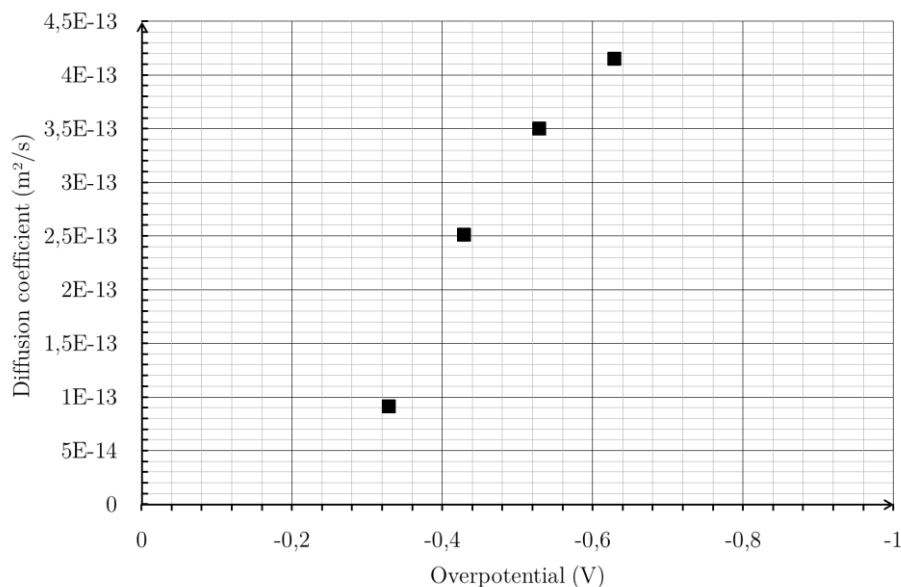


Figure 130 - Evolution of the hydrogen diffusion coefficient determined after each transient as a function of the applied potential during transients on Virgo™38 in the poisoned solution

However, these transients should be started on a reproducible surface. This virgin surface can be obtained after a long time uninterrupted cathodic polarization also called preconditioning of the sample surface [151] [152]. This step can correspond to the first transient presented previously. This approach is synthetized in Figure 131 [149].

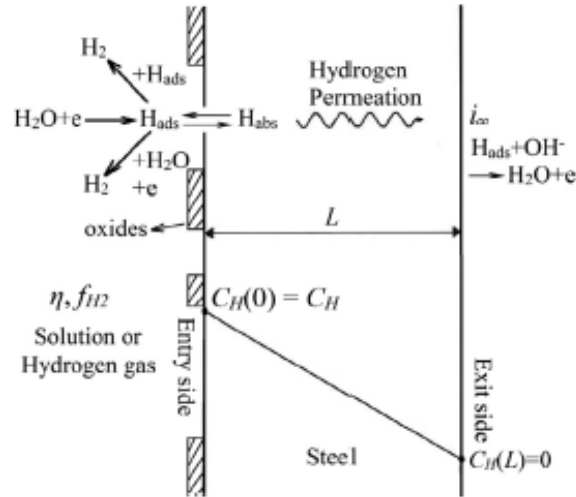


Figure 131 - Schematic representation of conditions at steady state for an ideal permeation test

Figure 132 shows the hydrogen permeation transients for different cathodic potentials applied at the input side of industrially heat treated Virgo™38 in the poisoned solution containing Na₂S and the steady-state hydrogen permeation rate i_{∞} versus overpotential η .

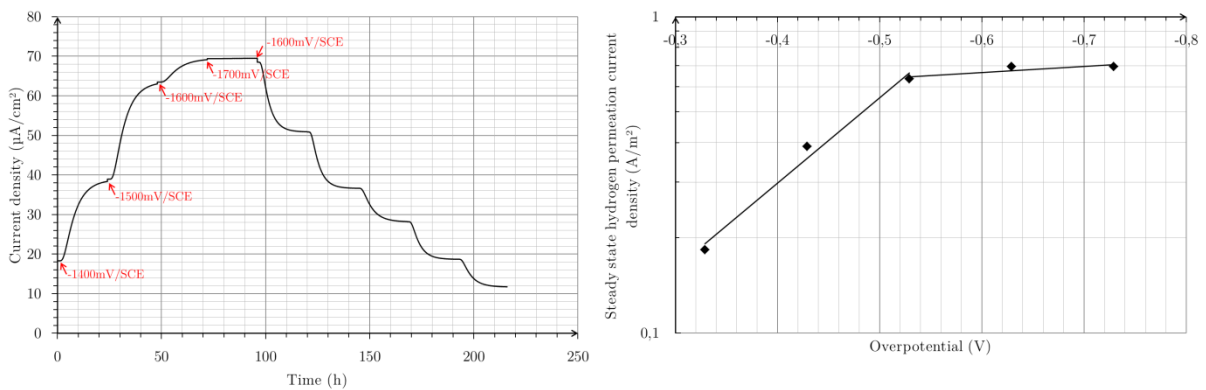


Figure 132 - Hydrogen permeation transients applied in the poisoned solution after 120h preconditioning at -1300mV/SCE: 24 hours for each transient from -1400mV/SCE to -1700mV/SCE every -100mV then back to -1200mV/SCE (left) and evolution of the steady state current density measured at the exit side as a function of the applied overpotential at the entry side

Similarly to the work of Liu et al. [149], we notice a change in the slope of the curve representing the evolution of the steady state current density as a function of the overpotential. This slope change was identified as being due to a change in the hydrogen charging mechanism. It evolves from a coupled discharge-recombination hydrogen charging mechanism at low overpotentials to a low discharge-fast electrochemical hydrogen charging mechanism at higher overpotentials. The relations can be written as:

$$\ln(i_{\infty}) = \begin{cases} -6.21\eta - 3.70 & \text{for } |\eta| < 0.5 \\ -0.44\eta - 0.67 & \text{for } |\eta| > 0.5 \end{cases}$$

As previously mentioned, to calculate the hydrogen fugacity by using equation (ii) and the previous experimental relation extracted from Figure 132-b, we need to determine the lattice diffusion coefficient which is expected to be higher than the one previously determined during preconditioning treatment ($9.1 \cdot 10^{-14} \text{ m}^2/\text{s}$). To do it, the use of the two following linear relations is possible (equation (v)):

Definition of an environment with elevated hydrogen activity to reproduce hydrogen embrittlement observed in service

- between the product of the steady state current density at the exit side and the sample thickness and the square root of the cathodic current at the entry side
- between the hydrogen concentration and the square root of the cathodic current at the entry side

$$C_H = a_1 \sqrt{i_c} + b_1 = \frac{i_{\infty} * e}{FD} \quad (iii)$$

$$i_{\infty} * e = a_2 \sqrt{i_c} + b_2 \quad (iv)$$

$$\rightarrow a_1 = \frac{a_2}{FD} \quad (v)$$

These two relations are presented in Figure 133 and enable us to determine that the lattice diffusion coefficient is $6.1 \cdot 10^{-13} \text{ m}^2/\text{s}$, effectively higher than the one determined previously, where trapping was taken into account.

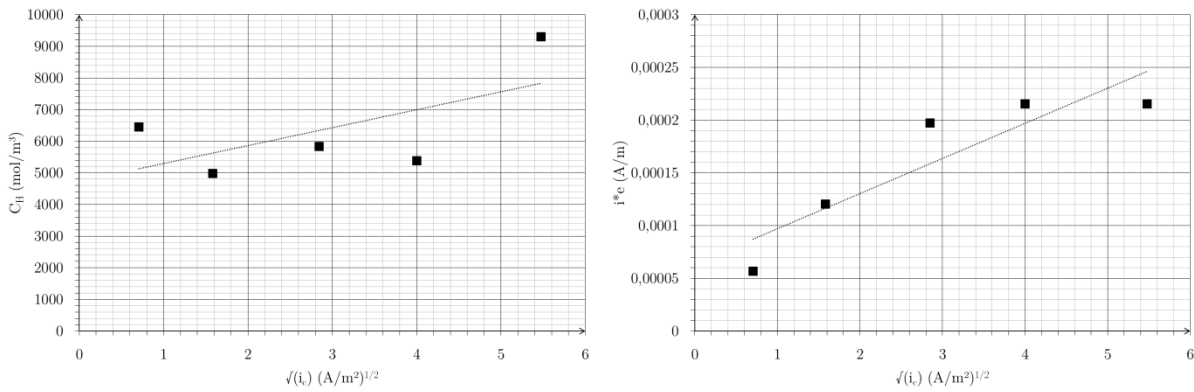


Figure 133 - Determination of the hydrogen lattice diffusion coefficient on Virgo™38

To calculate the hydrogen fugacity using equation (ii), we also need to determine the hydrogen solubility of Virgo™38. This could be done by performing a hydrogen permeation test in a solution of 0.1M NaOH as described by Liu et. al. [149]. The hydrogen fugacity of this environment as a function of the applied potential is expressed by [153]:

$$f_{H_2} = 10^{-1,5} * \exp\left(-\frac{F\eta}{2RT}\right)$$

where $F = 96485 \text{ C.mol}^{-1}$, $R = 8.314 \text{ J.mol}^{-1}.\text{K}^{-1}$, T is the temperature in K, η is the overpotential in V.

The hydrogen solubility can be calculated using the Sievert's law, knowing the hydrogen concentration at the entry side:

$$S = \frac{C_H}{\sqrt{f_{H_2}}}$$

The hydrogen concentration at the entry side can be determined by the permeation test at the considered potential:

$$C_H = \frac{i_{\infty} * e}{F * D_L}$$

where i is the steady state current density at the considered potential in A.m^{-2} , e is the sample thickness in m, F is the Faraday and D_L is the lattice diffusion coefficient of the alloy.

Chapter IV: Hydrogen embrittlement of Virgo™38 in different metallurgical states under cathodic charging in an environment containing Na₂S

With this technique, we were able to determine a hydrogen solubility of 48 mol.m⁻³.atm^{-1/2}, which corresponds to a concentration of around 100 wt. ppm of hydrogen under 1bar H₂. As the parameters used are related to the electrochemical parameters at the sample surface, this hydrogen concentration cannot be representative of the bulk concentration and is obviously higher. However, this value is in agreement with the literature for permeation tests on SMSS in presence of H₂S [148].

Knowing that applying a constant potential of -1300mV/SCE during SSRT tests or permeation tests corresponds to overpotential of η=-0.33V and that for “low” overpotentials (|η|<0.5), the parameters A and ζ calculated using the previous data are:

$$A = \frac{\exp(2b) * e^2}{(FDS)^2} = 7.31 \text{ atm}$$

$$\zeta = -\frac{F}{2aRT} = 3.15$$

where e = 310 μm is the sample thickness, F = 96485 C.mol⁻¹ is the Faraday, D is the lattice diffusion coefficient determined previously (6.1*10⁻¹³ m²/s), S is the solubility calculated previously (48.3 mol.m⁻³.atm^{-1/2}), R = 8.314 J.mol⁻¹.K⁻¹, T = 293 K, and a=-6.21 and b=-3.70 are the parameters determined in Figure 132-b for η=-0.33V. We can be confident in the ζ value found previously, as it lies within the usual range of 3.0 to 3.5 [154].

Using equation (i) and the parameters A and ζ calculated previously, we can estimate the hydrogen fugacity during SSRT tests under applied potential of -1300mV/SCE in the poisoned solution to be 437 atm. Within the literature [155], it is indicated that hydrogen activity is within the range 3-15ksi (i.e. 200 to 1000atm and 20 to 100MPa) in presence of H₂S which means that the poisoned solution containing Na₂S is perfectly adapted to reproduce hydrogen embrittlement in H₂S environments.

In the literature, high hydrogen activities measured in these conditions are attributed to the poisoning effect of adsorbed sulfur at the sample surface. Marcus et al. constructed E-pH diagrams for adsorbed species at the surface of different materials [156] [157] [158]. Furthermore, they showed by thermodynamics calculations that atomic sulfur adsorbed at the metal surface is stable, even when sulfides are unstable. The diagrams of adsorbed sulfur on the main component of SMSS (i.e. Fe, Cr and Ni) are presented in Figure 134.

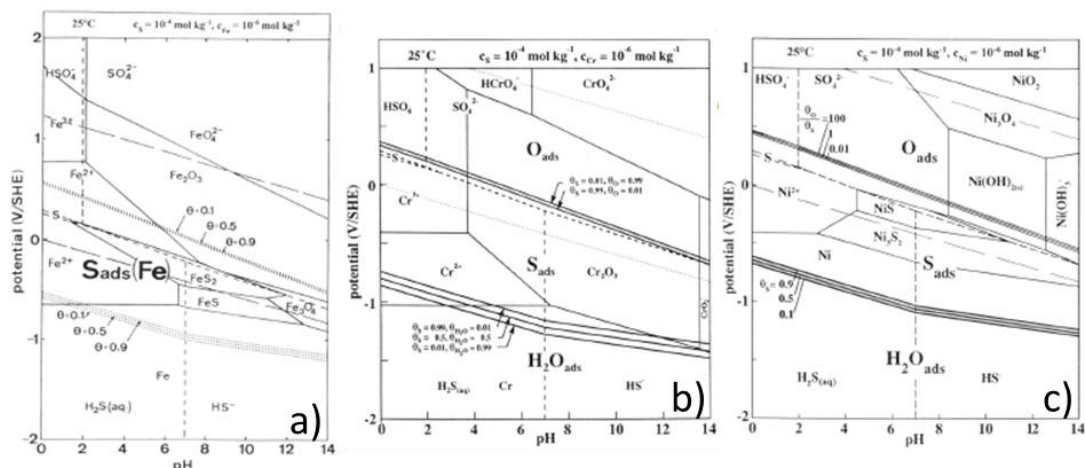


Figure 134 - E-pH diagrams for adsorbed sulfur on Fe [156], Cr [157] and Ni [158]

Definition of an environment with elevated hydrogen activity to reproduce hydrogen embrittlement observed in service

Considering that iron is the main component of SMSS, a simplified re-plot of the stability diagram for the adsorbed species on pure Fe is presented in Figure 135. It shows that the species adsorbed under cathodic conditions used in our study in the poisoned solution is atomic sulfur. Thus, adsorbed sulfur replaces adsorbed H_2O found in acid environment without poison, which leads to a less efficient hydrogen recombination at the sample surface. This observation can explain the high hydrogen activity measured in the poisoned solution under cathodic charging at -1300mV/SCE .

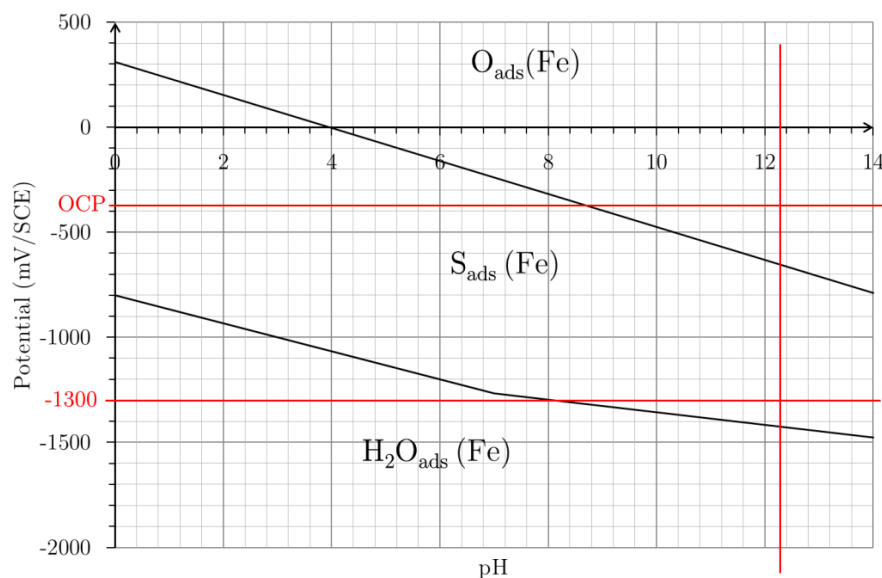


Figure 135 - Simplified re-plot of the stability diagram based on Marcus et al. data [156] for the adsorbed species on pure Fe showing that sulfur is the main element adsorbed at the surface in the cathodic charging conditions presented above while oxygen is the main element adsorbed at the OCP in the poisoned solution

The simplified re-plot presented in Figure 135 also confirms the change in charging mechanism between -1400mV/SCE and -1500mV/SCE observed in Figure 132-b. This change in the charging mechanism is attributed to the change in the adsorbed species at the sample surface. It is noteworthy that the OCP lies within the domain of adsorbed oxygen and that a low embrittlement is expected in this condition, at least as long as the potential is higher than -650mV/SCE (see next part).

1.3. Conclusions

The results of permeation tests confirmed that the hydrogen activity is increased by the addition of poison Na_2S under cathodic charging conditions. This increase of the hydrogen activity under cathodic charging is attributed to the adsorption of atomic sulfur at the surface which blocks hydrogen recombination and favors the entry of hydrogen, leading to higher hydrogen flux in the alloy.

The hydrogen fugacity of this environment, namely $0.1\text{M NaOH} + 0.02\text{M Na}_2\text{S}$, was estimated to be of the order of 320atm , which is, according to the literature, equivalent to the hydrogen fugacity in an industrial environment ($\text{pH}=4.5$ and $1\text{ bar H}_2\text{S}$).

Consequently, this environment has been validated for the study of the influence of the Virgo™38 microstructure on the embrittlement mechanisms due to hydrogen, as presented in the following parts of this chapter.

2. Effect of the microstructure on the resistance to HE of Virgo™38

2.1. Reference metallurgical state: Virgo™38 impeller industrially heat treated

Virgo™38 with an industrial microstructure as described in Chapter II was used. All specimens were machined with the tensile axis parallel to the impeller radius. The stress strain curves obtained in the tests in the poisoned solution containing Na₂S at the Open Circuit Potential and under cathodic polarization at a strain rate of 10^{-7} s^{-1} are presented in Figure 136.

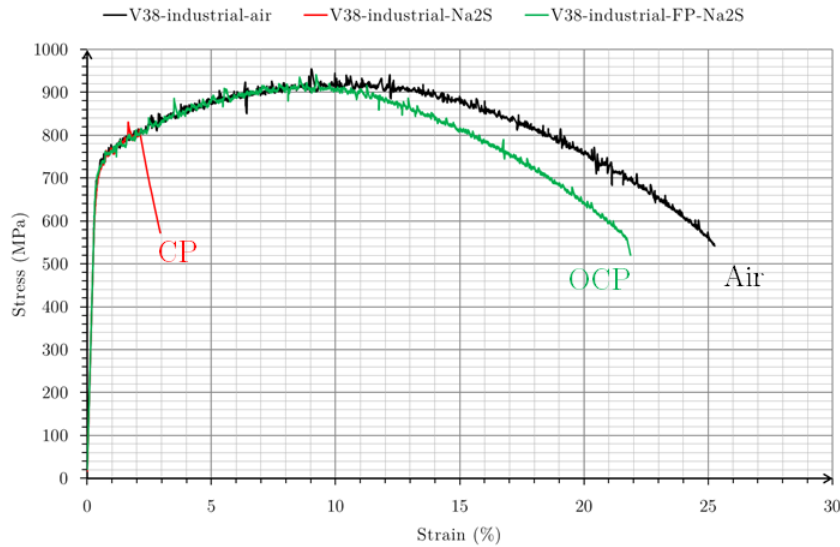


Figure 136 - Tensile curves of Virgo™38 in air at 10^{-5} s^{-1} (black curve), under open circuit potential (OCP, green curve) cathodic charging (CP, red curve) at -1300 mV/SCE in a solution containing $0.1 \text{ M NaOH} + 0.02 \text{ M Na}_2\text{S}$ purged with N_2 both at a strain rate of 10^{-7} s^{-1}

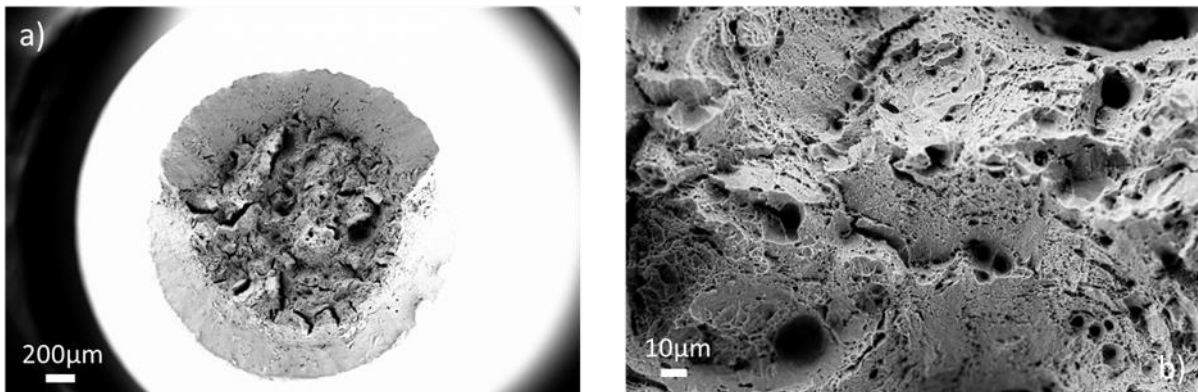


Figure 137 - Fracture surface of industrial Virgo™38 after SSRT test at a strain rate of 10^{-7} s^{-1} at the OCP in the poisoned solution containing $0.1 \text{ M NaOH} + 0.02 \text{ M Na}_2\text{S}$ purged with N_2

- a) Overview of the fracture surface
- b) Detailed image showing mainly ductile failure with some intergranular facets

The test at OCP in the poisoned solution gives a mainly ductile failure (Figure 137) with some intergranular facets. The absence of brittleness at the OCP matches with the data of Figure 135 where we can see that, at the OCP, sulphur does not promote the entry of hydrogen. However, as seen in Figure 136, necking starts at a lower plastic strain in presence of the poison than during the reference test in air.

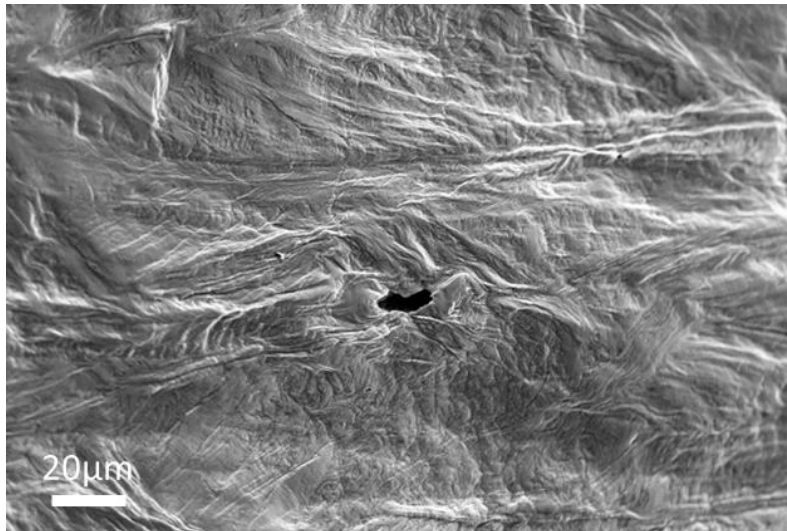


Figure 138 - Barrel surface of industrial Virgo™38 after SSRT test at a strain rate of 10^{-7}s^{-1} at the OCP in the poisoned solution containing 0.1M NaOH + 0.02M Na₂S purged with N₂ showing secondary crack initiation sites

The anticipated necking during the test at OCP in the poisoned solution can be attributed to local surface defects as visible in Figure 138, looking like cavities formed during mechanical damage. Effects of hydrogen on plastic localization could be at the origin of these little cavities which promote the triggering of the necking. Localization of hydrogen entry could be due to the effect of adsorbed sulphur on mechanical depassivation, as this element is known to hinder repassivation [159]. Indeed, during this test, due to the loading, the minimum potential recorded was of -654mV/SCE, which is in the domain of adsorbed sulfur (Figure 135), can explain its presence.

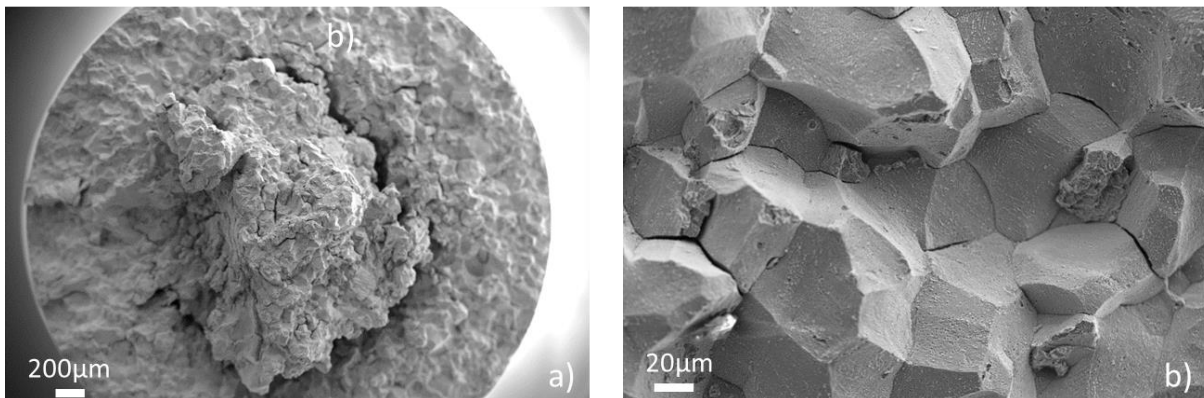


Figure 139 - Fracture surface of industrial Virgo™38 after SSRT test at a strain rate of 10^{-7}s^{-1} and under cathodic charging at -1300mV/SCE in a solution containing 0.1M NaOH + 0.02M Na₂S purged with N₂

- a) Overview of the fracture surface
- b) Detailed image showing fully intergranular mode of cracking

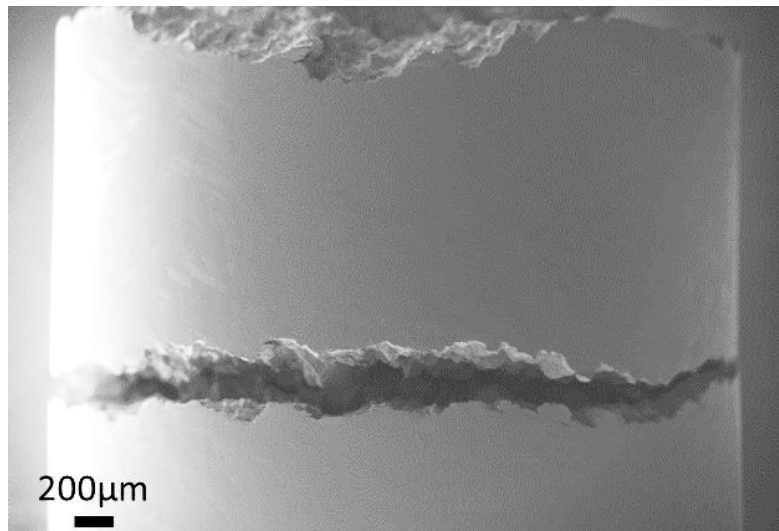


Figure 140 - Barrel surface of Virgo™38 after SSRT test at a strain rate of 10^{-7} s^{-1} and under cathodic charging at -1300 mV/SCE in a solution containing $0.1 \text{ M NaOH} + 0.02 \text{ M Na}_2\text{S}$ purged with N_2 showing a secondary crack through the whole specimen section

For cathodic discharge conditions, Figure 139 shows a majoritary intergranular fracture mode similar to the ones obtained in service in presence of H_2S . Contrary to what had been presented in the previous Chapter, even the center of the fracture surface contains intergranular areas, which is a consequence of the higher hydrogen activity than what was observed in acid environments. As we have seen previously in NaOH environment without sulfides, grain boundary facets present a roughness aspect linked to emergence of plasticity and ductile fracture. These features are less marked insofar as total elongation is much smaller with addition of H recombination poison.

The estimation of the diffusion distance of interstitial hydrogen during the test duration (which corresponds to about 170 hours) up to fracture, according to the relation \sqrt{Dt} , indicates that a crown of about $660 \mu\text{m}$ should have been hydrogenated (diffusion coefficient used equal to $6.1 \cdot 10^{-13} \text{ m}^2/\text{s}$). This distance is much smaller than brittle crowns obtained after SSRT tests, which suggests that hydrogen-plasticity interactions at crack tip must operate during tensile tests.

Two main cracks were initiated on this specimen, one having stopped before fracture. Moreover, other important secondary intergranular cracks are present on the barrel surface of the sample (Figure 140 and Figure 141). These secondary cracks are very useful because they enable to study the crack path and reveal the potential relationship with the microstructural elements.

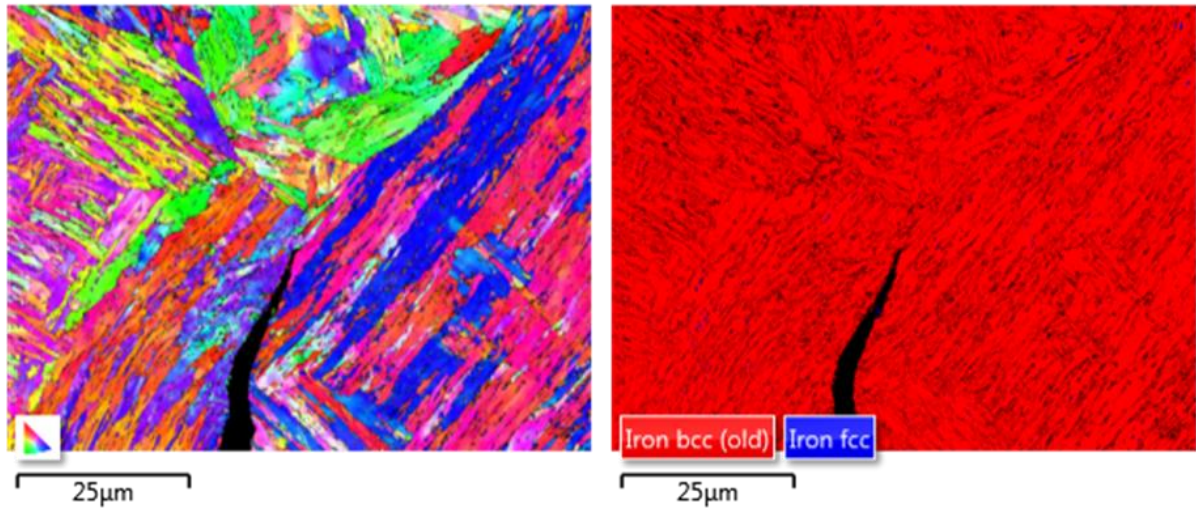


Figure 141 - Investigation of the crack propagation path by EBSD mapping at a crack tip of a secondary crack

One can see in Figure 141 that cracks propagate along former austenitic grain boundaries (left), which, it is recalled, are partially decorated with retained austenite. Unfortunately, no retained austenite is visible at the crack tip (right). Indeed, due to the large local strains achieved ahead of the crack tip, SIMT can happen and leads to the formation of fresh martensite.

In order to visualize the effect of Na_2S on embrittlement, Table 22 summarizes the results of SSRT tests realized in the environment containing Na_2S poison, compared to the most severe test performed in the acid environment presented in Chapter III.

Table 22 - Influence of the addition of Na_2S on the reduction in area RA, ratio of area reduction RAR, plastic elongation E_p and reduction of plastic elongation RE_p (parameters defined in Chapter III)

	RA (%)	RAR (%)	E_p (%)	RE_p (%)
Reference (air)	75	100	25	0
CP-pH= $1.5 \cdot 10^{-7}$ with pH control	6.5	9	4.5	82
CP-no $\text{Na}_2\text{S} \cdot 10^{-7}$	14	18.7	11	56
OCP- $\text{Na}_2\text{S} \cdot 10^{-7}$	68	90.6	21.5	14
CP- $\text{Na}_2\text{S} \cdot 10^{-7}$	1	1.4	1.8	93

The embrittlement produced during the tests at cathodic potential in acid environment and in the poisoned solution is very different, even if both lead to crack formations from the surface of the sample that propagate with a brittle mode. The propagation is even more intergranular when the hydrogen activity is high, particularly with addition of sulfides. However, adding Na_2S is not sufficient to obtain hydrogen embrittlement, probably due to the low hydrogen entry in the alloy, and it is necessary to apply simultaneously a cathodic overpotential that forces sulfur adsorption and hydrogen entrance.

2.2. Influence of the amount of retained austenite on the resistance to HE of Virgo™38

2.2.1. Influence of the heat treatment

This section is devoted to the study of the influence of the microstructure on the HE resistance of Virgo™38. To do it, different heat treatments were performed in order to modify the initial microstructure. Indeed, as presented in Chapter II, the tempering temperature influences the amount of retained austenite and the carbide precipitation. Figure 142 presents the effect of different heat treatments, performed after re-austenitization and quenching of the impeller, on the stress-strain curves that were obtained by SSRT tests under cathodic charging at -1300mV/SCE in the poisoned solution.

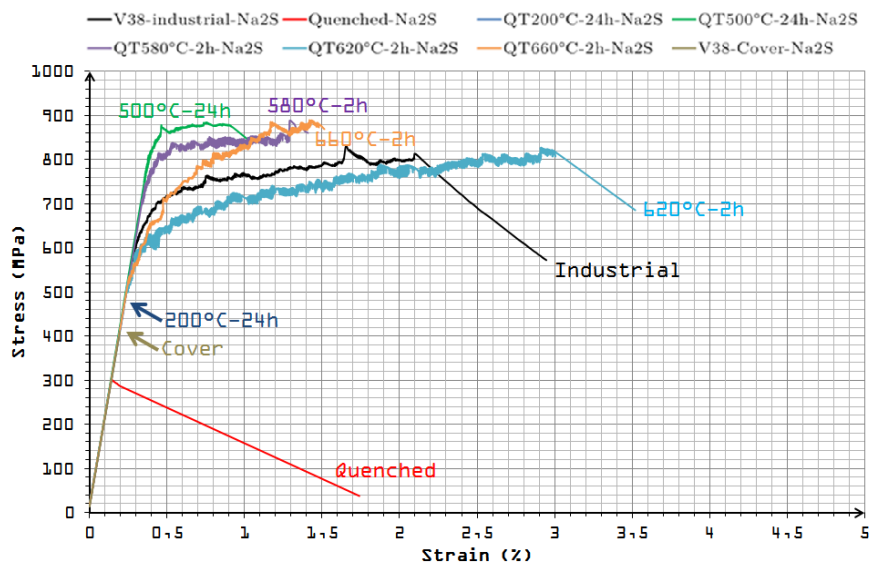


Figure 142 - Tensile curves of Virgo™38 obtained by SSRT tests under cathodic charging at -1300mV/SCE in a solution containing 0.1M NaOH + 0.02M Na₂S purged with N₂ and at a strain rate of 10⁻⁷s⁻¹. This set of curves shows the effect of different one step heat treatments after quenching.

One can notice that the shape of the curves in environment is similar to the one that had been observed in air (see Figure 68, Chapter II). The values obtained from these tests are summarized in Table 23. In the case of samples quenched and quenched plus tempered at 200°C, failure takes place before 0.01% yield stress is reached but for all other samples yielding starts (0.01% yield stress) at very similar stresses as those observed in tensile tests in air at the strain rate of 10⁻⁵s⁻¹.

Table 23 - Summary of the physical yield stresses, 0.2% proof stresses, UTS, plastic elongation at failure and RA obtained after HE tests for the different heat treatments performed on Virgo™38 (see Table 10 for values in air)

Heat treatment applied	0.01% yield stress (MPa)	0.2% proof stress (MPa)	Plastic elongation at failure E _p (%)	UTS (MPa)	RA (%)
Industrial (reference)	570	730	1.7	820	75
Quenched	Failure at 300	x	0	x	0.3
QT200°C-24h	Failure at 460	x	0	x	0.5
QT500°C-24h	760	870	0.5	910	1.5
QT580°C-2h	710	840	0.95	870	4.6
QT620°C-2h	490	635	2.6	820	5
QT660°C-2h	530	730	1.05	890	4.1

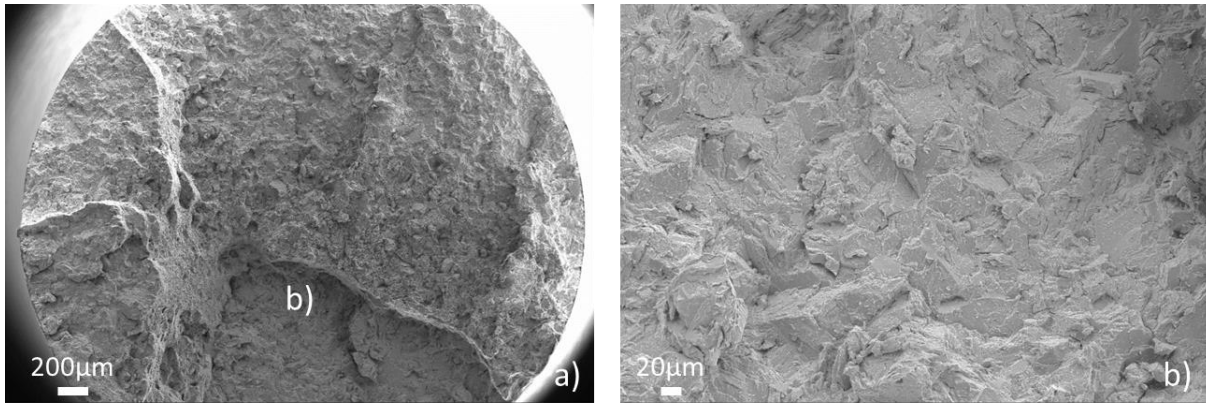


Figure 143 - Fracture surface of Virgo™38 in quenched state after SSRT test at a strain rate of 10^{-7} s^{-1} and under cathodic charging at -1300 mV/SCE in a solution containing $0.1 \text{ M NaOH} + 0.02 \text{ M Na}_2\text{S}$ purged with N_2
 a) Overview of the fracture surface, several initiation areas
 b) Detailed image showing fully transgranular mode of cracking

Fractographic observations show (Figure 143) that the cracking mode of the quenched material is entirely transgranular. This observation indicates a strong influence of the tempering treatment on the cracking mode under the same electrochemical conditions. Indeed, in the industrial state, fracture surfaces were mainly intergranular, as shown in Figure 139, while they are fully transgranular after quenching and before tempering. The influence of the heat treatment on the fracture mode will be discussed later in this chapter.

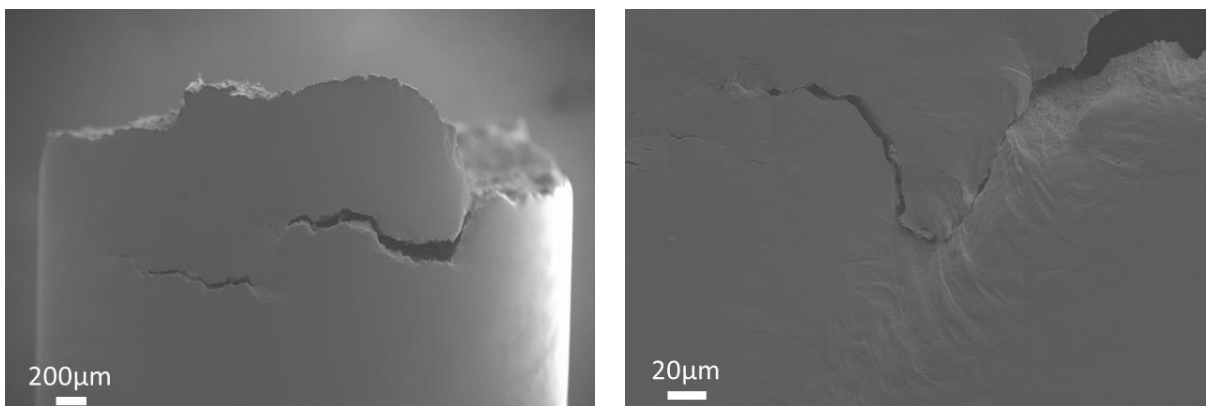


Figure 144 - Barrel surface of Virgo™38 in quenched state after SSRT test at a strain rate of 10^{-7} s^{-1} and under cathodic charging at -1300 mV/SCE in a solution containing $0.1 \text{ M NaOH} + 0.02 \text{ M Na}_2\text{S}$ purged with N_2 showing important secondary cracks

Figure 144 presents the barrel surface of a specimen in the quenched state after the SSRT test where one can see that several cracks were initiated and then coalesced. These fairly deep brittle cracks have coalesced at final fracture along shear bands that connected their tip and produce locally a high amount of plasticity visible at the surface, even if the macroscopic failure occurs within the elastic domain (red curve in Figure 142).

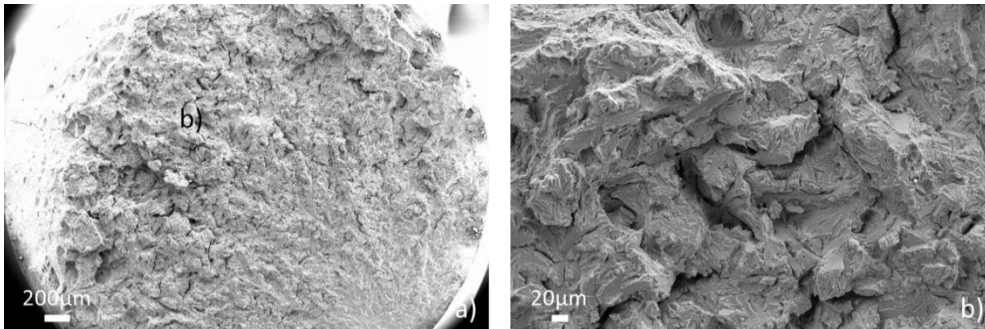


Figure 145 - Fracture surface of Virgo™38 in quenched and tempered state (24h at 200°C) after SSRT test at a strain rate of $10^{-7} s^{-1}$ and under cathodic charging at -1300mV/SCE in a solution containing 0.1M NaOH + 0.02M Na₂S purged with N₂
a) Overview of the fracture surface, crack initiation from the bottom right
b) Detailed image showing again a fully transgranular mode of cracking

After tempering at 200°C during 24 hours, the failure still occurs within the elastic domain (Figure 142 and Table 23). As previously, the failure is fully transgranular (Figure 145) although some little ductile cavities were observed between brittle planes of quasi-cleavage type. This observation is not surprising because, as it had been mentioned in Chapter II, no fundamental changes occurred during this tempering treatment. Indeed, only a slight recovery of the dislocation structure, certainly coupled with the relaxation of internal stresses compared to the quenched microstructure, is expected. The presence of these small ductile cavities can be explained by the recovery of the ductility with tempering completely relaxing the stresses, at least locally. The crack initiation density on the barrel is lower, and finally only one crack has led to the rupture of specimen.

This test enables us finding that, in the fully martensitic microstructure, the internal stresses induced by martensite transformation, and thus initial dislocation density and/or the hardness play an important role on the cracking resistance. Indeed, decreasing the initial mechanical properties by stress relaxation enable increasing the stress at failure from 300 MPa to 460 MPa (Table 23). Even if one cannot exclude the triggering of a microplasticity at these stress levels, the mechanism of rupture that seems to operate under these conditions (hydrogenated fully martensite microstructure) results from the reduction of the cohesion energy of some particular interfaces and crystallographic planes, as describe in the HEDE model. A high dislocation density contributes both to the increase the concentration of reversibly trapped hydrogen in the material and, if the internal stresses were not relaxed, to decrease the effective applied stress to initiate decohesion. All these elements indicate that initial dislocation density is an essential parameter influencing the cracking resistance as it was observed in other studies [86].

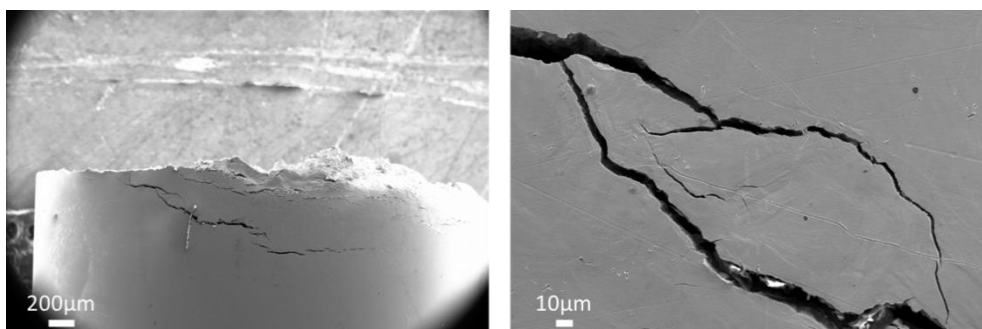


Figure 146 - Barrel surface of Virgo™38 in quenched and tempered state (24h at 200°C) after SSRT test at a strain rate of $10^{-7} s^{-1}$ and under cathodic charging at -1300mV/SCE in a solution containing 0.1M NaOH + 0.02M Na₂S purged with N₂ showing important secondary cracks

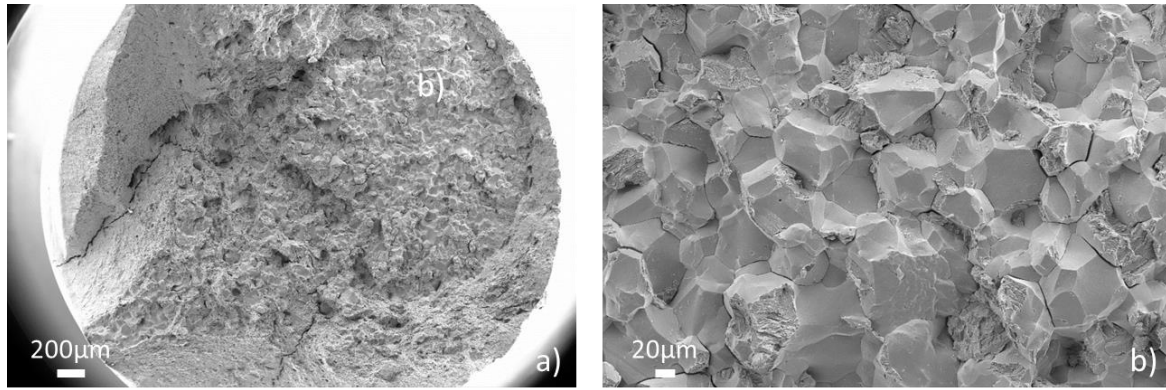


Figure 147 - Fracture surface of Virgo™38 in quenched and tempered state (24h at 500°C) after SSRT test at a strain rate of 10^{-7} s^{-1} and under cathodic charging at -1300mV/SCE in a solution containing 0.1M NaOH + 0.02M Na_2S purged with N_2
 a) Overview of the fracture surface
 b) Detailed image showing mainly intergranular mode of cracking

Tempering at a higher temperature (500°C/24h) leads to a significant change in material behavior. Fracture occurs after approximately 0.5% of plastic deformation and there is a strong proportion of intergranular areas on the fracture surface (Figure 147). Here again, some facets of grain boundaries observed at high magnification show marks of emergence of plasticity by location and very smooth facets. This plasticity seems to be located between laths of martensite. From the microstructural point of view, tempering at 500°C leads to precipitation of fine (3.5nm) carbides as presented in Chapter II. Consequently, the tempered BCC martensite becomes nearly carbon free and simultaneously further reduction of the dislocation density takes place. The size of carbides precipitated at 500°C being very small, it is unrealistic to consider that they could lead to dechromisation as observed in a past study [7] or that they could trap hydrogen. Furthermore, their location seems not to be compatible with the intergranular mode of cracking observed as they are expected to be located within tempered martensite. Consequently, grain boundary decohesion is supposed to be due to preferential hydrogen diffusion to prior austenite grain boundaries. Finally, these microstructural modifications allow the formation of larger grains favoring the mechanisms of dislocation multiplication and consequently, allowing the pile-up of dislocations on obstacles along slip bands such as grain boundaries or inter-laths boundaries with higher intensity. Actually, the marks of emergence of plasticity on grain boundaries facets and particularly those observed on their profile seem to confirm this mechanism (Figure 148).

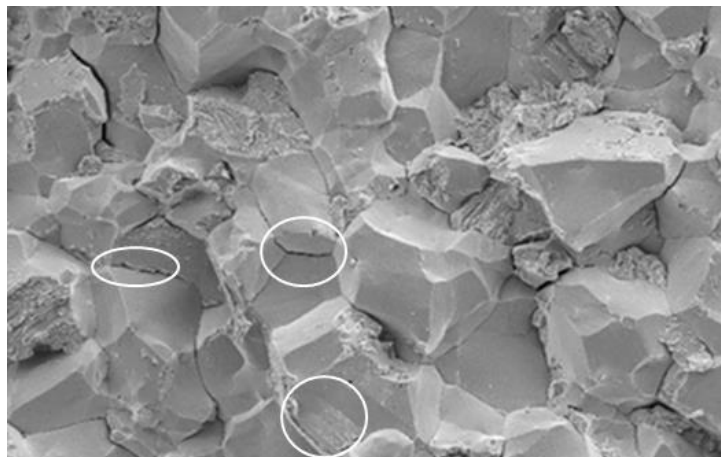


Figure 148 - Fracture surface of Virgo™38 in quenched and tempered state (24h at 500°C) after SSRT test at a strain rate of 10^{-7} s^{-1} and under cathodic charging at -1300mV/SCE in a solution containing 0.1M NaOH + 0.02M Na_2S purged with N_2 showing intergranular facets at higher magnification

Chapter IV: Hydrogen embrittlement of Virgo™38 in different metallurgical states under cathodic charging in an environment containing Na₂S

In contrast to quenched alloy and quenched plus tempered at 200°C alloy, where a high dislocation density allow achieving a higher hydrogen content at the crack tip, the critical stress of decohesion in martensite, certainly less weakened by the presence of hydrogen, cannot be achieved after tempering at 500°C. Crack initiation probably occurs at deformation localization sites, at the top of pile-up dislocations localized in slip bands, against grain boundaries and high disorientation inter-laths boundaries.

The question arises what microstructural changes not presented in Chapter II could be at the origin of smooth intergranular cracking. A specific bibliographic review focused on intergranular brittleness associated with low temperature tempering treatment reveals that Phosphorous Grain Boundary Segregation (PGBS) [160] is often at the origin of intergranular failures in steels. This effect of P is plausible due to its high content in the impeller grade and could explain, in relation with hydrogen, the intergranular fracture of Virgo™38. This element will be discussed later in this Chapter.

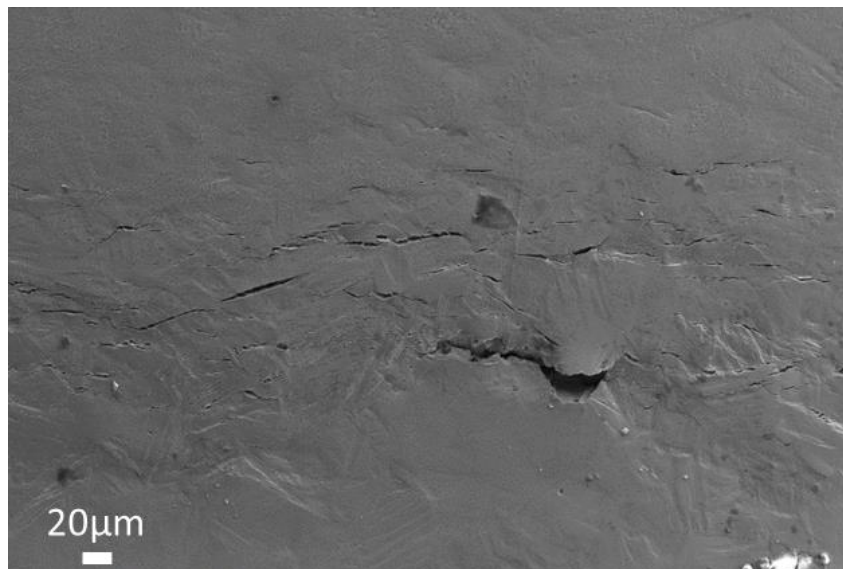


Figure 149 - Barrel surface of Virgo™38 in quenched and tempered state (24h at 500°C) after SSRT test at a strain rate of 10^{-7} s^{-1} and under cathodic charging at -1300mV/SCE in a solution containing 0.1M NaOH + 0.02M Na₂S purged with N₂ showing some small secondary cracks

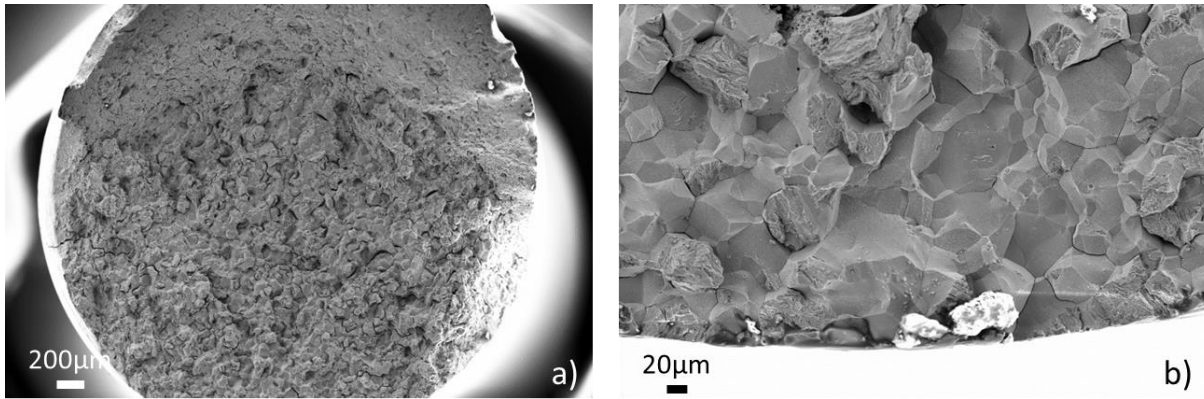


Figure 150 - Fracture surface of Virgo™38 in quenched and tempered state (2h at 580°C) after SSRT test at a strain rate of 10^{-7} s^{-1} and under cathodic charging at -1300mV/SCE in a solution containing 0.1M NaOH + 0.02M Na₂S purged with N₂
 a) Overview of the fracture surface, initiation from the bottom side
 b) Detailed image showing mixed intergranular and transgranular mode of cracking

After tempering at 580°C during 2 hours, a mixed intergranular-transgranular behavior, similar to that reported above, was observed (Figure 150). This microstructure contains the same volume fraction of carbides as after tempering at 500°C but with a slightly larger size. Consequently, their strengthening effect is weaker, as seen in Figure 142. In this microstructural state, a limited amount of retained austenite (around 3%) is formed between martensitic laths. As it was reported in the literature [100], retained austenite can act as hydrogen trap and lead to a decrease of ductility while transformed to martensite by SIMT. However, after this heat treatment, retained austenite is supposed to be stable regarding SIMT. This effect is thus probably not dangerous for this heat treatment. Furthermore, according to the conclusions of Chapter II, the mechanical properties of the retained austenite are similar or even superior to those of quenched martensite. The mechanisms explained previously concerning the localization of deformation can operate similarly. The difference with the tempering at lower temperatures is the presence of retained austenite with regard to the hydrogen trapping. Due to its higher solubility, the austenite acts as a trap in the microstructure which leads to decrease the diffusible hydrogen in the martensite and the hydrogen trapped at the grain boundaries. Considering the stress-strain curve, the presence of austenite could reduce the localization effects of plasticity in the martensite due to a lower concentration of hydrogen, and thus delay crack initiation.

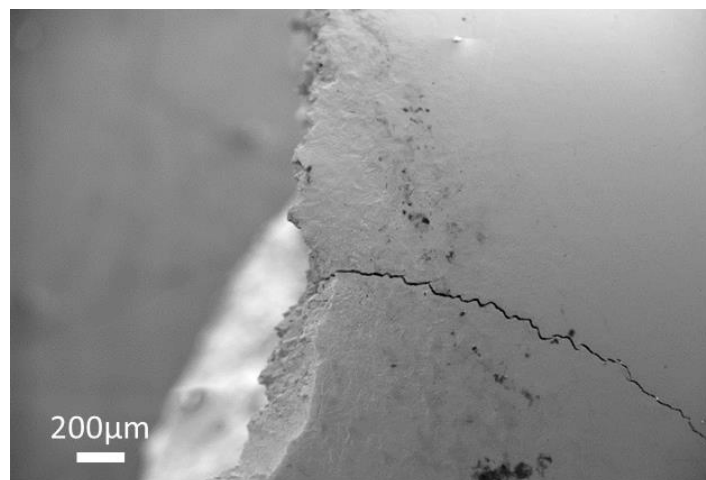


Figure 151 - Barrel surface of Virgo™38 in quenched and tempered state (2h at 580°C) after SSRT test at a strain rate of 10^{-7} s^{-1} and under cathodic charging at -1300mV/SCE in a solution containing 0.1M NaOH + 0.02M Na₂S purged with N₂ showing one longitudinal secondary crack coming from the fracture surface

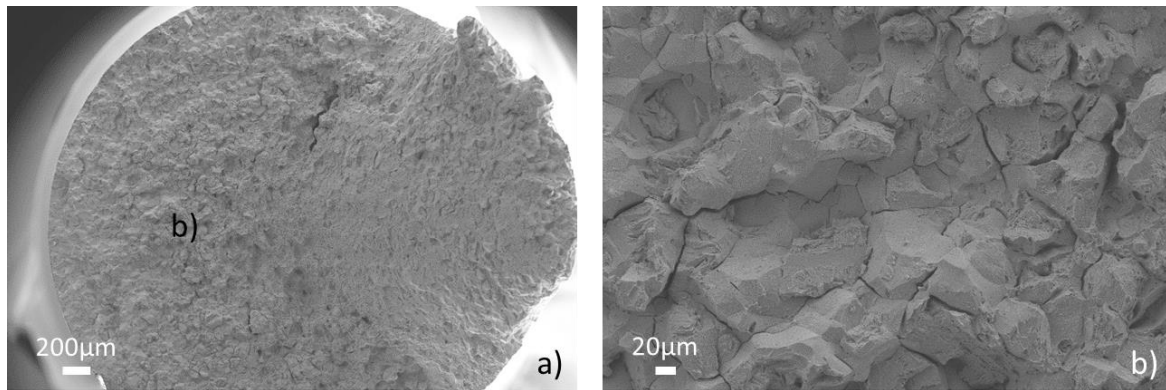


Figure 152 - Fracture surface of Virgo™38 in quenched and tempered state (2h at 620°C) after SSRT test at a strain rate of $10^{-7} s^{-1}$ and under cathodic charging at -1300mV/SCE in a solution containing 0.1M NaOH + 0.02M Na₂S purged with N₂

- a) Overview of the fracture surface, initiation from the left side**
b) Detailed image showing mixed intergranular and transgranular (close to initiation on the left) mode of cracking

After tempering at the peak temperature (2h at 620°C) identified in Chapter II, the failure is mixed intergranular with some transgranular areas close to the initiation point (Figure 152). The same manifestations of plasticity on a finer scale are observed. This metallurgical state provides the best elongation to failure after SSRT test in hydrogen charging conditions as visible in Figure 142. This observation suggests a beneficial effect of retained austenite on ductility even under strong hydrogen charging condition such as the one studied in this chapter. Indeed, retained austenite has been identified [148] to reduce the apparent diffusion coefficient of hydrogen in SMSS. Definitely, tempering at the peak temperature produces the microstructure with the maximal content of retained austenite and this microstructure provides the best resistance to hydrogen embrittlement. However, an alternative interpretation is possible in the light of results discussed in Chapter II. According to them, the ductility after tempering at peak temperature is the highest because this microstructure contains the highest amount of tempered and carbon-free martensite, with a low (450MPa) intrinsic elastic limit. The retained austenite, being the second principal element of microstructure, with a higher intrinsic elastic limit due to a high dislocation density, mainly influences the yield stress of the whole alloy. The ductility observed after tempering at $T > 620^{\circ}C$ is lower not because of a low austenite content but essentially due to a high amount of fresh martensite. We mentioned previously that retained austenite had been identified to act as an hydrogen trap increasing the brittleness in case of martensitic transformation [100]. That is why, the stability of retained austenite regarding deformation (SIMT) appears as a key parameter of crack propagation in SMSS. Indeed, retained austenite is supposed to contain high amount of hydrogen and consequently, following its transformation into martensite ahead of a crack tip, the released hydrogen leads to significant oversaturation which can dramatically decrease the resistance of the alloy. In the absence of SIMT, the austenite could remain sensitive to hydrogen effects through the interactions with dislocations leading to localized plasticity as discussed for martensite. Localized slip in thin γ laths both along grains boundaries and inter-laths boundaries can contribute to a ductile fracture on these interfaces. Nevertheless, this can only be considered for sufficiently large island sizes of austenite allowing their plastic deformation.

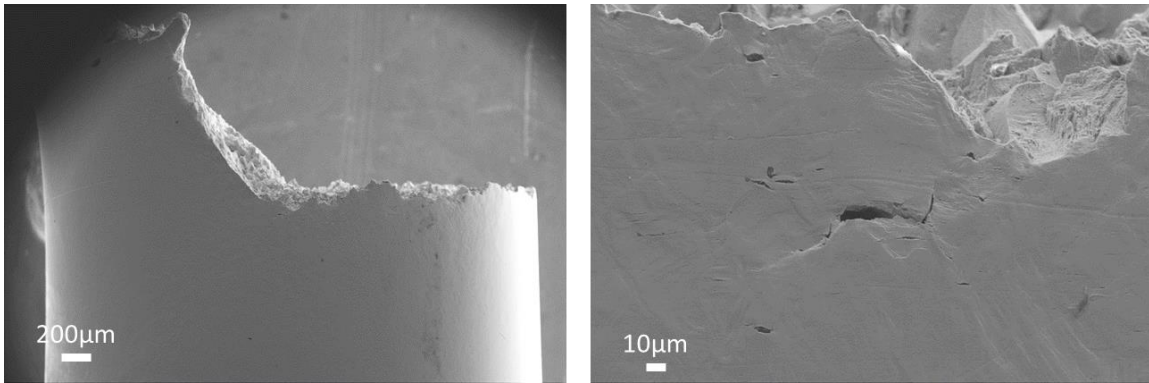


Figure 153 - Barrel surface of Virgo™38 in quenched and tempered state (2h at 620°C) after SSRT test at a strain rate of 10^{-7} s^{-1} and under cathodic charging at -1300mV/SCE in a solution containing 0.1M NaOH + 0.02M Na₂S purged with N₂ showing that two cracks have led to final failure and showing the tip of one of these cracks

In Figure 153, several marks of plasticity parallel to the secondary transgranular cracks show that crack path follows crystallographic planes. This example shows again that on tempered microstructures, mechanisms of crack initiation and crack propagation involve certainly more the hydrogen dislocation interactions than the decohesions due to hydrogen induced weakening of interatomic bonds.

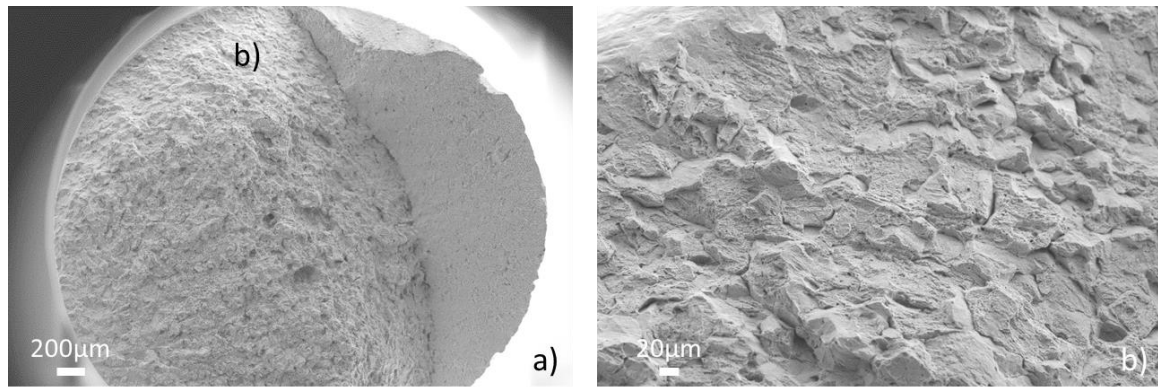


Figure 154 - Fracture surface of Virgo™38 in quenched and tempered state (2h at 660°C) after SSRT test at a strain rate of 10^{-7} s^{-1} and under cathodic charging at -1300mV/SCE in a solution containing 0.1M NaOH + 0.02M Na₂S purged with N₂
a) Overview of the fracture surface, initiation from the left side
b) Detailed image showing mainly transgranular mode of cracking

After tempering at 660°C and as presented in Chapter II, almost all the reverted austenite is unstable and transformed to martensite on cooling. The retained austenite content is thus very low (around 3%). Moreover, as seen in Chapter II, this reverted austenite was mainly formed between the laths of martensite and not on the old austenitic grain boundaries. In this case, the observed failure is transgranular (Figure 154) similar to that observed in the quenched state. The transgranular mode of cracking can be explained by the presence of fresh martensite where dislocation density and internal stresses are supposed to be high. As in the quenched and very low temperature (200°C) tempered states, the intrinsic elastic limit of fresh martensite is supposed to be high. In this case, we can also notice that the elongation at failure decreases in comparison to the state treated at the peak (Figure 142) but is comparable with the state containing the same amount of retained austenite (580°C/2h). This observation also goes in the sense of a beneficial effect of retained austenite on Hydrogen Embrittlement resistance of Virgo™38.

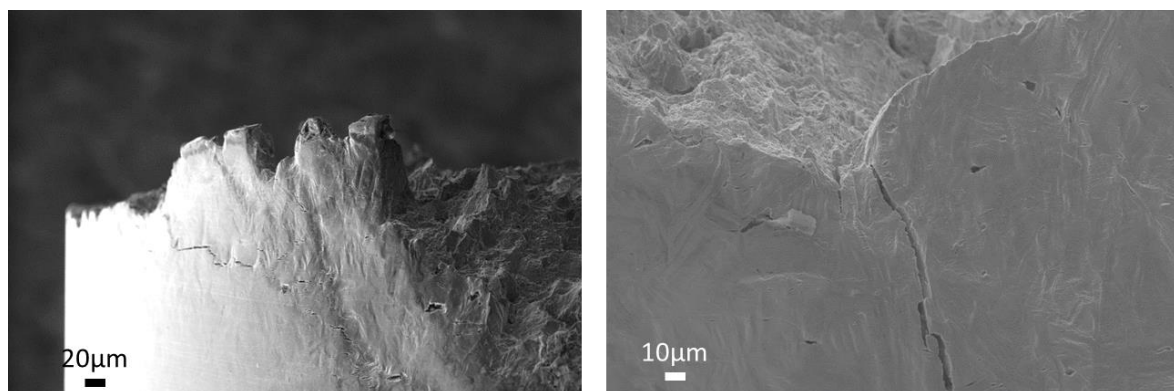


Figure 155 - Barrel surface of Virgo™38 in quenched and tempered state (2h at 660°C) after SSRT test at a strain rate of 10^{-7} s^{-1} and under cathodic charging at -1300mV/SCE in a solution containing 0.1M NaOH + 0.02M Na₂S purged with N₂ showing a significant number of secondary cracks that seem to be related to micro-plasticity at the surface

2.2.2. Influence of the pre-straining

As seen in Chapter II, another parameter that enables to modify the initial microstructure is plastic deformation. Indeed, deformation has evidently an influence on the dislocation density but also on the retained austenite content through the effect of SIMT described in Chapter II. The resulting microstructural changes can be observed in service in areas with high stress concentrations where local plastic deformation can be observed.

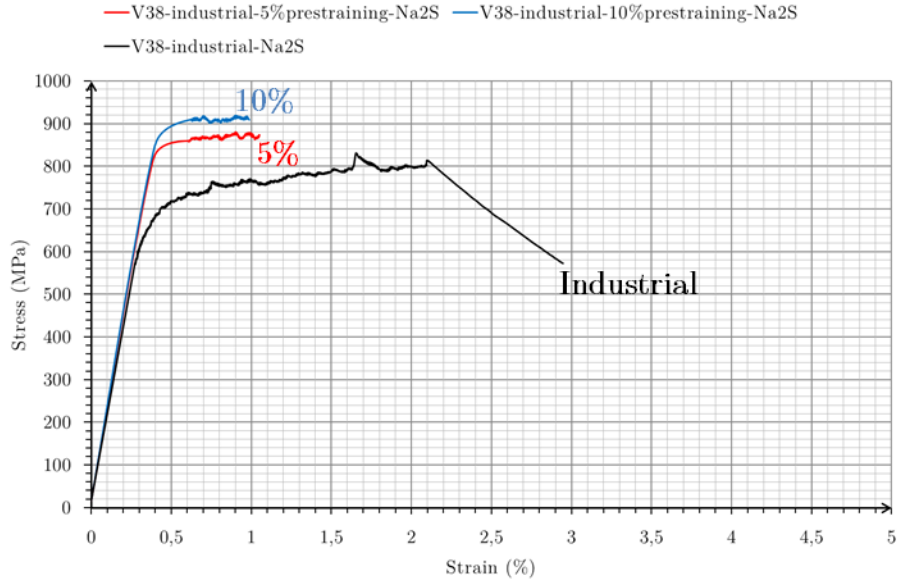


Figure 156 - Tensile curves of Virgo™38 in industrial state (black curve) and after different pre-straining ratios in air previous to the SSRT tests under cathodic charging at -1300mV/SCE in a solution containing 0.1M NaOH + 0.02M Na₂S purged with N₂ and at a strain rate of 10⁻⁷s⁻¹ (5% red curve and 10% blue curve of pre-straining in air)

One can directly see that pre-straining in air leads to a drastic decrease of the elongation to failure obtained after SSRT tests under cathodic charging in the poisoned solution (in the hydrogen embrittlement condition). The values obtained from these tests are summarized in Table 24.

Table 24 - Summary of the physical yield stresses, 0.2% proof stresses, UTS, plastic elongation at failure and RA obtained after HE tests for the different pre-straining ratios performed on Virgo™38

Pre-straining ratio applied	Expected retained austenite content (%)	0.01% yield stress (MPa)	0.2% proof stress (MPa)	Plastic elongation at failure E _p (%)	UTS (MPa)	RA (%)
Industrial (reference)	≈25%	570	730	1.7	800	1.4
5% pre-straining	≈16%	580	860	0.6	880	0.5
10% pre-straining	≈14.5%	585	905	0.5	910	2.6

We notice that the reduction in area is more important after a pre-straining of 10%. This is due to the pre-deformation performed in air where necking begins to occur (UTS at 9.5% in air see Table 10).

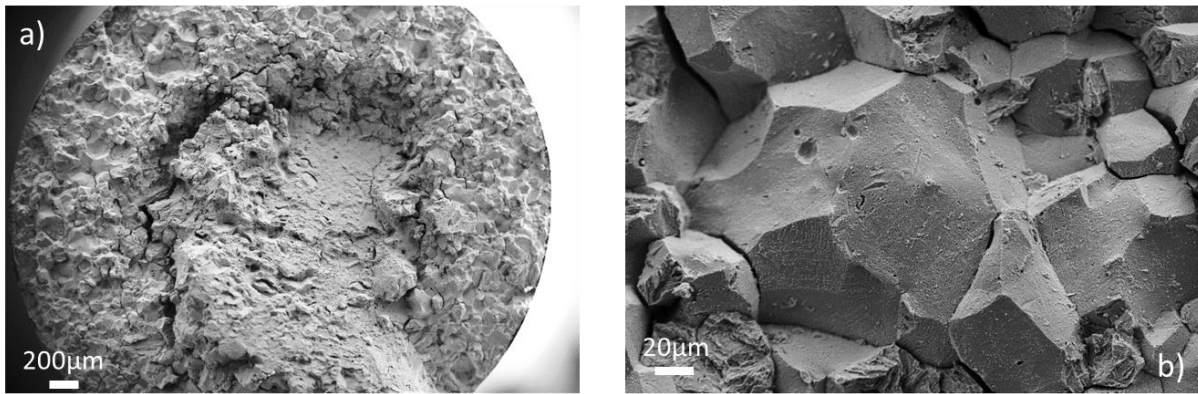


Figure 157 - Fracture surface of Virgo™38 after 5% pre-straining before SSRT test at a strain rate of 10^{-7} s^{-1} and under cathodic charging at -1300 mV/SCE in a solution containing $0.1 \text{ M NaOH} + 0.02 \text{ M Na}_2\text{S}$ purged with N_2

- a) Overview of the fracture surface
b) Detailed image showing mainly intergranular mode of cracking

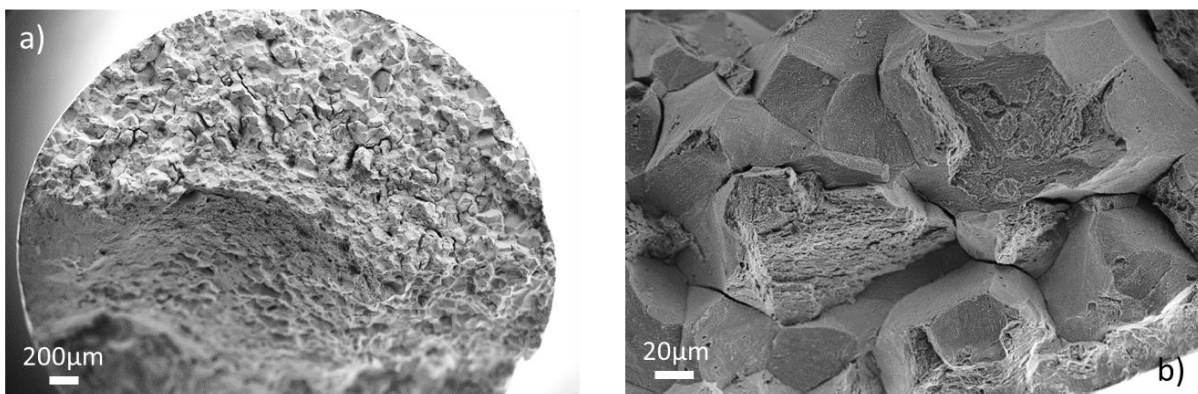


Figure 158 - Fracture surface of Virgo™38 after 10% pre-straining before SSRT test at a strain rate of 10^{-7} s^{-1} and under cathodic charging at -1300 mV/SCE in a solution containing $0.1 \text{ M NaOH} + 0.02 \text{ M Na}_2\text{S}$ purged with N_2

- a) Overview of the fracture surface
b) Detailed image showing mixed intergranular/transgranular mode of cracking

One can see in Figure 157 and Figure 158 that the mode of cracking is mixed intergranular and transgranular, compared to Figure 139 where we obtained purely intergranular failure on the industrial alloy after the HE test. Furthermore, the transgranular areas are more present after pre-straining at a higher level, as seen in Table 25, some of them presenting a ductile fracture with dimples. They are probably due to the beginning of the mechanical damage during pre-straining up to necking where micro-cavities start their growth. The fine observation of grain boundaries facets show that their surface is particularly rough, and does not present clear emergence of plasticity as previously observed.

Table 25 - Proportion of transgranular areas measured on the fracture surface as a function of the pre-straining ratio

Pre-straining ratio applied	Expected retained austenite content (%)	Proportion of transgranular areas measured on the fracture surface (%)
Industrial (reference)	≈25%	5.5±1.4%
5% pre-straining	≈16%	20.5±2.6%
10% pre-straining	≈14.5%	32.3±2.2%

During pre-straining, a part of retained austenite is transformed into martensite through SIMT as presented in Chapter II. Martensite transformation generates internal stresses distributed in the α' -matrix in the pre-strained samples which contributes to increase the transgranular mode of cracking. It is thus not surprising to observe more transgranular areas when the amount of pre-straining increases. Moreover, the level of stress reached with the hardening allows crack initiation by decohesion on the grain boundaries in the presence of hydrogen.

We have seen in this section that transgranular mode of cracking is favored under at least four circumstances: when the material is in the quenched state, or after very low temperature tempering, or after high temperature tempering or after high pre-straining. Intergranular mode of cracking is favored while the material is either properly tempered at 620°C or at lower temperatures (down to 500°C). The transgranular mode of cracking seems to be dependent on the internal stresses that are present in all the previously mentioned states, either due to raw quench, weak tempering or SIMT, while the intergranular mode of cracking seems to be dependent on the ability of the material to deform and on the localization of plastic deformation at grain boundaries. However, the appearance of very smooth grain boundaries facets let us think about the effect of the chemical composition close to the former austenitic grain boundaries, together with the hydrogen effects.

2.3. An industrial case study: the Cover

2.3.1. Description of the material: composition, metallurgy and industrial failure

This sub-section is devoted to an industrial component made of Virgo™38 that failed in service. This static component (as opposed to the rotating impeller) was a part of a cover of the compressor (Figure 1, Introduction) which is supposed to be exposed to a relatively low level of stresses. However, in contact with the environment containing H₂S, this component failed in less than one year. Different assessments that were performed at GE have led to the conclusion of an inappropriate heat treatment of this component due to its large dimensions [161].

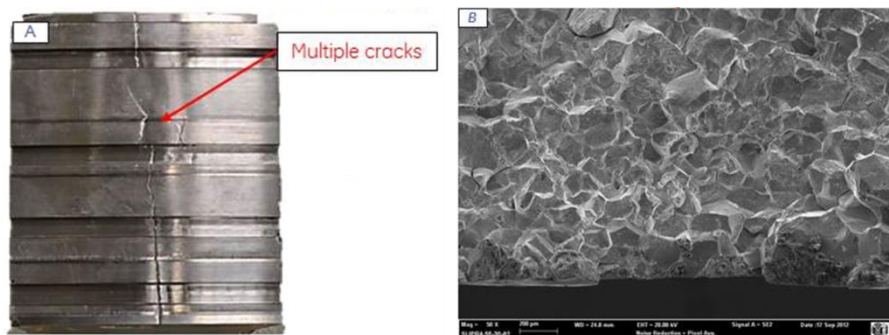


Figure 159 - Assessments performed on the Cover showing multiple cracks and intergranular failure on Virgo™38 [161]

This report concludes on a brittle failure due to hydrogen embrittlement in presence of H₂S and associated with a microstructure out of specifications. In the following, we will thus study this component under cathodic charging in our most severe environment presented at the beginning of this Chapter.

The composition of this component corresponds to Virgo™38 as indicated in Table 26. One can note that the phosphorous content in this component is however very high (250 wt. ppm) compared to the impeller. We also know that the hardness measured on this component was between 37 and

Chapter IV: Hydrogen embrittlement of Virgo™38 in different metallurgical states under cathodic charging in an environment containing Na₂S

39 HRC, which is close to the hardness of a quenched or only low temperature tempered material [161]. Surprisingly, its impact toughness is of only 10.5J/cm², which is far below that of the quenched alloy (110J/cm², such a high value being possibly due to the very low carbon content). Note that industrially treated Virgo™38 is characterized by the impact toughness of 150J/cm². Providing there is no doubt about chemical composition, the very low value measured on this component is extremely surprising and indicate potentially complex phenomena during the heat treatment.

Table 26 - Chemical composition (wt %) of the Cover

%C	%Cr	%Ni	%Mn	%Si	%Cu	%Mo	%P
0.05	15.32	4.64	0.7	0.39	0.06	0.11	0.025

Instructions that were given for the heat treatment of this component are presented in Figure 160. The tempering times were established with respect to the very large and unusual dimensions of this component (ϕ2m). In addition to the usual austenitization quenching and double tempering, a stress relief treatment was added in this component.

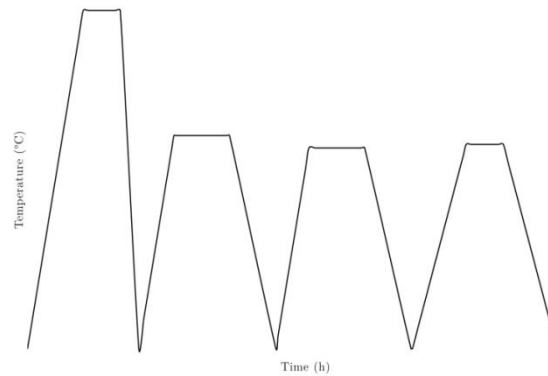


Figure 160 - Schematic representation of instructions given for the heat treatment of the Cover (the third “tempering” corresponds to the stress relief treatment after welding): temperatures at around 1000°C for austenitization, 620°C and 600°C for double heat treatment and 600°C again for stress relief HT with durations adapted to the size (internal GE rules)

2.3.2. Behavior of the Cover during SSRT test under cathodic charging

Stress-strain curves of the Cover after SSRT tests in air at 10⁻⁵s⁻¹ and in the poisoned solution under cathodic potential of -1300mV/SCE at 10⁻⁷s⁻¹, both at 20°C, are presented in Figure 161.

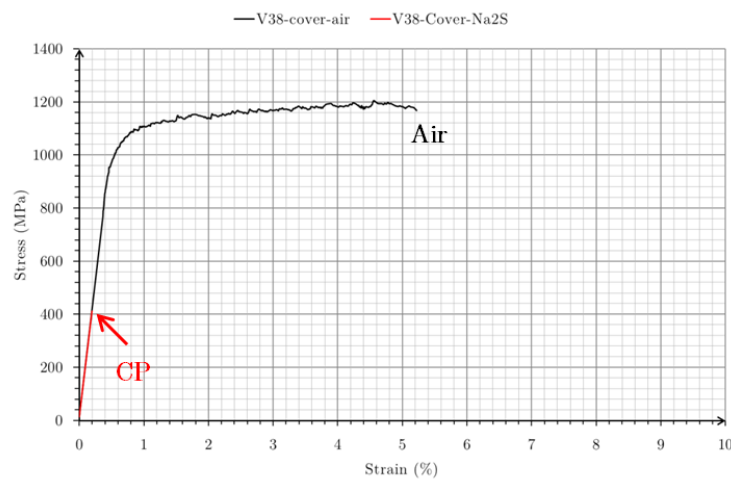


Figure 161 - Tensile curves of the Cover under cathodic charging at -1300mV/SCE in a solution containing 0.1M NaOH + 0.02M Na₂S purged with N₂ and at a strain rate of 10⁻⁷s⁻¹ (CP, red curve) and in air at a strain rate of 10⁻⁵s⁻¹ (black curve)

While the reference stress-strain curve obtained in air presents 5% elongation, the results obtained under hydrogen charging shows a completely brittle behavior with a fracture stress below half of the 0.2% proof stress. Tensile properties of the Cover are compared to those of industrial Virgo™38 with optimized microstructure in Table 27.

Table 27 - Comparison of the physical yield stresses, 0.2% proof stresses, UTS, plastic elongations at UTS and failure and reduction in area between industrial Virgo™38 and the Cover (see also Table 10 in Chapter II for other heat treatments)

	0.01% yield stress $\sigma_{0.01}$ (MPa)	0.2% proof stress (MPa)	Plastic elongation at failure E_p (%)	UTS (MPa)	Plastic elongation at UTS (%)	RA (%)
Industrial in air	570	735	25	920	9.5	75
Industrial HE	570	735	1.8	820	1.8	1
Cover in air	790	1060	4.7	1200	4	0.5
Cover HE	Failure at 430	x	0	x	x	0

The high values of 0.01% yield stress and 0.2% proof stress of the Cover coupled with the small elongation indicate a problem with the actual microstructure of the alloy. The high yield stress could be explained by precipitation and is discussed later by analogy with what was demonstrated in Chapter II.

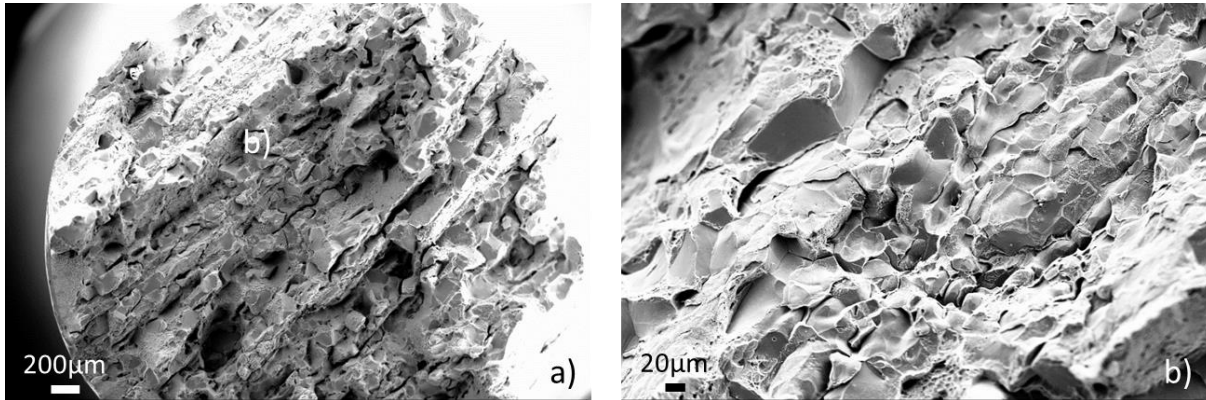


Figure 162 - Fracture surface of the Cover after tensile test in air at $10^{-5}s^{-1}$ showing brittle intergranular behavior with some ductile areas

It was unexpected to observe the intergranular behavior in air (Figure 162) taking into account that all heat treatments performed in Chapter II have resulted in ductile failures. Secondary cracks are also visible on the barrel surface of the sample after tensile test in air (Figure 163). One can also note that grain boundaries facets are completely smooth at high magnification.

This behavior could be due to a modification of composition in the vicinity of grain boundaries, such as precipitation or segregation. These possibilities will be discussed later and we can keep in mind that they can also influence crack propagation in hydrogen embrittlement tests.

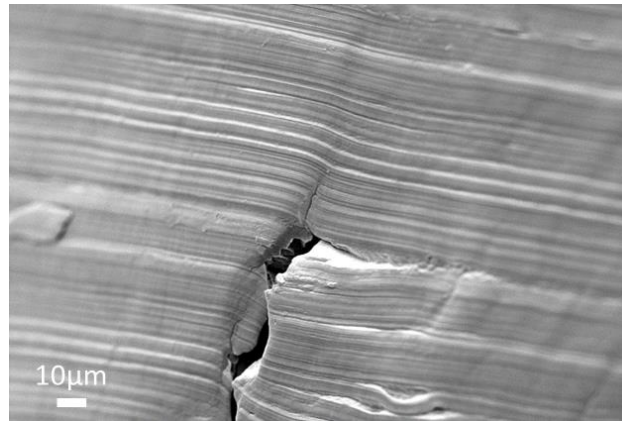


Figure 163 - Barrel surface of the Cover specimen after SSRT test at a strain rate of 10^{-5} s^{-1} in air showing secondary cracks

The failure observed after the SSRT test in hydrogen embrittlement conditions performed under cathodic charging in our poisoned solution is mixed intergranular with some transgranular areas of quasi-cleavage type (Figure 164). The majority of these facets appear smooth with few marks of plasticity. Furthermore, intergranular secondary cracks show a very thin opening without any roughness. The local directions of propagation in the quasi-cleavage mode of fracture seem to be independent on the radius direction of propagation.

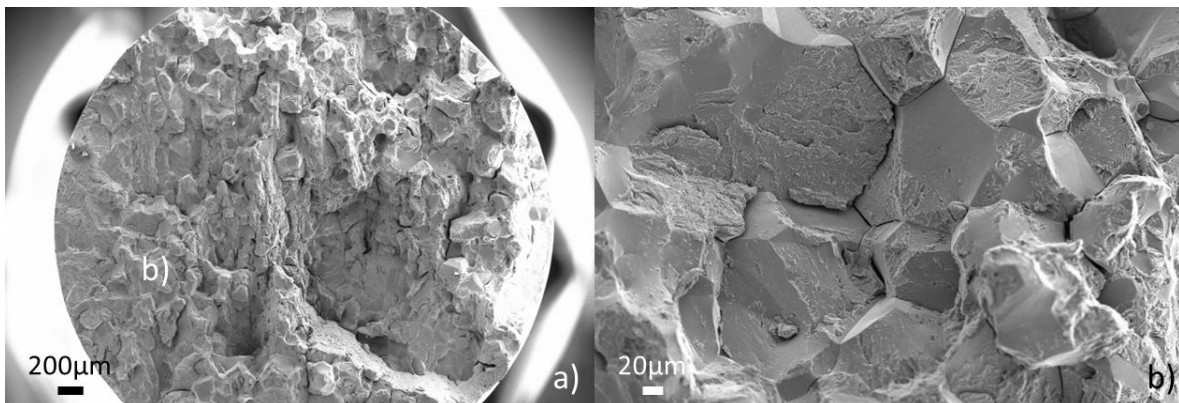


Figure 164 - Fracture surface of the Cover specimen after SSRT test at a strain rate of 10^{-7} s^{-1} and under cathodic charging at -1300 mV/SCE in a solution containing $0.1 \text{ M NaOH} + 0.02 \text{ M Na}_2\text{S}$ purged with N_2
a) Overview of the fracture surface
b) Detailed image showing mixed intergranular and transgranular modes of cracking

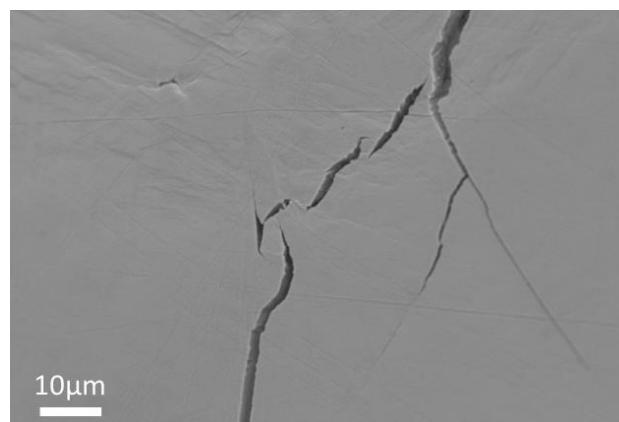


Figure 165 - Barrel surface of the Cover specimen after SSRT test at a strain rate of 10^{-7} s^{-1} and under cathodic charging at -1300 mV/SCE in a solution containing $0.1 \text{ M NaOH} + 0.02 \text{ M Na}_2\text{S}$ purged with N_2 showing a longitudinal secondary crack coming from the fracture surface

3. Discussion

During all the discussion and to simplify, SSRT tests under strong cathodic charging in the poisoned solution will be called "HE tests".

3.1. Summary of the results

Figure 166 summarizes the influence of the heat treatment on the resistance to HE of Virgo™38. It presents the evolution of the plastic elongation at failure (E_p) obtained after the HE tests as a function of the retained austenite content.

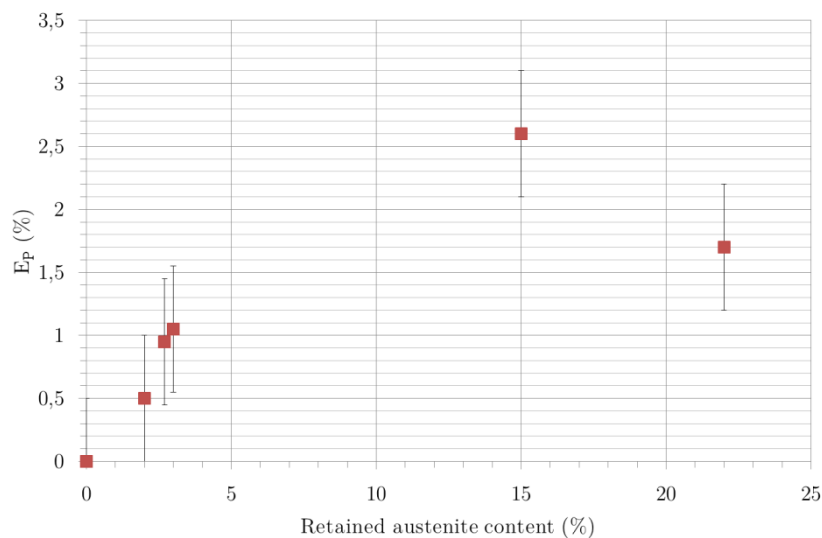


Figure 166 - Influence of the retained austenite content on the plastic elongation at failure E_p measured after SSRT tests under strong hydrogen charging conditions. From lower to higher retained austenite contents, treatments correspond to: quenched, QT500°C-24h, QT580°C-2h, QT660°C-2h, QT620°C-2h and industrial heat treatment

The curve goes through a maximum at 15% of retained austenite which corresponds to the single tempering treatment at 620°C during 2 hours after re-austenitization. The industrial heat treatment (double tempering) leads to a higher retained austenite fraction (22%) but a lower elongation after HE test. Furthermore, this representation does not directly indicate the evolution of the fracture mode from transgranular to intergranular observed in the previous section. Indeed, with increasing tempering temperature the amount of retained austenite increases till 620°C. The tempering treatment at 660°C leads however to a low amount of retained austenite but to a mainly transgranular fracture mode. Note that tempering at 580°C leads to the same amount of retained austenite but the fracture mode is mainly intergranular. The fracture mode is not only related to the retained austenite content but also to the residual stresses of the material and its sensibility versus SIMT, it is thus dangerous to interpret the fracture mode using Figure 166.

Figure 167 represents the predominant fracture mode as a function of tempering temperature, where we can see a clear transition from transgranular to intergranular and back to transgranular mode at high tempering temperatures. The tempering temperature has the advantage to indirectly indicate both the retained austenite content and the residual stress state of the sample, as previously discussed. Note that in this figure the quenching after re-austenitization was much faster than all quenches after tempering heat treatments with the range 200°C-660°C.

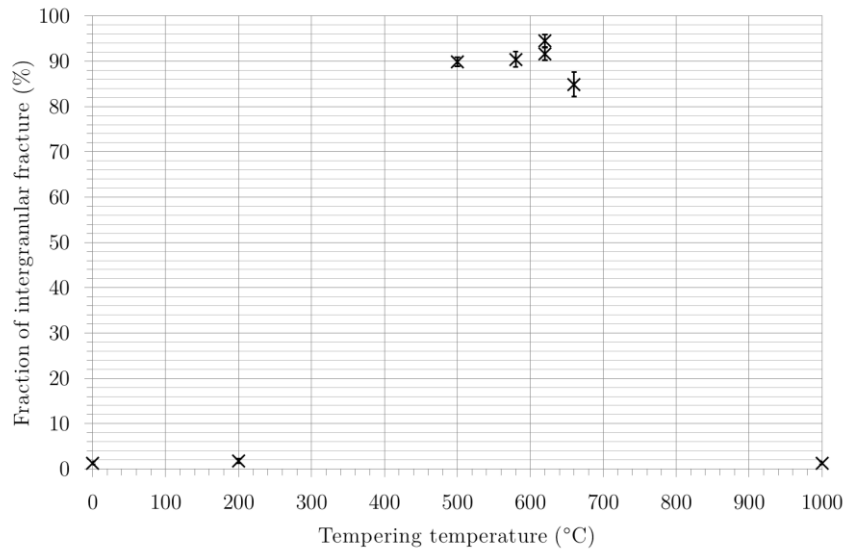


Figure 167 - Influence of the tempering temperature on the fracture mode observed after SSRT tests under strong hydrogen charging conditions

3.2. Interpretation on the optimal amount of retained austenite in terms of its quantity and stability

As visible in Figure 166, retained austenite is beneficial for elongation but this beneficial effect is limited to a certain amount of retained austenite. Beyond this critical amount, retained austenite is detrimental for elongation in SSRT tests under strong cathodic charging. Indeed, as seen in Chapter II, when the amount of retained austenite increases, it becomes more unstable due to the limited amount of γ forming elements. This instability can lead to an early transformation during the tensile test which has been identified as detrimental for HE resistance within the literature [100].

Below the critical amount of retained austenite, the elongation to fracture increases with its content. This effect is correlated with the decrease of the apparent hydrogen diffusion coefficient with the increasing retained austenite content as visible in Figure 168 and as identified within the literature on the same type of alloy [148]. As proposed by Oriani [162] local equilibrium exists between the diffusible interstitial hydrogen and that occupying reversible traps in the material. Assuming that both lattice and trap sites are finite population and no interactions occur between occupied sites, the equilibrium is written as:

$$K_{\theta} = \frac{1 - \theta_L}{\theta_L} \frac{\theta_T}{1 - \theta_T}$$

with θ_L and θ_T the fractional occupancy of lattice sites and trap sites. K_{θ} the constant of equilibrium only dependent on the temperature.

By increasing the amount retained austenite, the available total hydrogen content imposed by charging conditions is distributed between these sites according to the equilibrium. For a given global amount of hydrogen, its content in the lattice is thus decreased. There are two possible consequences: first, the decrease of the H-deformation interactions that results in decreasing the localization of plasticity and stress concentration on obstacle, and second, on the weakening of interface cohesion.

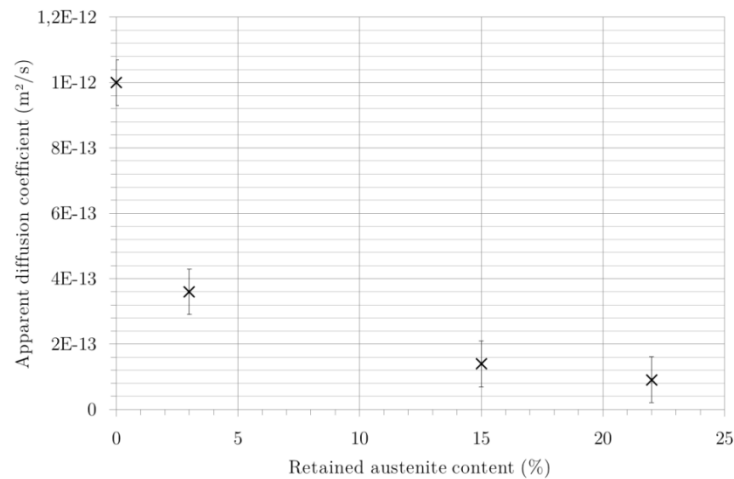


Figure 168 - Influence of the retained austenite content on the apparent hydrogen diffusion coefficient measured by electrochemical permeation

Literature data indicate [100] that retained austenite acts as a hydrogen trap. Indeed, as seen in Figure 169, hydrogen trapping increases with increasing the amount of retained austenite. This trapped hydrogen is not detrimental as long as the retained austenite is stable. However, when retained austenite becomes unstable (SIMT), trapped hydrogen is released within the newly formed martensite and leads to a drastic decrease of mechanical properties. This effect accounts for the decrease of the elongation at failure with an increasing fraction of (more and more unstable) retained austenite.

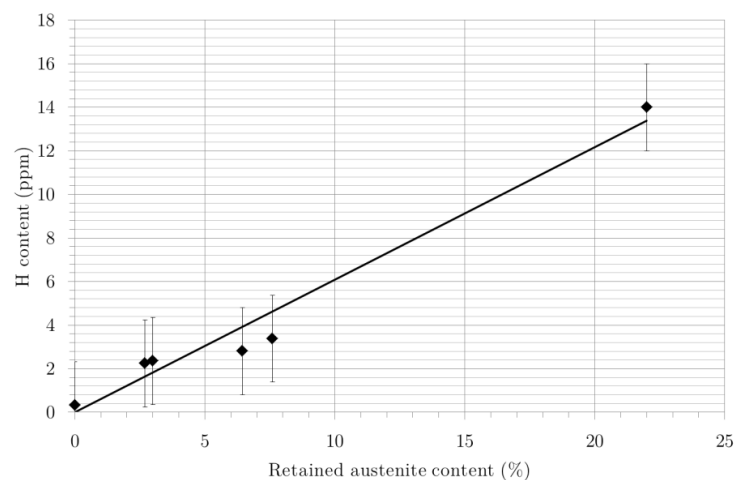


Figure 169 - Influence of the retained austenite content on the trapped hydrogen content measured after 72h cathodic charging at -1300mV/SCE in the poisoned solution. H contents were measured by fusion and thermal conductivity.

One can notice that the total hydrogen contents determined by melting and subsequent measurements (Figure 169) are far from those determined by permeation experiment in the same environment (around 10 times lower, as compared to 110ppm determined by permeation for the industrial sample containing 22% of retained austenite). Indeed, the solubility determined during permeation tests corresponds to the sub surface solubility which is higher than the bulk one due to the high hydrogen activity at the sample surface (oversaturation in the sub surface). Hydrogen in oversaturation at the subsurface diffuses quickly out of the sample at the end of charging and cannot be measured by melting. However, the values determined by melting are in agreement with the ones observed in the literature [100].

In summary, we can say that retained austenite is beneficial with respect to hydrogen embrittlement resistance as long as it does not transform into martensite. In addition to experiments discussed in this section, it would be useful to study the influence of the trapped hydrogen inside retained austenite on its resistance to SIMT. However, for industrial applications, SIMT is not supposed to occur as the machines are designed to work within elastic domain or at least with limited and controlled amount of plasticity in small areas. We can thus say that, from the industrial point of view, retained austenite is beneficial to the HE resistance of SMSS. However, if cracks are initiated, SIMT is certain to happen in the vicinity of cracks and local behavior of the material with respect to hydrogen embrittlement may be drastically modified.

3.3. Interpretation of the fracture mode

We have seen in the previous parts that, for industrially relevant microstructure, most of the failures due to hydrogen embrittlement are (at least partly) intergranular (Figure 167). In the same case, mainly with significant amounts of fresh martensite (quenched or overtempered states), the fracture surfaces were transgranular. In this section, we will discuss the influence of both residual stresses and grain boundary composition on the predominant fracture mode observed in the Na₂S containing environment.

As previously mentioned, transgranular fractures could be due to the concentration of residual stresses in some metallurgical states, especially in lathes after quenching or SIMT. The analysis of the residual stresses in individual grains can be theoretically done by high angular resolution EBSD, however these analysis were not performed in the frame of the present study.

The preferential intergranular crack path could be due not only to preferential hydrogen diffusion path in grain boundaries but also to the modified chemical composition near former austenitic grain boundaries that might enable, in relation with hydrogen, to facilitate grain boundary opening. Another element, which might provide an easy segregation path was proposed in chapter II, is based on the assumption of a non-complete transformation of intergranular regions of austenite during quenching. In this case, "prior" grain boundaries would remain "real" ones and the procedures applied to analyze intergranular segregation could be applied without restrictions.

To explain the intergranular fracture, we will focus on the grain boundary composition and especially the influence of the tempering treatment on Phosphorous Grain Boundary Segregation (PGBS). Indeed, phosphorous is known to segregate to grain boundaries at temperatures between 400°C and 600°C leading to intergranular failures, even in absence of hydrogen [163] [164]. However, this phenomenon of the reduction of grain boundary cohesion due to phosphorous is well known in ferritic steels but few data related to low carbon martensitic steels are available in the literature [165].

Quantitative analysis of grain boundary phosphorous segregation can be realized by Auger Electron Spectroscopy (AES) providing that grain boundary fracture can be achieved within the instrument i.e. either at room temperature or on cooling down to approximately -100°C and that the appropriate quantification model is used [166]. Clearly, it is mandatory to perform in situ intergranular fractures under ultra-high vacuum to prevent the areas of analysis from contamination.

Notched specimens ($1 \times 1 \times 20 \text{ mm}^3$) were carefully prepared, then fractured at -100°C in a vacuum of about 10^{-8} Pa and analyzed at 10kV. Around 10 intergranular facets were analyzed on each specimen. Figure 170 represents a typical Auger spectrum in derivative mode, where peak-to-peak intensities of Fe, Cr and P can be measured and used for quantitative analysis.

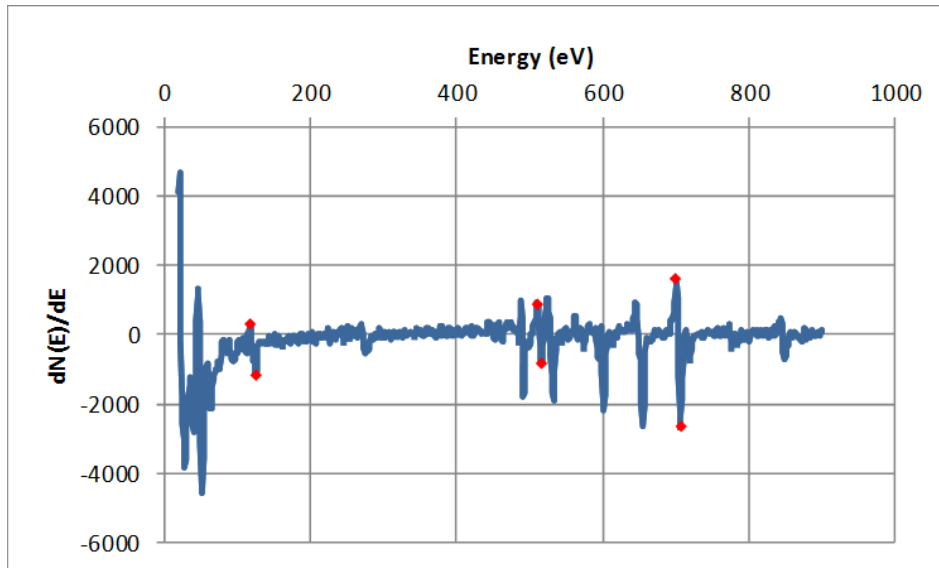


Figure 170 - Example of an Auger spectrum recorded from one intergranular facet after in situ failure under UHV showing P120, Cr529 and Fe703 peaks

As quantification procedures are more precise using X-rays Photoelectron Spectroscopy (XPS), a specific methodology was developed at École des Mines de Saint-Étienne to calibrate Auger measurements by performing both XPS and Auger analysis on the same area after in situ surface segregation by heating pure iron with known phosphorus concentration [internal non-published study]. This methodology enables to determine constants A and B that in turn enable to calculate the phosphorus fractional monolayer content in the grain boundary X_p as a function of the Fe703 and P120 peak intensities:

$$X_p = \frac{2 * \frac{I_{P,120}}{I_{Fe,703}}}{A * \frac{I_{P,120}}{I_{Fe,703}} + B} \quad (\text{i})$$

However, Virgo™38 is not a simple Fe-P alloy, it also contains a non-negligible amount of Cr (around 15 wt. %). The two main matrix elements (Fe and Cr) must thus be considered, the phosphorus grain boundary fractional monolayer content thus become calculated by (ii):

$$X_p = \frac{2 * \frac{I_{P,120}}{I_{Fe,703} + kI_{Cr,529}}}{A * \frac{I_{P,120}}{I_{Fe,703} + kI_{Cr,529}} + B} \quad (\text{ii})$$

where $k = \frac{I_{Fe}^0}{I_{Cr}^0} = 0.748$, $A = 0.5809$ and $B = 2.4117$.

After industrial heat treatment, Virgo™38 impeller shows the average phosphorous grain boundary fractional monolayer content of $9.3 \pm 3.9\%$ while the Cover shows a content of $11 \pm 3.2\%$ according to equation (ii). Extreme values, from different facets are 3.7% - 15.9% and 7.7% - 18% for

the impeller and the Cover respectively. The phosphorous fractional monolayer content usually admitted to induce sufficient embrittlement to obtain brittle intergranular fracture is 10% [167], which can certainly contribute to the explanation of brittle intergranular failure in air for the Cover and ductile failure for the impeller. However, the very low absolute difference in segregation level between these two components suggests some additional contribution either in terms of microstructure or in terms of mechanical properties.

In summary, we can say that tempering treatment enables reducing the amount of transgranular fracture by decreasing the residual stresses but, in the same time, it promotes PGBS that favors intergranular fracture. That is why, tempering treatment should be realized, with respect to PGBS, at a sufficiently high temperature in order to both sufficiently decrease the residual stresses and limit the thermodynamic equilibrium segregation level of PGBS. However, this tempering temperature is clearly driven by the optimization of the amount of stable reverted austenite, as currently done in the industrial process with a two-step heat treatment, both followed by air cooling, which by the way can only enhance P segregation, especially in slowly cooled thick components.

3.4. Proposed mechanisms of Hydrogen Embrittlement

In this part, we will mainly focus on intergranular fractures, which are the ones observed in service conditions, but we will also quickly discuss the possible causes of transgranular fracture.

3.4.1. Intergranular fractures

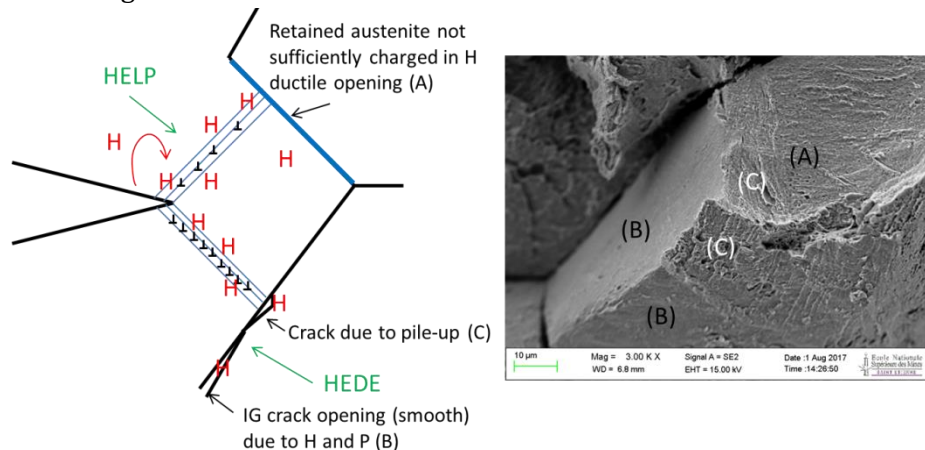


Figure 171 - Schematic representation of the proposed mechanism: overview

If one considers that intergranular fractures are due to a decrease of the cohesive energy of grain boundaries, the HEDE mechanism can apply. The grain boundaries are strong enough during tensile tests in air, which explains that failures are ductile in air if the proper heat treatment is applied. However, their cohesive energy can be decreased by the PGBS as it has been presented in this Chapter. In a few cases (the Cover) this segregation (coupled with some other microstructural elements) can be sufficient to obtain brittle intergranular fractures in air. However, in most cases (impeller treated in all the conditions presented in Chapter II) this segregation is not sufficient to obtain intergranular failure in air. Another element must thus be added in order to decrease the cohesive energy in order to obtain an intergranular fracture: hydrogen at a sufficiently high activity. Indeed, adding hydrogen is still not always sufficient to achieve intergranular failures during HE tests (Chapter III). Very high hydrogen activities such as the ones presented in this Chapter are needed to sufficiently decrease the cohesive energy.

We can propose the following mechanism of hydrogen embrittlement based on HEDE mechanism and on the previous observations:

1. We consider a SMSS composed of tempered martensite, retained austenite located between martensitic laths and at former austenitic grain boundaries and phosphorous segregated at former austenitic grain boundaries
2. Hydrogen is trapped in retained austenite due to the high hydrogen solubility in this phase (around 10ppm) while tempered martensite is almost hydrogen free (typically 2ppm) [100]. By applying Olden's model, one finds that martensite with 2ppm of hydrogen has a critical cohesive stress of approximately 1500MPa [100].
3. When a crack is initiated (by pitting corrosion for example), local deformations are very important ahead of the crack tip, which leads to the transformation of the retained austenite into fresh martensite (SIMT, see Chapter II)
4. The hydrogen trapped inside retained austenite is released inside the newly formed martensite where it is in oversaturation. By applying Olden's model on a martensitic matrix containing 10ppm of hydrogen, one finds that the critical cohesive stress is of the order of only 800MPa [100].
5. At the former austenitic grain boundaries, if one includes the PGBS, the critical cohesive stress will be much lower, leading to intergranular opening.

This mechanism can be represented as follow:

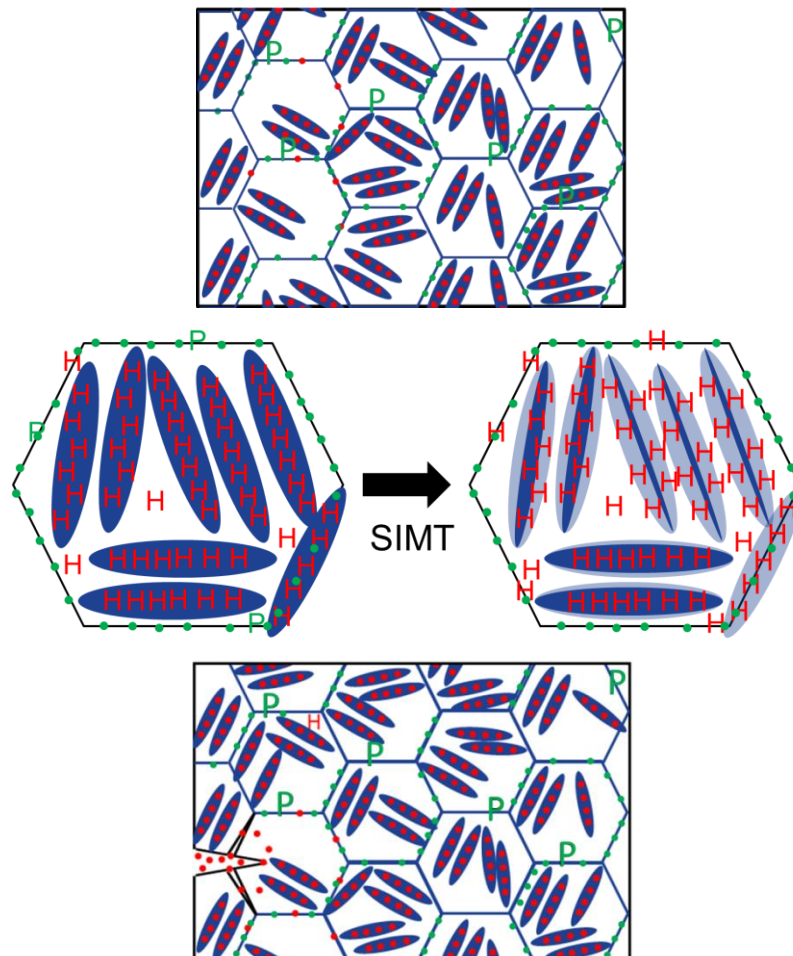


Figure 172 - Schematic representation of the Hydrogen Embrittlement mechanism based on HEDE proposed

3.4.2. Transgranular fractures

As the transgranular mode of cracking was related to the residual stresses in our experimental analysis, the HELP mechanisms can apply in these cases, hydrogen being ‘trapped’ by the high local dislocation density in laths. In the HELP mechanism, failure is obtained by a localized shear process occurring along slip planes. As retained austenite content is lower for all cases of transgranular fracture (due to tempering at very low or too high temperature or SIMT) and as PGBS can be neglected (either because no tempering is effectively applied due to too low temperature or because tempering temperature is too high leading to a low thermodynamical equilibrium) resulting in a better resistance of the grain boundaries, the weak point in the microstructure is thus located in laths where the interactions between dislocations are reduced by the ‘trapped’ hydrogen, the shear stress being more important. Likewise, in the case of low hydrogen content (low hydrogen activity), retained austenite will not be filled with hydrogen and hydrogen will be mostly associated to dislocations formed during tensile test. In this case, failures would be transgranular too.

3.5. Interpretation of the cracking of the Cover

3.5.1. Interpretation based on the retained austenite content and the fracture mode

The austenite content determined by X-ray diffraction on the Cover and calculated using the Rietveld method as indicated in Chapter II is of only $3.9\pm 2.0\%$, which is far below the targeted range of at least 20%. This seems to confirm an inadequate heat treatment. However, for the moment, we do not know if this austenite corresponds to residual or retained austenite. Indeed, the presence of residual austenite is possible in the case of improper quenching after austenitization and assuming that tempering was not applied. The other possibility is that quenching was performed properly but tempering treatment was performed either at too low or at too high temperature (see Chapter II).

In order to verify if austenite measured by XRD on the Cover corresponds to residual or retained austenite, it is possible to analyze its location. Indeed, retained austenite has the particularity to be present as fine grains located between martensite lathes while residual austenite is supposed to be held as big islands. EBSD mapping presented in Figure 173 shows that the austenite is located between the martensite lathes which means that it certainly corresponds to the retained austenite.

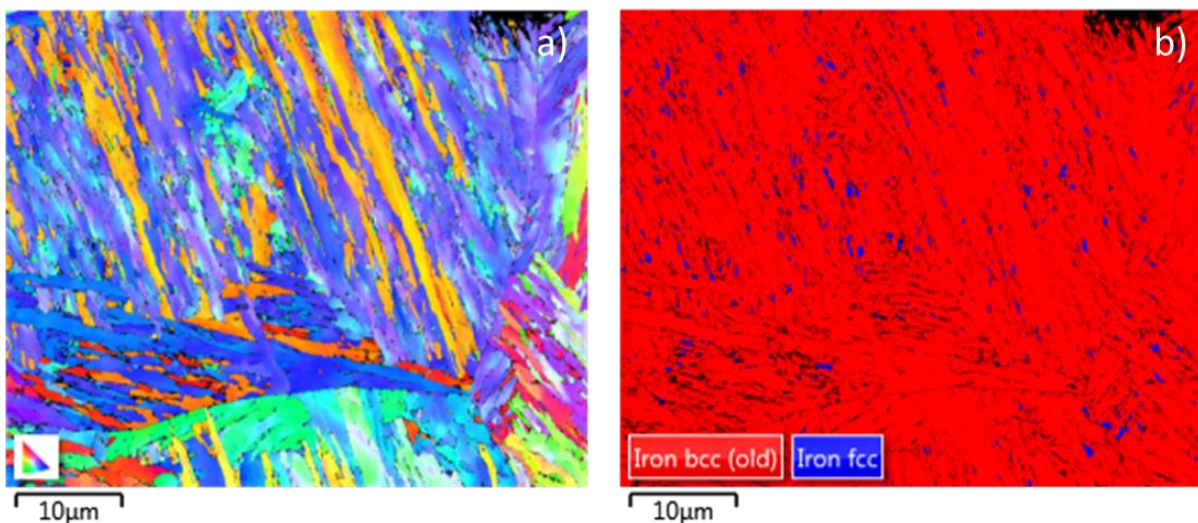


Figure 173 - EBSD maps (a) IPF and (b) phase map) of a specimen taken within the Cover

We now know that the low austenite content measured on the Cover corresponds to austenite formed during tempering treatment. In first approximation, we can thus compare the fracture mode obtained on the cover with these obtained as a function of tempering temperature in Chapter II, in order to eliminate some possible heat treatments.

As expected, the fracture mode of the Cover (purely intergranular) does not correspond to the one of the quenched state (purely transgranular) which confirms again that austenite is retained austenite and not residual austenite. High tempering temperature (660°C) provides an acceptable amount of retained austenite but does not lead to fully intergranular failure (Figure 167). The tempering treatment at the peak temperature (620°C) provides a similar fracture mode (mainly intergranular) but does not provide the proper amount of retained austenite. The two remaining treatments (500°C/24h and 580°C/2h) provide both the good amount of retained austenite (less than 5%) and a fully intergranular fracture mode (Figure 167).

Concerning the unknown heat treatment of the Cover, the most probable scenario is thus a low temperature tempering treatment after quenching. Indeed, this treatment is compatible with a low amount of retained austenite and can result in a purely intergranular failure as opposed to the high temperature tempering treatment which also provides a similar amount of retained austenite but leads to a mixed intergranular-transgranular mode of cracking.

Figure 174 presents the evolution of the reverted austenite fraction as a function of tempering temperature based on Thermocalc calculations. Considering that for temperatures below the maximum of retained austenite all reverted austenite is stable (clearly identified on experimental XRD curve, see Figure 54 in Chapter II) and that the tempering time of the Cover was long enough to achieve thermodynamic equilibrium, we can deduce, from the known amount of retained austenite of 4%, that the tempering temperature might have been between 500°C and 550°C. Note that this tempering temperature range necessarily leads to a specific stress strain behavior (Chapter II) and again comparing stress-strain curve of the Cover specimen (Figure 161) with a series of stress-strain curves on quenched and tempered specimens within the range 200°C-600°C (Figure 68 in Chapter II) suggests the actual tempering temperature for the Cover within the range 500°C-580°C. The thermodynamic approach being more precise in this analysis, we will conclude that the tempering temperature was between 500°C and 560°C.

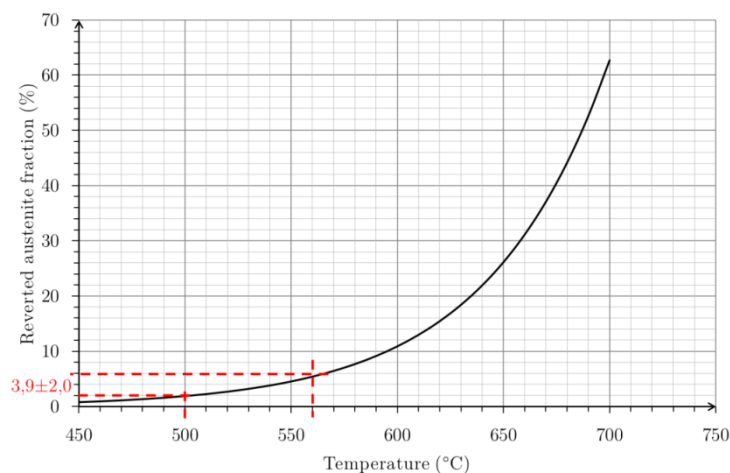


Figure 174 - Results of the Thermocalc® simulations showing the amount of reverted austenite at equilibrium as a function of the tempering temperature

3.5.2. Explanations based on the precipitation state on the Cover

While looking at the macroscopic mechanical behavior of the Cover (Table 27), the EBSD maps (Figure 173) and the brittleness in air (Figure 162), and according to the results presented previously, it is possible that the Cover was heat treated at a low temperature (500°C - 560°C) during a long time (>24h).

By analogy with the discussion concerning the microstructure given in Chapter II, we can try to identify mechanisms leading to the mechanical properties of the Cover. On the basis of Figure 175 which shows the results of the Prisma simulation for low tempering temperatures, we can reasonably assume that the very high hardness / yield stress of the Cover is due to a very fine precipitation of carbide. Indeed, as shown in chapter II, the most efficient way to harden Virgo™38 is to form fine and homogeneous population of carbides. Using the procedure proposed in Chapter II, i.e. assuming that 50% of precipitates contribute to strengthening and by applying equation (iii) in Chapter II we would find an equivalent precipitate size diameter of 3.3nm that could be obtained by tempering at around 475°C to 525°C for a long time.

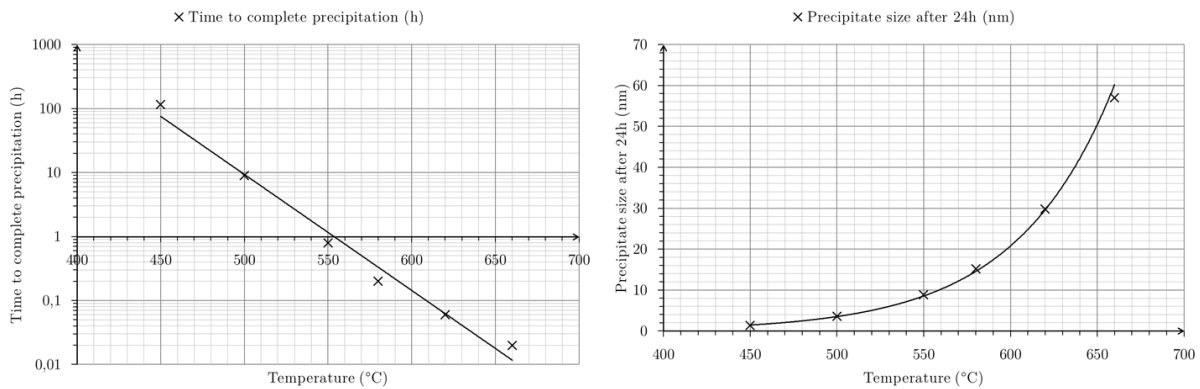


Figure 175 - Results of the Prisma simulations showing carbide precipitates size after 24h heat treatment and time to complete the precipitation as a function of the tempering temperature

This temperature range is in agreement with the retained austenite content **at equilibrium** obtained after ThermoCalc® simulations (Figure 174). With this new element, one can thus be even more precise and assume that the tempering temperature of the Cover lies in the range 500°C to 525°C.

3.5.3. Phosphorous Grain Boundary Segregation (PGBS) in the Cover

An alternative way to confirm the tempering treatment applied to the Cover can be based on the determination of the kinetics of PGBS. However, due to the difficulties to systematically obtain intergranular fractures inside the Auger analyzer, we have only a limited set of data, which will further imply a series of strong assumptions. Both impeller and Cover material were analyzed. The entire set of data available on Virgo™38 is presented in Table 28.

The impeller material was analyzed at two metallurgical conditions: first, after industrial heat treatment and second, after reaustenitization + quenching followed by heat treatment at 500°C during 24h. The Cover material is supposed being treated as follows: austenitization + quenching + heat treatment at 500-525°C during 24-90h. Note that the bulk phosphorous content is much higher in the Cover material.

Table 28 - Data relative to phosphorous grain boundary segregation available on Virgo™38

	P bulk concentration (at. ppm)	Heat treatment	X _p measured (number of facets analyzed)	Minimal X _p value obtained	Maximal X _p value obtained
Impeller	320	Industrial (estimated to be equivalent to 8h at 620°C)	9.3 ± 3.9% (15)	3.7%	15.9%
		Re-austenitized, quenched and tempered 24h at 500°C	6.8 ± 1.9% (5)	1.9%	9.4%
Cover	450	Unknown	11 ± 3.2% (10)	7.7%	18%

The following analysis will rely on the kinetics of grain boundary segregation according to McLean linear approximation [168] and on the Langmuir-McLean equilibrium segregation model [169] [170]. Figure 176 illustrates assumptions that were made [164].

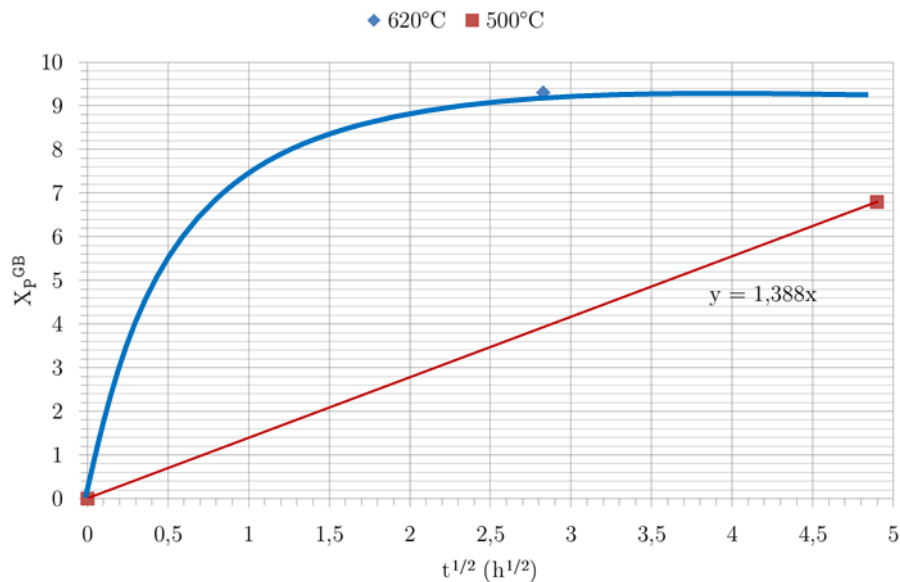


Figure 176 - Representation of the data available on Virgo™38 impeller and assumptions made: we consider that
1) 24h at 500°C is still within the application range of the McLean linear approximation
2) After the industrial heat treatment (considered equivalent to 8h at 620°C) we achieved saturation

Thermodynamically, the Gibbs free energy of phosphorous grain boundary segregation in Virgo™38 impeller ΔG_p can be estimated by using the Langmuir-McLean formalism if we consider that the maximal fractional monolayer content obtained after the industrial heat treatment corresponds to the equilibrium one (Figure 176). This is a reasonable assumption regarding the values of 10% obtained on 17-4PH after 8 hours heat treatment at 600°C [165], which are considered by the authors very close to equilibrium.

$$\Delta G_p = -RT \ln \left(\frac{X_P^{GB} / X_{P,max}^{GB}}{\left(1 - X_P^{GB} / X_{P,max}^{GB} \right) * X_P^B} \right) \quad (iii)$$

Chapter IV: Hydrogen embrittlement of Virgo™38 in different metallurgical states under cathodic charging in an environment containing Na₂S

In our case, the bulk concentration was $X_p^B = 320$ atm ppm within the Virgo™38 impeller used for this study and $X_p^{GB} = 9.3\%$, which gives $\Delta G_p = -42,1 \text{ kJ.mol}^{-1}$ considering that $X_{p,max}^{GB} = 1$ [171] and that we achieved saturation. This value, probably slightly underestimated, is still in agreement with other values found in the literature for 17-4PH [165] and for other martensitic stainless steels [172] [173]. For α iron, the Gibbs free energy of phosphorous grain boundary segregation is found in the range -30 to -50 kJ.mol^{-1} [174], which is also in agreement with our value previously determined.

The Gibbs free energy of phosphorous grain boundary segregation within the Cover cannot be calculated as we do not know with enough precision the heat treatment temperature (500°C - 525°C) and duration, moreover at such relatively low temperature conditions, thermodynamic equilibrium cannot be assumed and consequently McLean isotherm cannot be used.

The following analysis will be based on the kinetics of phosphorous grain boundary segregation which is a key point for this embrittlement mechanism. For short annealing times, the simplified McLean law can be applied and gives [175] [176]:

$$X_P^{GB} = \frac{4X_P^B\sqrt{Dt}}{d\sqrt{\pi}} \quad (\text{iv})$$

where D is the phosphorous diffusion coefficient at the considered temperature and d is the grain boundary thickness. It is commonly admitted that the grain boundary thickness is 0.5 nm [173].

Considering that phosphorous diffusivity follows an Arrhenius law with parameters close to the ones of 17-4PH given by Christien et al. [165] (Table 29), and knowing that the phosphorous bulk concentration in the Cover is 450 at. ppm (320 at. ppm in the impeller), we can deduce the approximate temperature of heat treatment of the Cover. As discussed previously and according to the hardness of the Cover, the potential tempering temperature should be within the range 450°C - 550°C .

Table 29 - Parameters of the Arrhenius law found by Christien et al. for 17-4PH alloy [165]

$D_0 = 0.183_{-0.174}^{+3.475} * 10^{-4} \text{ m}^2\text{s}^{-1}$
$Q = 229 \pm 19 \text{ kJmol}^{-1}$

In order to be more precise, we tried to determine our own parameters in order to get closer to the real tempering temperature. To do it, impeller specimens were re-austenitized, quenched and tempered at 500°C (close to the estimated tempering temperature of the Cover) during 24 hours. This tempering time has been chosen long enough to obtain sufficient grain boundary segregation to obtain intergranular failure but short enough in order to stay in the linear domain of application of the McLean formalism (equation iv) (Figure 176). These specimens were analyzed by AES as described previously and an average concentration of $6.8 \pm 1.9\%$ has been obtained.

We can assume that the McLean approximation is still valid after 24h at 500°C by comparing it to the results obtained in 17-4PH [165]. Thus, using equation (iv) with $X_p^{GB} = 6.8\%$ and $X_p^B = 320$ at. ppm provides us with an approximate diffusion coefficient of $2.57 \times 10^{-16} \text{ cm}^2/\text{s}$. If we consider that the activation energy is close to the one of Christien et al [165] in 17-4PH (229 kJ.mol^{-1}), then we obtain:

Table 30 - Parameters of the Arrhenius law found on Virgo™38 impeller by considering the McLean approximation

$D_0 = 0.766 \text{ cm}^2 \text{ s}^{-1}$
$Q = 229 \text{ kJmol}^{-1}$

However, using the McLean approximation implies a dependency of the D_0 factor to the phosphorous bulk concentration. As the bulk concentration is more important within the Cover, and if we consider that this approximation is still valid, we obtain the parameters presented in Table 31 for the Cover:

Table 31 - Parameters of the Arrhenius law found on Virgo™38 Cover by considering the McLean approximation

$D_0 = 0.54 \text{ cm}^2 \text{ s}^{-1}$
$Q = 229 \text{ kJmol}^{-1}$

One can notice that these parameters are in agreement with those found in 17-4PH. Using these parameters, it is then possible to determine the evolution of the phosphorous grain boundary content as a function of the tempering time for different temperatures (Figure 177).

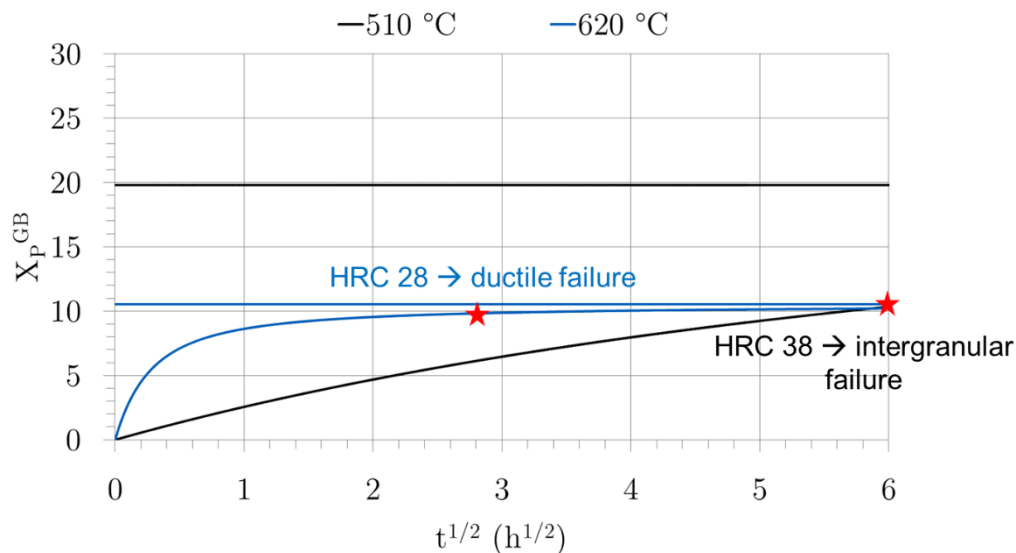


Figure 177 - Kinetics of phosphorous grain boundary segregation in Virgo™38 at different temperatures (impeller treated at around 620°C and Cover treated at 510°C) showing almost the same Phosphorous grain boundary content after two different heat treatment

All elements mentioned previously seem to indicate that the Cover was heat treated during around 40 hours at a temperature of 510°C (low temperature tempering, also in agreement with what was presented previously).

Even if our approach is based on some strong assumptions as stated before, including an isothermal heat treatment (as compared to probably a double tempering heat treatment of the Cover, according to NACE standards [3] for martensitic stainless steels and followed by a stress relief HT), we can be confident about this result as it enters into the previously estimated range between 500°C and 525°C.

The retained interpretation for cover embrittlement is as follows:

- The Cover presented a very high hardness (37-39 HRC) and 0.2% proof stress (1060 MPa): these very high mechanical properties have been identified to be due to fine carbide precipitation with the average diameter of around 3nm. Such mechanical properties are compatible with a low temperature tempering within the range 475°C-525°C during at least 24h hours (Figure 175)
- The Cover contains a limited amount of austenite (<4%): this austenite has been identified as retained austenite formed during a low temperature tempering (500°C-560°C) during a long time (to obtain saturation of the reverted austenite content) (Figure 174).
- The Cover contains a high P content (450 at. ppm): as quantified from Auger measurements, this element segregates to grain boundaries at temperatures close to 510°C (Figure 177) and induces grain boundary embrittlement.

All the previously presented elements converge to the explanation of the extreme brittleness of the Cover based on inappropriate heat treatment. Indeed, this component, due to its large dimensions, had been heat treated during a long time (around 40 hours) and the temperature was certainly close to 510°C as opposed to the requested double tempering close to Ac₁ temperature, namely close to 620°C followed by close to 600°C.

4. Conclusions

In the previous Chapter, it was shown that composition heterogeneities between both constitutive phases were at the origin of the Anodic Stress Corrosion Cracking mechanism. However, the mechanism of Hydrogen Embrittlement was not identified. In this Chapter, we have showed the synergy between Phosphorous Grain Boundary Segregation (PGBS) and hydrogen effect can be at the origin of intergranular failures of Virgo™38 in industrial conditions.

This study underlines that the microstructure has a significant impact on the cracking mechanisms of Virgo™38 super-martensitic stainless steel. Especially, the heat treatment conditions must be chosen very carefully and with the knowledge of all the microstructural changes that are implied. All these elements explain that Virgo™38 should be used in its “over-tempered” state regarding precipitation behavior as evocated within the conclusions of Chapter II. Indeed, small precipitates drastically increase the yield stress and can lead to brittle failures (even in air). It was also showed that a significant embrittlement of Virgo™38 due to Hydrogen Embrittlement is promoted by high hydrogen activity. Moreover, while phosphorous grain boundary content is not detrimental for the mechanical behavior of Virgo™38 in optimized heat treatment conditions (because its yield stress is limited) it becomes dangerous while coupled with hydrogen. It is thus now easier to understand some of the limitations imposed by the NACE standards, in particular the hardness limitation on SMSS which comes together with the limitation of the maximum yield stress.

The analysis of the intergranular fracture of this industrial component enabled us to highlight the synergy between Hydrogen Embrittlement and Phosphorous Grain Boundary Segregation. In order to quantify these interactions between hydrogen and PGBS it appears necessary to perform numerical simulations based on: first, Krom’s model and second, atomistic simulations. Taking into account hydrogen trapping in retained austenite as it has been done in very recent works on SMSS [148] and considering the decrease of grain boundary cohesion induced by the P segregation is mandatory. To our knowledge, such simulation work taking into account the synergy between trapped hydrogen and PGBS has never been performed. This constitutes a challenging prospect of the present work.

However, in this basic-poisoned environment presented in the Chapter, it is not possible to study the combined effect of Hydrogen Embrittlement and Stress Corrosion Cracking that can occur at the Open Circuit Potential in H₂S containing environments, that is why, Chapter V will be dedicated to the study of Sulfide Stress Cracking and Stress Corrosion Cracking of Virgo™38 in presence of H₂S.

**Chapter V:
Sulfide Stress Cracking and Stress Corrosion Cracking
assisted by H₂S of Virgo™38**

Chapter V: Sulfide Stress Cracking and Stress Corrosion Cracking assisted by H₂S of Virgo™38..... 189

1. Compositions of environments used and test conditions.....	193
2. Influence of the pH on the cracking resistance: a synthetic view.....	195
3. Detailed analysis of crack initiation and propagation in presence of H ₂ S and proposed mechanisms.....	200
3.1. Crack initiation	200
3.1.1. Experimental illustration of three different crack initiation mechanisms	200
3.1.1.1. 'Very low' pH domain	200
3.1.1.2. 'Low' pH domain.....	200
3.1.1.3. 'High' pH domain	201
3.1.1.4. Conclusions on the crack initiation mechanisms.....	201
3.1.2. Proposition of two crack initiation mechanisms	202
3.1.2.1. Crack initiation by chemical depassivation.....	202
3.1.2.2. Crack initiation by pitting corrosion	202
3.2. Crack propagation.....	204
3.2.1. 'Low' pH domain.....	204
3.2.2. 'High' pH domain	207
3.2.3. Proposition of two crack propagation mechanisms	209
3.2.3.1. Crack propagation assisted by dissolution	209
3.2.3.2. Crack propagation assisted by hydrogen: influence of experimental parameters and mechanism proposed.....	210
4. Conclusions	218

1. Compositions of environments used and test conditions

In order to get closer to possible new industrial applications and to confirm that the mechanisms are similar to the previously observed ones, laboratory Slow Strain Rate Tensile (SSRT) tests in H₂S containing environments were performed in collaboration with the French Corrosion Institute at Fraisses (France). Different solutions were used as described in Table 32 and four parameters were varied during the tests, namely: pH, H₂S partial pressure, strain rate and chloride content. All the tests were performed at room temperature and the solutions were purged 2h prior to loading. The influence of each parameter taken separately on the Z% factor is presented in appendix 3.

The solution is composed of 0.4g/L sodium acetate in deionized water with controlled conductivity (<5μS/cm). If any, chlorides are added in the form of NaCl and pH is decreased by adding HCl. As Virgo™38 is mainly used for Oil & Gas applications, we have chosen to stay close to the NACE solutions containing 0.4g/L sodium acetate and acidified by HCl even if the pertinence of this buffer begins to be discussed within the literature [56].

Table 32 - Compositions of the environments containing H₂S used for SSRT tests on Virgo™38

	Test number (interrupted tests number)	Initial pH (variation)	pH ₂ S (bar)	Strain rate (s ⁻¹)	[Cl ⁻] (ppm) (NaCl)
Influence of pH (low pH range)	1	2.5 (+0.15)	1	10 ⁻⁷	600
	2	3.0 (+0.18)			
	3	3.5 (+0.07)			
	4	4.0 (+0.25)			
Tests at very low pH	5	1.5 (+2.0)	1	10 ⁻⁷	0*
	10	2.0 (+2.0)			
Influence of PH ₂ S	3 (6)	3.5	1	10 ⁻⁷	600
	7 (8)		0.1 (in CO ₂)		
Influence of the strain rate	3	3.5	1	10 ⁻⁷	600
	11			4x10 ⁻⁷	
	12			10 ⁻⁶	
	1	10 ⁻⁷			
	19	2.5		10 ⁻⁶	
Influence of [Cl ⁻]	3	3.5	1	10 ⁻⁷	600
	17				0*
	18	2.5		10 ⁻⁶	0*
	19				600

Testing at 0ppm chlorides means that no NaCl is added but traces of chlorides are certainly present due to the addition of HCl to adjust the pH of the solutions. However, we consider that such low chloride content does not influence neither the passivity of the material nor cracking mechanisms.

For almost all the conditions presented above, the apparent 0.2% yield stress in environment is lower than the one determined in air (as shown, for example, in Figure 179), which means that cracks initiate and start propagating within the nominally elastic domain (i.e. below 0.2% proof stress) and that the conventional plastic elongation measured is due both to the crack propagation and to the plastic deformation of the remaining ligaments that decreases the effective area of the sample. Consequently, plastic elongation is probably not the most relevant parameter to compare the results obtained. That is why, in the following parts, the results will be discussed in terms of reduction in area (RA% or Z%). Furthermore, due to the complexity and the duration of such tests, only one sample has been tested in each condition.

The specimen's geometry corresponds to the reduced NACE tensile specimens as described in Figure 178. The experimental setup was similar to the one previously described except that the cell was made of glass in spite of polymer because polymer is porous to H₂S.

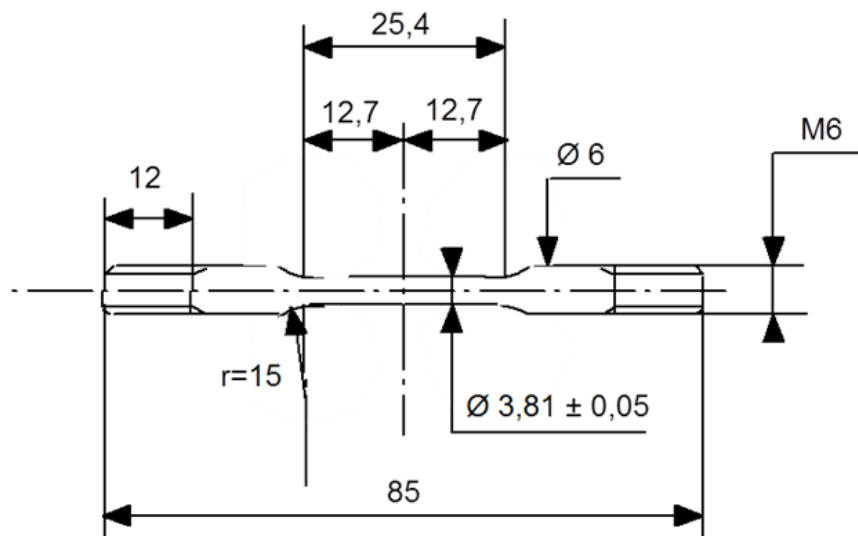


Figure 178 - Geometry of the reduced NACE tensile specimens used for SSRT tests in H₂S containing environments

As mentioned in Chapter III, before the tests, samples were manually polished up to 1 μ m using a conventional lathe, grinding papers and diamond pastes. After polishing, each sample is cleaned using acetone and its diameter is measured both by optical microscopy and using a digital caliper.

After this series of tests, two distinct domains of brittleness of Virgo™38 according to the initial pH of the solution were identified. In the following, we will thus present the results of SSRT tests as a function of the initial pH and we will discuss the different mechanisms involved in the cracking based on the influence of the other parameters varied during the tests.

2. Influence of the pH on the cracking resistance: a synthetic view

Figure 179 shows the tensile curves obtained for different initial pH values of the solution for tests 1 to 5 and 10 in presence of 0 or 600ppm of chlorides and at a strain rate of $10^{-7}s^{-1}$. This study was performed at a strain rate of $10^{-7}s^{-1}$ in order to favor [141] both the hydrogen plasticity interactions and corrosion plasticity interactions involved in the Sulfide Stress Cracking and Stress Corrosion Cracking phenomenon, which are the most reported during industrial failures in Oil & Gas industry and in presence of H_2S [5]. Tests from 1 to 4 correspond to solutions with 600 ppm Cl^- and pH ranged from 2.5 to 4.0, while tests 5 and 10 correspond to solutions at pH 1.5 and 2.0 respectively with no chlorides. In all these test conditions, cracks initiated within the nominally elastic domain, the apparent yield stress being lower than the one determined after the test in air on the same sample geometry. We can mention that the pH variation was not important during these tests except for tests 5 and 10 (Table 32) where after failure, pH increased up to 3.5 and 4.0 respectively.

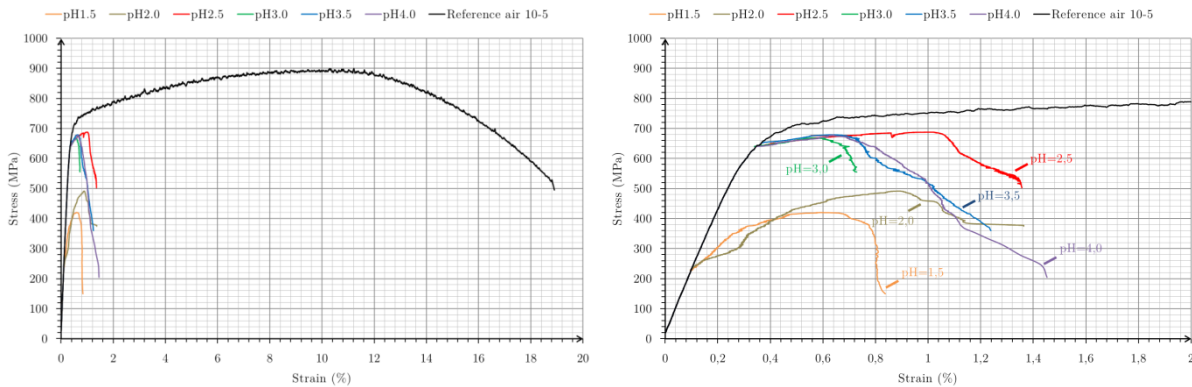


Figure 179 - Tensile curves of Virgo™38 obtained after slow strain rate tensile tests under 1bar H_2S , 0 or 1g/L NaCl and at a strain rate of $10^{-7}s^{-1}$: cracks initiate systematically within the elastic domain

Although in all cases reported in Figure 179 cracking starts below 0.2% proof stress, the results may be divided in two groups with respect to the 0.01% yield stress. SSRT tests at pH=1.5 and pH=2.0 led to crack initiation at approximately 250MPa which is significantly lower than 0.01% YS of the alloy (570MPa) and lower than the estimated physical yield stress of tempered martensite (450MPa). In these cases it seems appropriate to consider that cracking initiates under elastic stresses. At pH values of 2.5 and higher, the presence of cracks is only detected above 600MPa, i.e. above 0.01% yield stress. However, this observation must be moderated by the fact that only macroscopic cracks which contribute to a significant reduction of the sample section may be detected at stress-strain plots.

Figure 180 shows the evolution of the reduction in area measured after SSRT tests as a function of the initial pH of the solution. It shows two distinct domains of pH: a low pH region (at least $pH < 3.0$) and a higher pH region ($pH > 3.0$). In the following, these two domains will be named 'low pH domain' and 'high pH domain'. Actually, they will lead to different behavior of the material with regard to its passivity and to crack initiation and propagation.

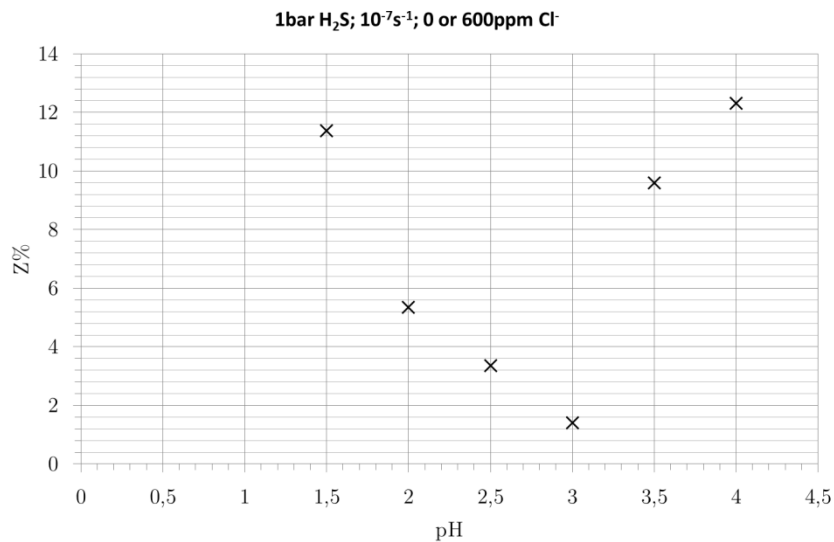


Figure 180 - Influence of the pH on the reduction in area (Z%) for slow strain rate tensile tests under 1bar H₂S, 0 or 1g/L NaCl and at a strain rate of 10⁻⁷s⁻¹

One can see in Figure 180 that, in the low pH region (below 3.0), decreasing the pH enables to increase the ratio of area reduction. In the same time, crack initiation seems to occur earlier at these pH. This evolution could be explained by a competition between cracking and generalized corrosion or dissolution. Indeed, the lower the pH, the higher the corrosion rate leading to the blunting of crack tips which explains that crack propagation (evaluated from the point of stress deviation and the UTS on the tensile curves) is lower and that the ratio of area reduction is increased. The test would have been certainly more aggressive at a strain rate of 10⁻⁶s⁻¹ as indicated in the literature for ASSC mechanism [141] as there is basically less time for dissolution so cracking would be favored. We will confirm this further.

Figure 181 represents the typical fracture surfaces obtained after the SSRT tests at pH lower (left) and higher (right) than 3.0. One can see that at low pH, fracture occurs along prior grain boundaries with several dissolution marks drawing the underlying microstructure and probably related to the electrochemical potentials of the phases as presented in Chapter III. The IG mode is identified on the fracture surface by the general aspect of crystallites. At higher pH, we observed a mixed intergranular and transgranular fracture with facets preserved from the dissolution that was active at low pH.

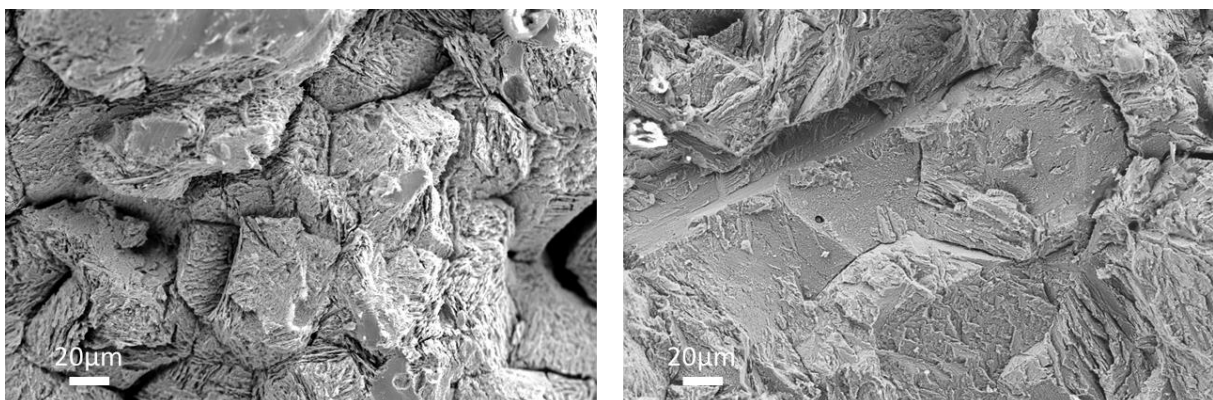


Figure 181 - Typical fracture surfaces obtained after tests at pH lower and higher than 3.0 showing fully intergranular fracture with dissolution marks at pH lower than 3.0 (left, test at pH=2.5) and mixed intergranular / transgranular failure at pH higher than 3.0 (right, test at pH=3.5).

At this stage, these first analyzes allow us to suppose that two different mechanisms of crack initiation and propagation are involved: one rather assisted by dissolution and the other involving the addition of another ingredient such as hydrogen (see further).

The observation of barrel surfaces (Figure 182 and Figure 183), in presence of 600ppm of chlorides at pH between 2.5 and 3.0 shows a stable generalized pitting corrosion on the entire surface, probably due to rupture of the passivity by slip-induced localized dissolution. These pits seem to be at the origin of cracking. For higher pH, visible pits at this scale are less numerous. Even if events of slip-induced depassivation occurred during loading, the higher pH allows the repassivation of the pits and leaves the metallic aspect of the barrel surfaces. The crack initiation and propagation in this case are rather governed by hydrogen effects which could explain this brittle appearance of the fracture. For lower pH ($\text{pH} \leq 2.0$) and in absence of chlorides, generalized active corrosion occurs. Three domains of crack initiation can thus be identified while looking at the barrel surfaces of the samples after SSRT tests.

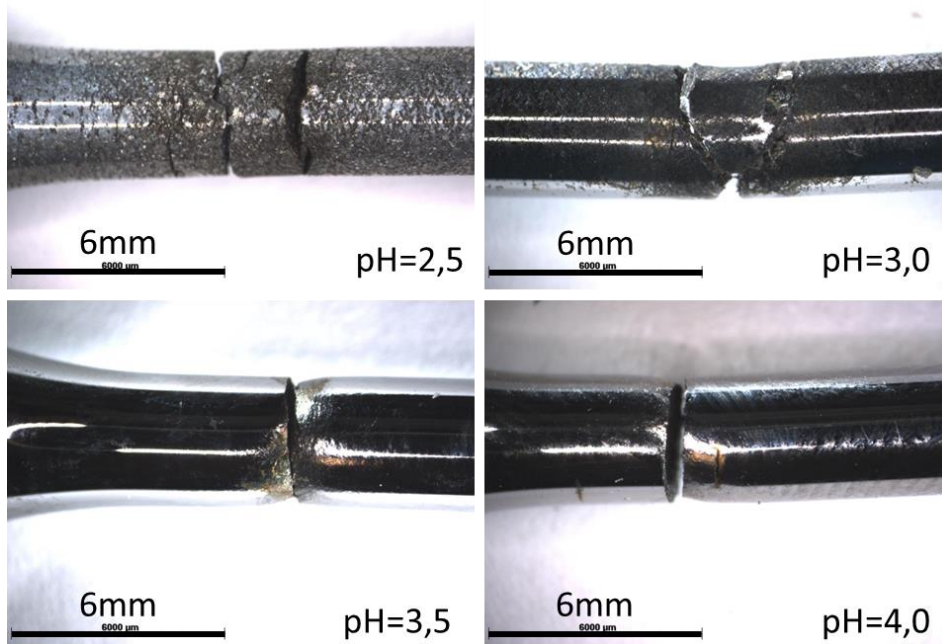


Figure 182 - Optical micrographs of barrel surfaces after SSRT tests in H_2S containing environments showing the influence of the pH and the gap between generalized and localized pitting corrosion

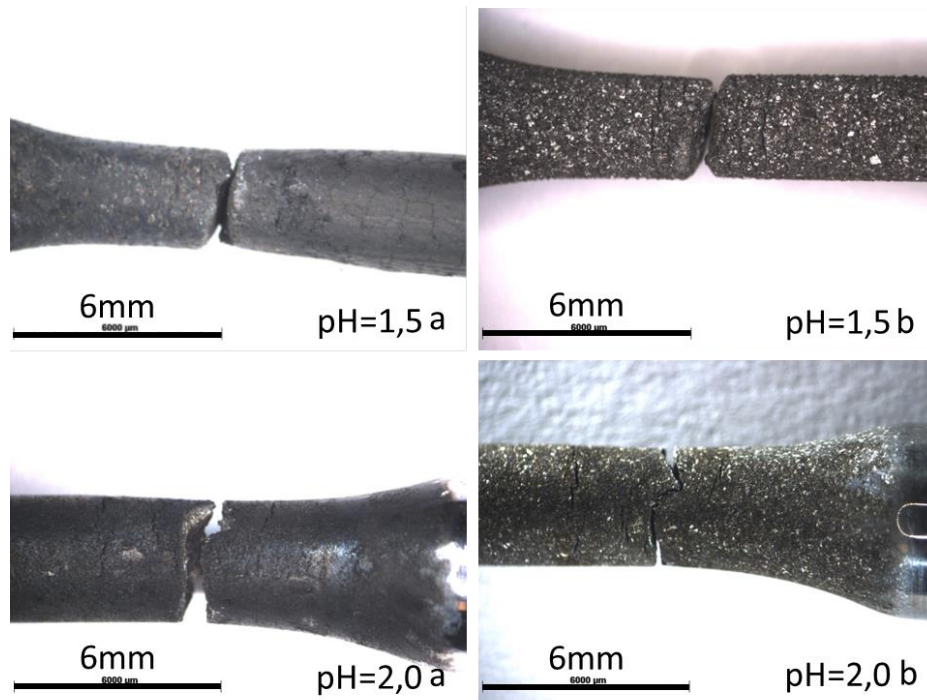


Figure 183 - Optical micrographs of barrel surfaces after SSRT tests in H₂S containing environments: influence of the pH without chlorides showing generalized corrosion with non-adherent corrosion products (before and after cleaning)

One can see on the micrographs of barrel surfaces (Figure 182 and Figure 183) that the density of secondary cracks increases when pH decreases. Furthermore, for the tests at very low pH (≤ 2.0 , tests 5 and 10), the surfaces are chemically active, while at higher pH with chlorides, tests 1 and 2 lead to pitting corrosion. The generalized active corrosion is explained by the chemical dissolution of the passive film for $\text{pH} \leq 2.0$ (Figure 183). Generalized pitting corrosion in presence of 600ppm of chlorides for pH between 2.0 and 3.0 reveals a weakening ability of Virgo™38 to repassivate under loading. The continuous micro-plasticity events at the origin of slip-induced dissolution prevent any pit repassivation, placing the material in the situation where it would be between its pitting potential and its repassivation potential. At pH higher than 3.0, the repassivation is easier and only one crack leads to final fracture with a very brittle aspect. The cracks are perfectly perpendicular to the tensile axis, and one can observe a slight necking of the last ligament before final fracture. One can suppose that initiation site depends on the preferential crystallographic orientation of former austenitic grains and/or the load applied favoring dislocation gliding and localized plasticity. Rare pitting and/or dissolution occur at these particular locations at “high” pH while it is more generalized at $\text{pH} = 3.0$ and under.

In summary, these observations of the barrel surfaces and the general shape of the curves lead us to make the assumption of two crack initiation mechanisms depending on the initial pH of the solution. Indeed, below $\text{pH} = 3.0$ stable regime of generalized pitting corrosion occurs and crack propagation is governed by dissolution, while for higher pH, pits due to slip-induced localized depassivation are quickly repassivated and do not allow crack initiation or propagation by dissolution. Hydrogen effects on the weakening of interatomic bonds on particular interfaces or on the hydrogen plasticity interactions are certainly involved in the cracking. At pH lower than 2.5, generalized corrosion results in an entire depassivation of the material. In this case, crack initiation and propagation assisted by dissolution could depend on the electrochemical behavior of each phase constituting Virgo™38. In the following, we will identify three domains (Figure 184):

- 'high' pH domain corresponding to tests at pH between 3.0 (included) and 4.0, characterized by localized corrosion produced by slip-induced dissolution mechanism, but also by the ability of the material to repassivate
- 'low' pH domain corresponding to tests at pH between 2.5 (included) and 3.0, characterized by generalized pitting corrosion without repassivation
- 'very low' pH domain corresponding to tests at pH lower than 2.0 (included), characterized by generalized corrosion

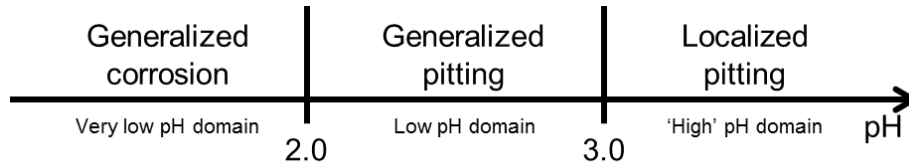


Figure 184 - Representation of the three domains identified for crack initiation

The low pH and very low pH regions correspond to crack propagation mechanism governed by dissolution with a more or less localized character, called Anodic Stress Corrosion Cracking (ASCC). On the other side, the crack propagation mechanism is probably different at higher pH, and involves hydrogen. That is why, while talking about crack propagation, only two domains will be mentioned: a low pH domain (containing low and very low pH domains previously mentioned) and a 'high' pH domain (Figure 185).

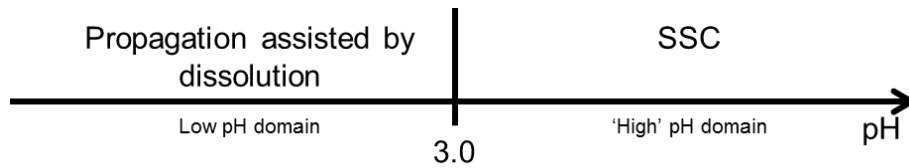


Figure 185 - Representation of the two domains identified for crack propagation and possible mechanisms involved

In conclusions of this first part, three domains involving different crack initiation mechanisms have been identified. Two domains involving different crack propagation phenomena are also observed. In the following, finer analysis of the cracking path will be done using, in particular, analysis of EBSD maps, and phenomenological model will be proposed.

3. Detailed analysis of crack initiation and propagation in presence of H₂S and proposed mechanisms

3.1. Crack initiation

3.1.1. Experimental illustration of three different crack initiation mechanisms

3.1.1.1. 'Very low' pH domain

Figure 186 presents the surface of a mirror polished sample after immersion in the solution at pH=2.0 (test 10) without applying mechanical stress. We can see a strong general dissolution and an intergranular corrosion that could correspond to the dissolution of retained austenite close to former austenitic grain boundaries. This observation, in comparison with what had been presented in Chapter III, confirms that at pH=2.0 we are below the depassivation pH of Virgo™38 in this environment. That is why, it can be concluded that crack initiation is mainly due to chemical depassivation in the very low pH domain.

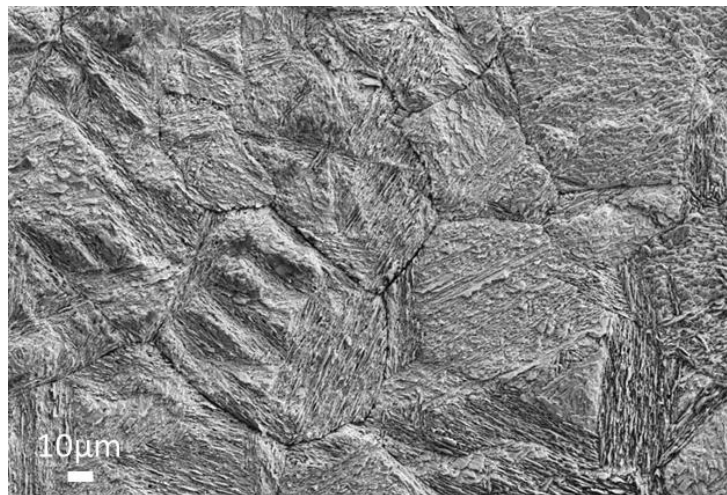


Figure 186 - Surface of a sample after immersion in the solution at pH=2.0 (test 10) without applying mechanical loading, showing intergranular corrosion

3.1.1.2. 'Low' pH domain

Figure 187 presents the barrel surfaces of specimens tested in conditions 1 and 2 at pH=2.5 and 3.0 respectively. It shows a combination of generalized dissolution of the passive film and stable pitting corrosion. It is highly probable that dissolution is activated in areas of high deformation or stress localization; indeed as shown in Chapter III, mechanical loading influences chemical depassivation. Stable pitting corrosion is homogeneously observed all along barrel surfaces in both cases.

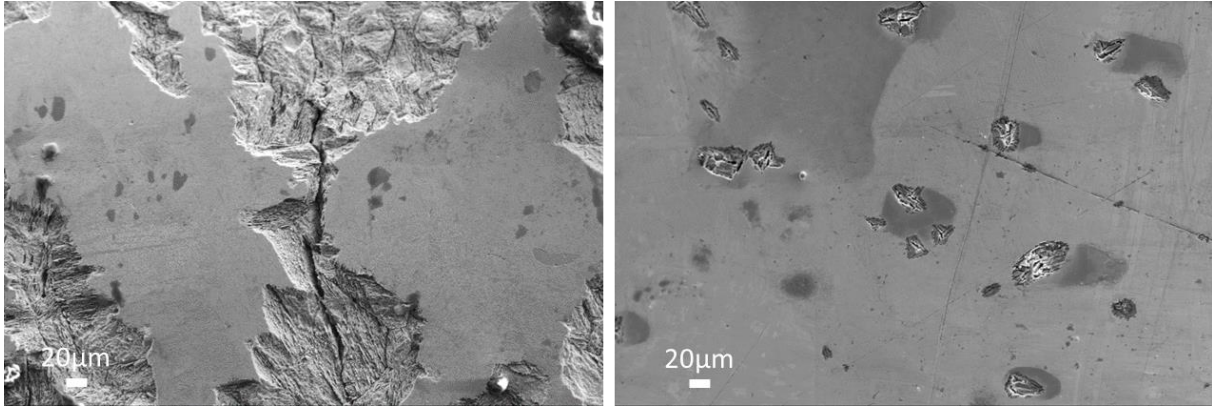


Figure 187 - SEM micrographs of barrel surfaces of tests 1 and 2 (pH 2.5 and 3.0 respectively) showing stable and generalized pitting corrosion and large areas of depassivation in probable areas of stress concentration

In conclusion, in the low pH domain, crack initiation is due either to chemical depassivation assisted by mechanical loading or to stable and generalized pitting corrosion.

3.1.1.3. 'High' pH domain

As previously, for higher pH (>3.0), tensile samples are still passivated except near the fracture surface, which means that cracks could be initiated even in the passive state of the material. In that case, initiation is probably due to metastable pitting corrosion and subsequent enhanced local hydrogen entrance which could be favored by micro-plastic deformations resulting in local destabilization of the passive film (Figure 188).

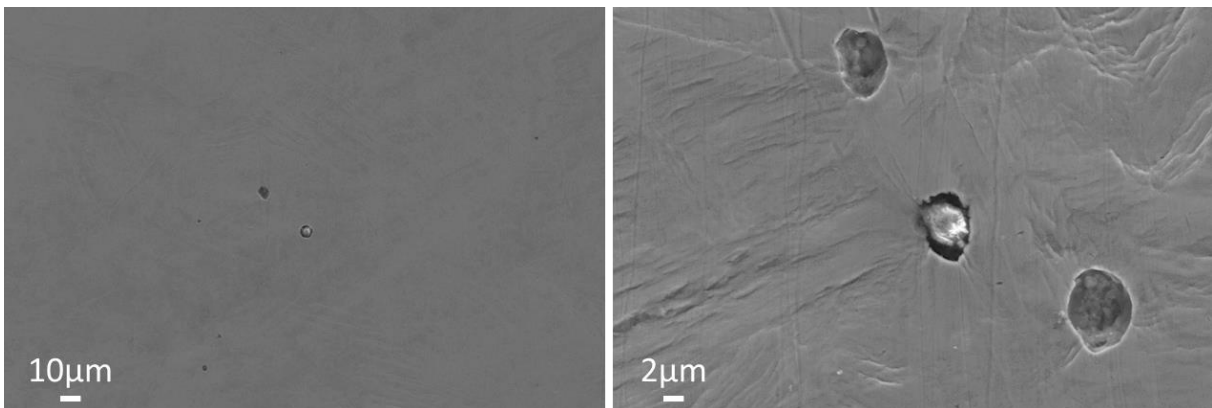


Figure 188 - SEM micrographs of barrel surfaces of tests 3 and 4 (pH 3.5 and 4.0 respectively) showing pitting corrosion that could be at the origin of the main crack

In conclusion, crack initiation in the 'high' pH domain is due to pitting corrosion assisted by mechanical loading.

3.1.1.4. Conclusions on the crack initiation mechanisms

We proposed to conclude that there are only two distinct crack initiation mechanisms: pitting corrosion above pH_0 and chemical depassivation below pH_0 .

3.1.2. Proposition of two crack initiation mechanisms

3.1.2.1. Crack initiation by chemical depassivation

The resistance of the passive film to chemical dissolution and the possible galvanic coupling (even if the potential difference is small, as mentioned in the conclusions of Chapter III) have been discussed in Chapter III in absence of H₂S but we consider that the mechanisms involved here are the same. Furthermore, knowing that H₂S increases the depassivation pH [56] (as compared to what had been presented in Chapter III) and according to what was observed in the very low pH domain, one can conclude that the depassivation pH of Virgo™38 in environments containing 1 bar of H₂S is close to 2.0. Applying mechanical loading shifts the depassivation pH to around 2.5, as observed in the low pH domain. As in Chapter III in absence of H₂S, we can consider that depassivation occurs in two steps and that the depassivation pHs of both phases are close but different.

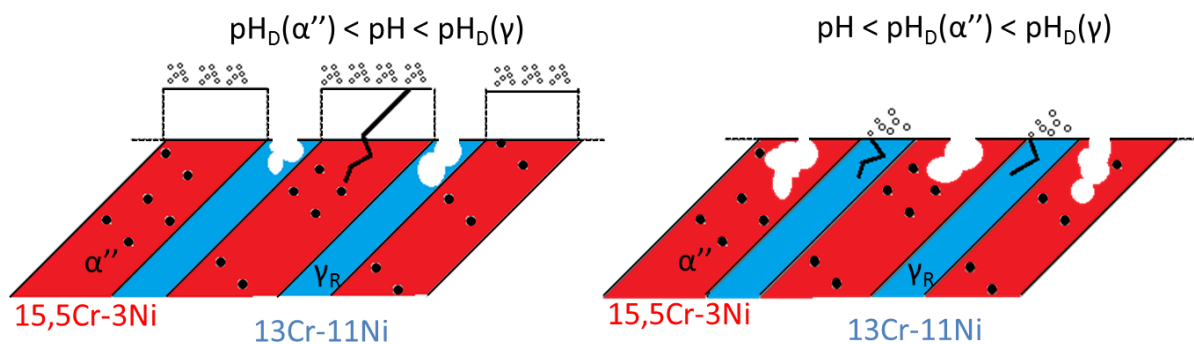


Figure 189 - Schematic representation of crack initiation due to chemical depassivation in two cases:
 a (left): one phase, namely gamma, is preferentially dissolved (see Chapter III), cathodic reactions occur at the surface of the other phase, namely alpha, leading to the development of HE cracks, due to their geometry, dissolved areas can also initiate cracks.
 b (right): generalized dissolution of both phases can result in galvanic coupling and enhanced dissolution of alpha phase with concomitant hydrogen discharge on gamma phase

Figure 189 shows a schematic representation of two possible crack initiation mechanisms assisted by chemical depassivation. In each case, one phase is preferentially dissolved: either retained austenite at intermediate pH (left) or tempered martensite at lower pH (right). Cathodic reactions occur at the surface of the second phase, leading to the development of hydrogen embrittlement cracks. Note that applying a mechanical loading will not change the mechanism itself but it will only favor its apparition at higher pH.

3.1.2.2. Crack initiation by pitting corrosion

Among all the parameters presented previously, chloride content is the most influencing one on the ratio of area reduction. Indeed, its increase induces an important decrease of the resistance to both HE and ASCC (see appendix 3). According to the literature and as previously mentioned, chloride content has mainly an influence on the crack initiation mechanism. Indeed, in presence of chlorides and as observed previously, the favored crack initiation mechanism is pitting corrosion (either stable or metastable according to the pH of the solution and the stress level). Furthermore, adsorbed sulfur is known to promote pitting corrosion by stabilizing pits. In this case, repassivation is hindered by sustaining active dissolution under conditions where the pits would have repassivated [159]. It is thus expected that the H₂S partial pressure also influences the pitting resistance.

According to the previous observations performed on the barrel surfaces after SSRT tests in different environments, we can conclude that 600ppm of chlorides in presence of H₂S is very damaging for Virgo™38 which presents a limited resistance of its passive film. Indeed, its targeted application range does not include environments with high amounts of chloride.

According to the pH and the stress level, pitting corrosion can be either stable and generalized (low pH, high stresses) or metastable and localized (high pH, low stresses). Both types of pitting corrosion have been observed during SSRT tests performed on Virgo™38 (Figure 190).

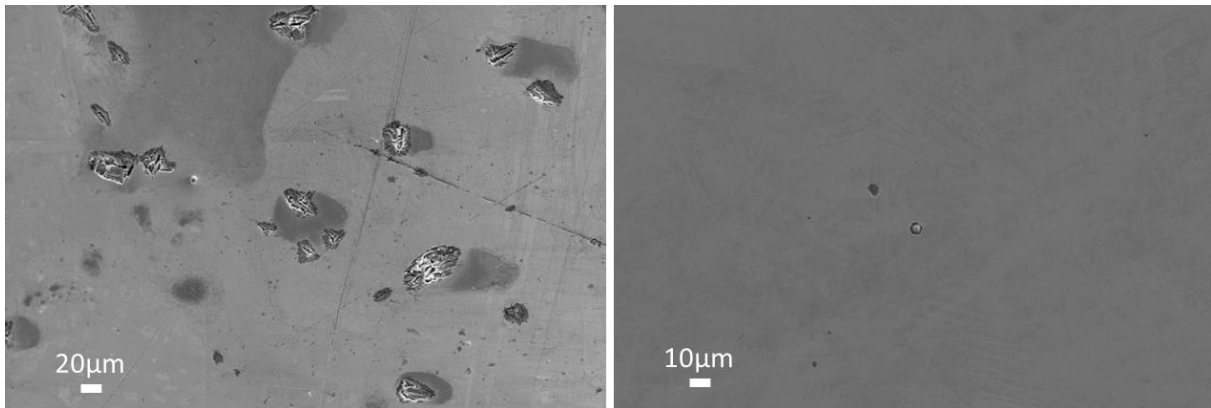


Figure 190 - Observation of the barrel surfaces after SSRT tests showing either stable (left, pH=3.0) or metastable (right, pH=3.5) pitting corrosion according to the pH of the solution at the same stress level of 680MPa

As shown for duplex stainless steels [177] where partitioning effect occurs as in Virgo™38 (see Chapter II), pitting is initiated on the phase which presents the lowest Pitting Resistance Equivalent Number (PREN). PREN can be calculated for each phase using the formulas given in Chapter I and according to the chemical composition of both phases calculated in Chapter II (Table 33).

Table 33 - Chemical composition of main elements of tempered martensite and retained austenite after industrial heat treatment according to ThermoCalc® and corresponding PREN as defined in Chapter I for each phases

	%Cr	%Mo	%Mn	PREN
Tempered martensite α''	15.5	0.06	/	15.7
Retained austenite γ_R	13	0.06	1.9	11.3

Thus, pits are supposed to be preferentially located within retained austenite due to its lower PREN. Furthermore, under mechanical loading, it is theoretically possible to observe pitting corrosion on fresh martensite formed by SIMT because it conserves the same composition as retained austenite, and thus presents a poor resistance to pitting corrosion (low PREN).

The influence of Cr content on HE resistance (after initiation by pitting corrosion) is presented in appendix 5 by comparison with another SMSS.

Moreover, industrial alloys contain inclusions that are much more damageable than retained austenite. Virgo™38 contains TiC for example, and it can be seen that pits mainly initiate on these inclusions (Figure 191).

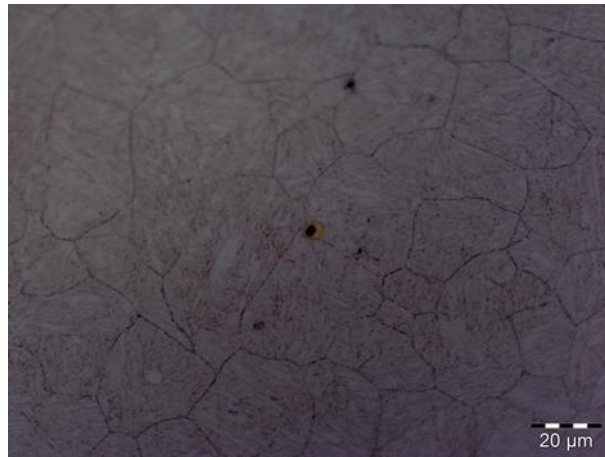


Figure 191 - Optical micrograph of a sample mirror polished after 30min immersion at the Open Circuit Potential in a solution containing 30g/L NaCl + 0.4g/L sodium acetate at pH=1.5 showing pitting corrosion of TiC

3.2. Crack propagation

3.2.1. 'Low' pH domain

As indicated in the literature [140], one of the most discriminating parameters to distinguish H-assisted cracking from Anodic SCC phenomenon is the strain rate. Indeed, for hydrogen assisted cracking it is expected that the brittleness increases with decreasing strain rate while for Anodic Stress Corrosion Cracking the existence of a critical strain rate for which embrittlement is maximal is supposed [141]. That is why we decided to perform tests at different strain rates in the two supposed domains of crack propagation.

Figure 192 shows the evolution of the reduction in area as a function of the strain rate in the low pH domain described previously (pH=2.5 presented in this case). At low pH, applying a higher strain rate is detrimental for the cracking resistance of Virgo™38.

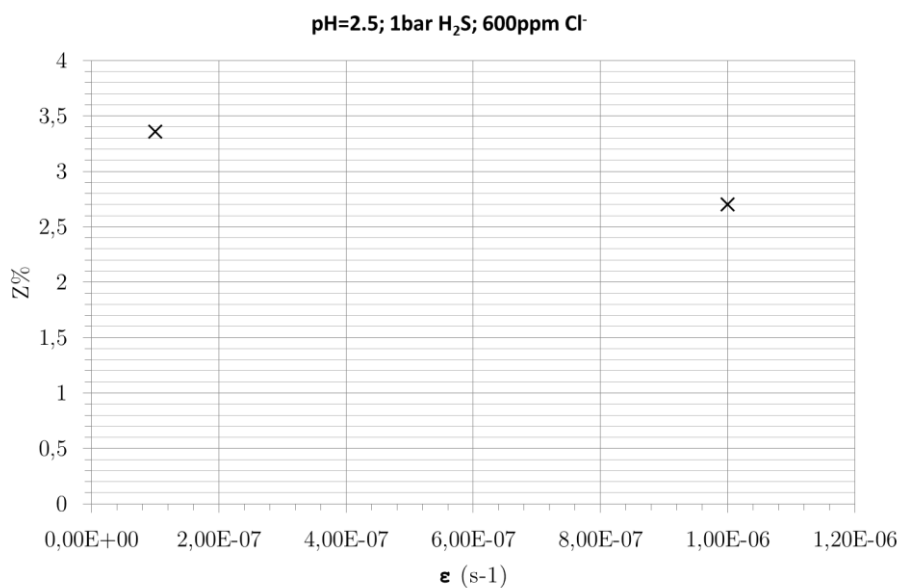


Figure 192 - Influence of the strain rate applied on the reduction in area (Z%) for slow strain rate tensile tests under pH=2.5, 1bar H₂S and 1g/L NaCl

According to Parkins et al. [141], this evolution is due to a synergy between repassivation and dissolution and is typical of ASSC phenomena. This competition can explain the presence of a critical strain rate that often corresponds to a strain rate of 10^{-6}s^{-1} in presence of H₂S.

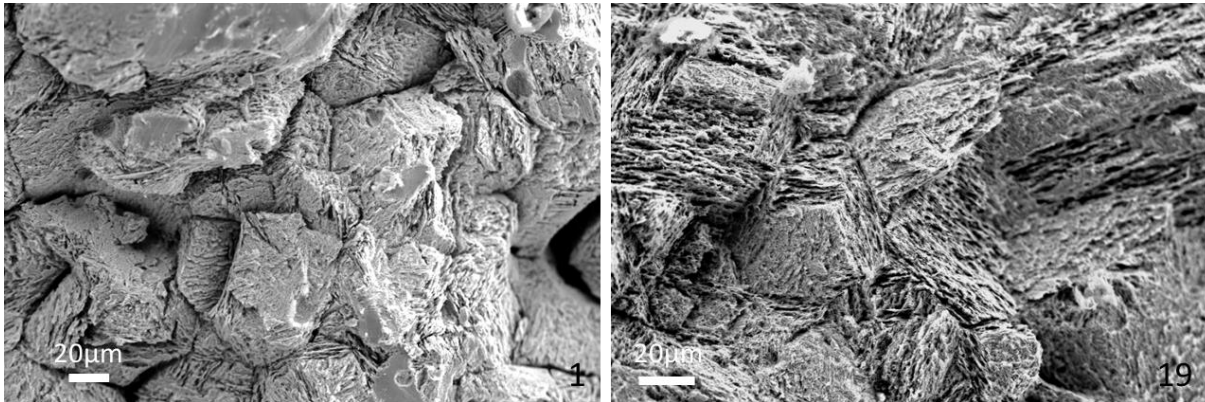


Figure 193 - Evolution of the fracture surface with the strain rate in the “low pH” domain showing mainly intergranular fracture with preferential dissolution in both cases (10^{-7} left and 10^{-6} right, respectively)

Figure 193 presents the fracture surfaces obtained and shows that severe dissolution marks the surface. Generalized dissolution affected also the barrel of the specimen. The diameter reductions are respectively 1.6% for test at 10^{-7}s^{-1} and 0.8% at 10^{-6}s^{-1} . The dissolution is less important when the strain rate is higher due to the duration of immersion. This observation accounts for the increase of area reduction for lower strain rates where generalized corrosion reduces the specimen diameter but also increases blunting of crack tips.

At very low pH (≤ 2.0), preferential dissolution of one phase seems to occur and assists crack propagation (Figure 194). This preferential dissolution can be explained by a kind of galvanic coupling between the phases due to difference of composition as explained in Chapter III (see further), even if the potential difference between both phases is small. Furthermore, this effect must also influence crack initiation as previously discussed. By comparison with Chapter III, it can be postulated that tempered martensite is dissolved preferentially at lower pH (1.5) and that retained austenite is preferentially dissolved at ‘higher’ pH (2.0 and higher). This seems to be confirmed by the observation of the crack paths by EBSD analysis (Figure 194). Note also that fresh martensite formed by stress induced martensitic transformation at the crack tip is of the same composition as retained austenite and can thus be also affected in the same way by preferential dissolution.

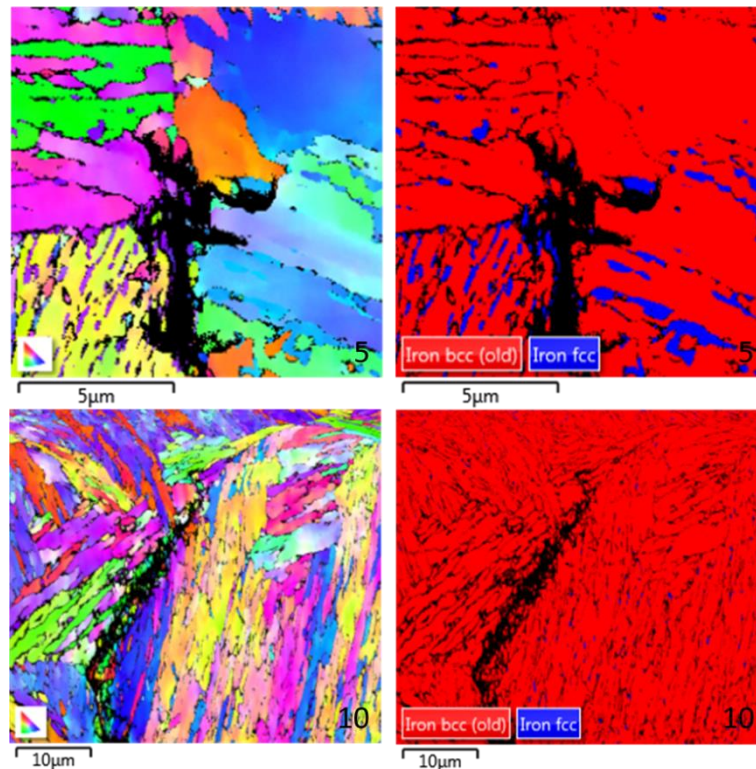


Figure 194 - EBSD maps on polished cross-sections after SSRT tests at pH certainly lower than pH_D without chlorides showing intergranular crack propagation and preferential dissolution of either martensite (test 5 at pH=1.5) or retained austenite (test 10 at pH=2.0) along crack path

Figure 195 shows the path of a secondary crack at low pH. As previously observed on the fracture surfaces (Figure 181), at low pH, the cracks propagate along prior grain boundaries with dissolution along the crack path. This dissolution is evidenced by the presence of an abnormally high Ni content inside the crack (black arrows in Figure 195 left).

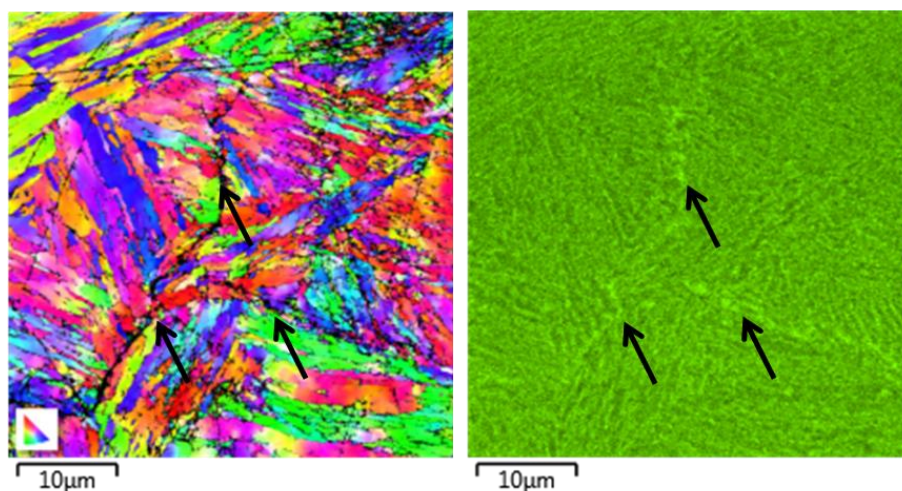


Figure 195 - EBSD maps on cross-section specimens after SSRT test showing secondary cracks representative of the crack propagation paths. Cracks propagate in an intergranular mode at low pH (pH=2.5). The enrichment of Ni in the crack at low pH can be associated with the presence of corrosion products (NiS) and indicates a crack propagation assisted by dissolution

In conclusion, the strain rate dependency and the study of the corrosion products along the crack path indicate that in the low pH region, phenomenon of Anodic Stress Corrosion Cracking with preferential dissolution is involved.

3.2.2. 'High' pH domain

As previously mentioned, the main discriminating factor is the strain rate dependency. Figure 196 shows the evolution of the reduction in area as a function of the strain rate in the high pH domain described previously (pH=3.5 presented in this case). It shows that decreasing the strain rate at high pH leads to a decrease of the reduction in area.

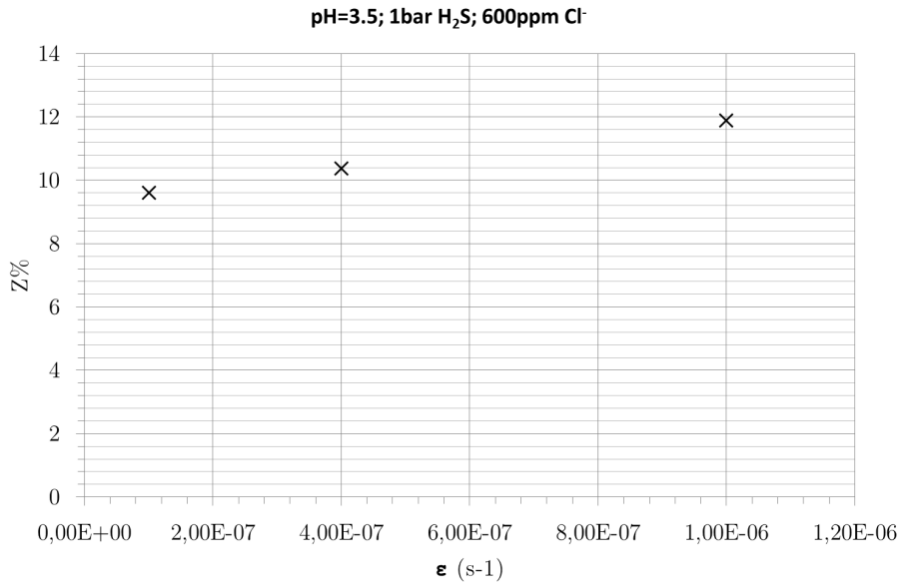


Figure 196 - Influence of the strain rate applied on the reduction in area (Z%) for slow strain rate tensile tests under pH=3.5, 1bar H₂S and 1g/L NaCl

According to the study realized by Parkins et al. [141], the high pH domain could correspond to hydrogen-assisted stress corrosion cracking. Indeed, the brittleness is always increasing with a decreasing strain rate which is coherent with these mechanisms. As presented in Chapter IV, the embrittlement mechanisms involved in this case can be related both to hydrogen dislocation interactions, which increase the localized character of the deformation and favor dislocation multiplication (HELP model), and to weakening of atomic bonds at interfaces (HEDE) which facilitates opening of the interfaces such as former austenitic grain boundaries and leads to intergranular mode of failures or interlaths for transgranular failures. Once again, even if the influence of these parameters was not studied in H₂S-containing environments, retained austenite localization and its stability are expected to influence crack path as we have seen in Chapter IV. The mechanisms involved will be discussed in the following parts of this chapter.

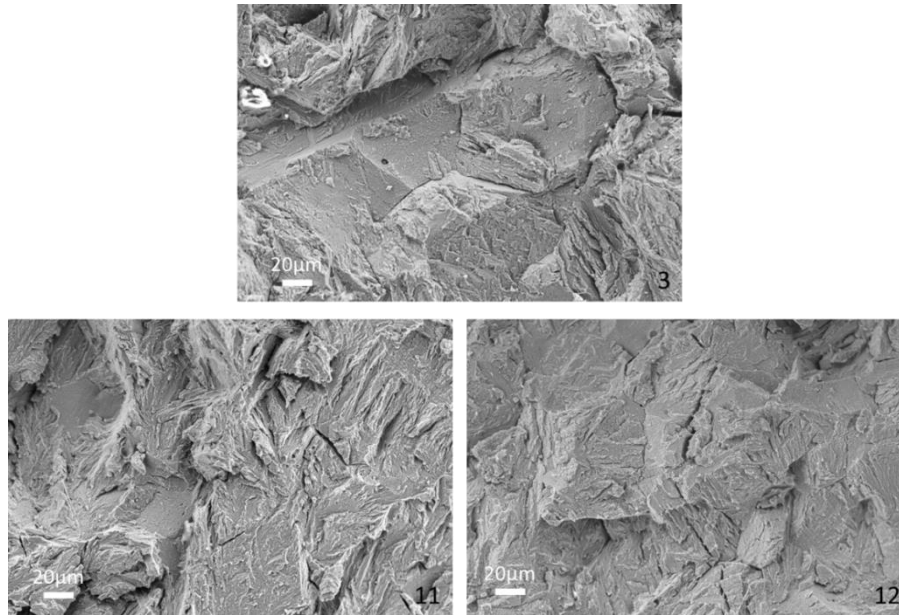


Figure 197 - Evolution of the fracture surface with the strain rate in the “high pH” domain showing a decrease of the intergranular fraction with an increasing strain rate (respectively 10^{-7} top, 4×10^{-7} left and 10^{-6} s^{-1} right)

Figure 197 presents the fracture surfaces obtained after the tests at different strain rates. It shows that the proportion of intergranular fracture decreases with an increasing strain rate. Indeed, the proportions of intergranular areas are of $34.9 \pm 0.6\%$, $6.9 \pm 1.9\%$ and $4.3 \pm 1.4\%$ for strain rates ranging from 10^{-7} to 10^{-6} s^{-1} respectively.

Contrary to tests performed in NaOH+Na₂S environment, the IG mode of cracking is significantly reduced. If we compare the hydrogenating conditions between the two environments, one can find in [178] that the permeation current in an ARMCO iron membrane at pH2.8 and 1 bar H₂S is equal to $60\text{-}70 \mu\text{A}/\text{cm}^2$, against $18 \mu\text{A}/\text{cm}^2$ in NaOH+Na₂S media and $4 \mu\text{A}/\text{cm}^2$ in NaOH media at cathodic potential for Virgo™38 SMSS. Although no permeation measurement was made on our alloy in H₂S-containing environments, it can be assumed that the activity of hydrogen in the sour media is higher and increases the total H content in the alloy. However, this does not explain the increase of transgranular cracking mode insofar as the same mechanisms explained in Chapter IV can operate and produce similar damage but probably at lower level of stress and plastic deformation.

A hypothesis related to this change of cracking mode could be related to the effects of hydrogen on the austenite to martensite transformation (SIMT). Few results exist in the literature on this topic, nevertheless the PhD work of Bricout [179] showed that the application of a high hydrogen fugacity on a steel with low diffusivity could favor the transformation $\gamma \rightarrow \varepsilon$, and consequently, the formation of the hydride ε in a metastable austenitic stainless steel. Conversely, stopping the cathodic charging and subsequent outgassing causes the following decomposition:



The latter transformation being initiated by relaxation deformation, this formed α' martensite is a real hardening martensite. The condition of H-charging in H₂S media being more severe, this mechanism could explain the appearance of the transgranular mode of cracking in such a large proportion. However, it remains to be explained how successive superficial compression/relaxation stresses required by this mechanism can be effectively generated.

Finally, at high pH (>3.0), the propagation is mainly transgranular with some intergranular areas (black arrow in Figure 198). No corrosion products are visible in this case. It can thus be concluded that the propagation is mainly due to hydrogen, even if the appearance of large amount of brittle transgranular cracking is not clearly explained. As previously mentioned, hydrogen activity influences the crack propagation mode: the general rule is that the higher the hydrogen activity, the higher the proportion of intergranular areas.

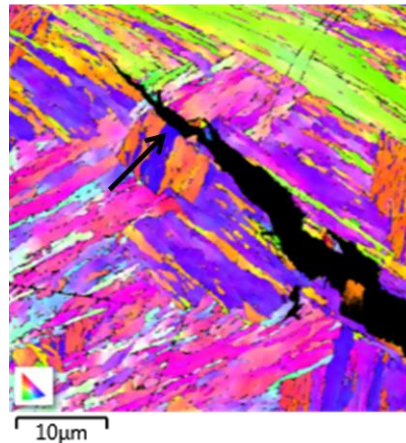


Figure 198 - EBSD maps on cross-section specimens after SSRT test showing a secondary crack representative of the crack propagation paths. Cracks propagate in a transgranular mode at 'high' pH (pH=4.0)

In summary, in the 'high' pH domain, no corrosion products are visible on the EBSD-EDX mapping and no dissolution is visible on the fracture surfaces, it is thus supposed that propagation is due to hydrogen effect rather than dissolution.

3.2.3. Proposition of two crack propagation mechanisms

3.2.3.1. Crack propagation assisted by dissolution

At low and very low pH, preferential dissolution was evidenced by EDX mapping on secondary cracks, and contributes to the progression of the crack. It is well known that hydrolysis reactions of metallic cations inside corrosion defects like pits, crevice or crack decrease the local environment pH as compared to the outside of the defect, which can fall under the depassivation pH. In this case, a kind of coupling between the two phases with different chemical composition can be the driving force for the preferential dissolution and maintain the progression of the crack rather than blunting it and stop its propagation. Indeed, as seen in Figure 199 even at 'high' pH local dissolution can occur.

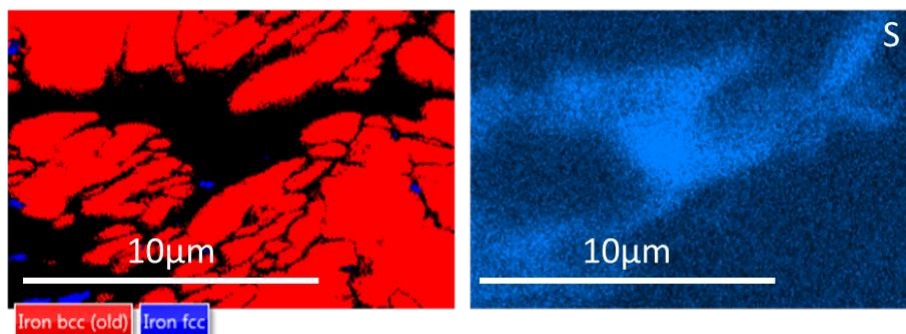


Figure 199 - EBSD and EDX maps on cross-section specimens after SSRT test showing sulfur enriched corrosion products indicating dissolution at a long crack tip. Such situation was systematically observed at very low and low pH, here is demonstrated even after test at 'high' pH (pH=4.0)

That is why, this mechanism of crack propagation by preferential dissolution should not be neglected even if it is not the predominant one. A schematic representation of the proposed mechanism is given in Figure 200.

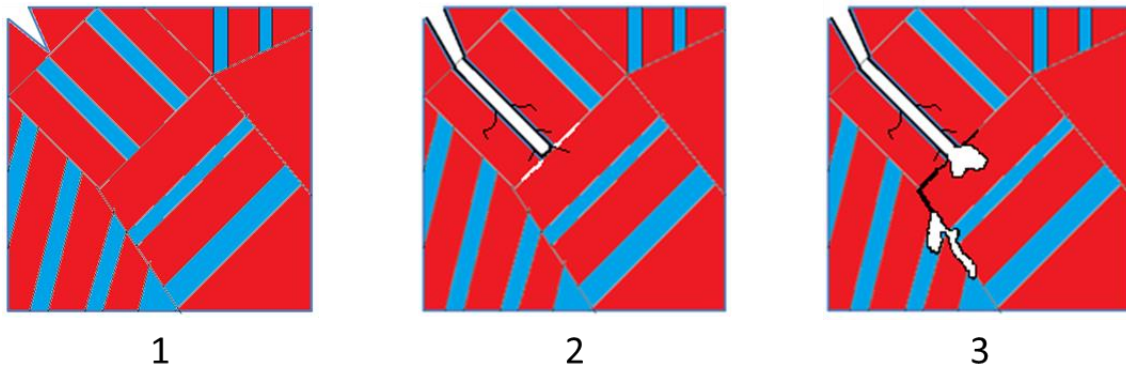


Figure 200 - Schematic representation of the proposed mechanism of crack propagation assisted by dissolution in the case of $pH_D(\alpha'') \leq pH \leq pH_D(\gamma)$: 1) crack initiation, 2) formation of the corrosion products (typically NiS) due to the dissolution of retained austenite, dissolution of retained austenite along former austenitic grain boundaries and development of HE cracks in martensite due to hydrogen formed by the cathodic reaction at its surface, 3) local acidification due to the confinement leading to dissolution of martensite ($pH < pH_D(\alpha'')$)

If we consider the case where the initial pH of the environment is between the depassivation pH of both constitutive phases, retained austenite located both at former austenitic grain boundaries and between martensitic laths will preferentially dissolve (see Chapter III) explaining the mixed transgranular-intergranular failures. The local acidification due to hydrolysis reactions of metallic cations in the confined environment at the crack tip will allow local depassivation of martensite and then the 'galvanic' coupling will result in martensite dissolution along interfaces with retained austenite, i.e. in area of potentially strong galvanic coupling. The initial dissolution of retained austenite leads to the formation of metallic ions that can precipitate with sulfur present in the solution: this phenomena leads to the formation of a corrosion products layer. As identified within the literature, for SMSS containing Ni, the most thermodynamically stable corrosion product is NiS but its influence on crack propagation remains controversial and was not taken into account in our interpretation.

If the initial pH of the environment is lower than the depassivation pH of martensite (thus also lower than the one of retained austenite, see Chapter III), then the final step described above will immediately operate, because the actual pH results in depassivation of both phases and activation of galvanic coupling. Tempered martensite will preferentially dissolve by galvanic coupling as evidenced by the electrochemical measurements presented in Chapter III. Moreover, the corrosion of martensite will favor the embrittlement of retained austenite due to the cathodic discharge of protons at its surface, but here we have been switching to the hydrogen assisted mechanism of crack propagation.

3.2.3.2. Crack propagation assisted by hydrogen: influence of experimental parameters and mechanism proposed

Crack propagation assisted by hydrogen is the main phenomena reported in industrial failures in Oil&Gas industry because the pH of industrial environments lies within the 'high' pH region identified previously. It usually leads to intergranular failures. In our work, depending on electrochemical and mechanical loading conditions, mixed intergranular and transgranular failures were observed. In the

following part, we will consider a given crack propagation mechanism (ASCC or HE) and we will discuss the difference of crack propagation mode based on the hydrogen content and the differences in hydrogen diffusion paths.

The exact crack propagation path usually depends on hydrogen activity, diffusion and trapping as explained in Chapter IV and as shown previously (Figure 197 for example). Indeed, in service conditions, due to the long life of machines (compared to our SSRT tests), hydrogen has much time to diffuse along grain boundaries and to be trapped inside retained austenite, that is why intergranular failures might be favored. Similarly, during standard tests under static loading, the duration of 720 hours enable to reach high hydrogen content in the microstructure. Furthermore, as demonstrated in Chapter IV, the grain boundary composition also influences the crack propagation mode.

The simplest way to vary hydrogen activity is to change the H₂S partial pressure or the strain rate. Figure 201 shows the evolution of the reduction in area (Z%) as a function of the H₂S partial pressure for a solution containing 600ppm of chlorides at pH 3.5 and for tests at 10⁻⁷s⁻¹. As previously mentioned, at high pH we are probably within the domain of HE, that is why we have performed the study of the influence of the H₂S partial pressure at a strain rate of 10⁻⁷s⁻¹. Indeed, it was shown previously that the lower the strain rates the higher the embrittlement for this phenomenon.

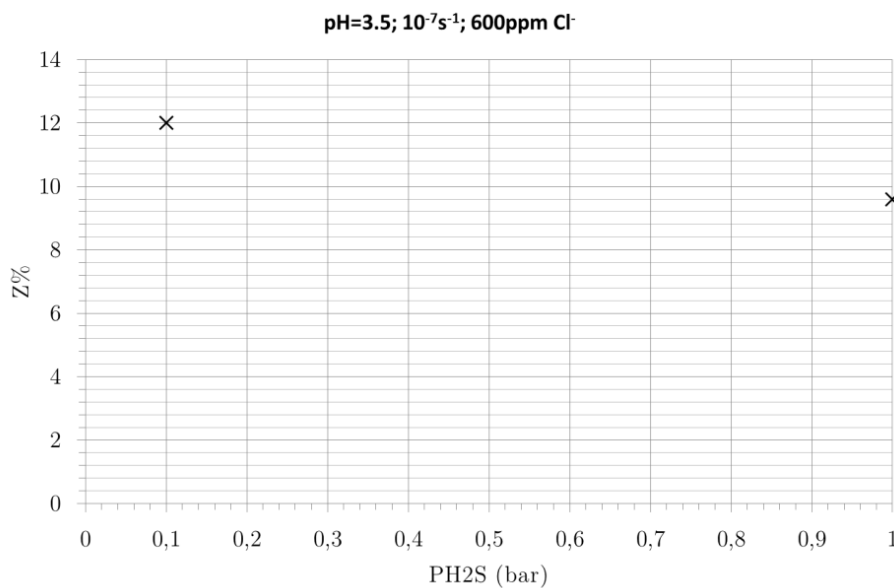


Figure 201 - Influence of the H₂S partial pressure on the reduction in area (Z%) for slow strain rate tensile tests under pH=3.5, 1g/L NaCl and at a strain rate of 10⁻⁷s⁻¹

H₂S is known to increase hydrogen activity by blocking hydrogen recombination at the sample surface [67], that is why, it is expected that increasing the H₂S partial pressure should lead to a decrease of the area reduction as observed in Figure 201. The differences observed on the final ratio of area reduction are thus mainly associated to the accelerated crack propagation in the case of a higher partial pressure of H₂S. To determine the influence of the partial pressure of H₂S on the hydrogen activity measured at the sample surface of SMSS Virgo™38, additional permeation tests in H₂S containing environments such as the ones performed in Chapter IV would be useful.

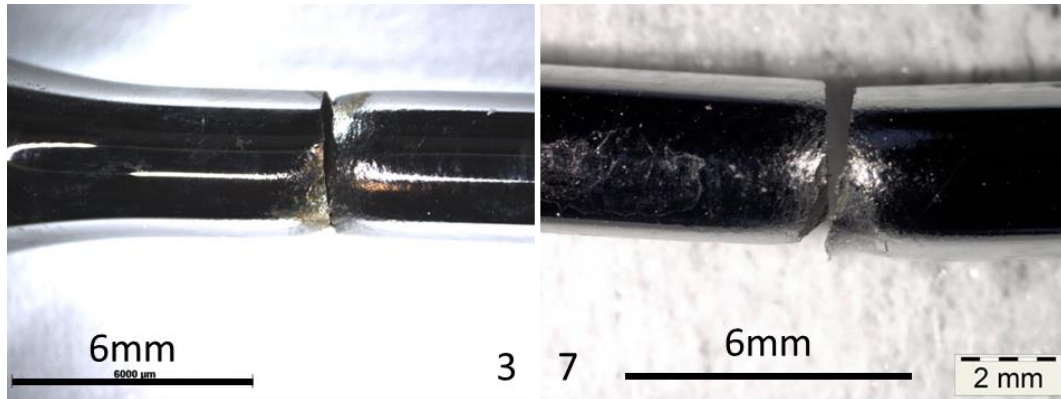


Figure 202 - Optical micrographs of barrel surfaces after SSRT tests showing the influence of the H₂S partial pressure in the high pH domain (pH=3.5) in presence of 600ppm of chlorides and at a strain rate of 10⁻⁷s⁻¹ (1 bar H₂S, left and 0.1 bar H₂S, right)

In both cases, crack initiation is not generalized (Figure 202) and we consider that only the crack propagation is modified.

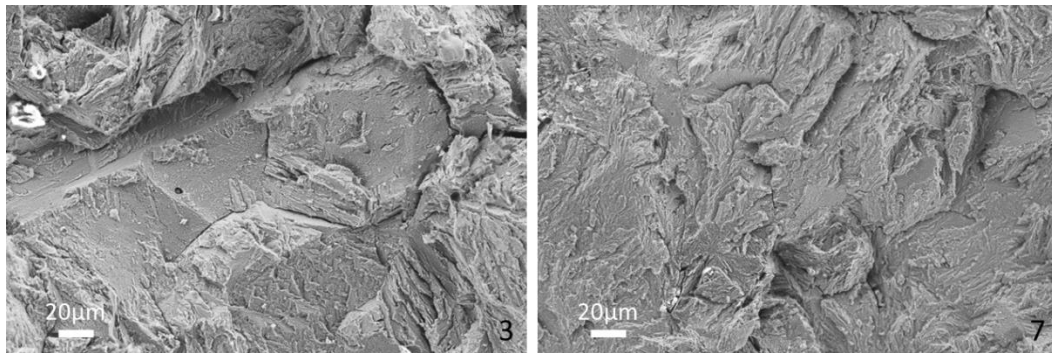


Figure 203 - Evolution of the fracture surface with the H₂S partial pressure in the high pH domain (pH=3.5) in presence of 600ppm of chlorides and at a strain rate of 10⁻⁷s⁻¹ showing that the proportion of intergranular areas is decreasing with decreasing H₂S content (1 bar H₂S, left and 0.1 bar H₂S, right)

The decrease of the hydrogen fugacity due to the reduction of the H₂S partial pressure favors the transgranular mode of cracking as shown in Figure 203 (34.9±0.6% and 17.1±2.1% of intergranular areas respectively). However, this effect is not visible on the cracks analyzed by EBSD following interrupted tests (Figure 204). Indeed, in these shorter tests, only a very limited amount of small cracks was observed, majority of them being transgranular.

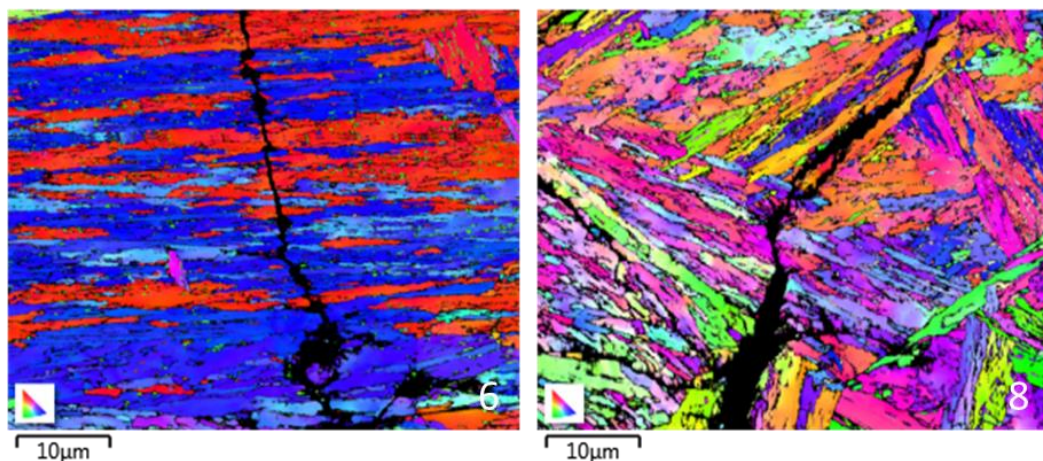


Figure 204 - EBSD maps on polished cross-sections after interrupted SSRT tests in conditions 6 and 8 (1 bar H₂S, left and 0.1 bar H₂S, right) showing fully transgranular propagation

Higher partial pressures of H₂S (up to 2bar) were tested on Virgo™38 during dead weight tests. The principal results of these tests are presented in Appendix 4.

As previously mentioned, the amount of diffusible and trapped hydrogen can be increased by decreasing the strain rate. In these cases (Figure 197), intergranular mode of cracking is also favored.

It is also possible to increase hydrogen induced damage by localizing the deformation. One SSRT test using a notched sample was performed in the same conditions as test 3 (i.e. 1 bar of H₂S, pH=3.5, 600ppm of chlorides, 10⁻⁷s⁻¹) in order to limit the influence of the crack initiation process by stress concentration on local pH decrease and consequently favor the analysis of the resistance of Virgo™38 to crack propagation under hydrogen embrittlement conditions. Indeed, the notch enables to localize the deformation such as it is the case at a bottom of a pit where additionally the pH is lower than close to the flat surface. The notch geometry used during this study is presented in Figure 205.

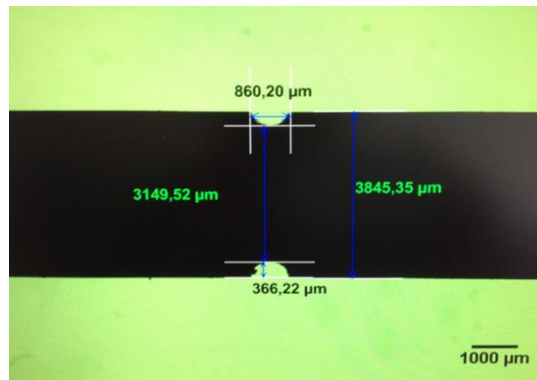


Figure 205 - Notch geometry before polishing

As expected, the reduction in area is of 0% in this case, probably due to the localization of the deformation. Indeed, in the previous cases, the reduction in area was due to the plastic deformation of remaining ligament after crack initiation. Since, in the case of a notched sample, cracks do not initiate on a cylindrical surface but at the bottom of the notch, there is no remaining ligament.

Figure 206 shows that the fracture occurs at the bottom of the notch. Furthermore, as in test 3 under the same environmental conditions, fracture occurs while the sample is still in the macroscopically passive state.

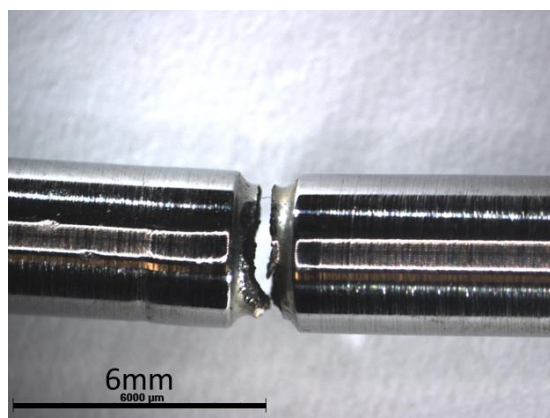


Figure 206 - Optical micrographs of barrel surfaces after SSRT on the notched samples showing that the fracture occurs inside the notch

As previously observed after the SSRT in condition 3, the fracture mode is mixed intergranular and transgranular as visible in Figure 207.

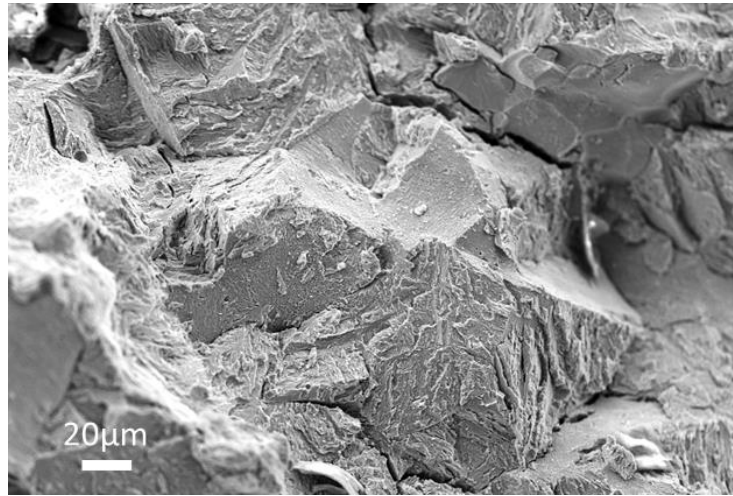


Figure 207 - Fracture surface obtained after SSRT on a notched sample tested under 1 bar of H₂S, in presence of 600ppm of chlorides at pH=3.5 and at a strain rate of 10⁻⁷ s⁻¹ showing a mixed intergranular / transgranular fracture

As expected, the proportion of intergranular fracture increases to 40.1±0.5% against 34.9±0.6% in a smooth sample. This observation confirms that hydrogen favors intergranular fractures.

Finally, grain boundary composition is also influencing crack propagation mode. To study this influence, we decided to perform a SSRT test on the Cover in the same conditions as test 3 (i.e. 1 bar of H₂S, pH=3.5, 600ppm of chlorides, 10⁻⁷ s⁻¹). The same sample geometry (reduced NACE tensile specimen) as described in the first part of this chapter was used. The material used is the same as described in Chapter IV (Table 26).

The ratio of area reduction (Z% factor) measured in this case was of 0%.

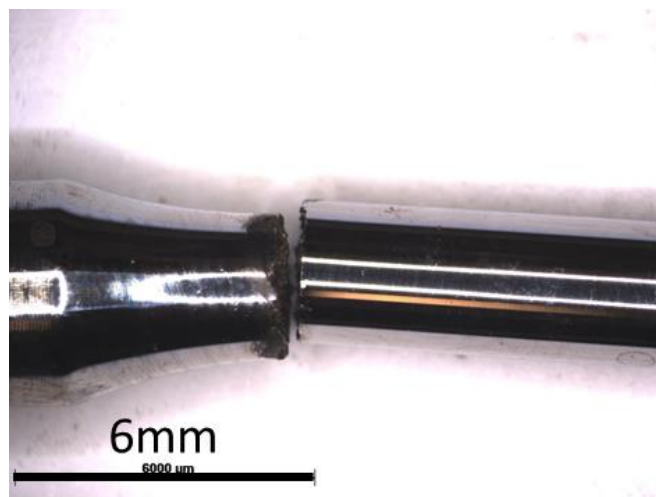


Figure 208 - Optical micrographs of barrel surfaces after SSRT test on the Cover sample showing some corrosion products on the fracture surface

As for all the tests in the 'high' pH domain, fracture occurs due to local defects and the passive film remains stable at the other locations on the barrel surface (Figure 208).



Figure 209 - Fracture surface obtained after SSRT test on the Cover sample tested under 1 bar of H₂S, in presence of 600ppm of chlorides at pH=3.5 and at a strain rate of 10⁻⁷s⁻¹ showing a fully intergranular fracture

Contrary to the test in the same conditions performed on the properly heat treated specimens of Virgo™38 (impeller test 3), Figure 209 reveals a fully intergranular fracture on the Cover (93.4±0.9% vs 34.9±0.6% for the impeller in the same conditions). Furthermore, several secondary cracks are visible on the intergranular facets. As concluded in Chapter IV, the extreme brittleness of the Cover component is due to a synergy between Phosphorous Grain Boundary Segregation (PGBS) and the high hydrogen activity encountered in H₂S containing environments.

The intergranular mode of propagation on the Cover is confirmed by the EBSD observations performed on secondary cracks as visible in Figure 210.

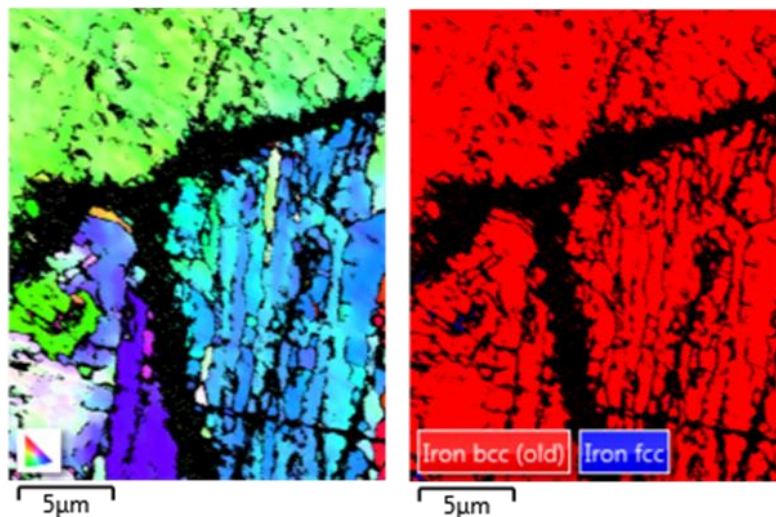


Figure 210 - EBSD maps on polished cross-section after SSRT test on the Cover showing an intergranular mode of crack propagation coupled with intense dissolution and the very low retained austenite content

To summarize, we have experimentally shown that the increase of hydrogen content within the material (by increasing the duration of the tests or by increasing the H₂S partial pressure) favors intergranular crack propagation. As the life duration of machine is long as compared to the duration of SSRT tests, it is not surprising to observe intergranular failures in service. In the following, we will propose a mechanism of hydrogen embrittlement based on the HEDE mechanism presented in Chapter I that can explain intergranular failures.

As in Chapter IV, the proposed mechanism is mainly the HEDE mechanism coupled with the transportation of H by dislocations. Furthermore, interactions between hydrogen and dislocations may contribute to localize plasticity and increase stress concentration at the dislocation pile-ups against grain boundaries (HELP). In the case of a rapid test or a low hydrogen fugacity, the fracture will occur on lath interfaces due to the low hydrogen content. If the test is longer and if the amount of hydrogen in retained austenite is higher, its transformation coupled with the hydrogen diffusion short-circuits will lead to intergranular failure. These hypotheses are schematically represented in Figure 211.

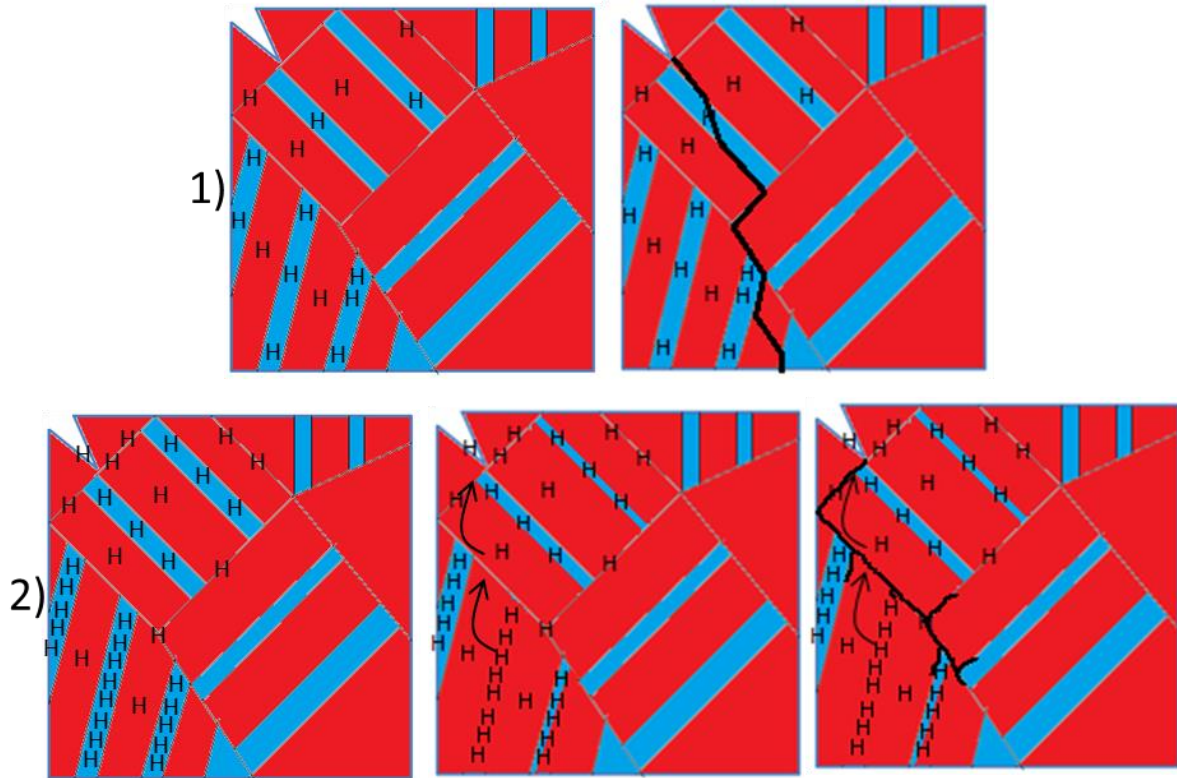


Figure 211 - Schematic representation of the proposed mechanisms of crack propagation assisted by H:

- 1) if hydrogen content is low (low fugacity or rapid test), austenite transformation at crack tip will release a limited amount of hydrogen to former austenitic grain boundaries which will be not harmful enough and failure will occur along the closest interfaces encountered: crack propagation is mainly transgranular.
- 2) if hydrogen content is high (higher fugacity or longer test), austenite transformation at crack tip will release an important amount of hydrogen to former austenitic grain boundaries, in fact hydrogen in oversaturation in freshly formed martensite will try to “escape” and diffuse along diffusion short-circuit (typically former austenitic grain boundaries). The high hydrogen content in grain boundaries coupled with PGBS will decrease the cohesive energy and facilitate grain boundary opening: crack propagation is mainly intergranular.

These two propagation mechanisms may be related to the duration of test (longer time under static charge or at lower strain rate in SSRT tests), which impacts the amount of hydrogen within the microstructure. In both cases, we consider that the crack is already initiated (see later) and we focus only on its propagation.

In the case of a rapid test, the amount of hydrogen inside the material is low at the moment when the crack propagates; the retained austenite is thus not saturated in hydrogen. The large local strains achieved at the crack tip induces the transformation of retained austenite to martensite (SIMT, see Chapter II) and a release of hydrogen in the martensite. As the hydrogen content in retained austenite was low, we can consider that there is no hydrogen oversaturation in the newly

formed martensite. There is thus no supplementary driving force for hydrogen diffusion. According to the HEDE mechanism, the newly formed martensite will fail leading to a mainly transgranular failure.

In the case of a longer test (or a more hydrogenative environment), we can consider that retained austenite is saturated in hydrogen. Its transformation at the crack tip by SIMT will induce an oversaturation of hydrogen in the newly formed martensite. There is thus a driving force for hydrogen diffusion (escaping martensite). Hydrogen will quickly diffuse out of the specimen by the diffusion short-circuit: mainly interlaths and former austenitic grain boundaries. The diffusion of hydrogen to former austenitic grain boundaries coupled with the PGBS lead to a decrease of the cohesive energy of the grain boundary. According to the HEDE mechanism presented in Chapter IV, intergranular failure will occur in this case.

4. Conclusions

As expected for the environmental conditions analyzed in this chapter, namely high H₂S pressure and pH<4, a severe embrittlement was observed in all SSRT tests. Cracks systematically initiated within the macroscopically elastic domain, even at a highest pH of 4.0. The influence of four main parameters, namely: pH, H₂S partial pressure, strain rate and chloride content were studied with respect to the behavior of Virgo™38. Several mechanisms of crack initiation and propagation were identified.

For pH higher than 3.0, i.e. above pH_D even under mechanical loading, crack initiation occurs on metastable pits or on mechanical defects present at the surface. Fracture surfaces are not affected by corrosion under these high pH conditions. The fracture mode is mixed with higher proportion of transgranular facets, probably through interfaces between packets and blocs of martensite laths. The density of secondary cracks clearly increases with decreasing pH. The mechanism leading to failures at pH>3.0 was identified as Hydrogen Embrittlement (HE).

For pH 1.5 and 2.0 in absence of chlorides (only a limited amount is present due to the addition of HCl) and for pH 2.5 in presence of chlorides, the material is active, i.e. below pH_D for both phases. Cracks initiate very quickly inside corrosion defects on the surface like preferential dissolution of either retained austenite or martensite, depending on both the pH of the solution and the depth of the secondary cracks. In these cases, generalized corrosion with galvanic coupling between phases was identified as the preferential mechanism (ASCC).

The dependency of the area reduction to the strain rate clearly confirmed the existence of these two different mechanisms involved in the embrittlement of Virgo™38. In fact, at very low pH (below 3.0) (which is not part of the actual application range of SMSS) Virgo™38 is susceptible to Anodic Stress Corrosion Cracking (ASCC) mechanism where dissolution rate increases with decreasing pH. The corrosion rates achieved under these conditions are much more important than the ones presented in Chapter III, consequently very strong embrittlement was observed. At 'high' pH dissolution is prevented, however material remains very brittle due to HE as postulated above.

In this Hydrogen Embrittlement domain, it was also shown that increasing the H₂S partial pressure leads to a decrease of the cracking resistance of Virgo™38. This decrease is associated with the increasing hydrogen activity in presence of H₂S only if it can enter the material. Indeed, if the passive film is stable enough to prevent hydrogen entrance, cracking is not supposed to occur. It was demonstrated that Virgo™38 can pass constant load tests even in 2bar of H₂S (appendix 4) if the load applied and the chloride content are sufficiently low and if pH is sufficiently high to prevent depassivation. The influence of the H₂S partial pressure has not been analyzed in the ASCC domain.

We observed that chlorides have a strong influence on both HE and ASCC resistance. Indeed, chlorides are responsible for pitting corrosion that enables hydrogen entry. We have seen that the two phase structure of Virgo™38 lead to the preferential localization of pit initiation on retained austenite. However, pits can also initiate on intermetallic particles such as titanium carbide.

All the results gathered enable to define areas of predominant crack initiation and propagation mechanisms (Figure 212).

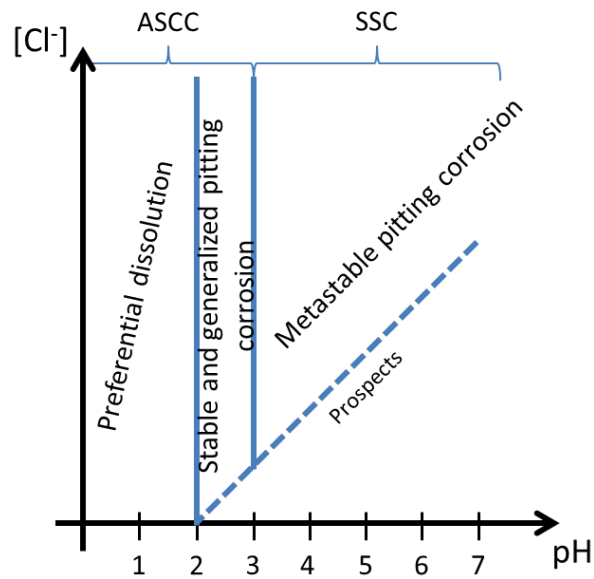


Figure 212 - Schematic representation of crack initiation and propagation mechanisms observed on Virgo™38 after SSRT tests under 1 bar H₂S

As a perspective, we can mention that several electrochemical measurements and SSRT tests with varying chloride content and pH must be realized in order to clearly define the missing frontier.

Our results confirms that Virgo™38 must be used in the (beginning of the) elastic domain and that local plasticization can be dangerous. Moreover, the passivity of Virgo™38 must be reinforced either by deposition or by readjusting the global chemical composition (by adding Mo for example). At higher pH (higher than 3.0), we confirmed that Virgo™38 is susceptible to Hydrogen Embrittlement (HE) as it was observed in the few industrial failures and as presented in Chapter IV.

General conclusions

The main objective of this PhD work was to identify the mechanisms involved during industrial failures of Virgo™38 in Oil & Gas applications and, more generally, to discuss the pertinence of all possible mechanisms that potentially reduce its resistance to Environmentally Assisted Cracking. To do it, we aimed to generate environmentally assisted cracking of Virgo™38 in conditions of Stress Corrosion Cracking (SCC) involving anodic phenomena and of Hydrogen Embrittlement (HE) involving cathodic phenomena. Three different types of environments were used, namely: H₂S containing environments close to in-field ones, in which both SSC and ASSC were investigated, a very acid environment supposed to generate damage through SCC and a poisoned basic environment in which HE was considered as the principal factor of material degradation.

Before analyzing the behavior of Virgo™38 in environments supposed to produce environmentally assisted cracking, its microstructure in microstructural states obtained through tempering at different temperatures and its tensile properties in air were investigated. The microstructure of the industrially treated grade is composed of tempered lath martensite ($\alpha'' \approx 75\%$) and 22-24% of retained austenite (γ_R), situated between α'' laths. It also contains less than 1% of fine M₂₃C₆ carbide particles of approximately 20nm diameter, according to both TEM observations and Thermocalc calculations. Quantitative EDX-TEM analyses demonstrate the partitioning of alloying elements, mainly of Ni, between FCC and BCC phases. This effect is responsible for modifying the stability conditions of austenite during tempering and allows obtaining microstructures with different retained austenite contents.

In the second step, the effect of tempering temperature on the phase composition and tensile properties of Virgo™38 was studied after a full 'reset' of the 'industrial' microstructure through re-austenitization and sub-zero quenching. This pre-treatment produces a quasi-single phase martensitic (α') microstructure containing a limited volume fraction of δ -ferrite. However, even a fast cooling from the austenitization temperature does not allow avoiding segregation of elements like Si to austenite grain boundaries before martensitic transformation sets off. This leads to a significant local decrease of M_s point whose potential consequence is that a thin ribbon of residual austenite might remain around grain boundaries after quenching. The fact that "prior" austenite grain boundaries might in fact be real ones would have decisive impact on segregation phenomena during tempering and on the cracking behavior in corrosive environments. However, the experimental evidence collected from HR-TEM observation is too scarce to confirm this assumption and further investigation is necessary.

EBSD and XRD analyzes were applied to study the effect of tempering temperature on the microstructure of Virgo™38. The observations realized were correlated with the results of tensile tests. We then applied classic models of crystal strengthening to estimate the dominating mechanisms and individual elastic limits of principal phases, as a function of tempering temperature. The results may be summarized as follows:

After tempering at 'low' temperatures (500°C and 580°C), 0.01% yield stress increases as compared with the quenched microstructure. We demonstrated, using Thermocalc and Prisma simulations that a fine dispersion of M₂₃C₆ carbide is responsible for the strengthening observed. Tempering at 620°C produces the maximal amount of retained austenite (γ_R) and a significant decrease of 0.01% yield stress as compared with tempering at lower temperatures. The size of M₂₃C₆ precipitates is now too high to produce any significant strengthening. At 'high' tempering temperature (660°C), the reverted austenite is not stable with respect to martensitic transformation above room temperature and secondary fresh martensite is formed, while the retained austenite content decreases. This microstructural evolution results in a limited increase of 0.01% yield stress which remains much

lower than that observed after 'low' temperature tempering.

The principal conclusion of the analysis of strengthening mechanisms is that retained austenite, if present, is the 'hard' phase as compared with tempered nearly carbon-free martensite, and that its intrinsic elastic limit is comparable with that of fresh martensite. This result is opposite to most suggestions proposed in the literature which are generally not supported by convincing arguments. The combination of minimal required yield stress and maximal hardness allowed in the 'industrial' microstructure of Virgo™38 is thus due to the mixture of a 'soft' phase which is tempered martensite and a 'hard' one which is retained austenite. Under applied charges close to 0.2% proof stress and more, plastic straining will thus undoubtedly start in the BCC phase, while the other one will remain in the elastic domain. This behavior may be decisive with respect to crack initiation and propagation in corrosive environments. It also allows interpreting why stress induced martensitic transformation (SIMT) of retained austenite starts at high stresses (700MPa) and is difficult to complete (at 10% elongation corresponding to UTS, 50% of austenite remain untransformed) although M_s is close to room temperature.

Once the metallurgy of our alloy understood, a detailed electrochemical study has been performed, which enabled us to determine the depassivation pH of both constitutive phases of Virgo™38. It has been demonstrated that retained austenite depassivates for higher pH than tempered martensite (1.6 against 1.5). This difference was attributed to the different oxide layers resulting from the different Cr contents of both phases. This study has also been performed under constant load and the influence of the mechanical stress on the depassivation was determined. Both depassivation pH and dissolution rates increased due to the applied loading.

The previous electrochemical study enabled us to precisely choose the potentials to be applied during cracking tests in acid environment under applied potential. We had chosen to limit our study to Slow Strain Rate Tensile tests (SSRT) as these tests allow studying both crack initiation and propagation. Indeed, these tests are known to reproduce cracking phenomena that occur in service and enable to observe crack propagation through the study of secondary cracks. However, as Virgo™38 is a very resistant alloy, it was difficult to reproduce in service failure by HE in this acid environments and it was necessary to drastically decrease the pH in order to achieve intergranular failures such as the ones observed industrially. The SCC behavior was also determined by applying constant potentials corresponding to the activity potentials of both constitutive phases such as determined after the electrochemical study. They showed a limited embrittlement as compared to what is observed during HE tests.

Following the conclusions of the previous section, a more severe environment had to be developed in order to generate material embrittlement and consecutive failure modes similar to those observed in industrial conditions. This new environment was designed with the help of permeation tests which showed that applying a cathodic potential in a basic environment containing a recombination inhibitor (such as Na_2S) enabled reaching hydrogen activities comparable to those obtained in presence of H_2S . The increase of hydrogen activity in this solution was attributed to the thermodynamic stability of adsorbed sulfur at the sample surface between -600mV/SCE and -1400mV/SCE, this element being known to facilitate hydrogen entry by blocking its recombination.

SSRT tests realized in the Na_2S -containing environment led to fully intergranular failure of Virgo™38 and made possible studying of crack propagation mechanisms. According to literature, the most plausible mechanism of HE of Virgo™38 is the HEDE mechanism. Tests realized on samples with different microstructures, obtained by varying the tempering temperature, showed that

microstructure had a significant impact on the resistance to HE. In particular, retained austenite had a beneficial effect, at least up to a certain level, close to 15% in our case. Beyond this amount, the mechanical instability of retained austenite led to a reduction of Virgo™38 resistance. This reduction was attributed to the release of the hydrogen trapped inside austenite during its transformation into the newly formed fresh martensite and its diffusion towards former austenitic grain boundaries. Hydrogen, however, is not the only element potentially responsible for intergranular failure of Virgo™38. Auger Electron Spectroscopy (AES) analyzes demonstrated that phosphorous segregation up to 10% of a monolayer at former austenitic grain boundaries is possible. This can lead to a reduction of the cohesion energy and facilitate grain boundary opening and intergranular failures. This effect was identified to be particularly damaging at tempering temperatures around 500°C, which are much lower than those applied in industrially applied cycles of heat treatment of Virgo™38.

In presence of H₂S, two crack initiation mechanisms were evidenced, namely: crack initiation by pitting corrosion at elevated pH (higher than 3.0) and general corrosion following chemical depassivation for lower pH. Indeed, for pH lower than 3.0 (i.e. below the estimated depassivation pH of Virgo™38 in presence of 1 bar H₂S), cracks initiate on corrosion defects formed by preferential dissolution of either retained austenite (at intermediate pH down to 2.0) or tempered martensite (at lower pH). As demonstrated in chapter III, the galvanic coupling between both phases due to the partitioning effect of alloying element was identified as responsible for crack initiation in this very low pH domain. On the contrary, at pH higher than the depassivation pH, namely at pH higher than 3.0, the crack initiation mechanism is pitting corrosion. Once again, it was identified that composition differences between retained austenite and tempered martensite lead to the formation of pits at the surface of retained austenite. However, in the case of pitting corrosion, inclusions such as titanium carbides were identified as more detrimental than retained austenite.

SSRT tests with varying strain rates performed in presence of H₂S, confirmed that both SSC and SCC mechanisms occurred in Virgo™38. The frontier between these two mechanisms of crack propagation was determined to be at pH=3.0. At low pH (lower than 3.0), Virgo™38 exhibited a susceptibility to Anodic SCC with high corrosion rates compared to those identified in chapter III. At higher pH, the mechanism of crack propagation involved hydrogen effects. It was demonstrated that, as expected in chapter IV, increasing the hydrogen activity led to a decrease of the cracking resistance of Virgo™38 providing that hydrogen effectively enters in the material.

For further investigations, it would be necessary to establish a precise relationship between retained austenite content and the elastic limit, in order to confirm definitely that γ_R is the 'hard' phase in tempered Virgo™38, with respect to α' . This could be done by realizing heat treatments with different holding times at 620°C, in order to vary the retained austenite content, and through consecutive tensile tests. The problem with such methodology is that the tempered martensite formed in these different states will not have the same properties as its tempering will be different, potentially masking the effect of retained austenite. Another solution would be to produce model single phased alloys with the same compositions as determined in Chapter II and the same dislocation densities in order to perform relevant tensile tests.

Further HR-TEM analyzes quenched martensitic Virgo™38 would definitely demonstrate the presence of residual austenite close to former austenite grain boundaries after sub-zero heat treatment. Another solution would be to perform metallographic etching to reveal potential residual austenite on the industrially quenched and sub-zero treated Virgo™38, the industrial sub-zero heat

treatment temperature probably being under the global M_F temperature but certainly higher than the local M_F temperature of the Si-enriched areas. This etching would then be compared to the one performed in a quenched a sub-zero treated in liquid nitrogen (-196°C) state, where sub-zero treatment temperature will obviously be lower than the M_F temperature, even in Si-enriched areas.

The galvanic coupling evidenced in chapter III must also be further studied in larger structures by producing, for example, model single phased alloys with the same compositions and the same dislocation densities as determined in Chapter II. Such model materials would also enable us studying the composition, thickness and relative organization of the passive layers at the surface of both tempered martensite and retained austenite as supposed in chapter III.

Furthermore, we expected an influence of the hydrogen activity on the cracking mode in the domain where hydrogen embrittlement of Virgo™38 is dominant. To justify this hypothesis, it can be possible to perform SSRT tests in different poisoned solutions as presented in chapter IV with varying amount of Na_2S , the hydrogen activities being determined by subsequent permeation tests, or with varying strain rates. Hopefully, we would conclude on a decrease of the IG mode of cracking for the benefit of transgranular mode of cracking with a decreasing hydrogen activity. The hydrogen activities determined in the different environments would be compared to the ones obtained in presence of H_2S that must be determined in turn by permeation tests.

An important hypothesis advanced in chapter IV is that tempering of martensite plays an important role (maybe even more important than the one of retained austenite) on the resistance to hydrogen embrittlement of SMSS. In fact, the beneficial effect of tempering treatment attributed to the presence of retained austenite could be only a beneficial effect of a more efficient tempering of martensite at higher temperatures. In this case, the decrease of the elongation observed after treatments at temperatures higher than the peak of retained austenite would not be due to the reduction of the retained austenite content but rather to the formation of fresh martensite. To prove this second hypothesis, it could be possible to produce a model single phased martensitic alloy with the same compositions and dislocation densities and to perform SSRT tests in poisoned solution after different tempering treatments (without forming retained austenite), and to hopefully show that the resistance is constantly increasing with the tempering of martensite. If this is effectively the case, improving actual Virgo™38 resistance could be done by increasing the tempering temperature. However, the risk would be not to satisfy mechanical properties due to a lack of retained austenite, which is supposed to ensure mechanical properties if it is effectively harder than tempered martensite. Forming as many retained austenite as presently by tempering at higher temperature could be possible by increasing the A_{c1} temperature by adding Mo or Cr in the alloy for example. Another solution would be to first temper Virgo™38 beyond the peak to improve tempering of martensite and then to temper it at the peak in a second time in order to both temper the newly formed fresh martensite and to form the required volume of retained austenite to ensure required mechanical properties of the alloy.

Finally, to improve the resistance of Virgo™38 in H_2S -containing environments, it is necessary to increase the stability of its passive film to both pitting corrosion and chemical depassivation. The easiest way to improve pitting corrosion is to reduce the amount of inclusions such as titanium carbides or nitrides.

Bibliography

- [1] H. Marchebois, J. Leyer, and B. Orleans-Joliet, "SCC Performance of a Super 13%Cr Martensitic Stainless Steel for OCTG: Three-Dimensional Fitness-For-Purpose Mapping According to PH₂S, pH and Chloride Content," *NACE*, 2007.
- [2] J. Reza, C. Nwaoha, and H. Tan, *Corrosion and Materials in the Oil and Gas Industries, Book*, 721p. 2016.
- [3] "Petroleum and natural gas industries - materials for use in H₂S containing environments in oil and gas production," *North Am. Corros. Eng. Stand.*, 2015.
- [4] J. Ramon and D. Mainy, "Expertise sur roue de compresseur KGB Lacq fissurée en service, internal document," 2004.
- [5] P.I. Nice, J.W. Martin, "Application limits for super martensitic and precipitation hardened stainless steel bar stock materials," *NACE*, 2005.
- [6] F. Millet, "Le Virgotm38 ou l'expertise du Creusot au niveau Mondial," in *Conférence à l'académie François Bourdon, Le Creusot*, 2011.
- [7] B. Hoerner, "Corrosion sous contrainte de l'acier inoxydable supermartensitique 12chrome 4. 5nickel 1. 5molybdène dans un milieu sans sulfure d'hydrogène, PhD thesis," Saint-Etienne, Ecole Nationale Supérieure des Mines, 2007.
- [8] P. Cunat, "Propriétés . Résistance à la Aciers inoxydables Propriétés . Résistance à la corrosion," *Tech. l'ingénieur M4541*, vol. 33, no. 0, 2000.
- [9] H. J. Niedereau, "A new low-carbon 16Cr-5Ni stainless martensitic cast steel," in *Stainless Steel Castings, ASTM STP 756, V. G. Behal and A. S. Melilli Eds. , American Society for Testing and Materials*, 1982, pp. 382–393.
- [10] E. Taban, E. Kaluc, and O. O. Ojo, "Properties, weldability and corrosion behavior of supermartensitic stainless steels for on- and offshore applications," *Mater. Test.*, vol. 58, no. 6, pp. 501–518, Jun. 2016.
- [11] G. Murry, "Transformations dans les aciers," *Tech. l'ingénieur M1115*, pp. 1–5, 2013.
- [12] L. Yahia, "Etude de la corrosion localisée par piqûres des aciers inoxydables 304L et 430 : effet de la déformation à froid par traction et laminage, PhD thesis," Université Constantine 1, 2013.
- [13] P. Cunat, "Aciers inoxydables - Critères de choix et structure," *Tech. l'ingénieur M4540*, 2000.
- [14] B. Appolaire, "Diagrammes de phases 4 aciers inoxydables," *Cours Univ. Lorraine*, 2005.
- [15] P. Lacombe, B. Baroux, and G. Beranger, *Les aciers inoxydables, book*. 1990.
- [16] F. Campbell, *Elements of Metallurgy and Engineering Alloys, book*, 637p. 2008.
- [17] C. Rodrigues, J. Pagotto, A. Motheo, and G. Tremiliosi-Filho, "The effect of titanium on pitting corrosion resistance of welded supermartensitic stainless steel," *Corros. Eng. Sci. Technol.*, vol. 52, no. 2, pp. 1–8, 2016.
- [18] A. Schaeffler, "Constitution diagram for stainless steel weld metal," *Met. Prog.*, vol. 56, p. 680–680B, 1949.
- [19] D. Harries, "Physical metallurgy of Fe-Cr-Ni austenitic steels," *Mech. Behav. Nucl. Appl. Stainl. steel Elev. Temp.*, vol. 14, no. 22, pp. 1–25, 1982.

- [20] N. Suutala, "Effect of manganese and nitrogen on the solidification mode in austenitic stainless steel welds," *Metall. Trans. A*, vol. 13A, pp. 2121–2130, 1982.
- [21] P. Lacombe and G. Beranger, "Structure et diagrammes d'équilibre des divers nuances d'aciers inoxydables : conséquences sur leur traitements thermiques," *Les éditions la Phys.*, pp. 13–58, 1990.
- [22] T. Gooch, P. Woolin, and A. Haynes, "Welding of low carbon 13%Cr martensitic steels," in *Supermartensitic stainless steels '99, Brussel*, 1999.
- [23] J. Guimaraes and V. Werneck, "The effects of strain rate, grain size and temperature on the yield stress of a metastable austenite," *Mater. Sci. Eng.*, vol. 34, pp. 87–90, 1978.
- [24] M. R. Berrahmoune, "Transformation martensitique et rupture différée dans l'acier austénitique instable 301LN, PhD thesis," Metz, ENSAM, 2006.
- [25] C. Wayman and H. Bhadeshia, *Phase transformations, nondiffusive, book*, Physical M. Amsterdam, The netherlands: Elsevier Science Publishers, 1996.
- [26] K. Irvine, D. Crowe, and F. Pickering, "The physical metallurgy of 12% chromium steels," *J. Iron Steel Inst.*, pp. 386–405, 1960.
- [27] J. Stolarz, "Influence of Silicon, Carbon and Phosphorus on Intergranular Corrosion of High Purity Austenitic Stainless Steels Under Transpassive Conditions," *J. Phys. iV*, vol. 5, pp. 423–428, 1995.
- [28] M. Léger, "Aciers moulés inoxydables martensitiques à 13% Cr," in *Revue de la métallurgie*, 1993.
- [29] J. Talonen, "Effect of Strain-Induced Transformation on mechanical properties of metastable austenitic stainless steels, PhD thesis," Helsinki University, 2007.
- [30] J. R. Patel and M. Cohen, "Criterion for the action of applied stress in the martensitic transformation," *Acta Metall.*, vol. 1, pp. 531–538, 1953.
- [31] T. Angel, "Formation of Martensite In Austenitic Stainless Steel," *J Iron Steel Inst.*, vol. 177, pp. 165–174, 1954.
- [32] J. Stolarz, "Effect of microstructure on martensitic transformation mechanisms in a cyclically strained high purity austenitic steel," *Solid-Solid phase Transform. Inorg. Mater. - TMS*, 2005.
- [33] A. Das, P. Chakraborti, S. Tarafder, and H. Bhadeshia, "Analysis of deformation induced martensitic transformation in stainless steels," *Mater. Sci. Technol.*, vol. 27, no. 1, pp. 366–370, 2011.
- [34] N. Baffie and J. Stolarz, "Influence of strain-induced martensitic transformation on fatigue short crack behavior in an austenitic stainless steel," *Matériaux Tech.*, vol. 5, no. 6, p. 57, 2000.
- [35] S. Hwan Bak, M. Abro, and D. Lee, "Effect of hydrogen and Strain-Induced Martensite on mechanical properties of AISI 304 stainless steel," *Metals (Basel)*, vol. 6, p. 169, 2016.
- [36] D. Porter and K. Easterling, *Phase transformations in metals and alloys, book*, 509p. 1993.
- [37] E. Deleu, A. Dhooge, and J. Dufrane, "Weldability and hot deformability of different supermartensitic stainless grades by weld simulation testing - paper n°27," in *International conference of Supermartensitic stainless steels 99*, 1999, pp. 232–240.
- [38] "Petroleum and natural gas industries - Materials for use in H₂S-containing

- environments in oil and gas production - Part 3: Cracking-resistant CRAs (corrosion-resistant alloys) and other alloys,” 2015, p. 28.
- [39] C. Gayton, C. Bosch, A. Rozinoer, F. Millet, K. Wolski, and J. Stolarz, “Effect of first tempering temperature on the amount of reversed and retained austenite in Virgo™ 38, a 16Cr-4Ni low-carbon super- martensitic stainless steel,” *Proc. Eurocorr*, 2015.
- [40] Y. L. Y. Song, X. Li, L. Rong, “The influence of tempering temperature on the reversed austenite formation and tensile properties in Fe–13%Cr–4%Ni–Mo low carbon martensite stainless steels,” *Mater. Sci. Eng. A*, no. 528, p. 4075–4079., 2011.
- [41] G. F. Lovicu, M. De Sanctis, R. Valentini, A. Dimatteo, R. Ishak, U. Migliaccio, R. Montanari, and E. Pietrangeli, “Influence of presence and stability of reverted austenite on mechanical properties of 16Cr-5Ni supermartensitic stainless steel after tempering treatment,” *La metallurgia italiana n°9*, 2013.
- [42] D. Lopez, T. Perez, and S. Simison, “The influence of microstructure and chemical composition of carbon and low alloy steels in CO2 corrosion. A state of the art appraisal,” *Mater. Des.*, vol. 24, no. 8, pp. 561–575, 2003.
- [43] P. Wang, N. Xiao, S. Lu, D. Li, and Y. Li, “Investigation of the mechanical stability of reversed austenite in 13%Cr–4%Ni martensitic stainless steel during the uniaxial tensile test,” *Mater. Sci. Eng. A*, vol. 586, pp. 292–300, Dec. 2013.
- [44] M. Giannozzi, L. Baldassarre, M. Cecconi, M. Camatti, D. Becherucci, X. Coudray, and C. Puaut, “About design, materials selection and manufacturing technologies of centrifugal compressors for extreme sour and acid service,” in *ADIPEC conference*, 2013.
- [45] T. G. Gooch, P. Woollin, and Haynes A., “Welding metallurgy of low carbon 13%chromium martensitic steels,” in *Supermartensitic Stainless Steel*, 1999.
- [46] D. Thibault, P. Bocher, M. Thomas, J. Lanteigne, P. Hovington, and P. Robichaud, “Reformed austenite transformation during fatigue crack propagation of 13%Cr–4%Ni stainless steel,” *Mater. Sci. Eng. A*, vol. 528, no. 21, pp. 6519–6526, Aug. 2011.
- [47] F. Ford and P. Anderssen, *Proceedings of the 3rd International Symposium on the environmental degradation of materials in nuclear power systems: water reactors, book*. Metallurgical Society, 1988.
- [48] R. Staehle, “Stress corrosion cracking of the Fe-Cr-Ni alloy system,” *theory Stress Corros. Crack. Alloy.*, p. 223, 1971.
- [49] J. Charles, “Some recent developments in Lean Duplex grades,” in *SSW 2013 Maastricht*, 2013.
- [50] J. Jonsson, “The two phased optimization of duplex stainless steels,” in *SSW 2013 Maastricht*, 2013.
- [51] P. R. Rhodes, “Mechanism of Chloride Stress Corrosion Cracking of Austenitic Stainless Steels,” *Corrosion*, vol. 25, pp. 462–472, 1969.
- [52] F. Ruel, D. Tite, A. Gaugain, S. Saedlou, and K. Wolski, “On the Depassivation Mechanism of Lean Duplex Stainless Steels and the Influence of the Partitioning of the Alloying Elements,” *Corros. Sci.*, vol. 9312, no. June, pp. 636–642, 2014.
- [53] I.-H. Lo and W.-T. Tsai, “Effect of selective dissolution on fatigue crack initiation in 2205 duplex stainless steel,” *Corros. Sci.*, vol. 49, no. 4, pp. 1847–1861, Apr. 2007.
- [54] I. Serre, D. Salazar, and J.-B. Vogt, “Atomic force microscopy investigation of surface

- relief in individual phases of deformed duplex stainless steel,” *Mater. Sci. Eng. A*, vol. 492, no. 1–2, pp. 428–433, Sep. 2008.
- [55] N. Mary, V. Vignal, R. Oltra, and L. Coudreuse, “Finite-element and XRD methods for the determination of the residual surface stress field and the elastic-plastic behavior of duplex steels,” *Philos. Mag.*, vol. 85, no. 12, pp. 1227–1242, 2005.
- [56] V. Richoux, H. El Alami, C. Millet, H. Evin, and G. Néel, “Influence of solution buffering on corrosion resistance of super martensitic stainless steels,” in *Eurocorr, Praha*, 2017.
- [57] P. Rhodes, “Stress cracking risks in corrosive oil and gas wells - paper n°322,” in *Corrosion Nace 86*, 1987.
- [58] H. Miyuki, J. Muraynama, T. Kudo, and T. Moroishi, “Localized corrosion of duplex stainless steels in Co₂-H₂S-Cl⁻ environments at elevated temperatures,” *Corros.* 84, 1984.
- [59] P. Marcus, “Sulfur-assisted corrosion mechanisms and the role of alloyed elements,” *Corros. Mech. theory Pract.*, pp. 239–263, 1995.
- [60] P. Marcus, A. Teissier, and J. Oudar, “The influence of sulphur on the dissolution and the passivation of a nickel-iron alloy - I electrochemical and radiotracer measurements,” *Corros. Sci.*, vol. 24, no. 4, pp. 259–268, 1984.
- [61] R. Parsons, “General equations for the kinetics of electrode processes,” *Trans. Faraday Soc.*, vol. 47, pp. 1332–1344, 1951.
- [62] J. Bockris and H. Mauser, “The kinetics of the evolution and dissolution of hydrogen at electrodes,” *Can. J. Chem.*, vol. 37, no. 2, pp. 475–488, 1959.
- [63] E. Protopopoff and P. Marcus, “Surface effects on hydrogen entry into metals,” *Corros. Mech. theory Pract.*, vol. 2nd ed, pp. 53–96, 2002.
- [64] J. Crolet, “Re-interpretation of the measurements of hydrogen permeation,” *La Rev. la métallurgie*, vol. 98, no. 5, pp. 501–518, 2001.
- [65] V. Olden, C. Thaulow, and R. Johnsen, “Modelling of hydrogen diffusion and hydrogen induced cracking in supermartensitic and duplex stainless steels,” *Mater. Des.*, vol. 29, no. 10, pp. 1934–1948, Dec. 2008.
- [66] M. Monnot, M. Mantel, G. Berthome, V. Roche, R. Nogueira, and E. Chauveau, “Sulfide Stress Corrosion study of a super martensitic stainless steel: role of H₂S on metallic sulfur formation and hydrogen embrittlement,” in *Eurocorr, Graz*, 2015.
- [67] R. D. Kane and M. S. Cayard, “Roles of H₂S in the behavior of engineering alloys: A review of literature and experience - paper n°274,” in *Corrosion 98*.
- [68] R. Iyer, I. Takeuchi, M. Zamanzadeh, and H. Pickering, “Hydrogen sulfide effect on hydrogen entry into iron - a mechanistic study,” *Corrosion*, vol. 46, no. 6, pp. 460–468, 1990.
- [69] J. Newmann and L. Shreir, “Role of hydrides in hydrogen entry into steel from solutions containing promoters,” *Corros. Sci.*, vol. 9, no. 8, pp. 631–641, 1969.
- [70] R. Oriani, “The diffusion and trapping,” *Acta Metall.*, vol. 18, no. 1, pp. 147–157, 1970.
- [71] J. Chene and A. Brass, “Interactions hydrogène métal en relation avec le processus de corrosion sous contrainte,” in *Corrosion sous contrainte - phénoménologie et mécanismes*, 1990, pp. 159–210.

- [72] D. Jiang and E. Carter, "Diffusion of interstitial hydrogen into and through BCC Fe from first principles," *Physical Rev. B*, vol. 70, no. 6, pp. 64–102, 2004.
- [73] A. Krom, R. Loers, and A. Bakker, "Hydrogen transport near a blunting crack tip," *J. Mech. Phys. Solids*, vol. 47, pp. 971–992, 1999.
- [74] R. Hutchings, A. Turnbull, and A. May, "Measurement of hydrogen transport in a duplex stainless steel," *Scr. Metall. Mater.*, vol. 25, no. 12, pp. 2657–2662, 1991.
- [75] A. Brass and A. Chanfreau, "Accelerated diffusion of hydrogen along grain boundaries in Nickel," *Acta Mater.*, vol. 44, no. 9, pp. 3823–3831, 1996.
- [76] J. Tien, A. Thompson, I. Bernstein, and R. Richards, "Hydrogen transport by dislocations," *Metall. Trans. A*, vol. 7, no. 6, pp. 821–829, 1976.
- [77] J. Chene, "L'hydrogène dans les matériaux métalliques en relation avec les interactions plasticité-environnement," in *Plastox 2007 Mécanismes et mécanique des interactions plasticité-environnement*, 2007, pp. 131–145.
- [78] J. Donovan, "Accelerated evolution of hydrogen from metals during plastic deformation," *Metall. Trans.*, vol. 7a, no. 11, pp. 1677–1683, 1976.
- [79] J. Galland, J. Sojka, and M. Jerome, *Introduction d'hydrogène dans les aciers*, book. 2004.
- [80] A. Brass, J. Chene, and L. Coudreuse, "Fragilisation des aciers par l'hydrogène : mécanismes," *Tech. l'ingénieur M176*, 2000.
- [81] P. Sofronis and R. McMeeking, "Numerical analysis of hydrogen transport near a blunting crack tip," *J. Mech. Phys. Solids*, vol. 37, no. 3, pp. 317–350, 1989.
- [82] I. Moro, "Fragilisation par l'hydrogène gazeux d'un acier ferrito-perlitique de grade API X80, PhD thesis," Université de Toulouse, 2009.
- [83] M. A. V. Devanathan and Z. Stachurski, "The adsorption and diffusion of electrolytic hydrogen in palladium," *Proc. R. Soc. London*, pp. 90–102, 1962.
- [84] F. Vucko, "Etude expérimentale et modélisation des effets de l'hydrogène sur les propriétés mécaniques et le comportement en fatigue d'un acier à haute limite d'élasticité, PhD thesis," Saint-Etienne, EMSE, 2014.
- [85] J. Crolet, "Vers un mécanismes unifié des diverses manifestations de l'hydrogène en corrosion aqueuse des aciers," *La Rev. métallurgie*, vol. 101, no. 12, pp. 1053–1086, 2004.
- [86] F. Christien, R. Le Gall, and G. Saindrenan, "Synergetic Effect of Hardness and Phosphorus Grain-Boundary Segregation on the Ductile-to-Brittle Transition Temperature of 17-4 PH Steel," *Metall. Trans. A*, vol. 34, no. November, pp. 2483–2491, 2003.
- [87] J. Sezgin, "Mécanismes de formation des DDH - Défauts dus à l'hydrogène dans l'acier 18MND5, PhD thesis," Saint-Etienne, EMSE, 2017.
- [88] F. Ruel, "Contribution électrochimique à l'étude de la corrosion sous contrainte des aciers inoxydables lean duplex en milieu purement chlorure et sous présence de sulfure d'hydrogène, PhD thesis," Saint-Etienne, EMSE, 2014.
- [89] N. Sridhar and J. Kolts, "Effects of nitrogen on the selective dissolution of a duplex stainless steel," *Corrosion*, vol. 43, no. 11, pp. 646–651, 1987.
- [90] S. Lynch, "Progress towards understanding mechanisms of hydrogen embrittlement and stress corrosion cracking," in *Corrosion Nace*, 2007.

- [91] S. Lynch, "Mechanisms of hydrogen-assisted cracking," *Proc. Met. Forum*, vol. 2, pp. 189–200, 1979.
- [92] A. Krom, "Numerical modelling of hydrogen transport in steel, PhD thesis," TU Delft, Delft University of technology, 1998.
- [93] A. Troiano, "The role of hydrogen and other interstitials in the mechanical behavior of metals," *Trans ASM*, vol. 52, pp. 54–80, 1960.
- [94] P. R. Rhodes, "Environment-Assisted Cracking of Corrosion-Resistant Alloys in Oil and Gas Production Environments: A Review," *Corrosion*, vol. 57, no. 11, pp. 923–966, Nov. 2001.
- [95] L. Coudreuse, "Fragilisation par l'hydrogène et corrosion sous contrainte," in *Corrosion sous contrainte - phénoménologie et mécanismes*, 1990.
- [96] A. Folkhard, "Welding metallurgy of stainless steels," *Metall. Phenom. Second. Cryst. Stainl. steels weld Met.*, pp. 78–102, 1988.
- [97] Y. Park, I. Maroef, A. Landau, and O. Dl, "Retained Austenite as a Hydrogen Trap in Steel Welds," *Weld J*, pp. 27–35, 2002.
- [98] M. Watkins and R. Ayer, "Microstructure - the critical variable controlling the SSC resistance of low alloy steels - Paper n°50," in *Corrosion NACE 95*, 1995, no. 329.
- [99] E. Cabanillas, L. Terminiello, N. Cantalejos, R. Versaci, and R. Mercader, "Mössbauer studies of strain-induced transformation of retained austenite in dual-phase steels," *Mater. Sci. Eng. A*, vol. 150, pp. 113–116, 1992.
- [100] K. G. Solheim, J. K. Solberg, J. Walmsley, F. Rosenqvist, and T. H. Bjørnå, "The role of retained austenite in hydrogen embrittlement of supermartensitic stainless steel," *Eng. Fail. Anal.*, vol. 34, pp. 140–149, Dec. 2013.
- [101] H. Townsend, "Hydrogen sulfide stress corrosion cracking of high strength steel wire," *Corrosion*, vol. 28, no. 1, pp. 39–45, 1972.
- [102] M. Giannozzi, L. Baldassarre, M. Cecconi, M. Camatti, D. Becherucci, X. Coudray, and C. Puaut, "Adipec 2013 Technical Conference Manuscript: About design, materials selection and manufacturing technologies of centrifugal compressors for extreme sour and acid service," in *Gas Processing rotating equipment*, 2013.
- [103] J. Kittel, J. Martin, T. Cassagne, and C. Bosch, "Hydrogen Induced Cracking (HIC) - Laboratory testing assesment of low alloy steel linepipe," *Corros. 08*, 2008.
- [104] T. Cassagne, M. Bonis, C. Duret, and J. L. Crolet, "Limitations of 17-4 PH Metallurgical, Mechanical and Corrosion Aspects." NACE International, 2003.
- [105] J. Man, K. Obrtlik, M. Petrevec, P. Baran, M. Smaga, A. Weidner, J. Dluhos, T. Kruml, H. Biermann, D. Eifler, and J. Polak, "Stability of austenitic 316L steel against martensite formation during cyclic straining," *Procedia Eng.*, vol. 10, pp. 1279–1284, 2011.
- [106] P. Chiu, K. Weng, S. Wang, J. Yang, Y. Huang, and J. Fang, "Low-cycle fatigue-induced martensitic transformation in SAF 2205 duplex stainless steel," *Mater. Sci. Eng. A*, vol. 398, pp. 349–359, 2005.
- [107] J. Stolarz, "Corrosion d'aciers inoxydables austénitiques au silicium dans les conditions transpassives, PhD thesis," Saint-Etienne, EMSE, 1989.
- [108] R. A. Young, *The Rietveld method, book*. Oxford: Oxford University Press, 1993.
- [109] C. F. Jaczak, J. A. Larson, and S. W. Shin, "Retained austenite and its measurement by

- X-ray diffraction: an information manual,” *Soc. Automot. Eng.*, 1980.
- [110] A. Bojack, L. Zhao, P. Morris, and J. Sietsma, “Austenite formation from martensite in a 13Cr6Ni2Mo Supermartensitic Stainless Steel,” *Metall. Mater. Trans. A*, vol. 47, no. 5, pp. 1996–2009, 2016.
- [111] J. Stolarz, “Materials Sciences lecture (Mines Saint-Etienne),” 1989.
- [112] S. Takaki, K. Ngo-huynh, N. Nakada, and T. Tsuchiyama, “Strengthening mechanism in Ultra Low Carbon Martensitic Steel,” *ISIJ Int.*, vol. 52, no. 4, pp. 710–716, 2012.
- [113] J. Pesicka, R. Kruzel, A. Dronhofer, and G. Eggeler, “The evolution of dislocation density during heat treatment and creep of tempered martensitic ferritic steels,” *Acta Mater.*, vol. 51, pp. 4847–4862, 2003.
- [114] S. Takebayashi, T. Kunieda, N. Yoshinaga, K. Ushioda, and S. Ogata, “Comparison of the dislocation density in martensitic steels evaluated by some X-ray diffraction methods,” *ISIJ Int.*, vol. 50, no. 6, pp. 875–882, 2010.
- [115] F. Montheillet, “Comportement rhéologique des matériaux métalliques multiphasés,” *Tech. l’ingénieur M3010V2*, 2012.
- [116] A. Oehlert and A. Atrens, “Room temperature creep of high strength steels,” *Acta Metall.*, vol. 42, pp. 1493–1508, 1994.
- [117] S. Rajasekhara, P. Ferreira, L. Karjalainen, and A. Kyrolainen, “Hall–Petch behavior in ultra-fine-grained AISI 301LN stainless steel,” *Metall. Mater. Trans. A*, vol. 38, pp. 1202–1210, 2007.
- [118] G. Olson, “A mechanism for the strain-induced martensitic transformations,” *J. less-common Met.*, vol. 28, pp. 107–118, 1972.
- [119] M. Cohen and G. Olson, “Kinetics of Strain-Induced Martensitic Nucleation,” *Metall. Trans. A*, vol. 6, no. April, pp. 791–795, 1975.
- [120] W. S. Li, H. Y. Gao, H. Nakashima, S. Hata, and W. H. Tian, “In-situ study of the deformation-induced rotation and transformation of retained austenite in a low-carbon steel treated by the quenching and partitioning process,” *Mater. Sci. Eng. A*, vol. 649, pp. 417–425, 2016.
- [121] D. De Knijf, C. Föjer, L. A. I. Kestens, and R. Petrov, “Factors influencing the austenite stability during tensile testing of Quenching and Partitioning steel determined via in-situ Electron Backscatter Diffraction,” *Mater. Sci. Eng. A*, vol. 638, pp. 219–227, 2015.
- [122] G. Lorang, M. Da Cunha Belo, A. Simoes, and M. Ferreira, “Chemical composition of passive films on AISI 304 Stainless Steel,” *Electrochem. Soc.*, vol. 141, no. 12, pp. 3347–3356, 1994.
- [123] K. Asami, K. Hashimoto, and S. Shimodaira, “XPS determination of compositions of alloy surface oxides on mechanically polished iron-chromium alloys,” *Corros. Sci.*, vol. 17, no. 9, pp. 713–723, 1977.
- [124] H. Mathieu and D. Landolt, “An investigation of thin oxide films thermally grown in situ on Fe₂₄Cr and Fe₂₄Cr₁₁Mo by auger spectroscopy and X-ray photoelectron spectroscopy,” *Corros. Sci.*, vol. 26, no. 7, pp. 547–559, 1986.
- [125] G. Lorang, M. Da Cunha Belo, and J. Langeron, “Sputter profiling of passive films in Fe–Cr alloys: A quantitative approach by Auger electron spectroscopy,” *J. Vac. Sci. Technol. A*, no. 5, p. 1213, 1987.

- [126] G. Lorang, F. Basile, M. Da Cunha Belo, and J. Langeron, "Quantitative auger analysis of passive films formed on stainless steels," *Surf. interface Anal.*, vol. 12, no. 7, pp. 424–428, 1988.
- [127] A. Aldykiewicz and H. Isaacs, "Dissolution characteristics of duplex stainless steels in acidic environments," *Corros. Sci.*, vol. 40, no. 10, p. 1627, 1998.
- [128] E. Symniotis, "Galvanic effects on the active dissolution of duplex stainless steels," *Corrosion*, vol. 46, no. 1, pp. 2–12, 1990.
- [129] B. Baroux, G. Béranger, and C. Lemaître, "Passivity and breakdown of stainless steels passivity," *Stainl. steels, Les Ed. la Phys. Fr.*, pp. 163–182, 1993.
- [130] K. Osozawa and H. Engell, "The anodic polarization curves of iron-nickel-chromium alloys," *Corros. Sci.*, vol. 6, no. 8, p. 389, 1966.
- [131] M. Pourbaix, "Atlas d'équilibres électrochimiques [Atlas of electrochemical equilibria]," 1963.
- [132] K. Hashimoto, "Passivation of amorphous metals and semi-conductors," in *Fifth international symposium on passivity*, 1983, pp. 235–246.
- [133] P. Keller, "XPS investigations of electrochemically formed passive layers on Fe/Cr alloys in 0.5M H₂SO₄," *Corros. Sci.*, vol. 46, no. 8, pp. 1939–1952, 2004.
- [134] T. Hoar and J. Scully, "Mechanochemical anodic dissolution of austenitic stainless steel in hot chloride solution at controlled electrode potential," *J. Electrochem. Soc.*, vol. 111, p. 348, 1964.
- [135] A. Despic, R. Raicheff, and J. O. Bockris, "Mechanism of the acceleration of the electrodic dissolution of metals during yielding under stress," *J. Chem. Phys.*, vol. 49, p. 926, 1968.
- [136] G. Demedts and A. Van Peteghem, "The transient response of the copper electrode potential to elastic straining and its relation to the reaction kinetics," *Corros. Sci.*, vol. 18, pp. 1029–1040, 1978.
- [137] M. A. V. Devanathan and M. Fernando, "Kinetics of charge transfer at mechanically strained copper electrodes - I Anodic dissolution," *Electrochim. Acta*, vol. 15, pp. 1623–1636, 1970.
- [138] E. Gutman, "Mechanochemistry of solid surfaces," *Wolrd Sci. Pub. Co. Pte. Ltd.*, 1994.
- [139] P. Combrade, "Corrosion sous contrainte et fatigue-corrosion," in *Les éditions de la physique*, 1990, pp. 335–410.
- [140] D. McIntyre, R. D. Kane, and S. Wilhelm, "Slow Strain Rate Testing for Materials Evaluation In High-Pressure H₂S environments," *Corrosion*, vol. 44, no. 12, pp. 920–926, 1988.
- [141] R. Parkins, "Predictive approaches to stress corrosion cracking failure," *Corros. Sci.*, vol. 20, pp. 147–166, 1980.
- [142] N. Greene and G. Saltzman, "Effect of plastic deformation on the corrosion of iron and steel," *Corrosion*, vol. 20, no. 9, pp. 293–298, 1964.
- [143] B. Lu, H. Yu, and J. Luo, "Effects of plastic Deformation and Carbon Dioxyde on corrosion of Pipeline Steel in Near-Neutral pHGroundwater," *J. Mater. Eng. Perform.*, vol. 22, no. 5, pp. 1430–1435, 2013.
- [144] A. Barbucci, M. Delucchi, M. Panizza, M. Sacco, and G. Cerisola, "Electrochemical and corrosion behaviour of cold rolled AISI 301 in 1M H₂SO₄," *J. Alloy. Compd.* 317-

- 318, pp. 607–611, 2001.
- [145] H. Taheri, S. Kakooei, I. MC, and A. Dolati, “The Effect of H₂S Concentration and Temperature on Corrosion Behavior of Pipeline steel A516-Gr70,” *Casp. J. Appl. Sci. Res.*, vol. 1, no. January 2012, pp. 41–47, 2012.
- [146] M. C. Fatah, M. C. Ismail, B. Ari-wahjoedi, and K. A. Kurnia, “Effects of sulphide ion on the corrosion behaviour of X52 steel in a carbon dioxide environment at temperature 40 °C,” *Mater. Chem. Phys.*, vol. 127, no. 1–2, pp. 347–352, 2011.
- [147] C. Bosch, D. Delafosse, and X. Longaygue, “Effects of strain and trapping on hydrogen-induced cracking in high strength low alloy steels,” in *Eurocorr, Moscow*, 2010, pp. 1558–1570.
- [148] M. Monnot, “Etude des mécanismes de corrosion sous contrainte des aciers inoxydables super-martensitiques en milieu H₂S, PhD thesis,” Grenoble, 2017.
- [149] Q. Liu, A. D. Atrens, Z. Shi, K. Verbeken, and A. Atrens, “Determination of the hydrogen fugacity during electrolytic charging of steel,” *Corros. Sci.*, vol. 87, pp. 239–258, 2014.
- [150] U. Hadam and T. Zakroczymski, “Absorption of hydrogen in tensile strained iron and high-carbon steel studied by electrochemical permeation and desorption techniques,” *Int. J. Hydrogen Energy*, pp. 2449–2459, 2009.
- [151] T. Zakroczymski, “Adaptation of the electrochemical permeation technique for studying entry, transport and trapping of hydrogen in metals,” *Electrochim. Acta*, vol. 51, pp. 2261–2266, 2006.
- [152] M. Aronniemi, J. Lahtinen, and P. Hautojarvi, “Characterization of iron oxide thin film,” *Surf. interface Anal.*, vol. 36, pp. 1004–1006, 2004.
- [153] J. Bockris and P. Subramanyan, “The equivalent pressure of molecular hydrogen in cavities within metals in terms of the overpotential developed during the evolution of hydrogen,” *Electrochem. acta*, vol. 16, pp. 2169–2179, 1971.
- [154] J. Bao and D. Macdonald, “Kinetics of the Hydrogen Electrode Reaction on Platinum in Alkaline Solutions at Elevated Temperatures,” *ECS Trans.*, vol. 11, no. 27, pp. 1–11, 2008.
- [155] L. Garverick, *Corrosion in the petrochemical industry, ASM international book*. 1994.
- [156] P. Marcus and E. Protopopoff, “Potential-pH diagrams for adsorbed species,” *J. Electrochem. Soc.*, vol. 137, pp. 2709–2712, 1990.
- [157] E. Protopopoff and P. Marcus, “Potential-pH diagrams for adsorbed species,” *J. Electrochem. Soc.*, vol. 144, pp. 1586–1590, 1997.
- [158] E. Protopopoff and P. Marcus, “Potential-pH diagrams for adsorbed species,” *J. Electrochem. Soc.*, vol. 140, pp. 1571–1575, 1993.
- [159] J. Enerhaug, “A study of localized corrosion in supermartensitic stainless steel weldments, PhD thesis,” Trondheim, NTNU, 2002.
- [160] A. Yen, W. Graham, and G. Belton, “The segregation of phosphorous to the free surface of a ferritic iron alloy at 723 to 823K,” *Metall. Trans. A - Phys. Metall. Mater. Sci.*, vol. 9, pp. 31–34, 1978.
- [161] M. Innocenti, “Internal Report n° 201205030557Rev00FA,” 2012.
- [162] R. Oriani and P. Josephic, “Equilibrium and kinetic studies of the hydrogen-assisted cracking of steels,” *Acta Metall.*, vol. 25, no. 9, pp. 979–988, 1977.

- [163] T. Morvan, P. Ganster, V. Barnier, and K. Wolski, "Surface and grain boundary segregation in 16MND5 steel," *Surf. interface Anal.*, vol. 49, no. 7, pp. 666–673, 2017.
- [164] J. Rice and J. Wang, "Embrittlement of interfaces by solute segregation," *Mater. Sci. Eng. A*, vol. 107, pp. 23–40, 1989.
- [165] F. Christien, R. Le Gall, and G. Saindrenan, "Phosphorus grain boundary segregation in steel 17-4PH," *Scr. Mater.*, vol. 48, pp. 11–16, 2003.
- [166] K. Wolski, N. Marie, and M. Biscondi, "AES quantification of intergranular film thickness in the Ni-Bi system with respect to the liquid metal embrittlement phenomenon," *Surf. interface Anal.*, vol. 31, pp. 280–286, 2001.
- [167] C. Naudin, J. Frund, and A. Pineau, "Intergranular fracture stress and phosphorous grain boundary segregation of a Mn-Ni-Mo steel," *Scr. Mater.*, vol. 40, no. 9, pp. 1013–1019, 1999.
- [168] R. Le Gall and G. Saindrenan, "Segregation interfaciale: applications aux matériaux industriels," *Rev. métallurgie*, vol. 2, pp. 169–176, 1998.
- [169] A. Fraczkiwicz and K. Wolski, "Intergranular segregation and crystalline material fracture," *Grain boundaries Cryst. Plast.*, pp. 281–327, 2011.
- [170] D. McLean, *Grain boundaries in metals*. London, oxford university press, 1957.
- [171] J. Janovec, D. Grman, J. Perhacova, P. Lejcek, J. Patscheider, and P. Sevc, "Thermodynamic of phosphorous grain boundary segregation in polycrystalline low alloy steels," *Surf. interface Anal.*, vol. 30, no. 1, pp. 354–358, 2000.
- [172] R. Guillou, M. Guttman, and P. Dumoulin, "Role of Molybdenum in Phosphorus induced temper embrittlement of 12%Cr," *Met. Sci.*, pp. 15–63, 1981.
- [173] M. Mackenbrock and H. Grabke, "Grain boundary segregation and diffusion of phosphorus in 12Cr–Mo–V steel," *Mater. Sci. Technol.*, vol. 8, no. 6, pp. 541–545, 1992.
- [174] P. Lejcek, *Grain boundary segregation in metals vol 136*. Springer Science & Business Media, 2010.
- [175] M. Militzer and J. Wieting, "Theory of segregation kinetics in ternary alloys," *Acta Metall.*, vol. 34, no. 7, pp. 1229–1236, 1986.
- [176] A. Larere, M. Guttman, and P. Dumoulin, "Auger electron spectroscopy study of the kinetics of intergranular and surface segregations in nickel during annealing," *Acta Metall.*, vol. 30, pp. 685–693, 1982.
- [177] Y. Prawoto, K. M. Ibrahim, and W. S. Wan Nik, "Effect of ph and chloride concentration on the corrosion of duplex stainless steel," *Arab. J. Sci. Eng.*, p. 115, 2009.
- [178] S. Duval, R. Antano-Lopez, C. Scomparin, M. Jerome, and F. Ropital, "Hydrogen permeation through ARMCO iron membranes in sour media," *NACE*, p. 4740, 2004.
- [179] J. Bricout, "Contribution à l'étude de la fragilisation par hydrogène des aciers inoxydables austénitiques instables, PhD thesis," Valenciennes, Université de valenciennes et du Hainaut-Cambresis, 1984.

Chapter VI: Appendixes

1. Sample preparation for EBSD and XRD

First, we used X-ray diffraction to investigate the effect of surface preparation techniques on the amount of austenite in the surface layer. Local strains induced by metallographic preparation appear to provide enough mechanical energy to set off stress induced martensite transformation. Moreover, the volume fraction of retained austenite in the surface layer (6.5%) is much smaller than the one measured after tensile and compression tests up to respectively 12% and 7.5%. Clearly, mechanical polishing leads to SIMT in Virgo™38. Consequently, the proportion of phases at the surface is very different from that of the bulk and strongly depends on surface preparation. This can only be avoided by following a strict procedure of surface preparation.

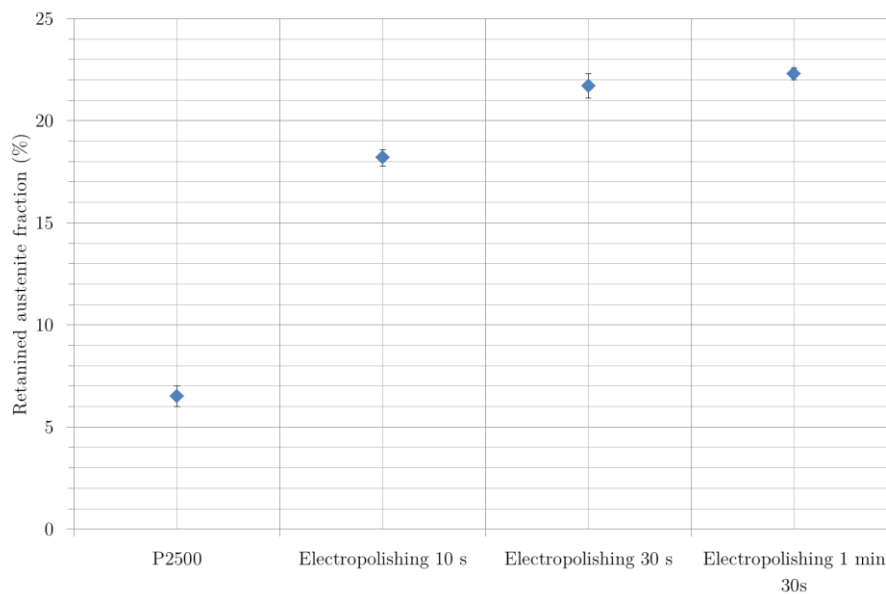


Figure 213 - Influence of the metallographic preparation on the retained austenite content measured by X-Ray Diffraction

However, it is not always possible to perform electropolishing on our samples. For example, when observing secondary cracks on sample cross section, electropolishing would blunt the crack tips (Figure 214) and lead to the loss of information. In those cases, the polishing procedure was manual mechanical grinding up to P4000 followed by manual mirror polishing using diamond pastes up to $\frac{1}{4}\mu\text{m}$ and a blend of high purity alumina and colloidal silica ($0.05\mu\text{m}$, $\text{pH}=9$). The final polishing step was 15 hours vibro-polishing in an alumina solution ($0.02\mu\text{m}$, $\text{pH}=7.8$).

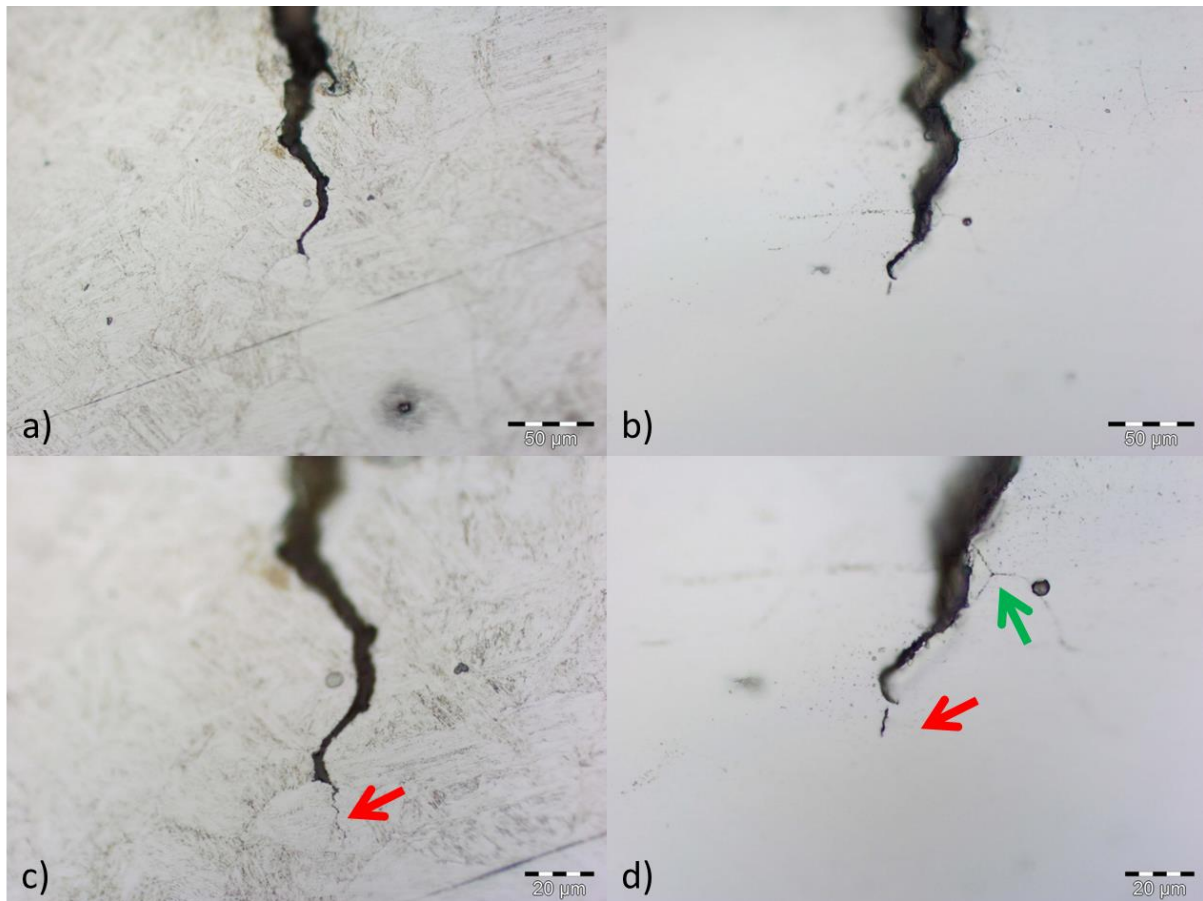


Figure 214 - Influence of the electropolishing on the observation of secondary cracks: Cross sections before (a and c) and after (b and d) only 10 seconds of electropolishing showing the blunting of the crack tip (red arrow in c and d) and an apparition of additional intergranular secondary cracks (green arrow in d)

XRD measurements reveal that the retained austenite content measured in both cases (vibro-polishing and electropolishing) is the same (around 22%).

2. Safety report for the use of Na₂S containing environments

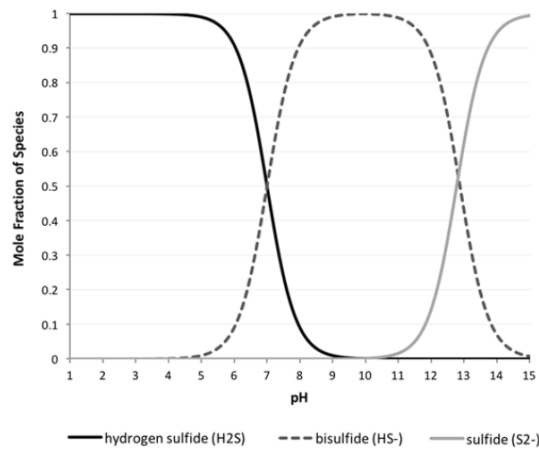
2.1. Présentation du banc d'essai

Le test décrit dans cette partie est un essai de traction lente en milieu désaéré contenant du Na₂S. La composition exacte du mélange étudié dans ce document est: 0.1M NaOH + 0.02M Na₂S. Le pH initial de cette solution se situe aux alentours de 12,3. Avant le test de corrosion sous contrainte, la solution est désaérée en circuit fermé avec de l'azote pendant 12h.

2.2. Analyse du risque

Les différents risques potentiels liés à cette expérience et leur analyse sont décrits dans le tableau suivant. Dans cette description, sont omis (mais non négligés) les risques courants d'un laboratoire de recherche ou d'une entreprise comme, par exemples, le risque de chute, les risques dus aux câbles électriques des machines ou les risques liés au bruit.

Danger	Risque	Conséquences	Mesures de sécurité
Manipulation de substance dangereuse (soude NaOH, Na ₂ S)	Contact cutané	Brûlure corporel	Port des EPI (Blouse, gants, lunettes, masque) et formation aux risques chimiques
	Contact oculaire	Brûlure des yeux	
	Inhalation de vapeur	Irritation des voies respiratoires	Mise en place des récipients étanches-ventilation
	Ingestion de produit	Irritation	Formation aux risques chimiques, bon sens
	Chute du récipient	Projection de verre et de produit	Port des EPI (Blouse, gants, lunettes, masque)
Dispersion des produits		Mise en place de bac de rétention et protection	
Manipulation de bouteille de gaz sous pression (N ₂)	Fuite de gaz	Asphyxie	Détecteur O ₂
		Incendie	Extincteur
	Explosion	Incendie et dégâts corporels	Fixation des bouteilles au mur
Risque lié au H ₂ S potentiellement libéré	Inhalation (catégorie 2)	5ppm odeur perceptible, 10ppm début d'irritation des yeux, 30ppm odeur forte, 100ppm irritation des yeux toux perte d'odorat, 250ppm conjonctivite, 500ppm perte de connaissance et arrêt respiratoire puis mort, 1000ppm et + perte de connaissance instantanée puis mort	Aspiration, maintien du pH élevé (voir schéma ci-dessous), EPI (Blouse, gants, lunettes, masque avec cartouche type EN14387 A2B2E2K2P3RD), détecteur H ₂ S avec alarme au-delà de 5ppm
		Explosion en présence de fortes chaleurs (>260°C)	Incendie et dégâts corporels
Danger lié à une panne électrique	Aspiration ne fonctionne plus	Non évacuation du H ₂ S	Vérification de la ventilation, manipulation avec la fenêtre ouverte



En maintenant un pH suffisamment élevé (>9), on évite la présence de H₂S.

La courbe ci-dessus indique que travailler avec le pH supérieur à 9 permet d'éliminer le risque du dégagement de H₂S. Le pH de la solution est mesuré deux fois par jour (port du masque, ouverture de la fenêtre). Le retour d'expérience de la première campagne (6 essais de 7 jours en moyenne) montre que le pH n'est jamais descendu en dessous de 12.

Par ailleurs, la quantité totale de Na₂S utilisée est de 6.25 grammes. En faisant l'hypothèse de chute drastique de pH (improbable puisque dissous dans du NaOH) conduisant à une transformation totale de Na₂S en H₂S, de plus concomitante avec l'arrêt accidentel de la ventilation et libération du H₂S dans la pièce, la quantité libérée serait de 0.0019m³, ce qui, ramené au volume de la pièce donnerait une concentration de 31 ppm. Cette concentration serait non seulement perceptible mais en plus conduirait au déclenchement d'alarme.

Un masque accessible en entrée du laboratoire permettrait dans ce cas de rentrer dans la pièce afin d'ouvrir les fenêtres et de réenclencher le système de ventilation sous hotte.

2.3. Documents utilisés pour prévenir le personnel

Les fiches de sécurité du produit Na₂S et des autres produits chimiques contenus dans la solution (NaOH par exemple) sont présentes dans les laboratoires et portées à la connaissance des utilisateurs. L'utilisation des produits chimiques est également référencée dans la fiche d'exposition aux produits chimiques personnelle. Les utilisateurs reçoivent également une explication des risques liés au H₂S et des explications des concentrations critiques (voir tableau ci-dessus). Il est aussi rappelé aux utilisateurs que le port des EPI est obligatoire (gants, lunettes, blouse, masque avec cartouche adéquat).

2.4. Vérifications et précautions avant et en cours de manipulation

Avant de lancer une expérience, l'utilisateur doit signaler sa présence et le démarrage de l'essai à un permanent. Au cours du test, le pH doit être vérifié régulièrement. Si une dérive importante est constatée, de la soude doit être ajoutée afin de faire remonter le pH. La ventilation doit être en marche permanente, du lancement de l'essai jusqu'à son nettoyage. En cours de nettoyage, il est conseillé d'ouvrir une fenêtre pour créer un flux d'air frais.

2.5. Procédure d'urgence mise en place

En cas de libération excessive de H_2S , le laboratoire doit être évacué et aéré (ouverture de la fenêtre). L'aspiration (fonctionnant en continue) permet d'évacuer le gaz. Une signalisation et une interdiction totale d'entrer doit être mise en place.

2.6. Check-list avant lancement de l'expérience

- Avertir personnel permanent (ne pas se mettre en position de travailleur isolé)
- Signaler avec pancarte (restriction d'accès)
- Vérifier l'activation et le bon fonctionnement de la hotte
- Vérifier régulièrement (2 fois/jour) le pH
- Mettre à disposition de la soude

2.7. Fin d'expérience

Récupérer la solution en bidon ainsi que les eaux de rinçage du montage. Faire évacuer les déchets par le service compétent en précisant la nature des composés chimiques présents. Porter les EPI.

2.8. Détails du calcul $Na_2S \rightarrow H_2S$

0.02M Na_2S , 4L de solution $0.02 \times 4 = 0.08 \text{ mol } Na_2S$

$M_{Na_2S} = 78.0452 \text{ g/mol}$

Donc $m_{Na_2S} = 6.243616 \text{ g}$

Volume de la pièce = $25 \text{ m}^2 \times 2.5 \text{ m} = 62.5 \text{ m}^3$.

$Na_2S + 2H_2O \rightarrow H_2S + 2NaOH$

Dans l'hypothèse d'une réaction totale, $x_{Na_2S} = x_{H_2S}$

Donc on formerait 0.08 mol H_2S , avec $V_{m_{H_2S}} = 0.024 \text{ m}^3/\text{mol}$ (à 20°C sous 1atm), on obtiendrait :

$V_{H_2S} = 0.00192 \text{ m}^3$ soit 30.72ppm ramené au volume de la pièce.

3. Influence of different parameters on cracking resistance of Virgo™38 in presence of H₂S

3.1. Influence of strain rate

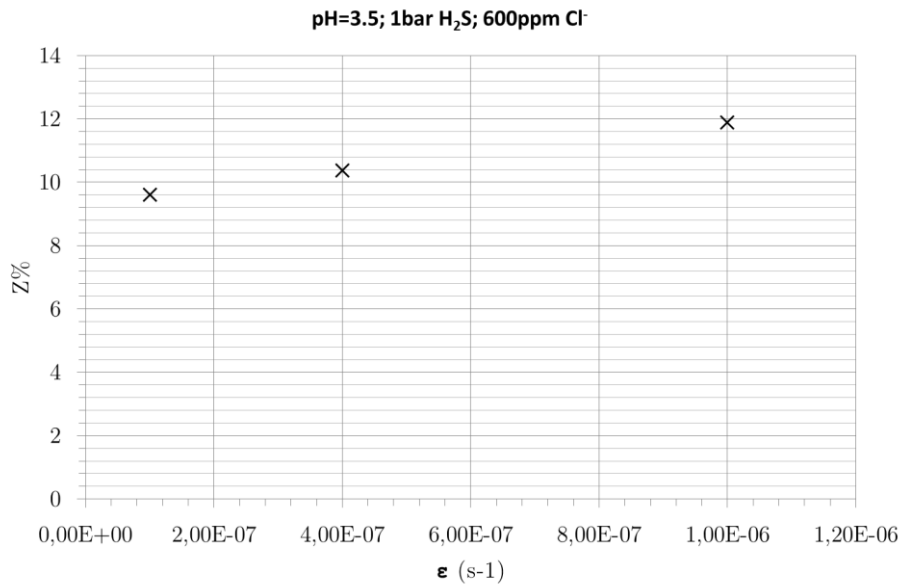


Figure 215 - Influence of the strain rate applied on the reduction in area (Z%) for slow strain rate tensile tests under pH=3.5, 1bar H₂S and 1g/L NaCl

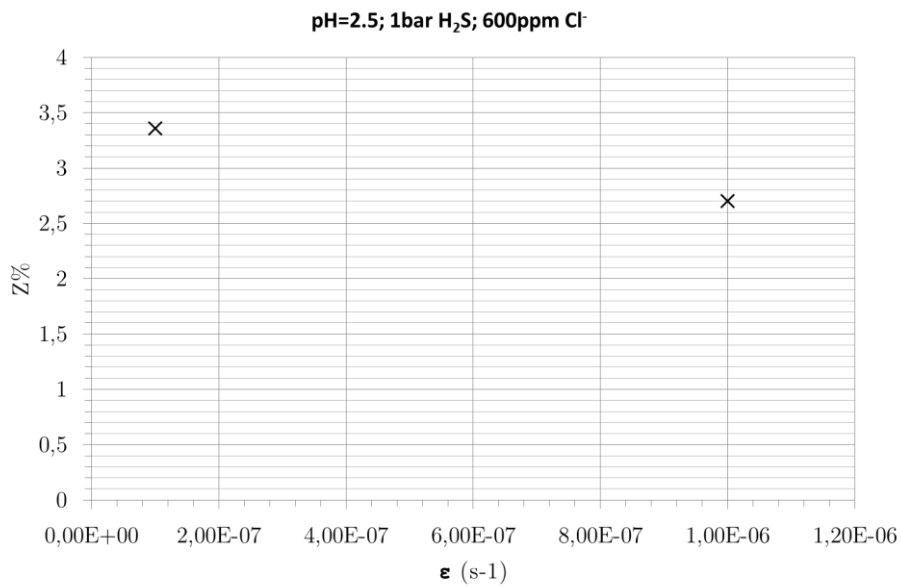


Figure 216 - Influence of the strain rate applied on the reduction in area (Z%) for slow strain rate tensile tests under pH=2.5, 1bar H₂S and 1g/L NaCl

3.2. Influence of H₂S partial pressure

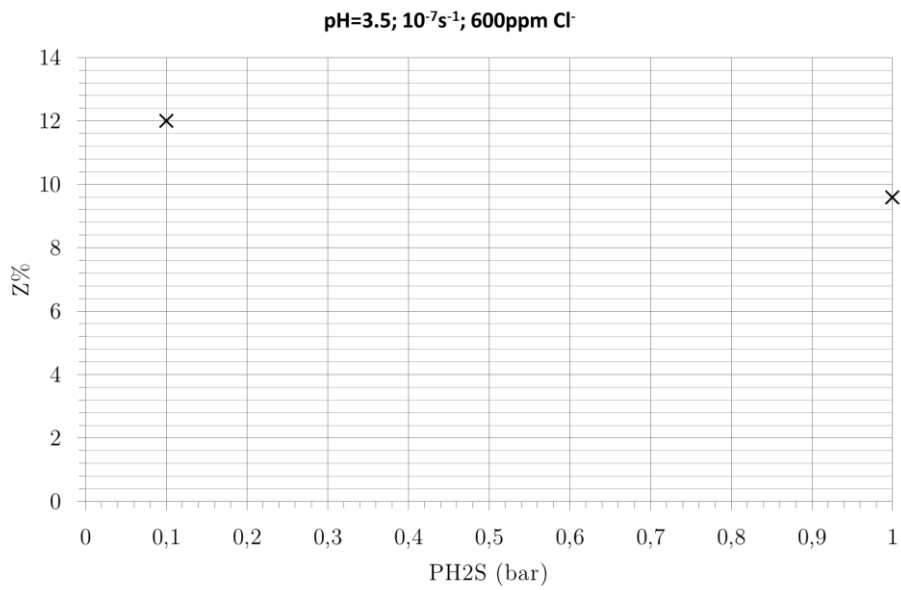


Figure 217 - Influence of the H₂S partial pressure on the reduction in area (Z%) for slow strain rate tensile tests under pH=3.5, 1g/L NaCl and at a strain rate of 10⁻⁷s⁻¹

3.3. Influence of chloride content

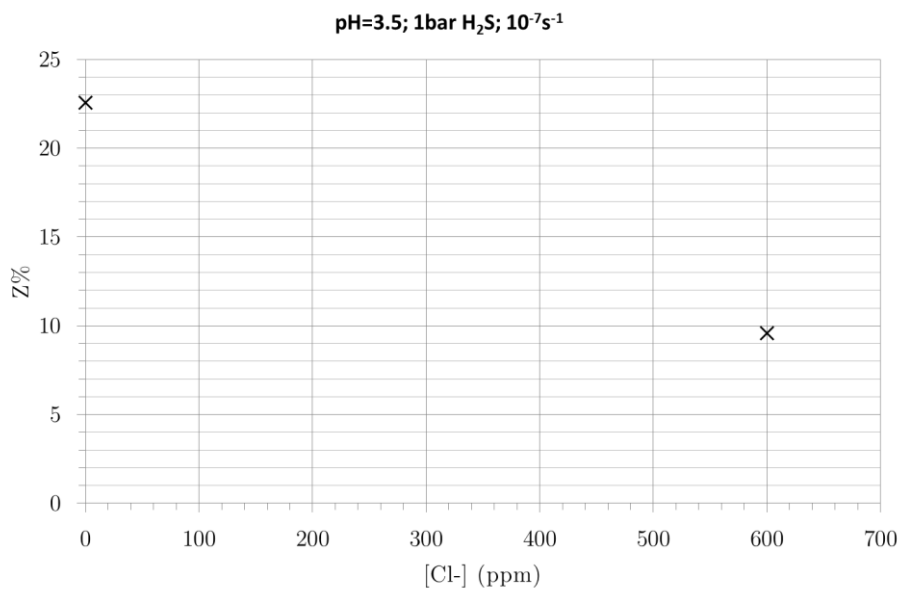


Figure 218 - Influence of the chloride content on the reduction in area (Z%) for slow strain rate tensile tests under pH=3.5, 1bar H₂S and at a strain rate of 10⁻⁷s⁻¹

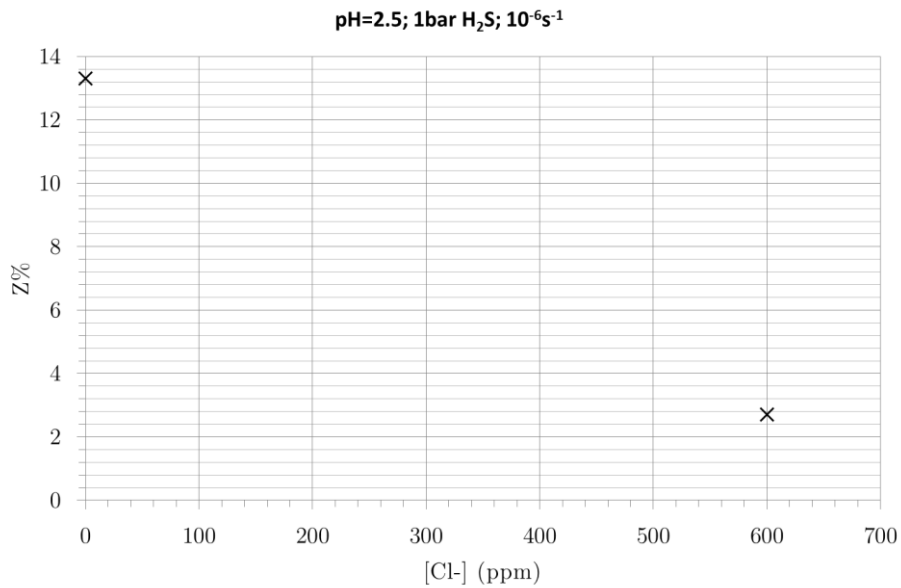


Figure 219 - Influence of the chloride content on the reduction in area (Z%) for slow strain rate tensile tests under pH=2.5, 1bar H₂S and at a strain rate of 10⁻⁶s⁻¹

3.4. Influence of stress localization

One SSRT test in a previously notched sample were performed in the same conditions as test 3 (i.e. 1 bar of H₂S, pH=3.5, 600ppm of chlorides, 10⁻⁷s⁻¹) in order to eliminate the influence of the crack initiation process on the final resistance of Virgo™38 to hydrogen embrittlement. Indeed, the notch enables to localize the deformation as it is the case at a bottom of a pit for example. The notch geometry used during this study is presented in Figure 220.

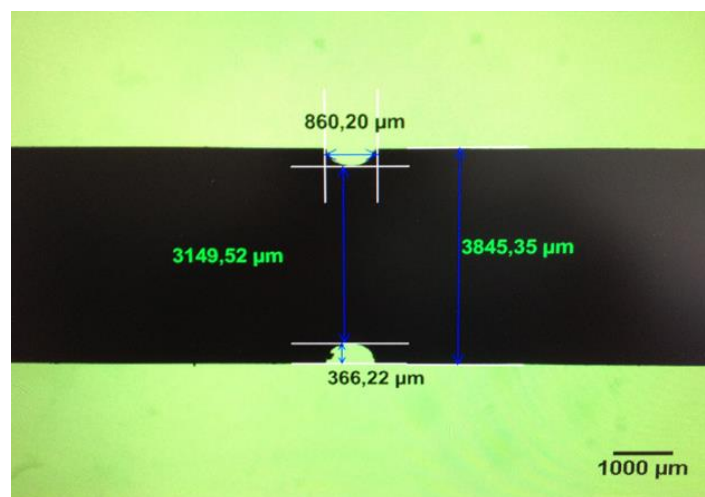


Figure 220 - Notch geometry before polishing

As expected, the reduction in area is of 0% in this case due to the localization of the deformation. The observation of the fracture surface reveals an average intergranular failure of 40.1±0.5% compared to 34.9±0.6% in the not notched sample.

3.5. Influence of the grain boundary composition (study on the Cover)

As in Chapter IV, we chose to reproduce the Hydrogen Embrittlement phenomena that occurred in service on this component. To do it, we carried out SSRT test in the same conditions as test 3 (i.e. 1 bar of H_2S , $\text{pH}=3.5$, 600ppm of chlorides, 10^{-7}s^{-1}). The reduced NACE tensile specimen as described in the first part of this chapter was used.

The ratio of area reduction (Z% factor) measured in this case was of 0% compared to 9.60% in the same conditions on the properly industrially heat treated Virgo™38 impeller.

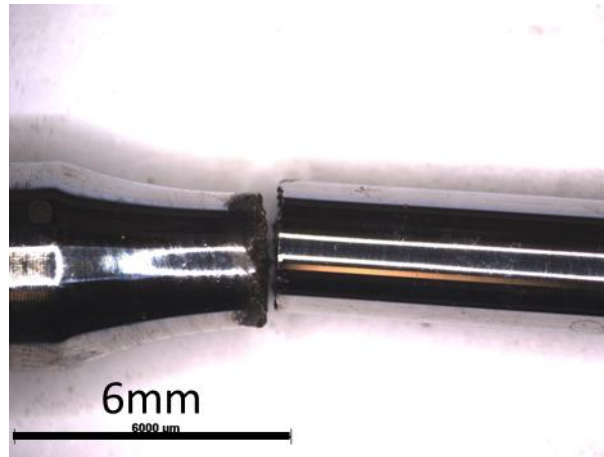


Figure 221 - Optical micrographs of barrel surfaces after SSRT test on the Cover sample showing some corrosion products on the fracture surface

As for all the tests in the Hydrogen Embrittlement domain, fracture occurs due to local defects and the passive film remain stable at the other location on the barrel surface (Figure 221).

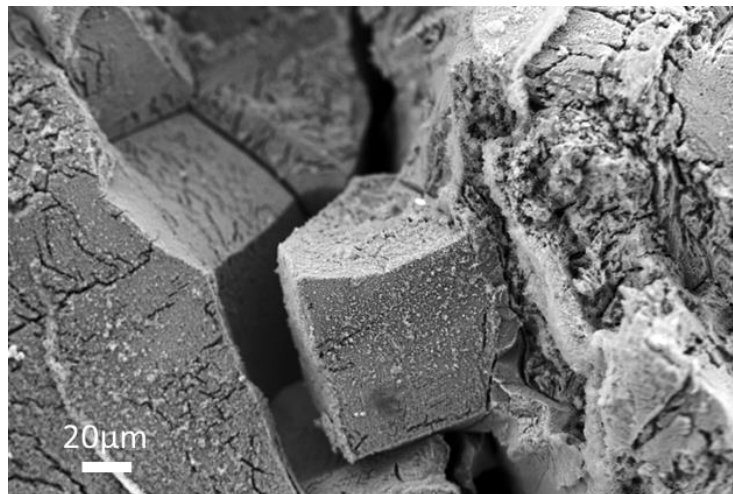


Figure 222 - Fracture surface obtained after SSRT test on the Cover sample tested under 1 bar of H_2S , in presence of 600ppm of chlorides at $\text{pH}=3.5$ and at a strain rate of 10^{-7}s^{-1} showing a fully intergranular fracture

Contrary to the test in the same conditions performed on the properly heat treated specimens of Virgo™38 (impeller test 3), Figure 222 reveals a fully intergranular fracture on the Cover ($93.4\pm 0.9\%$ vs $34.9\pm 0.6\%$ for the impeller in the same conditions). Furthermore, several secondary cracks are visible on the intergranular facets. As concluded in Chapter IV, the extreme brittleness of the Cover

component is due to a synergy between Phosphorous Grain Boundary Segregation (PGBS) and the high hydrogen activity encountered in H₂S containing environments.

The intergranular mode of propagation is confirmed by the EBSD observations performed on secondary cracks as visible in Figure 223.

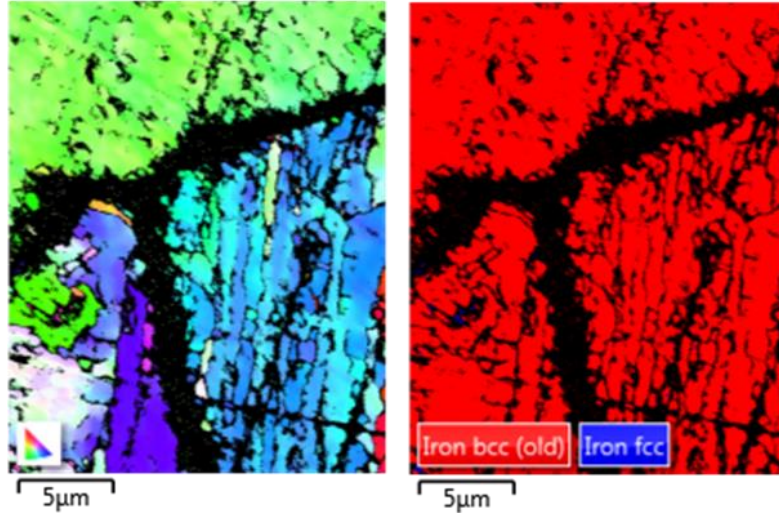


Figure 223 - EBSD maps on cross-section specimens after SSRT test on the Cover showing an intergranular mode of crack propagation and the very low retained austenite content

3.6. Influence of δ -ferrite on the crack propagation

Even if the δ -ferrite content is conformed in all the heat studied during this work, i.e. <5vol.%, it can be observed that cracks are affected by the presence of δ -ferrite grains (Figure 224).

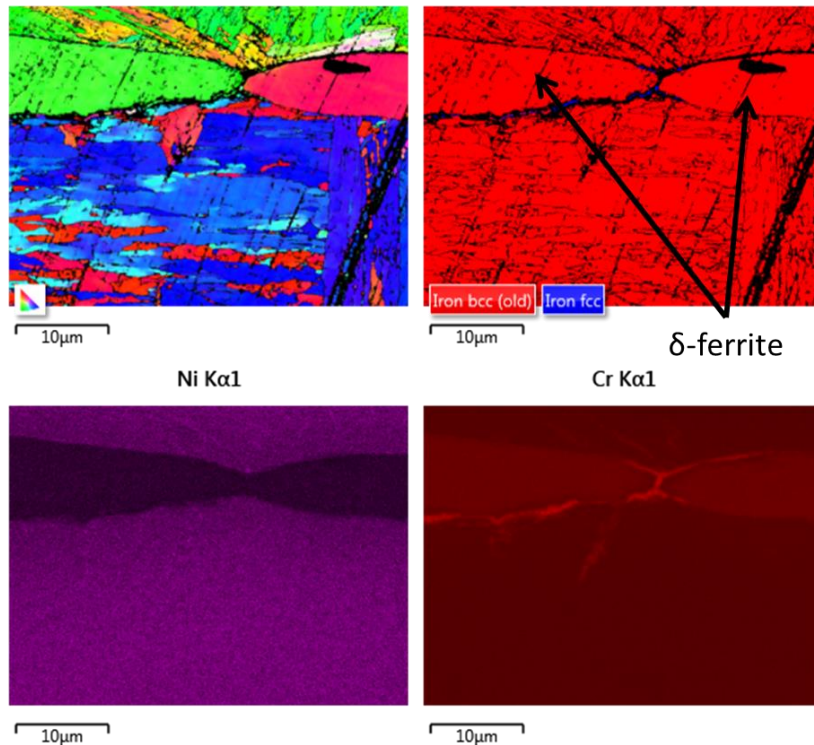


Figure 224 - EBSD map on cross-section specimens after SSRT test showing crack propagation around δ -ferrite grains

4. Dead weight tests at H₂S a partial pressure of 2 bar

4.1. Conditions

Method: NACE TM0177:2005 Method A

Solution: demineralized water + 50ppm chlorides (NaCl) + 0.4g/L sodium acetate

P_{H₂S} = 2bars

pH = 3.7

Constant load = 350 MPa

2 samples tested in parallel

4.2. Results obtained

Both samples do not fail before 720 hours. However, pits are observed on the sample surface. Further analyses are ongoing to determine the pit depth and if cracks initiated down that pits.

5. SSC study of F6NM supermartensitic stainless steel

5.1. Composition of the alloy and conditions of the tests

The composition of F6NM treated as required by NACE standards used in this study is given in the Table below. The main difference with Virgo™38 lies in the chromium content.

	Fe	%C	%Cr	%Ni	%Mn	%Si	%Cu	%Mo	%P	Ac ₁ calculated
Virgo™38	Bal.	0.035	15.2	4.63	0.64	0.34	0.10	0.07	0.018	623°C
F6NM	Bal.	0.025	12.68	3.93	0.67	0.48	0.16	0.56	0.031	670°C

Two comparative SSRT tests in presence of H₂S were performed. The conditions chosen were the same as the ones presented in Chapter V on Virgo™38 for tests number 3 and 17, as indicated in the table below:

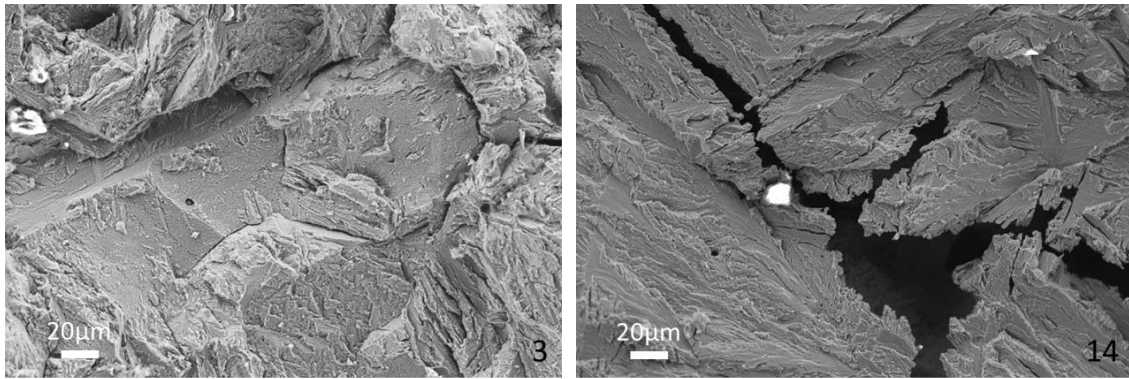
Test number	Initial pH	pH ₂ S (bar)	Strain rate (s ⁻¹)	[Cl ⁻] (ppm) (NaCl)
14 (3)	3.5	1	10 ⁻⁷	600
15 (17)	3.5	1	10 ⁻⁷	0

These two conditions were chosen within the pH range where hydrogen embrittlement is the predominant mechanism, and compatible within the actual applications range.

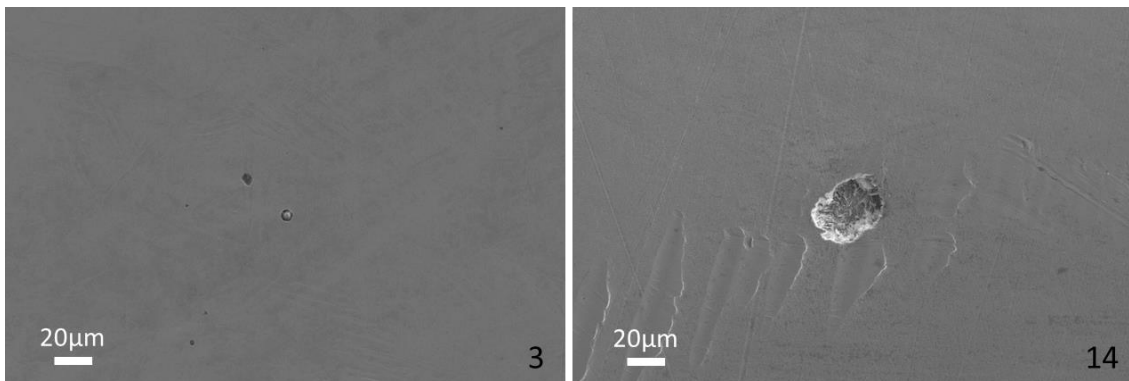
5.2. Results

Both tests show a higher embrittlement as compared to Virgo™38.

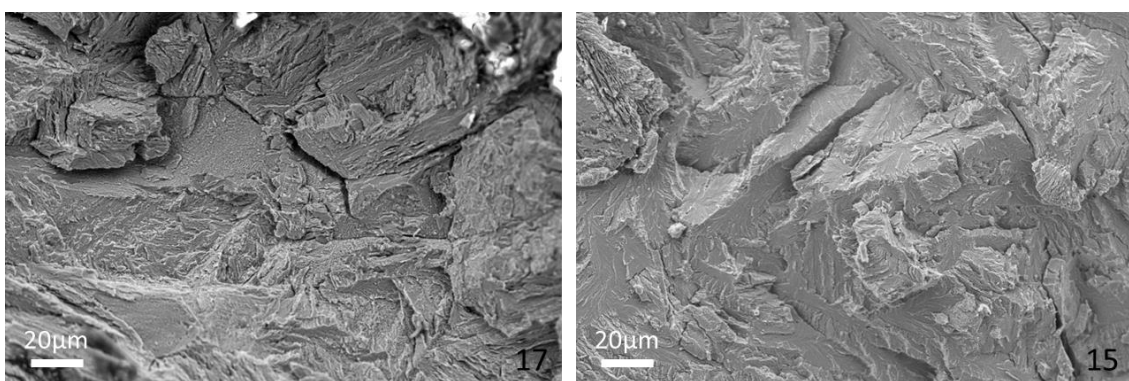
In presence of 600ppm of chlorides at pH=3.5 under 1bar of H₂S (tests 3 and 14) the reductions in area are of 9.60% and 8.86% for Virgo™38 and F6NM respectively. The comparative observations of the fracture surfaces are presented below.



As for Virgo™38 in the same conditions, the fracture is mainly transgranular. However, it seems that F6NM is subjected to dissolution in such conditions, which could be explained by a lower resistance due to the low chromium content. This observation seems to be confirmed by the observations of the barrel surfaces, where we can see that stable pitting corrosion occurs on F6NM while only metastable pitting corrosion is visible on Virgo™38.



In absence of chlorides at pH=3.5 under 1bar of H₂S (tests 17 and 15) the reductions in area are of 22.56% and 15.20% for Virgo™38 and F6NM respectively. The comparative observations of the fracture surfaces are presented below.



In both cases the fracture is mainly transgranular with some intergranular areas.

In conclusion, Virgo™38 seems to be more resistant to SSC due to its higher chromium content. It would be useful to study the influence of the chromium content on the resistance of both pitting corrosion and chemical dissolution of the passive film.

6. Summaries in French

6.1. Table des matières

Introduction générale

Chapitre I : Étude bibliographique

1. Description des aciers inoxydables (super-)martensitiques

1.1. Introduction

1.2. Composition

1.2.1. Éléments majoritaires : Fe-C-Ni-Cr

1.2.2. Éléments secondaires : Mn-Mo-Ti

1.2.3. Relations d'équivalence

1.3. Microstructure des aciers inoxydables supermartensitiques

1.3.1. Martensite α'

1.3.2. Austénite γ

1.3.3. Les différentes transformations martensitiques

1.3.4. Plan d'habitat entre austénite et martensite

1.3.5. Précipitation de carbures

1.4. Traitements thermiques des aciers inoxydables supermartensitiques pour des applications pétrole/gaz

1.4.1. Traitement standard imposé par la norme NACE MR0175

1.4.2. Stabilité de l'austénite en fonction de sa composition et du traitement thermique

2. Fissuration des aciers inoxydables (super-)martensitiques

2.1. Introduction

2.2. Amorce de fissure

2.2.1. Amorce par piqûration

2.2.2. Amorce par dépassivation chimique

2.2.3. Amorce par dépassivation mécanique

2.2.4. Influence de l' H_2S sur l'amorce

2.3. Adsorption, absorption et désorption de l'hydrogène

2.3.1. Formation de l'hydrogène

2.3.2. Adsorption de l'hydrogène

2.3.3. Absorption et recombinaison de l'hydrogène

2.3.4. Désorption de l'hydrogène

2.3.5. Influence de l' H_2S

2.4. Interactions entre l'hydrogène et le métal

2.4.1. Hydrogène diffusible

2.4.2. Hydrogène piégé

2.4.3. Équilibre entre l'hydrogène diffusible et l'hydrogène piégé

2.4.4. Mesure de la diffusion et du piégeage de l'hydrogène par perméation

électrochimique

2.5. Propagation de fissure

2.5.1. Différentes formes de fissuration

2.5.2. Différents mécanismes de fragilisation par l'hydrogène et de propagation de fissure

2.6. Reproduction de la sensibilité à la fissuration par des essais de corrosion sous contrainte

- 2.6.1. Différents types d'essais
- 2.6.2. Différents types de milieux
- 2.7. Paramètres influençant la résistance à la fragilisation par hydrogène
 - 2.7.1. Paramètres métallurgiques
 - 2.7.2. Autres paramètres
- 3. Résumé et objectifs de la thèse

Chapitre II : Métallurgie et propriétés mécaniques du Virgo™38

1. Métallurgie du Virgo™38

- 1.1. Composition et métallurgie de l'alliage industriel
- 1.2. Influence de traitement thermique sur la microstructure
 - 1.2.1. Microstructure de l'alliage remis en solution et influence de la trempe à température négative
 - 1.2.2. Influence du traitement thermique sur le taux d'austénite de réversion
 - 1.2.2.1. Influence de la température de revenu
 - 1.2.2.2. Influence du temps de maintien à 620°C
 - 1.2.2.3. Influence du second revenu
 - 1.2.3. Influence du traitement thermique sur la précipitation des carbures de chrome

2. Propriétés mécanique du Virgo™38

- 2.1. Influence de la direction de prélèvement des échantillons dans la pièce forgée
- 2.2. Propriétés mécaniques en fonction du traitement thermique appliqué
 - 2.2.1. Propriétés du Virgo™38 en traction dans différents états métallurgiques
 - 2.2.2. Résilience du Virgo™38 dans différents états métallurgiques
 - 2.2.3. Relation entre la microstructure et la limite d'élasticité du Virgo™38
- 2.3. Stabilité mécanique de l'austénite de réversion après le traitement industriel
- 2.4. Résumé

Chapitre III : Fragilisation par l'hydrogène et corrosion sous contrainte du Virgo™38 en milieux acides

1. Etude de la dépassivation du Virgo™38 par une approche électrochimique

- 1.1. Procédure expérimentale
- 1.2. Étude de la dépassivation du Virgo™38 sans contrainte
- 1.3. Étude de la dépassivation du Virgo™38 sous charge constante
- 1.4. Paramètres influençant la dépassivation du Virgo™38
 - 1.4.1. Influence des hétérogénéités de composition
 - 1.4.1.1. Influence du taux de Cr
 - 1.4.1.2. Influence du taux de Ni
 - 1.4.2. Influence de la charge appliquée
- 1.5. Interprétations sur la dépassivation du Virgo™38

2. Méthodes expérimentales

3. Fragilisation par l'hydrogène du Virgo™38 à l'état industriel pendant des essais de traction lente

- 3.1. Conditions des essais
- 3.2. Étude du Virgo™38 sous chargement cathodique en milieu acide
- 3.3. Conclusions sur la fragilisation par l'hydrogène sous chargement cathodique en milieu acide

4. Corrosion sous contrainte l'hydrogène du Virgo™38 à l'état industriel pendant des essais de traction lente

- 4.1. Conditions des essais

- 4.2. Comportement du Virgo™38 en corrosion sous contrainte sous potentiel imposé
 - 4.2.1. Essais de traction lente à un potentiel imposé dans le domaine de dissolution de la martensite
 - 4.2.2. Essais de traction lente à un potentiel imposé dans le domaine de dissolution de l'austénite
- 4.3. Conclusions sur la corrosion sous contrainte à potentiel imposé en milieux acide
- 5. Conclusions

Chapitre IV : Fragilisation par l'hydrogène du Virgo™38 dans différents états métallurgique sous chargement cathodique dans un milieu contenant Na₂S

- 1. Définition d'un milieu à haute activité d'hydrogène permettant de reproduire la fragilisation par l'hydrogène observée en service
 - 1.1. Composition du milieu contenant Na₂S et conditions
 - 1.2. Influence du poison de recombinaison sur le comportement du Virgo™38 à l'état industriel
 - 1.2.1. Essais de référence en milieu basique ne contenant pas de poison de recombinaison
 - 1.2.2. Influence de l'ajout de Na₂S sur l'activité de l'hydrogène
 - 1.3. Conclusions
- 2. Influence de la microstructure sur la résistance à la fragilisation par hydrogène du Virgo™38
 - 2.1. État métallurgique de référence : Virgo™38 industriellement traité
 - 2.2. Influence du taux d'austénite de réversion sur la résistance à la fragilisation par hydrogène du Virgo™38
 - 2.2.1. Influence des traitements thermiques
 - 2.2.2. Influence de la pré-déformation
 - 2.3. Étude de cas industriel : le couvercle
 - 2.3.1. Description du matériau : composition, métallurgie et rupture industrielle
 - 2.3.2. Comportement du couvercle en traction lente sous chargement cathodique
- 3. Discussion
 - 3.1. Résumé des résultats obtenus
 - 3.2. Interprétations du taux optimal d'austénite de réversion en termes de quantité et stabilité
 - 3.3. Interprétations du mode de rupture
 - 3.4. Mécanismes de fragilisation par hydrogène proposés
 - 3.4.1. Ruptures intergranulaires
 - 3.4.2. Ruptures transgranulaires
 - 3.5. Interprétations sur la fissuration du couvercle
 - 3.5.1. Interprétations basées sur le taux d'austénite de réversion et le mode de rupture
 - 3.5.2. Interprétations basées sur la précipitation dans le couvercle
 - 3.5.3. Ségrégation du phosphore aux joints de grains dans le couvercle
- 4. Conclusions

Chapitre V : Fragilisation par hydrogène et corrosion sous contrainte assistées par l'H₂S

- 1. Composition des différents milieux utilisés et conditions appliquées
- 2. Influence du pH sur la résistance à la fissuration : vue d'ensemble
- 3. Analyse détaillée de l'amorçage et de la propagation de fissures en présence d'H₂S et mécanismes proposés
 - 3.1. Amorçage de fissures
 - 3.1.1. Observation expérimentale de trois mécanismes d'amorçage différents

- 3.1.1.1. A très bas pH
- 3.1.1.2. A bas pH
- 3.1.1.3. A 'haut' pH
- 3.1.1.4. Conclusions sur les mécanismes d'amorce de fissure
- 3.1.2. Proposition de deux mécanismes d'amorçage
 - 3.1.2.1. Amorçage par dépassivation chimique
 - 3.1.2.2. Amorçage par piqûration
- 3.2. Propagation de fissures
 - 3.2.1. A bas pH
 - 3.2.2. A 'haut' pH
 - 3.2.3. Proposition de deux mécanismes de propagation
 - 3.2.3.1. Propagation de fissures assistée par la dissolution
 - 3.2.3.2. Propagation de fissure assistée par l'hydrogène : influence des paramètres expérimentaux et mécanisme proposé

4. Conclusions

Conclusions générales

Annexes

6.2. Introduction

Ce travail est dédié à l'étude des mécanismes de fissuration sous environnement très agressif d'un acier inoxydable super-martensitique utilisé dans le milieu Oil&Gas. Ce travail a été réalisé au sein du centre SMS de l'École des Mines de Saint-Étienne (France) en partenariat CIFRE avec Thermodyn SAS au Creusot (France), une entreprise du groupe Baker Hughes – General Electric.

Cette étude a été motivée par un cas industriel de fissuration assisté par l'environnement d'une roue de compresseur centrifuge travaillant en milieu H₂S et CO₂. Les compresseurs centrifuges sont des turbomachines avec un ou plusieurs étages de compression. Le nombre d'étage est adapté au taux de compression visé. Le domaine d'application est très large étant donné qu'ils peuvent compresser tout type de gaz avec un flux allant de 200 à 200 000 m³/h. La pression en sortie peut atteindre 700 bars. Les compresseurs construits au Creusot ont un débit maximal de 1000 000m³/h et une pression de 250 bars en sortie. Les roues sont montées en série sur un arbre en rotation. L'entrée d'une roue est alimentée en gaz par la sortie de la roue précédente (Figure 1).

Le gaz devant être compressé entre dans la roue par un orifice appelé « œil » de la roue et s'écoule au travers des pales (Figure 2). La rotation rapide de la roue entraîne un gain de moment du gaz lors de son passage et, à la sortie de la roue, le gaz est envoyé dans un diffuseur stationnaire ayant pour but de décroître sa vitesse pour augmenter sa pression dynamique en pression statique.

En régime stationnaire, les compresseurs centrifuges sont des machines à flux stable ce qui permet de réduire les vibrations de la machine. Néanmoins, localement, les contraintes peuvent dépasser les 500 MPa. Ces importantes sollicitations mécaniques à hautes températures et sur de longues périodes accroissent le risque de rupture due à la fatigue ou au fluage. Cependant, le risque

majeur pour le matériau reste la synergie entre les interactions mécaniques et l'environnement agressif.

Dans notre approche, nous allons nous concentrer sur les environnements les plus sévères qui peuvent être rencontrés. A savoir, ceux contenant de l' H_2S , du CO_2 , des chlorures et à bas pH. Des exemples de composition de gaz qui peuvent être rencontrés avant raffinage sont donnés dans les tableaux 1 et 2.

L' H_2S est un gaz corrosif et poison qui est de plus en plus présent dans les nouveaux gisements exploités à travers le monde. Sa pression peut atteindre plusieurs dizaine de bars. Il a été identifié comme étant un promoteur de l'entrée d'hydrogène dans les matériaux métalliques, responsable de la corrosion sous contrainte et de la fragilisation par l'hydrogène.

L' H_2S n'est pas seulement nocif pour les métaux ; c'est également un gaz inflammable et extrêmement toxique comme nous pouvons le voir dans le tableau 3. Par conséquent, son utilisation dans le domaine de la recherche est très limitée et seule une poignée de laboratoires sont habilités. L'École des Mines de Saint-Étienne n'est pas habilitée mais elle a cependant développé des partenariats avec des entreprises spécialisées comme l'Institut de la Corrosion de Fraisses (France) par exemple.

La sélection des matériaux pour les roues de compresseurs doit donc prendre en compte plusieurs éléments. Cette sélection est principalement influencée par le pH équivalent déterminé par la composition du champ de gaz en fonction des données du client. Des formules empiriques ont été développées pour calculer ce pH équivalent en fonction des pressions de CO_2 et d' H_2S .

Le taux de chlorure est également un point important qui influence la sélection des matériaux ; l'objectif principal étant d'éviter la piqûration.

Les aciers inoxydables supermartensitiques sont fréquemment utilisés dans le domaine Oil&Gas car ils présentent une bonne résistance à la corrosion en environnement agressif et une combinaison intéressante de haute résistance mécanique et de bonne ténacité. Ces aciers sont également une excellente solution économique comparé aux aciers inoxydable super-duplex ou au alliage base Ni. Cependant, pour être utilisé en toute sécurité dans le domaine Oil&Gas, les aciers inoxydables supermartensitiques doivent satisfaire de conditions strictes, notamment en termes de compromis entre une limite d'élasticité élevée, combinée à une forte ductilité. Par conséquent, leur domaine d'application est limité. Les conditions à satisfaire sont publiées dans la norme NACE MR0175.

Le Virgo™38 (X4CrNi 16-4), est un acier inoxydable supermartensitique à basse teneur en carbone de la famille des aciers sans précipitation. Il appartient à GE Oil&Gas (anciennement Creusot Loire) depuis 2002. Plus de 200 compresseurs en service sont équipés avec des roues faites en Virgo™38.

A l'origine, en 1960, le Virgo™38 était développé pour des applications en eau de mer. Ces premières applications dans le domaine de la compression de gaz agressifs furent sur le domaine de Lacq en France. Ce champ est connu pour être l'un des plus agressifs à cause de sa haute teneur en chlorure. Cette teneur avait initialement été sous-estimée et a conduit à la première rupture du

Virgo™38 en 2004. Cette rupture est intervenue lors d'un arrêt de la machine. De nos jours, environ 30% des machines installées par Thermodyn sont équipées avec des roues en Virgo™38.

Comme évoqué précédemment, cet alliage est très utilisé car il représente un avantage stratégique de part ces hautes caractéristiques mécaniques, sa haute limite d'application au sens de la norme NACE et son faible cout de production comparé au 17-4PH ou au superalliage Inconel. De plus, contrairement à ses concurrents, le Virgo™38 peut être brasé, ce qui évite l'utilisation du soudage, connu pour être dommageable pour la résistance en environnement agressif.

Cependant, les normes actuelles de la NACE limitent l'application des aciers inoxydables supermartensitique à un niveau de dureté inférieur à 23HRC à cause de quelques cas inexplicés de fissuration, et ce, même si les autres conditions étaient remplies. Comme le Virgo™38 ne peut pas satisfaire cette condition (HRC=28), il n'est pas considéré comme un alliage certifié NACE, même s'il est utilisé avec succès dans les mêmes environnements.

Des essais normalisés NACE ont été réalisés sur le Virgo™38 pour expliquer les quelques cas de fissuration qui se sont produits. Cependant, pour l'heure, aucun mécanisme n'a été identifié. C'est pourquoi, à l'heure actuelle, pour certaines applications, les certifications internes à GE Oil&Gas, calquées sur les recommandations NACE, imposent l'utilisation d'alliage base Ni, même si, comme évoqué précédemment, le Virgo™38 avait précédemment fait ses preuves.

Récemment, un compresseur centrifuge en Virgo™38 a présenté un nouveau cas de fissuration intergranulaire isolé non seulement sur ses roues mais également sur ses pièces statiques (Figure 3).

Ces cas isolés de fissuration ont motivés cette étude, dans le but d'identifier les mécanismes impliqués pour définir de manière plus précise les limites d'utilisation du Virgo™38. De plus, la connaissance de ces mécanismes pourraient permettre d'étendre le domaine d'utilisation des supermartensitiques ce qui entrainerait une réduction des coûts par le remplacement d'alliage de Ni.

Donc, le principal objectif de cette thèse est de comprendre les mécanismes impliqués dans les ruptures du Virgo™38. La fissuration sous environnement agressif des aciers inoxydables supermartensitiques dans le domaine Oil&Gas doit également être mise en regard de sa microstructure complexe. Le premier objectif est donc de comprendre et d'être capable de contrôler la microstructure et les propriétés mécaniques en résultant.

Le deuxième objectif est de vérifier si le Virgo™38 est capable de résister à la fragilisation dans des milieux peu agressifs en espérant, par des tests de traction lente, démontrer que c'est effectivement le cas.

Ensuite, il est nécessaire de reproduire les ruptures intergranulaires observées en service afin d'analyser les mécanismes. Pour se faire, des tests de traction lente en milieu très agressifs vont être utilisés. La plupart des expériences ont été réalisées dans un environnement agressif contenant un poison de recombinaison de l'hydrogène sous la forme Na_2S développé dans cette thèse. L'objectif étant de trouver un milieu suffisamment hydrogénant permettant d'obtenir le même type de rupture qu'en service et de déterminer le principal mécanisme de fissuration.

Au final, plusieurs tests en présence d'H₂S ont été réalisés dans des conditions très éloignées des applications actuelles du Virgo™38 dans le but de valider les mécanismes précédemment évoqués et en prévision d'un potentiel élargissement du domaine d'application actuel. Comme évoqué précédemment, ces tests ont été réalisés en partenariat avec l'Institut de la Corrosion.

Cette thèse sera divisée en cinq chapitres, le premier étant une revue bibliographique.

La compréhension et la maîtrise de la microstructure étant un point clé pour les aciers inoxydables super-martensitiques, le chapitre 2 sera dédié à l'étude de la microstructure et des propriétés mécaniques du Virgo™38 dans différents états métallurgiques.

Le troisième chapitre est dédié à l'étude du comportement du Virgo™38 en milieux acides sous potentiel imposé. Des tests avec une sévérité croissante seront présentés entraînant une réduction progressive de la ductilité de l'alliage. Deux phénomènes seront mis en évidence dans ce chapitre : La fragilisation par hydrogène et la corrosion sous contrainte assistée par la dissolution.

Le chapitre 4 sera centré sur le développement d'un milieu très hydrogénant et sur les tests de traction lente associés. La résistance à la fragilisation par l'hydrogène du Virgo™38 sous chargement cathodique sera également étudiée. De plus, comme la fragilisation est étroitement liée à la microstructure, ce chapitre traitera également de l'influence de la microstructure sur la résistance à la fragilisation par hydrogène du Virgo™38. Une attention particulière sera portée sur le rôle de l'austénite de réversion et sur la composition chimique des anciens joints de grains austénitiques (où la fissuration se produit). Nous considérons que les conditions proposées dans ce chapitre sont représentatives des conditions industrielles en présence d'H₂S.

Finalement, le chapitre 5 sera consacré à l'étude du comportement du Virgo™38 en présence d'H₂S. Il est important de noter que, dans ce chapitre, la plupart des conditions étudiées sont en dehors du champ d'application actuel des aciers inoxydables supermartensitiques dans le domaine Oil&Gas et que les mécanismes présentés ne correspondront pas nécessairement à ceux rencontrés en service actuellement. Cependant, cela nous permet de définir et d'étudier deux mécanismes comme la très répandue fragilisation par l'hydrogène en présence d'H₂S ou la moins connue corrosion sous contrainte assistée par la dissolution préférentielle.

6.3. Chapitre I

L'étude bibliographique présentée au cours de ce chapitre met en évidence la complexité des différentes microstructures des aciers inoxydables super-martensitiques trempés et revenus. Ces alliages sont polyphasés et principalement composés de martensite revenue (α'') et d'austénite de réversion (γ_R). La microstructure est caractéristique d'une martensite en latte avec l'austénite de réversion située entre les lattes de martensite et aux anciens joints de grain austénitiques. Cette microstructure conduit à des propriétés mécaniques correspondantes aux demandes de la norme NACE pour des applications Oil&Gas. Néanmoins, des cas isolés de rupture en service ont été observés par le passé et les mécanismes impliqués ne sont pas toujours complètement compris. Il est cependant sûr que l'amorce et la propagation de fissures dans les milieux hydrogénants de type Oil&Gas sont étroitement liées à la microstructure de l'alliage. Les deux phases principales des aciers inoxydables supermartensitiques sont caractérisées par un comportement totalement différent vis-à-vis de l'hydrogène (solubilité, coefficient de diffusion...). De plus, la transformation de

phase sous sollicitation mécanique ne peut pas être négligée, en particulier dans les régions de forte concentration de contrainte comme la zone déformée en pointe de fissure. Ce phénomène pourrait affecter la distribution de l'hydrogène dans la microstructure et influencer la sensibilité de l'alliage à la fissuration sous environnement agressif.

Comme vu tout au long de ce chapitre et par analogie avec la microstructure et les applications industrielles des aciers inoxydables duplex, en première approche, des mécanismes de fissuration peuvent être considérés comme étant similaires entre les aciers duplex et les aciers supermartensitiques. Il est possible de trouver plusieurs types d'endommagement en milieux acides dans la littérature concernant l'utilisation des duplex dans le milieu Oil&Gas, à savoir Corrosion Sous Contrainte (CSC), la Fragilisation par l'Hydrogène (FPH) ou la fragilisation par l'H₂S (SSC) par exemple. Le troisième chapitre de cette étude sera donc centré sur l'étude de deux de ces mécanismes (CSC et FPH) en milieux acides. Pour ce faire, des tests de traction lente (TL) sous potentiel imposé sont utilisés. Les potentiels imposés sont choisis au regard d'une étude électrochimique détaillée du Virgo™38.

Comme précédemment évoqué, l'une des particularités des milieux Oil&Gas est la présence d'H₂S qui entraîne une forte activité d'hydrogène qui peut provoquer la fragilisation des aciers suite à la dépassivation locale ou généralisée. Ces très hautes activités d'hydrogène peuvent être reproduites en utilisant des milieux empoisonnés comme celui utilisé au chapitre 4 de cette étude. Ce chapitre est également dédié à l'étude de l'influence de la microstructure, et notamment l'influence de l'austénite de réversion et de la précipitation, sur la résistance à la FPH.

Cependant, les résultats des tests présentés aux Chapitres 3 et 4 ne permettent pas d'identifier les mécanismes d'amorce de fissures rencontrés en service. C'est pourquoi le Chapitre 5 de cette étude est focalisé sur l'étude de la résistance du Virgo™38 en présence d'H₂S dans le but de nous rapprocher des conditions de service. Dans ce chapitre, les ruptures obtenues seront comparées aux mécanismes précédemment identifiés aux chapitres 3 et 4 et nous concluons sur les paramètres les plus impactant sur la sensibilité à la fissuration sous environnement agressif. La piqûration étant le mécanisme principal d'amorçage de fissures, son rôle est également discuté.

6.4. Chapitre II

Avant d'analyser le comportement du Virgo™38 sous environnement agressif, sa microstructure et ses propriétés mécaniques à l'air ont été étudiées dans différents états de traitement thermique. La microstructure de l'alliage industriel reçu est composée d'environ 75% de martensite revenu α'' et de 22% à 24% d'austénite de réversion, située entre les lattes de martensite. La microstructure contient également moins de 1% de carbures de chrome (M₂₃C₆) d'environ 20nm de diamètre selon les observations MET et les simulations Thermocalc. Une analyse quantitative par EDX dans un MET a montré la répartition hétérogène des éléments d'alliage tel que le Ni entre les phases CC et CFC. Cet effet est la cause de la modification de la stabilité de l'austénite pendant le revenu et permet d'obtenir des microstructures avec différents taux d'austénite de réversion.

Dans un second temps, l'effet de la température de revenu sur les compositions de chacune des phases et sur les propriétés en traction du Virgo™38 a été étudié à partir d'une microstructure ré-austénitisée, trempée et traitée à température négative. Ce traitement de 'remise à zéro' produit

une microstructure quasiment exclusivement martensitique contenant un faible taux de ferrite delta. Cependant, la trempe, aussi rapide soit elle, ne permet pas d'éviter la ségrégation du Si aux joints de grains austénitiques, entraînant une baisse localement significative de la température M_s . Les conséquences sont la présence potentielle d'un film fin d'austénite résiduelle non transformée proche des joints de grains. Ces « anciens » joints de grains austénitiques se trouveraient alors être de vrais joints qui auraient un impact fort sur les phénomènes de ségrégation pendant le revenu et sur la fissuration en environnements agressifs. Cependant, les preuves expérimentales récoltées par MET haute résolution sont trop rares pour confirmer cette hypothèse et plus d'investigations sont nécessaires.

Les analyses EBSD et DRX ont été utilisées pour étudier l'effet de la température de revenu sur la microstructure du Virgo™38. Ces observations ont été mises en relation avec les propriétés en traction à l'air et, en utilisant les modèles classiques de durcissement, il a été possible de déterminer les mécanismes de durcissement prépondérants et les limites élastiques des deux phases principales de l'alliage en fonction de la température de revenu. Les résultats peuvent être résumés comme suit :

Après un revenu à 'faibles' températures (500°C et 580°C), la limite à 0.01% d'allongement augmente par rapport à l'état trempé. Par des simulations Thermocalc et Prisma, nous avons montré que la précipitation de fins carbures $M_{23}C_6$ est à l'origine du durcissement observé. Un revenu à 620°C produit le maximum d'austénite de réversion et une limite à 0.01% plus faible que dans les états précédents. Les carbures formés à cette température sont trop gros pour produire un durcissement significatif. Après un revenu à haute température (660°C), l'austénite de réversion produite en température est instable et se transforme en martensite fraîche secondaire lors du refroidissement. Le taux d'austénite de réversion présent à température ambiante est donc plus faible que dans l'état précédent. Une augmentation modérée de la limite à 0.01% est également observée, mais cette dernière reste nettement inférieure à celles observées après un revenu à faibles températures.

La conclusion principale de l'analyse des mécanismes de durcissement est que lorsque l'austénite de réversion est présente, elle se trouve être la phase dure de l'alliage en comparaison à la martensite revenue qui est dépourvue de carbone. La limite d'élasticité de l'austénite de réversion est comparable à celle de la martensite de trempe. Ce résultat est à l'opposé de la plupart des hypothèses proposées dans la littérature qui ne s'appuient cependant pas sur des arguments irréfutables.

La combinaison entre le minimum de limite d'élasticité requis et la dureté maximale imposée est donc obtenue par une microstructure composée d'une phase 'molle', étant la martensite revenue, et d'une phase 'dure', étant l'austénite de réversion. Donc, en appliquant une charge proche de la limite à 0.2% et au-delà, la déformation plastique commencera indéniablement dans la martensite alors que l'austénite de réversion restera élastiquement déformée. Ce comportement pourrait s'avérer être décisif par rapport à l'amorce et la propagation de fissures en environnement agressif. Cette conclusion permet également de comprendre pourquoi la transformation de phase sous contrainte de l'austénite de réversion commence à une valeur élevée de contrainte (700MPa) alors que sa température M_s est proche de la température ambiante. Cette transformation est également

dure à mener à terme puisque seulement 50% de l'austénite est transformée après un allongement de 10% (correspondant à la R_m).

6.5. Chapitre III

L'étude de la corrosion en milieux acides a commencé par l'étude de la stabilité du film passif dans ces milieux par l'intermédiaire de mesures électrochimique. Il a été démontré que le pH de dépassivation des deux phases étaient différents (1.5 pour la martensite et 1.6 pour l'austénite de réversion). Cette différence s'explique par le phénomène de répartition des éléments d'alliage mis en évidence au chapitre précédent, et notamment par la différence de Cr dans chacune des phases. Des mesures XPS nous ont permis de conclure que le film passif formé en surface de l'austénite est plus épais que celui en surface de la martensite mais qu'il contient également significativement moins de Cr et plus de Fe. L'application d'une charge constante correspondant à 100% de la limite à 0.2% de l'alliage nous a permis de démontrer que le pH de dépassivation des deux phases augmenté jusqu'à 2.0 et 2.2 respectivement suite à une déstabilisation mécanique.

Deux mécanismes de fragilisation assistée par l'environnement ont été détaillés dans ce chapitre : la Fragilisation par Hydrogène (FPH) sous chargement cathodique et la Corrosion Sous Contrainte Anodique (CSCA) en imposant un potentiel égal au pic d'activité de chacune des phases. Ces deux mécanismes ont été étudiés en milieu acide à un pH inférieur au pH de dépassivation déterminé sous chargement constant.

Le faible taux de fragilisation obtenu sous chargement cathodique démontre que le Virgo™38 est assez résistant à la FPH lorsque le H_2S n'est pas présent, et ce, même lorsque le pH est très faible (jusqu'à 1.5). Cependant, ces conditions ne sont probablement pas très représentatives des conditions de service dû à la baisse importante de pH nécessaire à l'obtention d'un minimum de fragilisation. Même si les tests de FPH montrent le plus fort taux de fragilisation, la fugacité d'hydrogène ne semble pas être suffisante pour reproduire les ruptures intergranulaires obtenues en service. Le chapitre suivant sera dédié à l'étude de la FPH dans un environnement où l'activité d'hydrogène est nettement supérieure. Ce milieu nous permettra de conclure sur un possible mécanisme de propagation de fissure.

Lorsque le potentiel appliqué pendant les essais de traction lente est proche de l'un ou l'autre des potentiels d'activité, il a été montré au cours de ce chapitre que le Virgo™38 était plus sensible à la FPH qu'à la CSCA. La différence entre les potentiels d'activité des deux phases, due à l'effet de répartition hétérogène des éléments d'alliage comme démontré dans ce chapitre, semble être à l'origine de la dissolution préférentielle soit de l'austénite de réversion (à 'haut' pH, entre 1.5 et 1.6) soit de la martensite revenue (à bas pH, <1.5). La résistance à la dissolution anodique est plus faible pour la martensite que pour l'austénite de réversion. Les essais de traction lente à potentiel libre ont montré que le mécanisme était la CSCA entraînant la dissolution de l'une ou l'autre des phases, cela étant dû à des micro-couplages entre ces deux phases. Ce mécanisme sera également observé en présence d' H_2S dans le chapitre 5 de cette étude.

6.6. Chapitre IV

Nous avons vu au chapitre précédent que les hétérogénéités de composition entre les deux phases constituant notre alliage étaient à l'origine du phénomène de corrosion sous contrainte. Cependant, le phénomène de fragilisation par hydrogène fréquemment rencontré conduisant à des ruptures fragiles de type intergranulaire n'avait pas pu être étudié. C'est pourquoi, un milieu contenant un poison de recombinaison d'hydrogène (Na_2S) a été utilisé. Les tests de perméation électrochimique réalisés ont confirmés que l'ajout de 0.02M de Na_2S permettait d'augmenter l'activité de l'hydrogène sous chargement cathodique à -1300mV/ECS. Cette augmentation de l'activité d'hydrogène est attribuée à l'adsorption en surface du soufre qui favorise l'entrée d'hydrogène dans le métal par la réduction de la cinétique de recombinaison en surface. Le flux d'hydrogène résultant est donc nettement supérieur et, selon la littérature, équivalent à celui mesuré dans un milieu industriel contenant 1 bar H_2S et à pH=4.5, soit environ 50MPa.

Dans ce chapitre, nous avons également mis en évidence une synergie entre la ségrégation du phosphore aux joints de grain et l'effet de l'hydrogène qui peut être l'une des causes à l'origine des ruptures intergranulaires du Virgo™38.

Cette étude souligne l'importance de la microstructure qui a un impact fort sur les mécanismes de fissuration de l'acier inoxydable supermartensitique Virgo™38. En particulier, les conditions de traitement thermique doivent être choisies très précisément et en connaissance de toutes les modifications microstructurales qu'il implique. Tous ces éléments expliquent que le Virgo™38 doit être utilisé dans l'état sur revenu d'un point de vue de la précipitation des carbures de chrome comme défini au chapitre 2. En effet, les petits précipités entraînent une forte augmentation de la $R_{p0.2}$ pouvant entraîner des ruptures fragiles en environnement voire à l'air. Il a également été montré qu'une forte activité d'hydrogène conduisait à une fragilisation significative du Virgo™38. De plus, alors que la ségrégation du phosphore n'est pas préjudiciable pour la résistance mécanique du Virgo™38 dans les conditions de traitement optimisées (car sa limite d'élasticité est faible), elle devient dangereuse lorsqu'elle est couplée avec l'hydrogène. Il est maintenant plus facile de comprendre certaines limitations des normes NACE, en particulier la limitation de la dureté des super-martensitiques qui est indirectement reliée à une limitation de limite d'élasticité.

L'analyse des ruptures intergranulaires du couvercle nous a permis de mettre en évidence la relation entre la ségrégation de phosphore et la fragilisation par hydrogène. Dans le but de quantifier ces interactions entre hydrogène et ségrégation, il apparaît primordial de réaliser des simulations numériques basées sur le modèle de Krom d'une part et sur des simulations atomistiques d'autre part. La prise en compte du piégeage de l'hydrogène dans l'austénite de réversion comme il a été fait très récemment et la considération de la diminution de l'énergie de cohésion des joints de grain due à la ségrégation du phosphore apparaît indispensable. A priori, un tel travail de simulation prenant en compte à la fois la ségrégation du phosphore et le piégeage de l'hydrogène n'a jamais été réalisé jusqu'à présent. Cela constitue un challenge intéressant pour une poursuite de cette étude.

Cependant, dans le milieu présenté au cours de ce chapitre, il n'est pas possible d'étudier les effets combinés et la compétition entre la fragilisation par hydrogène et la dissolution anodique qui peut intervenir à potentiel libre dans les milieux contenant de l' H_2S . C'est pourquoi, le chapitre 5 va

être dédié à l'étude de la fragilisation par hydrogène et de la corrosion sous contrainte du Virgo™38 en présence d'H₂S.

6.7. Chapitre V

Comme attendu pour les conditions de test choisies au cours de ce chapitre, une forte fragilisation a été obtenue. Les fissures ont quasiment toutes étaient amorcées dans le domaine élastique macroscopique, ce qui confirme bien que le Virgo™38 doit être utilisé élastiquement et que la plastification locale peut être dommageable. Les quatre paramètres étudiés dans cette étude (pH, pH₂S, vitesse de déformation et concentration en chlorure) ont tous une influence différente sur le comportement du Virgo™38 et plusieurs mécanismes ont pu être identifiés.

Pour des pH supérieurs à 3.0, l'amorçage de fissures se produit sur des piqûres métastables ou sur des défauts mécaniques présents en surface. Ces sites semblent étroitement liés aux interactions entre la corrosion et la déformation puisque peu (ou pas) de piqûres sont observés dans les congés de l'éprouvette. Les faciès de rupture ne sont pas affectés par la corrosion dans ce domaine de pH et le mode de rupture est majoritairement transgranulaire. La densité de fissure secondaire augmente très nettement lorsque le pH diminue, sans pour autant que cela est une influence majeure sur le comportement macroscopique. Ces phénomènes ont été identifiés comme étant de la FPH.

A des pH très bas (1.5 et 2.0 en absence de chlorure et 2.5 en présence de 600ppm de chlorures), le Virgo™38 est dans le régime actif. Les fissures s'amorcent très rapidement en fond des défauts de corrosion créés à la surface. Des signes de dissolution de la martensite ou de l'austénite de réversion ont également été observés en fonction du pH initial et de la profondeur de fissure. Dans ces cas, le mécanisme identifié est celui de la CSCA.

La relation entre la réduction d'aire et la vitesse de déformation nous a permis de valider la présence de deux mécanismes de propagation de fissures impliqués dans les phénomènes de fragilisation du Virgo™38. Aux très bas pH (inférieur à 3.0), il a été prouvé que notre alliage était sensible à la CSCA. Les vitesses de corrosion atteintes dans les milieux étudiés au cours de ce chapitre sont nettement supérieures à celle rencontrées au cours du chapitre 3, ce qui explique la fragilisation importante du Virgo™38. A des pH plus élevés (supérieur à 3.0), la relation entre la réduction de section des éprouvettes testés et la vitesse de déformation nous permet de conclure que le Virgo™38 est sensible à la FPH, comme il avait été démontré au cours des quelques ruptures intergranulaires intervenues en service.

Dans le domaine de pH favorisant la FPH, une augmentation de la pression partielle d'H₂S entraîne une augmentation de la fragilisation du Virgo™38. Cette augmentation est attribuée à la plus forte activité d'hydrogène dans ces conditions. En effet, comme nous l'avions évoqué au chapitre précédent, une augmentation de l'activité d'hydrogène entraîne une diminution de la réduction de section. Cependant, l'activité d'hydrogène n'a d'influence sur la fissuration que lorsque l'hydrogène peut effectivement pénétrer dans le matériau. En effet, si le film passif est suffisamment stable pour éviter l'entrée d'hydrogène alors les fissures ne pourront pas se développer et le matériau pourrait théoriquement à des pressions d'H₂S très importantes (cf annexe 4).

Nous avons également observé que les chlorures jouent un rôle prépondérant sur la fissuration assistée par l'environnement du Virgo™38. Les hétérogénéités de composition mises en évidence au

chapitre 2 entraînent une localisation de la piqûration sur l'austénite résiduelle. Des piqûres se développent également sur les quelques inclusions présentes dans le matériau comme les carbures de titane par exemple.

6.8. Conclusions et perspectives

Le principal objectif de cette thèse était de déterminer quels étaient les mécanismes impliqués dans les quelques ruptures survenues en milieu industriel sur le Virgo™38 et, de manière plus générale, de déterminer quel est l'ensemble des mécanismes pouvant réduire sa résistance à la fissuration en environnement agressif. Pour se faire, la fissuration du Virgo™38 a été reproduite en laboratoire dans différentes conditions : la Corrosion Sous Contrainte (CSC) impliquant des phénomènes de type anodique et la Fragilisation par l'Hydrogène (FPH) impliquant des phénomènes de type cathodique. Trois milieux différents ont été utilisés au cours de cette étude, à savoir : un milieu industriel contenant de l'H₂S dans lequel la CSC et la FPH ont pu être étudiées, un milieu très acide ne contenant pas d'H₂S dans lequel la CSC a été mise en évidence et un milieu à pH élevé contenant un poison de recombinaison d'hydrogène sous forme Na₂S dans lequel la FPH a pu être étudiée.

Avant d'analyser le comportement du Virgo™38 sous environnement agressif, sa microstructure et ses propriétés mécaniques à l'air ont été étudiées dans différents états de traitement thermique. La microstructure de l'alliage industriel reçu est composée d'environ 75% de martensite revenu α'' et de 22% à 24% d'austénite de réversion, située entre les lattes de martensite. La microstructure contient également moins de 1% de carbures de chrome (M₂₃C₆) d'environ 20nm de diamètre selon les observations MET et les simulations Thermocalc. Une analyse quantitative par EDX dans un MET a montré la répartition hétérogène des éléments d'alliage tel que le Ni entre les phases CC et CFC. Cet effet est la cause de la modification de la stabilité de l'austénite pendant le revenu et permet d'obtenir des microstructures avec différents taux d'austénite de réversion.

Dans un second temps, l'effet de la température de revenu sur les compositions de chacune des phases et sur les propriétés en traction du Virgo™38 a été étudié à partir d'une microstructure ré-austénitisée, trempée et traitée à température négative. Ce traitement de 'remise à zéro' produit une microstructure quasiment exclusivement martensitique contenant un faible taux de ferrite delta. Cependant, la trempe, aussi rapide soit elle, ne permet pas d'éviter la ségrégation du Si aux joints de grains austénitiques, entraînant une baisse localement significative de la température M_s. Les conséquences sont la présence potentielle d'un film fin d'austénite résiduelle non transformée proche des joints de grains. Ces « anciens » joints de grains austénitiques se trouveraient alors être de vrais joints qui auraient un impact fort sur les phénomènes de ségrégation pendant le revenu et sur la fissuration en environnements agressifs. Cependant, les preuves expérimentales récoltées par MET haute résolution sont trop rares pour confirmer cette hypothèse et plus d'investigations sont nécessaires.

Les analyses EBSD et DRX ont été utilisées pour étudier l'effet de la température de revenu sur la microstructure du Virgo™38. Ces observations ont été mises en relation avec les propriétés en traction à l'air et, en utilisant les modèles classiques de durcissement, il a été possible de déterminer les mécanismes de durcissement prépondérants et les limites élastiques des deux phases principales de l'alliage en fonction de la température de revenu. Les résultats peuvent être résumés comme suit :

Après un revenu à 'faibles' températures (500°C et 580°C), la limite à 0.01% d'allongement augmente

par rapport à l'état trempé. Par des simulations Thermocalc et Prisma, nous avons montré que la précipitation de fins carbures $M_{23}C_6$ est à l'origine du durcissement observé. Un revenu à 620°C produit le maximum d'austénite de réversion et une limite à 0.01% plus faible que dans les états précédents. Les carbures formés à cette température sont trop gros pour produire un durcissement significatif. Après un revenu à haute température (660°C), l'austénite de réversion produite en température est instable et se transforme en martensite fraîche secondaire lors du refroidissement. Le taux d'austénite de réversion présent à température ambiante est donc plus faible que dans l'état précédent. Une augmentation limitée de la limite à 0.01% est également observée, mais cette dernière reste nettement inférieure à celles observées après un revenu à faibles températures.

La conclusion principale de l'analyse des mécanismes de durcissement est que lorsque l'austénite de réversion est présente, elle se trouve être la phase dure de l'alliage en comparaison à la martensite revenue qui est dépourvue de carbone. La limite d'élasticité de l'austénite de réversion est comparable à celle de la martensite de trempe. Ce résultat est à l'opposé de la plupart des hypothèses proposées dans la littérature qui ne s'appuient cependant pas sur des arguments irréfutables.

La combinaison entre le minimum de limite élastique requis et la dureté maximale imposée est donc obtenue par une microstructure composée d'une phase 'molle', étant la martensite revenue, et d'une phase 'dure', étant l'austénite de réversion. Donc, en appliquant une charge proche de la limite à 0.2% et au-delà, la déformation plastique commencera indéniablement dans la martensite alors que l'austénite de réversion restera élastiquement déformée. Ce comportement pourrait s'avérer être décisif par rapport à l'amorce et la propagation de fissures en environnement agressif. Cette conclusion permet également de comprendre pourquoi la transformation de l'austénite de réversion sous contrainte commence à une valeur élevée de contrainte (700MPa) alors que sa température M_s est proche de la température ambiante. Cette transformation est également dure à mener à terme puisque seulement 50% de l'austénite est transformée après un allongement de 10% (correspondant à la R_m).

Une fois la métallurgie de notre alliage maîtrisée, une étude électrochimique détaillée a été faite, ce qui nous a permis de déterminer les pH de dépassivation de chacune des phases en présence. Il a été démontré que l'austénite de réversion se dépassivait à des pH plus élevée que la martensite (1.6 contre 1.5 respectivement). Cette différence est attribuée à la différence de Cr dans les couches passives de chacune des phases. Cette étude électrochimique a également été réalisée sous charge constante correspondant à 100% de la limite à 0.2%. Il a été montré que les vitesses de corrosion et les pH de dépassivation augmentés.

Cette étude préliminaire nous a permis de choisir précisément les potentiels à appliquer lors des essais de traction lente en milieu acide. Nous avons limité notre étude aux essais de traction lente car ils permettent d'étudier à la fois l'amorce et la propagation des fissures. En effet, ces tests sont connus pour reproduire fidèlement les phénomènes de fissuration grâce à l'étude des fissures secondaires. Cependant, comme le Virgo™38 est un alliage très résistant, il a été difficile de reproduire le mécanisme de FPH dans ce milieu et il a fallu décroître de manière importante le pH afin d'obtenir des ruptures intergranulaires. La CSC a également été étudiée grâce à des tests de traction sous potentiels imposés. Les potentiels ont été choisis en regard de la précédente étude électrochimique sous contrainte. Ces tests ont montré un faible taux d'endommagement comparés à ceux observés au cours des tests de FPH.

En raison de l'endommagement limité obtenu précédemment, un milieu plus agressif devait être développé dans le but d'obtenir une plus forte fragilisation et par conséquent d'obtenir des ruptures comparables à celles observées industriellement. Ce nouveau milieu a été développé en appui sur des expériences de perméation électrochimique qui ont montré qu'appliquer un potentiel cathodique dans un milieu basique contenant du Na_2S permettait d'atteindre des activités d'hydrogène équivalentes à celles mesurées en présence d' H_2S . La hausse de l'activité d'hydrogène a été attribuée à l'adsorption en surface de soufre dans une gamme de potentiel allant de -600mV/ECS à -1400mV/ECS . En effet, cet élément est connu pour faciliter l'entrée d'hydrogène au sein des matériaux métalliques en bloquant sa recombinaison en hydrogène gazeux à la surface des alliages.

Des essais de traction lente dans ce nouveau milieu ont conduit à la rupture totalement intergranulaire du Virgo™38 et ont permis l'étude des mécanismes de propagation impliqués. Selon la bibliographie, le mécanisme de FPH le plus probable est le mécanisme *HEDE*. Des essais réalisés sur des éprouvettes ayant différentes microstructures, obtenues par traitement thermique ou écrouissage, ont montré que la microstructure avait une importance primordiale sur la résistance à la FPH. En particulier, l'austénite de réversion semble avoir un effet bénéfique, du moins jusqu'à un taux de 15%. Au-delà de cette valeur, son instabilité mécanique entraîne une réduction de la résistance du Virgo™38, due à la libération et à la répartition de l'hydrogène qu'elle contenait avant sa transformation. L'hydrogène n'est cependant pas le seul élément responsable des ruptures intergranulaires identifiées dans cette étude. En effet, des mesures Auger ont démontré une ségrégation fragilisante du phosphore aux joints de grains jusqu'à 10% d'une fraction de monocouche atomique. Cela entraîne une réduction de l'énergie de cohésion de cette interface et facilite alors son ouverture. Cet effet s'est retrouvé être particulièrement préjudiciable lors de revenus proche de 500°C , qui sont bien en deçà de ceux appliqués industriellement.

En présence d' H_2S , deux mécanismes d'amorce de fissure ont été mis en évidence : la piqûration à pH élevé (>3.0) et la corrosion généralisée faisant suite à une dépassivation chimique à pH plus faible. En effet, à des pH inférieurs à 3.0 (c-à-d sous le pH de dépassivation) les fissures peuvent s'amorcer par dissolution préférentielle de l'austénite ou de la martensite selon le pH de milieu. Comme démontré au chapitre 3, le couplage galvanique entre les deux phases dû à l'effet de répartition hétérogène des éléments d'alliage a été identifié comme le responsable de l'amorce des fissures à bas pH. Au contraire, à des pH plus élevés, l'amorce de fissure est due à la piqûration. Une fois encore, il a été identifié que les hétérogénéités de composition entre les deux phases entraînent la localisation des piqûres sur l'austénite de réversion. Cependant, les inclusions présentes dans le matériau industriel s'avèrent être plus dommageable d'un point de vue de la résistance à la piqûration. Les tests de traction lente à différentes vitesses de déformation ont confirmé que les deux mécanismes (CSC et FPH) se produisaient. La frontière a été établie à un pH de 3.0. Aux pH les plus bas, le Virgo™38 est sensible à la CSC anodique comme étudié lors du chapitre 3, tandis qu'à des pH plus élevés, correspondant au domaine d'application, le mécanisme impliqué était de type FPH. Comme démontré au chapitre 4, l'augmentation de l'activité d'hydrogène entraîne une diminution de la résistance du Virgo™38.

Pour la suite, il serait nécessaire d'établir précisément la relation entre le taux d'austénite de réversion et la limite d'élasticité de l'alliage biphasé, dans le but de confirmer que l'austénite est bel et bien la phase dure dans le Virgo™38 traité industriellement. Cela pourrait être fait en réalisant des traitements thermiques avec des temps de maintien différents (dans le but de varier le taux

d'austénite de réversion) et de réaliser les tests de traction. Le problème de cette approche réside dans le fait que la martensite revenue ne serait pas la même dans tous les états, ce qui pourrait potentiellement masquer l'effet de l'austénite de réversion. Une autre solution serait l'élaboration de matériaux modèles monophasés de même composition et densité de dislocation que celles déterminées au chapitre 2.

Des analyses approfondies par MET haute résolution sur l'état trempé nous permettraient de démontrer formellement la présence d'austénite résiduelle proche des anciens joints de grain austénitique. Une alternative à l'étude MET serait une étude métallographique après attaque chimique dans 2 états : un état trempé et traité à température négative industriellement (où la température est plus faible que le M_f global mais certainement plus élevée que le M_f des zones enrichies en Si) et un état trempé et traité à -196°C dans l'azote liquide (où la température serait bien entendu inférieure au M_f des zones enrichies en Si).

L'effet de couplage galvanique mis en évidence au chapitre 3 devrait également être étudié sur des structures plus larges par exemple par l'intermédiaire d'élaboration d'alliages modèles monophasés. Ces matériaux modèles nous permettraient également d'étudier la composition des films passifs de manière plus aisée.

De plus, nous avons envisagé l'influence de l'activité de l'hydrogène sur le mode de rupture. Pour justifier les hypothèses avancées, il serait intéressant de réaliser des essais de traction lente dans des milieux contenant différents teneurs en Na_2S et de déterminer les activités d'hydrogène correspondantes par des mesures de perméation électrochimique. Nous espérons pouvoir démontrer que le taux de rupture intergranulaire diminue avec l'activité d'hydrogène décroissante. Il serait également utile de comparer les flux d'hydrogène obtenus dans ces milieux modèles à ceux obtenus en présence d' H_2S .

Une hypothèse importante avancée au chapitre 4 stipulait que l'adoucissement de la martensite jouait un rôle majeur dans la résistance à la FPH du virgo™38. En fait, l'effet bénéfique du traitement au pic de formation de l'austénite a été attribué à la présence du taux maximal d'austénite alors qu'il pourrait s'agir uniquement d'un effet bénéfique de l'adoucissement de la martensite. Dans ce cas, la diminution de l'allongement pour des revenus hautes températures seraient non pas dû à la diminution d'austénite de réversion mais bel et bien à l'apparition de martensite fraîche secondaire. Afin de prouver cette dernière hypothèse, il serait bon de réaliser un alliage modèle 100% martensitique et de réaliser différents traitements d'adoucissement de la martensite. Notre espoir est de montrer que la résistance de cet alliage augmente avec l'adoucissement progressif de la martensite lors de l'augmentation de la température de revenu (sans former d'austénite de réversion). Si tel est le cas, la résistance du Virgo™38 pourrait être nettement améliorée par un revenu à plus haute température, mais le risque serait alors de former moins d'austénite et donc de ne pas satisfaire les propriétés mécaniques désirées (si l'on considère que l'austénite est effectivement la phase durcissante). Il faudrait alors augmenter la température $\text{Ac}1$ par l'ajout de Cr ou de Mo dans l'alliage ou alors réaliser le premier revenu NACE à plus haute température.

Pour finir, pour améliorer la résistance du Virgo™38 en présence d' H_2S , il apparaît primordial d'augmenter la résistance de son film passif et en particulier sa résistance à la piqûration et à la dépassivation. La solution la plus simple paraît être de réduire le taux d'inclusions de carbures et nitrures.

NNT : *Communiqué le jour de la soutenance*

Clément GAYTON

EMBRITTEMENT MECHANISMS OF THE X4CrNi16-4 SUPER-
MARTENSITIC STAINLESS STEEL VIRGO™38: EFFECTS OF HEAT
TREATMENTS AND CORROSIVE ENVIRONMENTS CONTAINING Na₂S
OR H₂S

Speciality: Materials Science and Engineering

Keywords: Supermartensitic stainless steel, hydrogen embrittlement, preferential dissolution, PGBS

Abstract:

This PhD thesis is focused on the study of embrittlement mechanisms in a 16Cr-4Ni low carbon supermartensitic stainless steel (Virgo™38) used for the construction of rotating parts of centrifugal compressors produced by GE Oil&Gas.

It is shown that the morphologically complex multiphase microstructure of this alloy is very sensitive to the heat treatment conditions. In particular, the fraction and repartition of retained austenite, the presence of chromium carbides and the phosphorous grain boundary segregation (PGBS) are evidenced consecutive to several heat treatments. PGBS is one of the mechanisms leading to brittle failure of Virgo™38 after specific heat treatments.

The presence of retained austenite is not only beneficial for toughness but also leads to hydrogen trapping in this phase. Due to the mechanical instability of retained austenite, its transformation under applied stress leads to the release of trapped hydrogen into newly formed martensite and thus to a local overconcentration of hydrogen. Hydrogen embrittlement is the second mechanism studied in this report.

Mechanisms involved during the formation of retained austenite lead to the heterogeneous repartition of alloying elements (partitioning). One of the consequences being the selective dissolution of one or the other phase of the alloy as a function of the pH of the environment and of the load applied. Preferential dissolution is the third mechanism studied.

NNT : *Communiqué le jour de la soutenance*

Clément GAYTON

MÉCANISMES DE FRAGILISATION DE L'ACIER INOXYDABLE SUPER-
MARTENSITIQUE X4CrNi16-4 VIRGO™38 : EFFETS COUPLÉS DES
TRAITEMENT THERMIQUE ET DES MILIEUX CORROSIFS
CONTENANT Na₂S OU H₂S

Spécialité: Sciences et Génie des Matériaux

Mots clefs : Acier inoxydable supermartensitique, fragilisation par hydrogène, dissolution préférentielle, ségrégation intergranulaire

Résumé :

Ce travail de thèse porte sur l'étude de divers mécanismes de fragilisation d'un acier inoxydable super-martensitique 16Cr-4Ni à basse teneur en carbone (Virgo™38) utilisé pour la fabrication des éléments tournants des compresseurs centrifuges produits par GE Oil&Gas. Il a été montré que la microstructure fine, polyphasée et morphologiquement très complexe de cet alliage était sensible aux conditions de traitement thermique. Notamment, la proportion et la répartition de l'austénite de réversion, la présence de carbure de chrome et la ségrégation intergranulaire d'éléments fragilisant tel que le phosphore ont été mis en évidence suite à plusieurs traitements thermiques. La ségrégation du phosphore aux joints de grain (SPJG) est l'un des mécanismes entraînant la fragilisation du Virgo™38 sous certaines conditions de traitement thermique.

La présence d'austénite de réversion n'entraîne pas seulement une amélioration de la ténacité de l'alliage mais également le piégeage de l'hydrogène dans cette phase. Etant donnée la grande instabilité mécanique de l'austénite, sa transformation sous contrainte provoque la libération de cet hydrogène piégé et ainsi une surconcentration locale en hydrogène. La fragilisation par hydrogène est le deuxième mécanisme entraînant la fragilisation du Virgo™38 étudié dans cette thèse.

Les mécanismes mis en jeu lors de la formation de l'austénite de réversion conduisent à la répartition hétérogène des éléments d'alliage. L'une des conséquences de cette répartition hétérogène est la corrosion sélective de l'une ou l'autre des phases de l'alliage en fonction du pH de l'environnement et de la charge appliquée. La dissolution préférentielle est le dernier mécanisme abordé entraînant la fragilisation du Virgo™38.